UNIVERSITÀ DEGLI STUDI DELL'INSUBRIA
DOCTORAL PROGRAMME IN ASTRONOMY AND ASTROPHYSICS
XXVIII CYCLE – 2015/2016

ANGULAR RESOLUTION IMPROVEMENT OF SLUMPED THIN GLASS OPTICS FOR X-RAY TELESCOPES

Ph.D. Thesis by:
Bianca Salmaso

Supervisor:	Dr. Daniele Spiga
Tutor:	Dr. Roberto Della Ceca
The Chair of the Doctoral Program:	Prof. Aldo Treves
Committee:	Prof. Mosè Mariotti
	Prof. Gianpaolo Rosati
	Prof. Piero Rosati

The research reported in this thesis was carried out at the
Osservatorio Astronomico di Brera-Merate, Italia.

To my three wonderful kids: Federico, Chiara, and Francesca

Abstract

Current X-ray telescopes such as Chandra and XMM were designed and built to privilege the angular resolution or the collecting area respectively, but using two different manufacturing techniques, and these two key aspects could not be optimised at the same time. The result is that the high-redshift X-ray Universe is still too unresolved to provide us with the understanding of the time evolution of the universe as we see it nowadays. Now the ATHENA mission, approved for the L2 slot in the Cosmic Vision program, is required to have an effective area of 2 m^2 at 1 keV and an angular resolution better than 5 arcsec Half-Energy Width (HEW). At this regard, in addition to the baseline solution based on Silicon Pore Optics (SPO), thin glass foils are considered a viable alternative. Slumped glass foils are also considered as substrates for X-ray optics being developed in other projects; for example, the X-ray Surveyor mission being developed at SAO/CfA in USA, and the AXYOM project being developed in Italy. They both foresee the use of piezo-electric actuators to correct the shape errors of the mirrors.

The Brera Astronomical Observatory (INAF-OAB, Merate - Italy) has been working, from 2009 till 2013, under ESA contract aimed to develop in Europe a Slumped Glass Optics (SGO) technology, alternative to the one based on silicon pores, and based on the slumping of thin glass foils, in parallel to the work being carried out at NASA/GSFC and other institutes. The INAF-OAB innovation is the use of pressure in the hot slumping process to replicate the mould figure. This technology is coupled with an integration process able to damp low frequency errors.

My Ph.D. activity, carried out at the INAF-OAB, is devoted to the advancement in the hot slumping technology assisted by pressure, for the production of glass mirrors for future X-ray telescopes. As a preliminary work, I have developed a new method to precisely characterise the mid frequency errors of the glass foils. An existing model, developed by Jimenez-Garate in 2003 to account for the relaxation of ripples in the slumped glass foil when in contact with the slumping mould, was modified to include the application of pressure, and the model was compared to the experimental results. The pressure was found to be essential, also from the the theory viewpoint, to reduce mid-frequency errors in the profile of slumped glass foils, which crucially degrade the performances of the optics. As for the slumping process, I have introduced a new glass material (Corning Eagle XG) combined with the Schott Zerodur K20, already chosen at earlier times as slumping mould material for its anti-sticking properties. I have developed cleaning protocols, used different thermal cycles and different pressures conditions, and reconditioned the pressure control system. I have also optimised the mould height with experiments based on Finite Element Analysis, and reduced the thermal gradients inside the mould and the glass foils.

The final result obtained in this research are slumped glass foils with angular resolution improved from the initial 7 arcsec to 2.2 ± 0.3 arcsec in single reflection, as expected from metrology at 1 keV X-ray energy and 0.7 incidence angle, and computed by simulating a perfect integration.

This result has to be compared with 2 arcsec defined as the error budget allocated for the slumped glass foils. About 1 arcsec is due to replication of the mid-frequency errors in the slumping mould which, owing to the improved result in the slumping, are now a limiting factor in the quality of the slumped glass foils. From the roughness point of view, the contribution to the HEW is guaranteed to be less then 1 arcsec at 1 keV, with an rms improvement from 21 to 11 Å throughout my Ph.D. Moreover, the last tests carried out proved that the roughness of the slumped glass foils can be further reduced to $\sim$ 7 Å, making the technology attractive also for higher X-ray energies and higher incidence angles.

The glass foils slumped during this Ph.D. have been used for the production of two SGO Proof Of Concept prototypes (POC) for the ATHENA mission: the POC#3, (with 2 glass foils assembled) is characterised by HEW value of 5.5 arcsec at 0.27 keV in the best portion of the module, as tested at the PANTER facility; the POC#4 (with 8 glass foils) has expected HEW of about 15 arcsec from metrological data, but the result in X-ray was much higher because of accidental problems during the integration. The next prototype, the POC#5 (with the best eight glass foils produced during my Ph.D. activity), will soon be integrated and tested in X-rays, to assess the improvement already proven by metrology and simulations. Some of the produced slumped glass foils have also been used for studies of active profile corrections with piezoelectric elements, both for the AXYOM project and X-ray Surveyor mission.

Alternative materials and techniques have been used in this research to further improve the result. To reduce the surface micro-roughness of the slumped glass foils, I have proven that the slumping technique with pressure application can also be suited in the indirect slumping, in which the optical surface of the glass is not in contact with the mould, thus preserving its initial surface smoothness. Moreover, the dip coating technique was studied to fill the micro-pores present on the surface of the glass foils slumped with the direct technique. Alternative materials for the slumping mould were tested, defining Si_3N_4 as a very promising candidate, owing to its higher rigidity with respect to Zerodur K20 and therefore preferable to avoid mould deformations with the slumping, as experienced with K20. The Gorilla glass (normally used for smartphones and tablets), was proven to preserve the surface quality of the glass foils, once slumped and chemically tempered to increase the mirror endurance against the vibrations experienced at launch.

Finally, I have also studied the scattering and the reflectivity properties of multilayer coatings for X-ray optics. I have upgraded an IDL code to simulate the roughness growth in the multilayer deposition process, extending the computations from periodic to the more general case of graded multilayers. I have also contributed to the X-ray measurements at the BEAR beamline of the Elettra synchrotron in Trieste, on multilayers deposited on glass, silicon and electroformed nickel, for the polarimetric LAMP project.

Introduction

Aiming to observe astronomical X-ray sources, it was necessary to wait the advent of the space era, because X-rays cannot penetrate the Earth's atmosphere. After the discovery in 1962 of Sco X-1, the first extrasolar X-ray source, a diffused Cosmic X-ray Background was observed by Riccardo Giacconi. By now, the uniform X-ray glow is thought to result from an integrated contribution of discrete sources rather than a truly diffused emission. We nowadays know that there are diverse astrophysical objects that emit X-rays, such as X-ray binary stars (XBN), supernova remnants, galaxy clusters, black holes in active galactic nuclei, gamma ray bursts. The understanding of their physics requires detailed information, from both spatial and spectroscopic point of view. Starting from the Einstein observatory, carrying the first X-ray imaging telescope in the 70's, much progress in resolution and capability to collect photons has been made. Nowadays, four X-ray observatories, Chandra, XMM-Newton, Suzaku, and NuSTAR, are acquiring data of unprecedented quality. Chandra and XMM, the telescopes with the best resolution out of these four, were designed and built to privilege either in the first case the resolution or in the second one the collecting area, but not both. The result is that the high-redshift X-ray Universe is still too unresolved to provide us with the understanding of the time evolution of the universe as we see it nowadays.

A further leap forward in X-ray astronomy could then be done by the realisation of X-ray optics that combine a large effective area, i.e. a large number of mirrors, and the high figure accuracy needed to achieve high angular resolution. This is the challenging goal of the ATHENA (Advanced Telescope for High Energy Astrophysics) mission, approved for the L2 slot in the ESA Cosmic Vision program with launch in 2028, with optics of 2 m^2 effective area at 1 keV and 5 arcsec resolution. The main issue to be faced is to combine these requirements with the mass constraints imposed by the operation in space. Mirrors lighter than thick Zerodur glass (as used for Chandra) or Nickel (as used for XMM) are therefore to be considered: at this regard, silicon and glass represent two natural choices because of their low density and optimal quality of the surfaces produced with the present technology.

The Silicon Pore Optics (SPO) was defined as the baseline technology to be used since 2004 for the production of the ATHENA telescope. It is developed by ESA and Cosine Measurements Systems, and utilises commercially available silicon wafers which have surface figure and roughness quality ideal for X-ray optics applications. Silicon is a new material for astronomical mirrors, but benefits from a consolidated technology in the micro-electronic field.

Thin glass foils are also considered as an alternative to silicon. The Slumped Glass Optics (SGO) technology is already experimented for X-ray astronomical mirrors: at first it was used on the HEFT balloon experiments for small size hard X-ray optics, and then used in the NuSTAR mission, lunched in 2012, and currently on duty. The glass foils were formed to the proper figure

by hot slumping and integrated in stack with ribs in graphite, at NASA Goddard Space Flight Center. However the quality of the overall process needs to be improved to bring the resolution from the 58 arcsec of NuSTAR to the 5 arcsec required for ATHENA. Concerning large size X-ray optics, glass foils were firstly considered by NASA during the development of the Constellation-X optics and then studied again by NASA for the IXO project. In Europe, at first in the context of XEUS, afterwards in the context of IXO, and now for ATHENA, the thin glass approach was also developed. The Brera Astronomical Observatory (INAF-OAB) has been developing the SGO technology with an ESA contract from 2009 till 2013: thin glass foils (0.4 mm thin) are formed by direct hot slumping assisted by pressure, and then stacked with an integration process able to damp low frequency errors. Finally, thin glass foils with piezo-electric actuators are also considered at SAO/CfA in USA to manufacture the mirrors of the X-ray Surveyor mission and are also studied in Italy for the AXYOM project.

My Ph.D. activity, carried out at the INAF-OAB (Merate, Italy), is devoted to the advances in the hot slumping technology assisted by pressure, for the production of glass mirrors for future X-ray missions, mostly focusing on ATHENA in the context of a research to consider SGOs as a viable alternative to SPOs.

In the first chapter I give an overview of the historical evolution of the instruments, which led to the discovery of new X-ray sources and a growing understanding of the X-ray sky. The ATHENA science goal and the importance of the mission, to understand the evolution of the universe and the key role of the black holes, are presented, together with the technological parameters required to reach these goals.

In the second chapter I provide a brief introduction to the reflection of X-rays. Two aspects, that sensitively affect the focusing performances, are discussed in details: the mirrors shape design to correctly focus X-rays in double reflection and the smoothness of the surface as a key point to avoid scattering. The scattering from single and multilayer coatings are presented, multilayers being essential for the reflection in the hard X-ray region. The past and present available technologies to manufacture X-ray mirrors are presented. An overview of the ATHENA telescope and the SPO/SGO technology is also presented.

Chapter 3 describes the thermal forming process of glass foils. In this chapter I introduce the glass properties and qualities as a function of the composition, and the different materials used for the moulds, i.e. the shape template for the glass foils. I describe an existing model, developed by Jimenez-Garate in 2003, which account for the relaxation of ripples in the slumped glass foil when in contact with the slumping mould; we (myself and C. Brizzolari) have modified this model, to include the application of pressure (described in chapter 6 together with the experimental results). I finally describe the different slumping approaches developed in the different laboratories; the integration methods are also presented, being the final performance of the telescope a combination of the quality of the glass substrate and the accuracy of the integration process. Finally, the error budget in the SGO technology developed at INAF-OAB is presented.

Chapter 4 describes the instruments and the methods used for mould and glass foils characterization, in terms of both shape and roughness. Concerning the shape, I have introduced a new technique to precisely characterise the mid frequency errors of the glass foils. This allowed us to accurately compute the resolution expected from the focusing mirrors and give a feedback to the slumping process. The methods for data analysis are presented. The damping of low frequency errors to simulate an ideal integration is described. The PSF computation method based on Fresnel diffraction is presented: this method was developed at INAF-OAB by L. Raimondi and D. Spiga to simultaneously accounts for shape and roughness, and was extensively used in my work to predict the performances of the slumped glass foils.

Chapter 5 describes in detail the hot slumping process assisted by pressure developed at INAF-OAB. I have modified the process and the setup with respect to the one previously used: while keeping keatite as slumping mould material, I have changed the glass type from Schott AF32 to Corning Eagle XG. I have developed cleaning protocols, used different thermal cycles and different pressures conditions, and reconditioned of the pressure control system. I have optimised

the mould height with experiments based on Finite Element Analysis, and reduced the thermal gradients inside the mould and the glass foils.

Chapters 6 shows the advances I have obtained by changing the parameters discussed in Chapter 5. It is the core work of my Ph.D. and, at the end of this chapter, I presents the results obtained, evidencing the positive trend of the key parameters adopted to measure the glass foils quality. The final results of the optimization work carried out in my Ph.D. research are slumped glass foils with expected HEW values from profile data of 2.2 $\pm$ 0.3 arcsec in single reflection, at 1 keV X-ray energy and 0.7 incidence angle. This value is computed by simulating a perfect integration, i.e. without accounting for errors introduced either by the integration moulds or by the glue shrinkage. This result has to be compared with 2 arcsec defined as the error budget allocated for the slumped glass foils, and 7 arcsec obtained before my Ph.D. About 1 arcsec is due to replication of the mid-frequency errors in the slumping mould which, owing to the improved result in the slumping, are now a limiting factor in the quality of the slumped glass foils. From the point of view of roughness, the contribution to the HEW, of the slumped glass foils, is guaranteed to be less then 1 arcsec at 1 keV, with an improvement from 21 to 11 Å. Very recent results prove that the roughness of the slumped glass foils can be further reduced to $\sim$ 7 Å, making the technology attractive also for higher X-ray energies and higher incidence angles.

Chapter 7 presents the results obtained with different materials to address some critical points faced during this work. This chapter intend to give the base for a further activity. I have investigated the effect of chemical tempering on Corning Gorilla® glass, tested different materials for the slumping mould, and defined Si_3N_4 as a very promising candidate. I have tested different sealing materials in order to avoid the dust problems sometimes encountered, studied dip coating technique as a cheap solution to fill the pores present in the optical glass surface and critical for high X-ray energies. Finally, I have shown that the present setup for pressure application can also be applied for the indirect slumping, a possible solution to preserve the optical glass surface.

During my Ph.D. activity, two integrated prototypes (Proof Of Concept, POC) have been realised by my group and tested in X-ray at the PANTER facility (MPE-Germany), using glass foils I have produced. The results obtained in X-ray and UV are presented in Chapter 8. The POC#3, (with 2 glass foils assembled) is characterised by HEW value of 5.5 arcsec at 0.27 keV in the best portion of the module, as tested at the PANTER facility; the POC#4 (with 8 glass foils) has expected HEW of about 15 arcsec from metrological data, but the result in X-ray was much higher because of accidental problems during the integration. The next prototype, the POC#5 (with the best eight glass foils produced during my Ph.D. activity), will soon be integrated and tested in X-rays, to assess the improvement already proven by metrology and simulations.

In chapter 9, I briefly present two projects for active profile corrections with piezoelectric elements, the AXYOM (Italy) and the X-ray Surveyor (USA). Some of the glass foils slumped during this work were used as substrates for the optics of these projects.

Finally, chapter 10 presents my work on multilayer coatings for X-ray optics. I have upgraded an IDL code to simulate the roughness growth in the multilayer deposition process, extending the computations from periodic to the more general case of graded multilayers. I have also contributed to the X-ray measurements at the BEAR beamline of the Elettra synchrotron in Trieste, on multilayers deposited on glass, silicon and electroformed nickel, for the polarimetric LAMP project.

Chapter 11 summarizes the conclusions and states possible developments.

Acronyms

AFM	Atomic Force Microscope
AGN	Active Galactic Nuclei
ACIS	Advanced CCD Imaging Spectrometer
ASCA	Advanced Satellite for Cosmology and Astrophysics
ATHENA	Advanced Telescope for High-ENergy Astrophysics
AXYOM	Adjustable X-raY optics for astrOnoMy
BEAR	Bending magnet for Emission, Absorption and Reflectivity
BH	Black Hole
BLR	Broad Line Region
CfA	Center for Astrophysics
CHR	CHRocodile
CTE	Coefficient of Thermal Expansion
CUP	Characterization Universal Profilometer
CXB	Cosmic X-ray Background
eROSITA	extended ROentgen Survey with an Imaging Telescope Array
E-ELT	European Extremely Large Telescope
ESA	European Space Agency
ESRF	European Synchrotron Radiation Facility
FEL	Free Electron Laser
FEA	Finite Element Analysis
FOV	Field Of View
FWHM	Full Width Half Maximum
GRB	Gamma-Ray Burst
GSFC	Goddard Space Flight Center
HEAO	High-Energy Astrophysics Observatory

HEFT	High Energy Focusing Telescope
HEW	Half Energy Width
HMXB	High-Mass X-ray Binary
HPD	Half Power Diameter
IDL	Interactive Data Language
IMA	Integration MAchine
INAF	Istituto Nazionale di AstroFisica
ISM	InterStellar Medium
IXO	International X-ray Observatory
JAXA	Japan Aerospace eXploration Agency
JET-X	Joint European Telescope X
JUICE	JUpiter ICy moon Explorer
KB	Kirkpatrick-Baez
LAMP	Lightweight Asymmetry and Magnetism Probe
LMXB	Low Mass X-ray Binary
LTP	Long Trace Profilometer
MFT	Micro Finish Topographer
MLT	Media Lario Technologies
MPE	Max Planck Institut fur Extraterrestrische Physik
NASA	National Aeronautics and Space Administration
NGO	New Gravitational wave Observatory
NHXM	New Hard X-ray imaging and polarimetric satellite Mission
NLR	Narrow Line Region
NuSTAR	Nuclear Spectroscopic Telescope Array
OAB	Osservatorio Astronomico di Brera
PIXI	Princeton Instruments X-ray Imager
POC	Proof Of Concept
PPM	Pythonic Program for Multilayers
PSPC	Position Sensitive Proportional Counter
PSF	Point Spread Function
PP	Plate Pair
PSD	Power Spectral Density
PV	Peak to Valley
rms	Root Mean Square
ROSAT	Roentgen SATellite
RT	Room Temperature
SAX	Satellite per Astronomia X (*X-ray Astronomy Satellite*)
SAO	Smithsonian Astrophysical Observatory
SGO	Slumped Glass Optics
SMART-X	Square Meter Arcsecond Resolution X-ray Telescope
SNR	SuperNova Remnant
SPO	Silicon Pore Optics
SR	Strehl Ratio
TRoPIC	Third Roentgen Photon Imaging Counter
VFT	Vogel-Fulcher-Tamman
XEUS	X-ray Evolving Universe Spectroscopic mission
X-IFU	X-ray Integral Field Unit
XIPE	X-ray Imaging Polarimetry Explorer
XBN	X-ray Binary Star
XMM	X-ray Multimirror Mission
XOU	X-ray Optical Unit

XRD X Ray Diffraction
XRR X Ray Reflection
XRS X-Ray Scattering
XRT X-Ray Telescope
WFI Wide-Field Imager
WFXT Wide Field X-Ray Telescope

Contents

CHAPTER 1

The X-ray universe

1.1 Evolution of instruments and deeper insight in the X-rays sky

The X-rays discovery dates back to 1895 when W.C. Röngten produced and detected a new kind of radiation named "X" to denote its unknown nature (Fig. 1.1). Von Laue and Bragg could produce the first X-ray image using diffraction from crystals (1912). Einstein was the first to recognise X-ray total external reflection (1918) that Compton demonstrated afterwards (1923) as a property of very smooth surfaces when the light impinges at very shallow angles (grazing incidence). In 1948 Kirkpatrick and Baez [Kirkpatrick & Baez1948] proposed the first optical system to focalise X-rays, using two reflections (Fig. 1.2). Finally, Wolter proposed in 1952 [Wolter 1952] a system to improve the properties of the focusing systems in order to reduce off-axis aberrations and enlarge the field of view, based on a double reflection onto conical surfaces.

The first detection of X-rays by astronomical sources was reached in 1948, when a V2 rocket could expose some photographic plates to the radiation of the high atmosphere, pointing out the *Sun* as a source of UV and X-rays radiation. Actually, because of its proximity to us, the Sun is the brightest source of X-rays in the sky and thermal X-ray emission was quite expected. Spectroscopic observations identified emission lines from iron and other heavier elements, whose electrons have been stripped in the 1 to 2 million degrees temperature environment of the solar corona. However, the emission of X-rays from distant stars was seemingly difficult, because in thermal sources (with temperature of $\sim 10^3 - 10^4 K$) only the tail of the blackbody spectrum is made of X-rays. It was therefore realised that, to detect X-ray sources other than the Sun, it was necessary to develop instruments more sensitive by several order of magnitudes. To this aim, in 1960 B. Rossi and R. Giacconi suggested to adopt also for astronomy the optics that Wolter was proposing for X-ray microscopy.

In 1962 the first extrasolar X-ray source Sco X-1 was found, using a highly sensitive non-imaging soft X-ray detector, launched on a rocket. Surprisingly, the X-rays from this source exceeded the Sun's entire energy output by a factor of 100, and exceeded its X-ray output by a factor of about one hundred million. The angular resolution of the detector did not initially allow

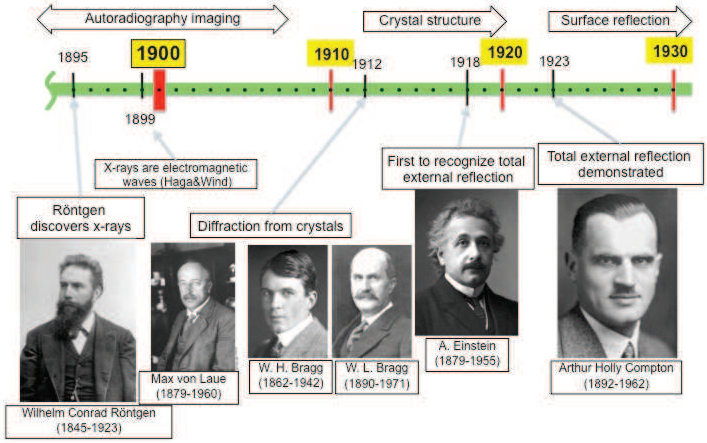

Figure 1.1: *: X-ray history. Credits: Peter Takacs, Brookhaven National Laboratory*

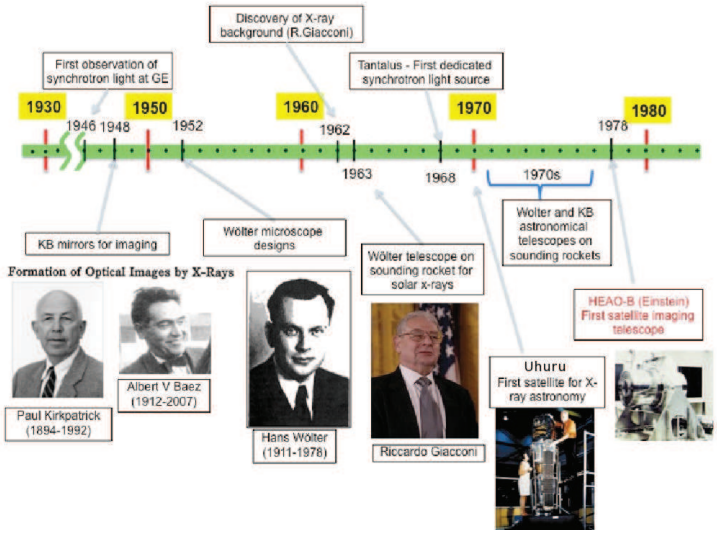

Figure 1.2: *: X-ray history. Credits: Peter Takacs, Brookhaven National Laboratory*

the position of Scorpius X-1 to be accurately determined, but on 1967 it was found that it was a *binary star*, with a neutron star accreting matter from the companion. In the data from this rocket flight, Riccardo Giacconi recognised the presence of a diffused cosmic X-ray background (*CXB*): unlike the optical, the X-ray sky is not dark. We now know that the observed X-ray background is the result from an integrated contribution by discrete sources, AGN and Galaxy Clusters, rather than a truly diffused emission.

In 1964 the first *supernova remnant* (SNR), the Crab Nebula, was identified as another source of X-ray radiation, during a lunar occultation using a rocket born detector.

As the sensitivity of the observations increased, other sources were discovered outside our galaxy. The first extragalactic source discovered was the *active galaxy* M87 on 1965 with a rocket based geiger counter. The first survey of the sky in X-ray was possible in 1970 with the launch of Uhuru, the first X-ray orbiting satellite, which discovered a powerful X-ray source in the Cygnus constellation, named, Cyg X-1, which we now know to be an accreting system with a BH. At that time many *quasars*, *active galaxies* and *cluster of galaxies* were added to the catalogue of extragalactic X-ray sources.

In 1978 the first X-ray imaging telescope, Einstein, was launched. Einstein was the first X-ray telescope equipped with focusing optics and could make X-ray astronomical images. Among its scientific discoveries, there are the X-rays emission of planets, the X-ray jets of *active galactic nuclei* (AGN), the *pulsars* and the resolution of the CXB below 4 keV into discrete sources, whose optical counterparts are mainly AGN with a minority of Clusters of Galaxies.

ROSAT (Fig. 1.3) (the Roentgen SATellite) was launched in 1990: it could perform, for the first time, the entire survey of the X-ray sky with an imaging telescope and discover cosmic X-ray sources ten million fainter than Sco X-1. With this mission, it was found that almost all astronomical objects emit X-ray radiation, including the Moon, comets, stars, X-ray binary stars, neutron stars, supernovae and supernova remnants, the interstellar medium, galaxies, active galactic nuclei, black holes, nebulae. It was recognised that the process responsible for X-ray emission are very often non-thermal, but arise from violent shocks and particle acceleration phenomena.

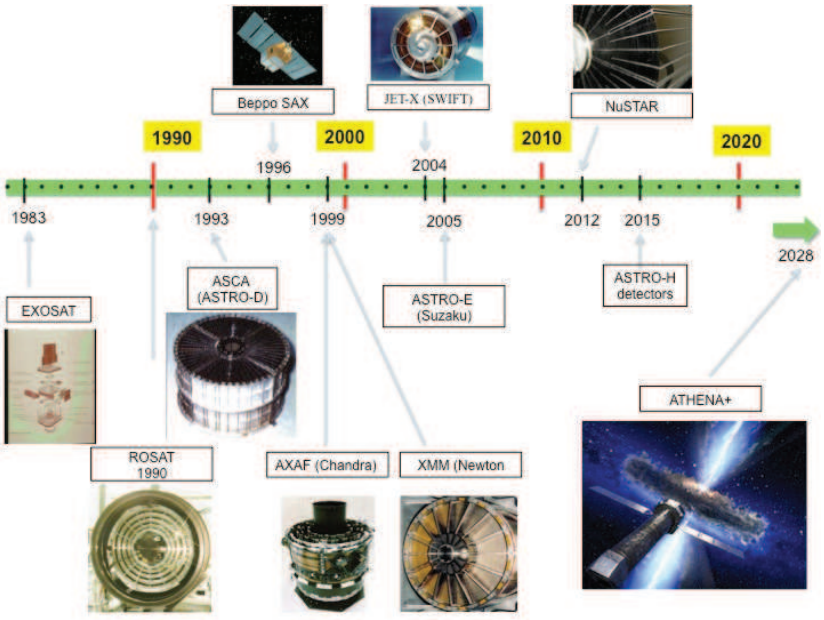

Figure 1.3: *: X-ray history. Credits: Peter Takacs, Brookhaven National Laboratory*

ASCA, launched in 1993, was the first satellite to use CCD detectors for X-ray astronomy and the first X-ray mission using aluminium thin foils to produce lightweight X-ray optics, owing to a dense mirror nesting that enabled reaching a high effective area. By this telescope it was possible to detect the broad Fe lines from AGN, probing the strong gravity near the central engine. Another discovery obtained by ASCA was the detection of non-thermal X-rays from SN1006, a site of cosmic ray acceleration.

In 1996 BeppoSAX was launched. It was the first telescope with optics produced with the replication technique, where Nickel electroformed mirrors are replicating from a super polished mandrel in Aluminum. It was able for the first time to observe a few sources (Blazars) in which the peak of the synchrotron emission reached 100 keV, showing the presence of cosmic rays with energies in the TeV range. Moreover, it could, for the first time, measure the position of the *gamma ray bursts* (GRB), on rapid time scale, with the precision of few arc minutes. With BeppoSAX the GRB's afterglow was also detected for the first time: this is of primary importance as the evolution of the spectral components (like the fluorescence line of the Fe K) is essential to understand the GRB origin. More recently, this has been studied with the Swift satellite, devoted to measure the position, spectrum, and brightness of GRBs and afterglows over a wide dynamic range covering more than 7 orders of magnitude in flux (https://www.swift.psu.edu/xrt/).

Nowadays, four high resolution X-ray observatories for imaging, Chandra, XMM-Newton, Suzaku, and NuSTAR, are currently in operation, XMM and Chandra being synergic in terms of their spatial resolution and spectral capabilities:

- Chandra [0.1 - 10 keV] is the telescope with the best angular resolution (0.5 arcsec Half Energy Width, HEW). Owing to its superb resolution, it returns high quality images. However, the reduced effective area makes it difficult to operate for spectroscopy of distant sources. Fig. 1.4 shows the improvement in imaging quality, obtained with Chandra, for the Crab Nebula;

- XMM [0.1 - 12 keV], thanks to its large collecting area, has excellent spectroscopy capabilities, but worst spatial resolution if compared to Chandra;

- Suzaku [0.2 - 12 keV] is also devoted to spectroscopy. It is a re-flight of the failed Astro-E satellite. Suzaku is the first satellite with a new type of X-ray Spectrometer (XRS), the X-ray micro-calorimeter. Unfortunately, XRS lost its coolant shortly after launch and therefore it has never been possible to see its full potential;

- NuSTAR [6 - 79 keV] is a telescope for hard X-rays with a factor 50-100 sensitivity improvement with respect to previous instrument operating in the same energy band: this could be reached with depth-graded multilayer coated mirrors, also called "supermirrors", that replaced the single-layer reflection mirrors used by previous missions (Sect. 2.5). It was also the first telescope to be based on slumped glass foils.

Finally the last active X-ray mission that is carrying on board an X-ray telescope is Swift, launched on 2004: it mounts the spare Flight Module optics of the never-launched JET-X instrument on the Spectrum X-Gamma mission. The primary scientific objectives are to determine the origin of Gamma Ray Burst (GRB) and to pioneer their use as probes of the early universe.

In the near future, other two X-ray missions will be launched:

1. ASTRO-H, a JAXA mission with US contribution will fly in 2016. The hard X-ray telescopes are made with thin aluminum foils, just like Suzaku, but they are using Pt/C depth-graded multilayer coatings to reach the X-ray energy range above 10keV, and therefore to study the non-thermal phenomena due to particles accelerations

2. in 2017, eROSITA will be launched to perform the first imaging all-sky survey in the medium energy X-ray range up to 10 keV, to be compared with the 0.1-2 keV energy range of ROSAT.

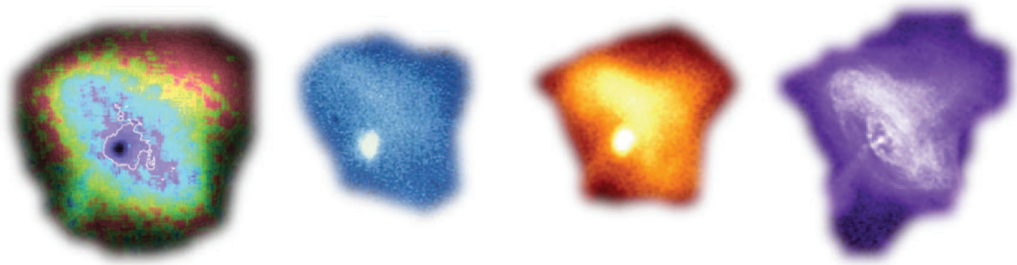

Figure 1.4: *: X-ray images of the Crab Nebula illustrate the importance of the angular resolution to the study of structure in cosmic sources. From left to right, HEW are approximately 15 arcsec (XMM-Newton), 10 arcsec (Einstein), 5 arcsec (ROSAT) and 0.5 arcsec (Chandra). Only the highest resolution image shows detailed structure from the inner ring. (Credits: O'Dell 2011)*

Finally in the next future, ATHENA will be launched in 2028 (see paragraph 1.3): it will combine a high resolution (5 arcsec) with a large collecting area (2 m^2 at 1 keV) in order to perform imaging and spectroscopy of distant and faint X-ray sources. It will therefore provide answers regarding the evolution of the ordinary matter to form galaxies and galactic clusters, and regarding the influence of the BH to their surrounding medium. Silicon Pore Optics (SPO) is defined as the baseline technology to be used for the ATHENA telescope. However, thin glass foils are also considered as a valuable alternative to silicon.

1.2 Some X-ray astronomical sources

Some classes of astronomical objects visible in the X-ray energy band are hereafter listed.

1.2.1 Stars

The corona of our Sun was the first celestial X-ray source to be detected. Some stars have far more active coronae than our Sun: in some cases, a more rapid rotation leads to stronger, and more twisted magnetic fields, which make the corona more active. X-ray emission mostly results from shocks in the corona, but details are not yet understood. We expect to understand from X-ray observation which process is mainly responsible for energy transfer from the photosphere to the corona.

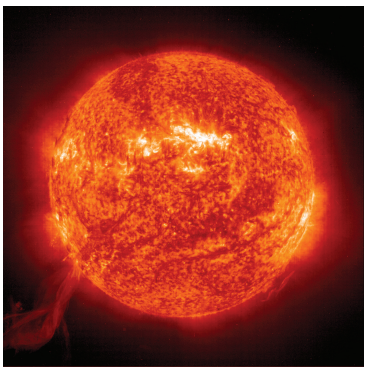

Figure 1.5: *: Image of the Sun in X-rays from the SOHO satellite. Credits: NASA*

1.2.2 X-ray binary stars

Binary star systems contain two stars that orbit around their common centre of mass. A special class of binary stars are X-ray binaries, first discovered as very strong X-ray sources. X-ray binaries are made up of a main sequence star and a collapsed star (neutron star or black hole). These pairs of stars produce X-rays if the stars are close enough together that material is pulled off the normal star by the gravity of the dense, collapsed star. The X-rays come from the area around the collapsed star where the material that is falling toward it is heated to very high temperatures. This area is known as the accretion disk.

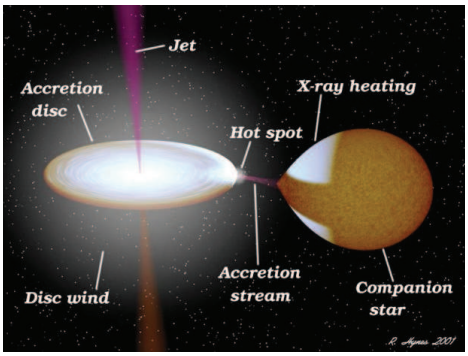

Figure 1.6: *: Sketch of a low mass X-ray binary. Credits: [Web reference: LMXB]*

X-ray binary stars mainly divide into:

1. high-mass X-ray binary (HMXB) in which the material is transferred onto the compact object by a powerful stellar wind from a massive star. For HMXBs, the X-ray spectra is hard, with photon energy extending above 15 keV.

2. low-mass X-ray binary (LMXB) in which the mass-loosing star is of low mass. They do not have a strong stellar wind and hence the X-ray source cannot be powered by the same mechanism as in the HMXBs. The two stars are usually closer than in the case of HMXB: the shape of the mass loosing star is distorted by the degenerated companion to create a stream that impacts the accretion disk where X-rays are generated by the strong gravitational and frictional forces. LMXBs are dominated by soft X-ray spectra, usually below 15 keV, but an important component of hard X-rays is also present. Such an emission cannot result from a thermal process, hence models including an optical thin corona have been proposed.

Cataclysmic variables are X-ray binaries, with a white dwarf instead of a black hole or a neutron star. A white dwarf has mass comparable to the Sun but is closer to the Earth in size (neutron stars and black holes are much smaller still, with radii about 1/1000th of that of the Earth). Because the gravitational potential well of a white dwarf is not as deep as for a neutron star or a black hole, a cataclysmic variable is not as X-ray bright as the X-ray binaries, while the maximum of the emission spectrum is typically in UV range. But there are many more cataclysmic variables, some of them relatively close to the Sun. So we can often study the details of the accretion process better in a cataclysmic variable than in an X-ray binary [Falanga et al. 2014].

1.2.3 Supernovae Remnants

When a massive star explodes in a supernova, it ejects a large amount of material (often many times more than the mass of the Sun) at thousands of kilometers per second. This high speed gas then collides with the interstellar medium and heats it up to millions of degrees. Electrons

are separated from atoms and thermal X-rays are radiated profusely, generated by fast electrons colliding with positive ions or by electron-ion recombination. For the next 20,000 years or so, a hot ball of gas is left, glowing in X-rays: this is called a supernova remnant. This material is then used to create the next generation of stars and planets; Earth and the elements of our bodies are originated from this same material; also radioactive elements such as ^{56}Ni, ^{56}Co, ^{44}Ti are produced, with characteristic X-ray lines [Web reference: SNR]. The first two isotopes have a rather short half-life and start decaying on timescales of a few to several hundreds of days. ^{44}Ti instead has about about 60 years life time and is able to keep supernova remnants shining for about three years. Detecting these isotopes therefore allows a precise determination of the SN blast. Also polarised emission, usually interpreted as synchrotron light, is observed (e.g. in the Crab Nebula).

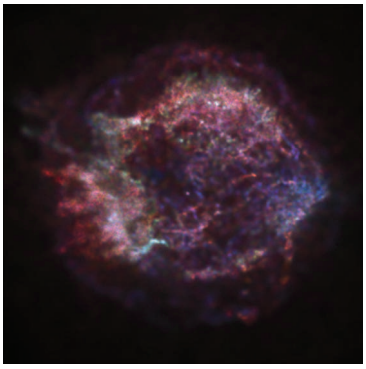

Figure 1.7: *: Chandra X-ray image of the supernova remnant Cassiopeia A: the red, green, and blue regions show where the intensity of low, medium, and high-energy X-rays, respectively, is largest. The red material on the left outer edge is enriched in iron, whereas the bright greenish white region on the lower left is enriched in silicon and sulfur. Credits: NASA.*

In a supernova remnant, three physical processes contribute to the emission of X-rays. There is thermal bremsstrahlung emission from the hot gas, which is a continuum determined only by temperature. There can be presence of spectral lines, which can reveal the elemental composition of the gas. The presence of a magnetic field causes the synchrotron radiation from relativistic electrons. The spectrum of the synchrotron is a power law. During the first phase after the outburst, SNRs are also characterised by a blackbody radiation with photons in the X-ray, that is produced by the newly formed neutron star.

1.2.4 Clusters of galaxies

Clusters of galaxies were first detected as a collection of galaxies, gravitationally bound to each other. A vast cloud of hot gas fills the entire clusters of galaxies and, being at temperature of tens of millions degrees, is a strong source of X-ray emission by thermal bremsstrahlung. Also metallic X-ray lines are usually observed. From X-ray observations, it turned out that the mass of this gas exceeds that of the stars in their optical counterparts. Moreover both optical and X-ray observations suggest that, to hold the cluster together, an even larger amount of dark matter is needed. A key question to be answered is how these structures have evolved over time. The spectral capabilities of ATHENA can therefore provide key observables such as the gas temperature, abundance, velocity and ionization stage, that are necessary to understand the evolution of the baryons in the dark matter potential (see paragraph 1.3).

1.2.5 Active Galactic Nuclei

Many galaxies, if not all, appear to contain a massive black hole at their centre. When they accrete matter, they become some of the most luminous objects in the universe: quasars, blazars

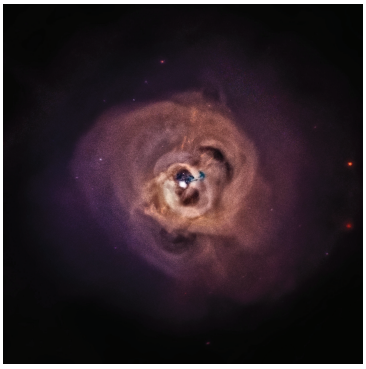

Figure 1.8: *: Chandra X-ray image of the Perseus Cluster: red, green, and blue show low, medium, and high-energy X-rays respectively. Credits: NASA*

and Seyfert galaxies. They are nowadays explained by the so called *Grand Unified Models of AGNs* (Fig. 1.2.5). At the center of the AGN there is a supermassive black hole ($10^9 - 10^{10} M_\odot$). Around it there is an accretion disk which is the major source of power. An obscuring torus, located several parsec from the black hole, intercepts part of the radiation produced by the disk and re-emits in the infrared. Less than a parsec away from the black hole, there is a region of rapidly moving clouds. They intercept $\sim 10\%$ of the ionizing radiation of the disk and re-emit it in form of lines. Doppler shift broadens these lines, hence the name Broad Line Region (BLR). At larger distance, ~ 100 pc,another region is located where less dense clouds are moving less rapidly, the Narrow Line Region (NLR). Based on this model, we can understand the two types of AGNs by an inclination effect:

1. type I AGN: if viewed at low inclination angle, one gets an unobscured view of the nucleus, with both broad and narrow lines in the energy spectrum;

2. type II AGN: if viewed at high inclination angles, the central source of X-ray radiation is highly obscured by the torus of thick dusty material: only narrow lines are present in the energy spectrum.

Cosmic X-ray Background (CXB), observed for the first time by Riccardo Giacconi in 1962, is by now known to result from an integrated contribution of discrete sources rather than a truly diffused emission. AGNs, in a mixture of type I and type II (to a ratio of 1:3), can explain the broad maximum around 30 keV of the Cosmic X-ray Background (*CXB*): in fact, in the highly obscured AGNs, the low energy part of the emitted spectrum is lost by photoelectron absorption (the cross section of photoelectron absorption is strongly energy dependent being $\sigma \sim E^{-3}$) and the high part is lowered in energy by Compton reflections, thus giving the peak at 30 keV.

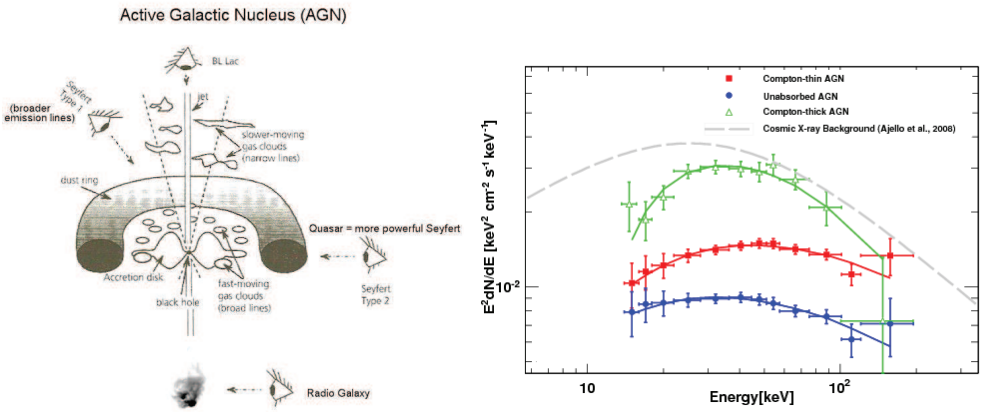

Figure 1.9: *: Left: the scheme of unified model of AGN (Credits: [Liddle & Loveday 2009]). Right: a population of heavily absorbed active galaxies (green curve) is thought to make the greatest contribution to the cosmic X-ray background (grey curve).*

1.3 The science goal and the key parameters of the ATHENA mission

The ATHENA observatory, currently under development by ESA, and accepted for the L2 slot with launch in 2028, will study the hot and energetic Universe. It will make space-based observations in the X-ray band, spatially-resolved X-ray spectroscopy and deep wide-field X-ray spectral imaging; the planned performance greatly exceedes that offered by the current X-ray observatories like XMM Newton and Chandra, or by missions soon to be launched such as Astro-H and eROSITA. Compared to current facilities, privileging either the spatial resolution (like Chandra) or the collecting area (like XMM), ATHENA will combine the two aspects and will therefore move beyond simple source detection into the spectral domain, where the real astrophysics of the sources is revealed. Until now in fact, the spectacular images from Chandra could not be combined with spectroscopical informations, due to its poor collecting area, while XMM often could not access the objects of interest because of source confusion, due to its poor spatial resolution. ATHENA will address two key questions in astrophysics:

- how and why does ordinary matter assemble into the galaxies and galactic clusters that we see today
- how do black holes grow and influence their surroundings

Addressing the first question involves mapping of large hot gas structures in the Universe, determining their physical properties, and tracking their evolution through cosmic time. In fact the today's massive clusters of galaxies, the largest bound structures in the Universe, grow over cosmic time by accretion of gas from the intergalactic medium. The velocities, thermodynamics and chemical composition of the gas has to be measured, mapping the Universe from the formation epoch of the clusters of galaxies at $z \sim$ 2-3 to the present day. Therefore the breakthrough is to enable spectroscopic observation of clusters beyond the local Universe, out to z = 1 and beyond. An angular resolution of 5 arcsec is needed to disentangle small structures in clusters, groups and galaxies. With respect to previous generation X-ray telescopes, a factor of 10 increase in both telescope throughput and spatial resolving power for high resolution spectroscopy is necessary. This will lead to a factor of 10 improvement in sensitivity, being the sensitivity limit inversely proportional to the telescope effective area (section 2.2). The ATHENA flux sensitivity will be $\sim 10^{-17}$ erg/(cm^2 s) in the 0.5-2 keV band, to be compared with the XMM sensitivity of 3.1 and 14×10^{-16} ergs/(cm^{2}sec) in the 0.5-2 and 2-10 keV bands respectively [Web reference: XMM] (for an observation duration of about 10^5 sec).

To answer the second question it is necessary to reveal supermassive black holes, even in obscured environments, out into the early Universe, and understand both the inflows and outflows of matter and energy as the black holes grow. In fact, processes originating at the scale of the black hole event horizon seem able to influence structures on scales 10 orders of magnitude larger, giving energies to the baryonic matter with a mechanism known as feedback, in which jets heat the hot gas, suppressing star formation and regulating their own fuel supply. The current generation of X-ray observatories, Chandra and XMM-Newton, have revealed a complex interplay between cooling and heating, via spectroscopic measurements of gas cooling and detailed imaging of the interactions of jets and gas in cluster cores. However, the physics of how the balance between these processes is established and maintained can only be glimpsed in a few nearest systems and so remains poorly understood. For a complete understanding of galaxies, it is therefore necessary to track the growth of their central supermassive black holes through cosmic time. The goal then is to push the frontiers of black hole evolution to the redshifts where the first galaxies are forming, at z = 6-10: therefore high throughput and high resolution are necessary. The spectral resolution of 2.5 eV will provide informations on the chemical composition and dynamics of hot gas in the most obscured black holes at the peak of both star formation and accretion activity occurring at z = 1-4. These spectra will show, for example, if the heavily obscured phase of black hole evolution is associated with the termination of star formation in galaxies via feedback.

The illustration of the power of spatially resolved high-resolution X-ray spectroscopy is provided in Figure 1.10 below, taken from Croston, Sanders et al. 2013. This is the simulation of a 50 ks X-IFU (X-ray Integral Field Unit) exposure of the Perseus cluster, compared to the Chandra-ACIS (Advanced CCD Imaging Spectrometer) spectra. Such measurements will enable to pinpoint the locations of jet energy dissipation, determine the total energy stored in bulk motions and weak shocks, and test models of AGN fuelling so as to determine how feedback regulates hot gas cooling.

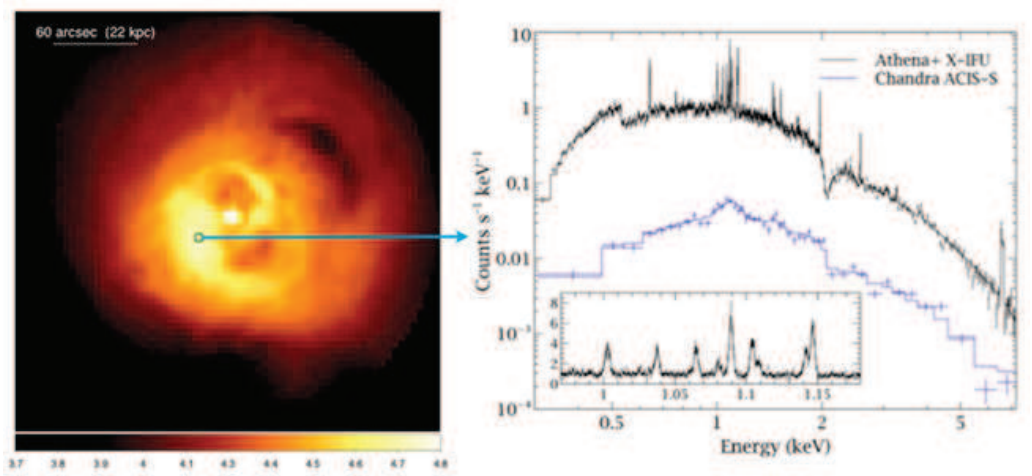

Figure 1.10: *: Predicted ATHENA observation of the centre of the Perseus cluster (0.5 to 7 keV, from Chandra image Fig. 1.8). The left panel shows a simulated 50 ks X-IFU observation (0.5-7 keV), displayed on a log scale. The spectrum on the right is from the single 5 arcsec x 5 arcsec region marked by the box, with a Chandra spectrum of the same observation length for comparison. The inset shows the region around the iron L complex. (Credits: [Croston et al. 2013])*

Fig. 1.11 shows four examples of simulated ATHENA spectra, compared where appropriate to Chandra-ACIS spectra:

1. a broad iron K_α line, whose shape reflects that it has been generated in the general relativistic environment of a black hole. No Chandra simulation is shown, as the source is too bright to be observed by ACIS without pileup.
2. an ultra-obscured supermassive black hole in the centre of a distant galaxy. The signature of obscuration, an intense fluorescence iron K_α line, is revealed by Athena but invisible with Chandra
3. a high redshift galaxy group, barely detected by Chandra, but with clear emission lines in the WFI spectrum which trace the thermal and chemical evolution of hot baryons throughout cosmic time
4. the Galactic Centre itself. Athena will reveal the astrophysics of hot cosmic plasmas.

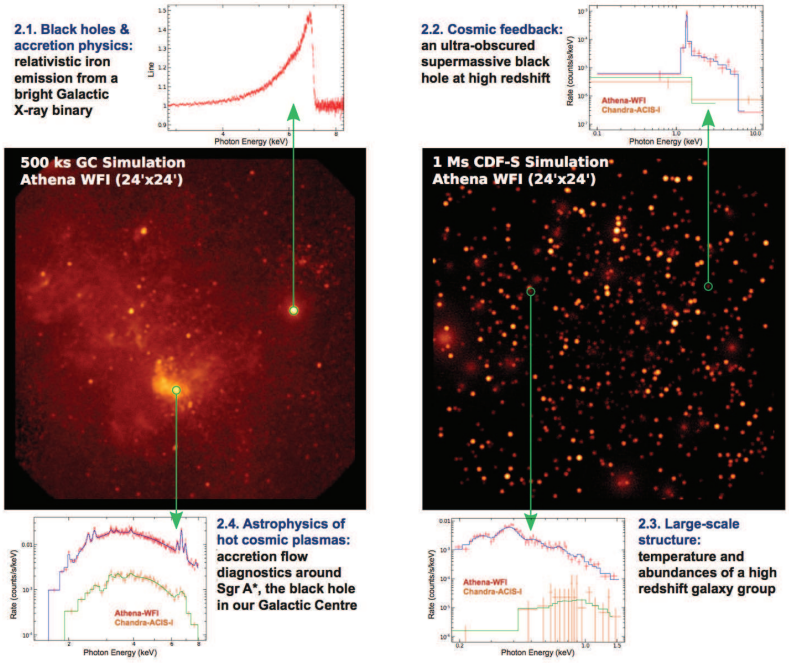

Figure 1.11: *: Predicted ATHENA images. Left: a field centred on Sgr A^*, the black hole in Galactic Centre (GC, 500 ks exposure). Right: an extragalactic survey field, the Chandra Deep Field South (CDFS, 1 Ms). Predicted ATHENA spectra from previous images, compared where appropriate to Chandra-ACIS spectra. Top-left: a broad iron K_α line, whose shape reflects that it has been generated in the general relativistic environment of a black hole. Top Right: an ultra-obscured supermassive black hole in the centre of a distant galaxy. Bottom Right: a high redshift galaxy group, barely detected by Chandra, but with clear emission lines in the WFI spectrum. Bottom Left: the Galactic Centre itself. Athena will reveal the astrophysics of hot cosmic plasmas. (Credits: [ATHENA assessment study report 2011]*

CHAPTER 2

X-ray telescopes

2.1 Grazing-incidence X-rays reflection

The method for focusing the X-rays is very different from that for visible light. The reason lies in the different values taken on by the optical constants of the materials when approaching the energies of the X-rays. It was already noted by Röntgen that, for the X-ray radiation is extremely hard to refract, and on normal incidence the reflection is nearly zero. The refractive index *n* of a material in the X-ray region is normally written, using the optical constant δ and β, as

$$n = 1 - \delta + i\beta = 1 - \frac{N_A r_e}{2\pi A}\lambda^2\rho(f_1 + if_2), \tag{2.1}$$

where δ is the deviation of the refractive index from 1, β is the absorption index, f_1, f_2 are the real and imaginary parts of the atomic scattering factors, N_a is the Avogadro number, r_e is the classical electron radius, A is atomic mass, and ρ is the density. Typical values are $\delta \approx 10^{-4} \div 10^{-5}$ and $\beta \approx 10^{-5} \div 10^{-6}$.

The reflectivity is given by the ratio between the reflected intensity and the intensity of the incident beam. It depends on the polarisation of the incident radiation. Let's consider s the component of the wave electric field perpendicular to the incidence plane (given by the propagation direction of the incident beam and the perpendicular to the surface), p the component in the incidence place. Equations 2.3 and 2.2 report the reflectivity Fresnel formulae for s and p polarisations, considering a ray travelling in vacuum and impinging on a material with refractive index n, being θ_i and θ_r the incident and refracted grazing angles, respectively:

$$r_s = \frac{\sin\theta_i - n\sin\theta_r}{\sin\theta_i + n\sin\theta_r}, \tag{2.2}$$

$$r_p = \frac{\sin\theta_r - n\sin\theta_i}{\sin\theta_r + n\sin\theta_i}. \tag{2.3}$$

The incident and refracted grazing angles are related by the usual Snell law:

$$\cos\theta_i = n\cos\theta_r. \tag{2.4}$$

Being the real part of n less than 1, the refracted X-ray approaches the surface, and there will be a critical angle $\theta_i = \theta_c$ beyond which the X-ray beam is totally reflected. This condition is $n = \cos\theta_c$.
Since $n \sim 1$, the Fresnel equations give a X-ray reflectivity very close to 0 except for very small incident angles, where the Fresnel equations for the reflected ray may be approximated by:

$$r_s = -r_p = +\frac{\delta}{2\sin^2\theta_i}. \tag{2.5}$$

Eq. 2.5 would diverge for θ_i approaching 0, but in fact the critical angle θ_c is setting a limit for Eq. 2.5 to hold, since at θ_c the reflectivity equal 1.
Owing to the very small angle at play, we can write

$$1 - \delta = \cos\theta_c \approx 1 - \theta_c^2/2; \tag{2.6}$$

therefore, combing Eq. 2.6 with Eq. 2.1, and approximating $f_1 \sim Z$ (as it can be assumed for energies much above the K-edge) the critical angle can be written as

$$\theta_c \approx \sqrt{2\delta} = \sqrt{\frac{N_a r_e}{\pi A}\lambda^2\rho Z} \propto \frac{\sqrt{\rho}}{E}. \tag{2.7}$$

From this equation, it can be seen that

- the critical angle is always very shallow (less than a few degrees: for gold and E = 1 keV, θ_c = 4 deg)
- the critical angle increases for larger reflecting material density, thus explaining why denser materials (Au, Ir, Pt) are usually used as reflective coating of X-ray mirrors
- the critical angle decreases with increasing energy, thus explaining why hard X-rays are difficult to be reflected with a single reflecting layer. Over 10 keV, even the critical angles of the densest coatings become too small and the mirror cross section offered to the incident flux becomes too low to return a sufficient effective area. For this reason multilayer coatings are used (see sect. 2.5).

The X-ray reflectivity of glass and gold (for an ideally smooth surface) is shown in Fig. 2.1, where it appears evidently the cut-off angle and energy.

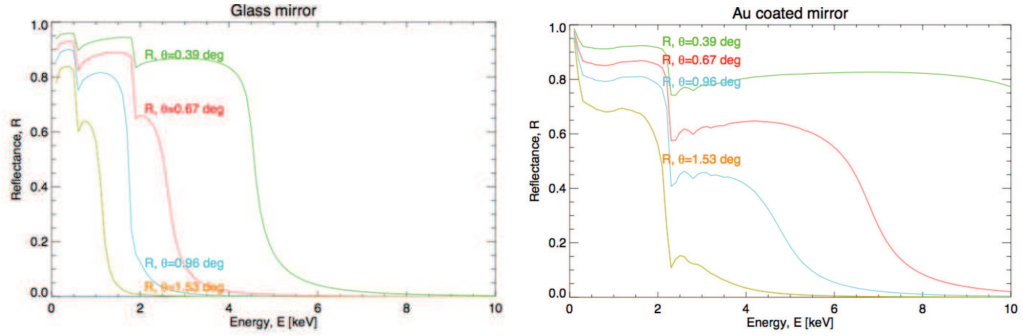

Figure 2.1: *: X-ray reflectivity curves of glass (left) and Au coated glass (right) at different incident angles. The reflectivity is near 100%, for very small incident angles, up to a cut-off energy, where the reflectivity suddenly drops; the use of a high Z coating extends the reflectivity beyond the cut-off energy. Credits: D.Spiga.*

2.2 Figures of merit

2.2.1 Angular resolution

Just like the optical telescopes, also in X-ray the angular resolution is computed from the Point Spread Function (PSF), the degree of spreading of the point source measuring the quality of the imaging system. Nevertheless, two aspects make the treatment for X-ray telescopes very different from the optical ones:

- since the wavelength of X-rays is very small, the resolution limit is, as of today, not dictated by diffraction; in astronomical terms, we can express it via the Strehl Ratio (SR), i.e. the ratio of the peak value of the PSF over the peak of the diffraction figure of a flawless mirror with the same geometry. Nowadays the SR of most astronomical X-ray optics is $\ll 1$;
- for faint X-ray sources, the FWHM (Full Width Half Maximum) is not representative of the resolution capability of the mirror. Usually the HEW (Half Energy Width) is used, defined as the angular diameter in the focal plane which include the 50% of the focused photons. This quantity expresses not only the width of the PSF (which is seldom Gaussian), but also the amount of power collected in the focus vicinities.

The angular resolution of an X-ray mirror depends on the nominal design, the shape errors and the surface roughness. The nominal design is addressed in Sec. 2.3. The treatment of shape errors and surface roughness is traditionally approached considering geometrical optics for shape errors and the first order scattering theory for surface roughness. A novel approach, based on Fresnel diffraction, has been developed at INAF-OAB by L. Raimondi and D. Spiga, which simultaneously accounts for shape and roughness (see Sec. 4.4).

2.2.2 Effective area

For a grazing-incidence mirror, the collecting geometrical area, is the projection of the parabola on the aperture plane. As we will see in Sec. 2.3, in X-ray astronomical mirrors, rays are reflected two times, and the relation between the radius r of the mirror, the focal length f and the incidence angle θ is:

$$r = f\tan(4\theta) \sim f4\theta, \tag{2.8}$$

where the approximation holds only for very small angles. Using 2.8, the collecting area A_{coll}, for a source on-axis at infinity, can be well approximated by the expression

$$A_{coll} = 2\pi r\Delta r = 2\pi rL\tan\theta \simeq 8\pi fL\theta^2, \tag{2.9}$$

where Δr is the width of the projection of the mirror on the aperture plane and L the mirror length.
The Effective Area A_{eff} is defined as the ratio between the focused flux detected on the mirror focal plane and the incidence flux per unit area. For a double reflection mirror, the effective area will depends on the squared reflectivity of the mirror:

$$A_{eff}(E) = A_{coll}R(E)^2 \simeq 8\pi fL\theta^2R(E)^2, \tag{2.10}$$

being $R(E)$ the reflectivity of the mirror at the X-ray energy E.

As θ has to be less than $\theta_c(E)$ in order to keep $R(E)$ at high value (Eqs. 2.5 and 2.7), the incidence angles have to be very shallow, and the effective area of a single mirror is very low. In order to increase the effective area of a telescope, a number of coaxial and confocal mirrors with decreasing radii ("mirror shells") are assembled, with the incidence angle decreasing from the outer to the inner shells. The nesting efficiency is determined by the mirror shell thickness, by the minimum radial mirror separation which is required for integration and alignment, and by the need to leave some clear aperture and mitigate the obstruction of off-axis rays [Spiga 2011]. The thinner the mirror shells, the denser the nesting can be and the larger is the collecting area.

2.2.3 Sensitivity

The sensitivity of a focusing optics is defined as the minimum detectable flux. It is limited by the background noise B, defined as the number of background counts per unit time, per energy band and per detector unit area. For a focusing optics, with effective area A_{eff}, which focuses the flux S on a fraction ϵ of the detector area A_d, the sensitivity is [Spiga Ph.D. thesis 2005]:

$$S = \frac{N}{A_{eff}\eta_E}\sqrt{\frac{2BA_d\varepsilon}{\Delta t \Delta E}}, \tag{2.11}$$

where N is the sigma confidence limit, η_E is the quantum efficiency of the detector at the photon energy E, Δt is the collection time, ΔE is the energy band of the detector. In this expression the source is detected over $N\sigma$. Eq. 2.11 shows that a focused telescope improves linearly the sensitivity in proportion to A_{eff}, versus an improvement $\propto 1/\sqrt{A_d}$ for purely-collimated detectors. Eq. 2.11 shows that high sensitivity is reached not only by achieving large effective area (large A_{eff}) but also having a tight focusing (small ε), i.e. a small value of HEW.

2.3 Mirror design

As an X-ray focusing optic needs to be reflective and work in grazing incidence, the first idea, proposed by Giacconi in 1960, was to use a parabolic surface to concentrate the paraxial rays in its focus (see Figure 2.2).

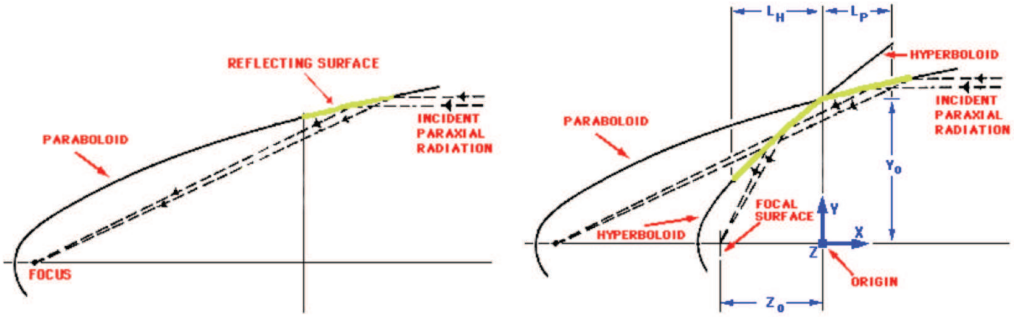

Figure 2.2: *: Left: A simple parabolic mirror. Right: Wolter-I configuration. Credits: [Van Speybroeck & Chase 1972].*

Anyhow, the parabolic shape is not convenient to make grazing incidence telescopes, because they would be affected by a strong coma aberration, that is the dependence of the focal length on the reflection position when an off-axis beam strikes on it. A coma-free optic may be obtained by satisfying the Abbe condition:

$$\frac{h}{\sin\theta} = f, \tag{2.12}$$

where *h* is the distance of the X ray from the optical axis, θ is the angle formed by the focused ray and the optical axis, f is the focal length of the system. Eq. 2.12 means that the incident and the focused rays (or their extensions) have to intersect at a spherical surface (the so-called *Principal Surface*) to avoid coma aberration. For a single reflection this should coincide with the mirror surface; if this is a paraboloid, the Abbe condition is fulfilled only near the vertex, where R(E) $\simeq 0$.

2.3.1 Wolter I

H. Wolter showed in 1952 [Wolter 1952] that the combination of two confocal and coaxial conical surfaces (Figure 2.2), would allow the Abbe sine condition to be nearly satisfied. Moreover

the double reflection has the advantage to reduce the focal length by a factor of two, which is important for optics that have to work in space. The most convenient is the Wolter-I, consisting of a paraboloid and an hyperboloid that are coaxial and confocal. Their equations can be written in cylindrical coordinates as [Van Speybroeck & Chase 1972]

$$r_p^2 = P^2 + 2PZ + [4e^2Pd/(e^2-1)] \qquad \text{paraboloid} \tag{2.13}$$

$$r_h^2 = e^2(d+Z)^2 - Z^2 \qquad \text{hyperboloid} \tag{2.14}$$

In the above equations the origin is at the focus for axial rays, *Z* is the coordinate along the axis of symmetry, and *r* is the radial coordinate. The common focus of the two surfaces is at $Z = [-2e^2d/(e^2-1)]$. There are thus three independent parameters, e, d, and P, which describe the surfaces: e is the eccentricity, while P and d are two parameters that are linearly related to the focal length f (the distance from the axial ray focus to the intersection plane of the paraboloid and hyperboloid (Z_0 in Fig. 2.2) and r, the radius of the surfaces at their intersection (related to f by Eq. 2.8). When the angles of incidence on the parabola and hyperbola sections are equal, in the case of an on axis source at infinite distance, e, P and d are defined as:

$$e = \cos(4\theta)[1 + \tan(4\theta)\tan(3\theta)], \tag{2.15}$$

$$P = f\tan(\theta)\tan(4\theta), \tag{2.16}$$

$$d = f\tan(\theta)\tan(4\theta). \tag{2.17}$$

2.3.2 Wolter-Schwarzschild

In order to satisfy the Abbe sine condition it is sufficient to perform very small corrections (sub-μm to one μm) of the axial mirror profile from its nominal second-order shape [Aschenbach 2009]. The exact surface shape has been derived by Wolter by extending the solutions to grazing incidence which Karl Schwarzschild had already obtained for normal incidence in 1905. Therefore these systems are named Wolter-Schwarzschild (W-S) telescopes. The off-axis angular resolution is much improved using the W-S design with respect to Wolter I type design. In a nested configuration, the join plane (principal surface of the optic) must necessarily be a sphere of radius equal to the focal length, rather than a flat plane as in the conventional Wolter I design (see app. A).

2.3.3 Double cone

If the angular requirement is not a strict requirement, the Wolter I profile may be substituted by a double cone approximation. A double cone focuses only in the azimuthal direction, not in the radial one, hence the size of the spot on the focal plane is $L\theta$. The half diameter is $L\theta/2$, and since $\theta = r/(4f)$ we obtain

$$HEW = \frac{Lr}{8f^2}, \tag{2.18}$$

where L is the mirror length. In this case the production process is much simpler, because the longitudinal profiles have more relaxed tolerances. This solution was adopted for the ASCA, Beppo-SAX, Suzaku, NuSTAR and Astro-H. It was also used for the first SPO prototypes (see app. A).

2.3.4 Polynomial

More general mirror designs than Wolter's exist, in which the primary and secondary mirror surfaces are expanded as a power series. These polynomial solutions are well suited for optimization purposes, which may be used to increase the angular resolution at large off-axis positions, degrading the on-axis performances. The idea is to transfer the principle of the Ritchey-Chretien Cassegrein telescope, widely used in optical astronomy, to grazing incidence optics. By deliberately compromising the on-axis performances, one can introduce aberrations (mainly spherical) that tend to cancel or reduce the off-axis aberrations [Conconi & Campana 2001]. Such a profile is to be adopted in telescopes with large field of view such as WFXT [Conconi et al. 2010], but are also considered for ATHENA as a viable alternative to the Wolter.

2.3.5 Kirkpatrick-Baez

The first two-dimensional X-ray image ever obtained with grazing-incidence reflection was taken in the laboratory by Kirkpatrick and Baez [Kirkpatrick & Baez1948]. The configuration in shown in Figure 2.3-A. The incident rays are focused to a line image by a parabolic mirror. On their path to the line focus, the rays are reflected by a second parabolic mirror, oriented at right angle to the first one, to achieve a point-like focus. This is true for rays parallel to the centre lines of the parabolas. In order to increase the collecting area a stack of parabolas of translation can be constructed (Fig. 2.3b). However, in contrast to the single double-plate system, the image of a point-like source starts to become increasingly extended in size as the number of plates involved increases. Since this was the first imaging telescope used for non-solar X-ray astronomy, the Kirkpatrick-Baez system is worthy of mention only for historical reasons. A typical application of the KB systems is however common at facilities such as synchrotrons and Free Electron Laser (FEL), where it is important having very small spot (on the order of a few microns) and high intensity flux for microscopy studies. It is also worth noting that a KB geometry was proposed for the XEUS optics [Ghigo et al. 2008].

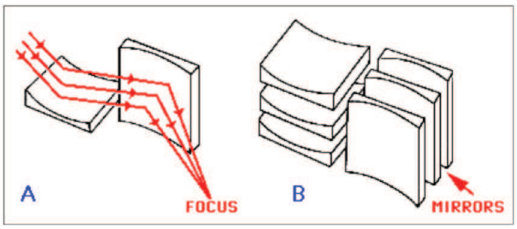

Figure 2.3: *: The Kirkpatrick-Baez X-ray Telescope Design.*

2.4 X-ray reflectivity and scattering off a rough surface

2.4.1 X-ray reflectivity off a rough surface

The reflectivity can be computed by the Fresnel equations 2.2 and 2.3 only for an ideally smooth surface.
An ideally flat surface can be described as $z(x, y) = z_0$. However, a real surface $z(x, y)$ has a "rough" topography, and its deviation from ideality can be characterised by the rms value:

$$\sigma^2 = \frac{1}{L}\int_0^L [z(x, y) - z_0]^2 \, dx. \tag{2.19}$$

If the *smooth surface condition*, $2\pi\sigma \sin\theta_i \ll \lambda$, is fulfilled, we can still assume Eqs. 2.2 and 2.3 as valid and treat the roughness as a perturbation. The result [Michette 1986] is a reduction of the

reflectivity expressed by the *Debye-Waller formula* :

$$R_\sigma = r^2 \exp\left[-\left(\frac{4\pi}{\lambda}\sigma \sin\theta_i\right)^2\right], \tag{2.20}$$

where r is the Fresnel reflectivity, θ_i is the incidence angle and λ is the wavelength of the incident ray.
This formula shows that:

- the reflectivity decreases exponentially as the roughness increases;
- the reflectivity reduction is more severe for small λ (hard X-rays);
- the reflection at large incidence angles is more sensitive to the roughness effect.

Fig. 2.4 shows the reflectivity dependence on the surface roughness and incidence angle, for a Nickel surface polished at different levels.

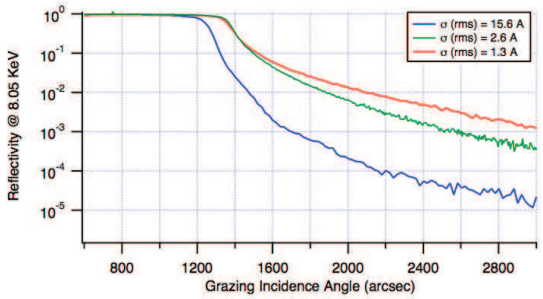

Figure 2.4: *: Reflectivity of three Ni samples, polished at different levels: the reflectivity decreases as the roughness increases.*

2.4.2 X-ray scattering off a rough surface

The X-ray scattering off a reflective surface, at wavelength λ, can be computed by using the first order perturbation theory in grazing incidence, assuming the surface to be smooth and isotropic. Let's consider a X-ray, with wavelength λ, impinging on a rough surface with an incidence angle θ_i, and scattered off the surface with a scattering angle θ_s (Fig. 2.5). For a single boundary characterized by a single Power Spectral Density (PSD), the relation is a simple proportionality between the scattered intensity per angle unit and the monodimensional PSD, $P(\nu)$, where ν is the spatial frequency (Stover 1995, Church 1986):

$$\frac{1}{I_0}\frac{\mathrm{d}I_\mathrm{s}}{\mathrm{d}\theta_\mathrm{s}} = \frac{16\pi^2}{\lambda^3} Q_\mathrm{is}\, \sin^2\theta_\mathrm{s} \sin\theta_\mathrm{i}\, P(\nu), \tag{2.21}$$

The spatial frequencies ν are related to the X-ray wavelength, the incident angle and the scattering angle by:

$$\frac{1}{\nu} = \frac{\lambda}{|\cos\theta_\mathrm{i} - \cos\theta_\mathrm{s}|}. \tag{2.22}$$

The Q_is *polarization factor* is related to the reflectivity computed with the Fresnel equations, and can be computed as $\sqrt{R(\theta_s)R(\theta_i)}$ in the Rayleigh-Rice vector theory.
Eqs. 2.21 and 2.22 are useful not only to predict the impact of XRS on the angular resolution, but also as a diagnostic tool for the PSD of the surface roughness (see Chapter 4).

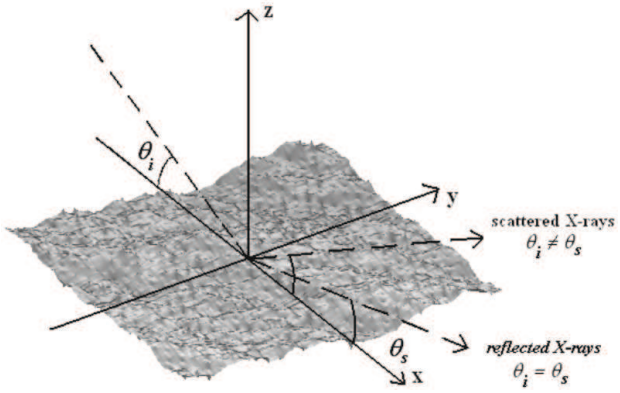

Figure 2.5: *: Sketch of an incident ray impinging of a rough surface: θ_i is the incidence angle and θ_s is the scattering angle. Credits: [Spiga 2007]*

2.5 X-ray reflectivity and scattering off a multilayer coating

As pointed out in Section 2.1, the reflectivity in the X-rays drops off as the incidence angle increases beyond θ_c. Anyway, keeping the incidence angle very small, reduces the mirror cross-section and the effective area (see Sect. 2.2.2). A way to overcome this problem is to adopt a multilayer instead than a single layer coating. Multilayers consist of an alternance of two layers with very different densities and therefore different refractive index in X-rays. The constructive interference of the reflected rays builds up high reflectivity at some combinations of angles-energies if the stack is designed smartly. In particular:

- multilayers with constant period will have high reflectivity only at specific wavelengths, therefore acting as monocromators;
- multilayers that change their period through the stack, the so-called graded multilayers, can reflect a continuum set of wavelengths and therefore are very useful in X-ray astronomy. They have a lower peak reflectivity in comparison to the constant period-type, but the reflectivity is extended over decades of keV's (up to 100 keV).

2.5.1 Periodic multilayer

A periodic multilayer is a succession of N identical bilayers, each of them being a superposition of two thin films with a large density contrast (Fig. 2.6). The heavier elements (high Z) is called $absorber$, the lighter one (low Z) is the $spacer$. The absorber and the spacer keep the interfaces at the right distance to build up the constructive interference of reflected wavelets.

When all of the layer pairs in a multilayer have identical thickness, the reflectivity is concentrated at energy peaks given by the Bragg equation:

$$n\lambda = 2d\sin\theta, \tag{2.23}$$

where n is an integer, λ is the wavelength of incident wave, d is the period of the multilayer, and θ is the incidence angle.

2.5.2 Graded multilayer

To obtain a broadband reflector, it is possible to use a depth graded multilayer, where the top layers have large d-spacing to reflect the lower energies and the bottom layers have small d-spacing to

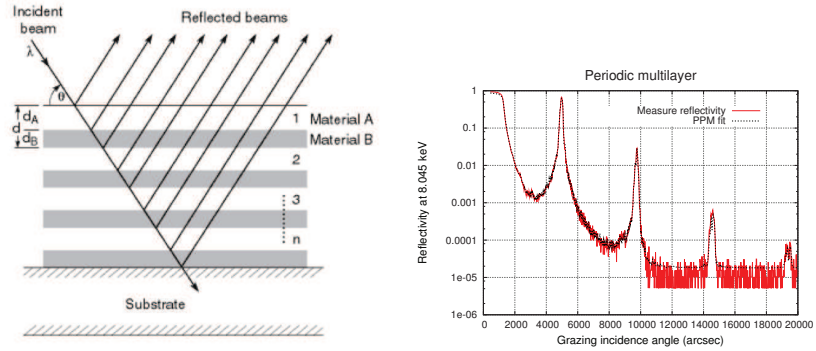

Figure 2.6: *: Left: scheme of a multilayer reflector of N bilayer pairs. Credits: J.H. Underwood. Right: Measured reflectivity of a silicon wafer coated with a periodic W/Si and Pt/C multilayer with 60 bi-layers.*

reflect the higher energies (see Fig. 2.7). This arrangement minimizes losses due to absorption because lower energy photons travel through a lower absorption thickness.

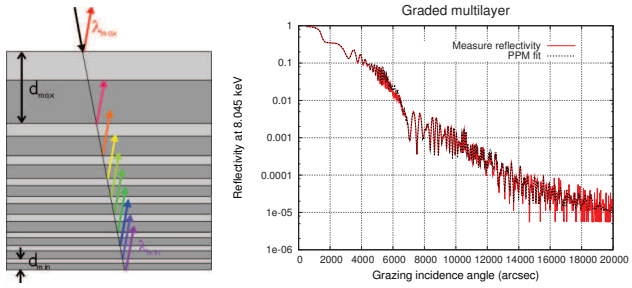

Figure 2.7: *: Left: scheme of a graded multilayer. Credits: [Windt 2015] Right: Reflectivity of a a silicon wafer coated with a graded W/Si and Pt/C multilayer with 100 bi-layers.*

The typical bilayer thickness distribution is defined by a power law with three parameters:

$$d(i) = \frac{a}{(b+i)^c}, \tag{2.24}$$

where a, b, and c are constants, and i is the bilayer index ranging from 1 to N. This concept was introduced first for neutron mirrors by Mezei in 1988 and after developed by Joensen in 1993 for X-ray astrophysics. Eq. 2.24 defines the so-called $supermirror$. a, b, and c are parameters to be optimised for the target effective area [Cotroneo et al. 2009].

2.5.3 X-ray scattering off a multilayer

The X-ray scattering from a single reflective surface was given in 2.21. In the case of a stack of alternated N layers, this relation is complicated by the interference effects among interfaces (Fig. 2.8). If the roughness is isotropic and the incidence angle is beyond the critical angles for total reflection of both materials, the scattering diagram can be expressed in terms of the interfacial Power Spectral Densities (P_j) and the Crossed Spectral Densities (C_{jm}) for all the couples of interfaces, using the following equation (Spiga 2005), which represents a generalization of

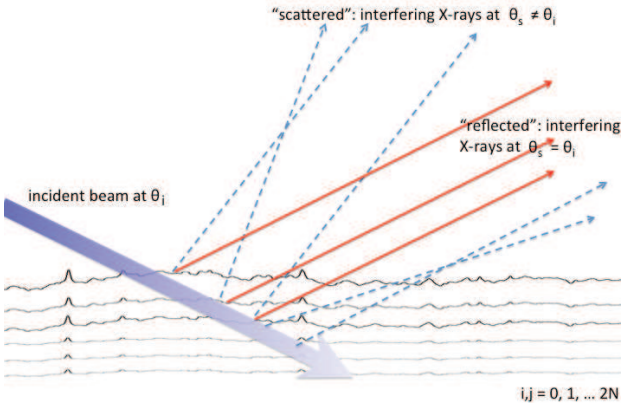

Figure 2.8: *: Scheme of X-ray scattering in a multilayer stack. Both "reflected" (i.e., in the direction specular to that of incidence) angle and "scattered" (i.e. in non-specular directions) rays result from the interference of elementary waves scattered at each boundary in the multilayer.*

Eq. 2.21:

$$\frac{1}{I_0}\frac{\mathrm{d}I_\mathrm{s}}{\mathrm{d}\theta_\mathrm{s}} = K(\lambda,\theta_\mathrm{s},\theta_\mathrm{i})\left[\sum_{j=0}^{N} T_j^2 P_j(\nu) + 2\sum_{j<m}(-1)^{j+m} C_{jm}(\nu) T_j T_m \cos(\alpha\Delta_{jm})\right]. \quad (2.25)$$

In Eq. 2.25 the layers are numbered from the substrate toward the surface. The spatial frequency ν is still related to the scattering and the incidence angles via Eq. 2.22, $\alpha = 2\pi(\sin\theta_\mathrm{s} + \sin\theta_\mathrm{i})/\lambda$, T_j is the field amplitude transmittance in the j^{th} layer, $\Delta_{jm} = \langle z_j\rangle - \langle z_m\rangle$ is the average distance between the j^{th} and the m^{th} interface, and

$$K(\lambda,\theta_\mathrm{s},\theta_i) = \frac{16\pi^2}{\lambda^3} Q_\mathrm{is}\ \sin^2\theta_\mathrm{s}\sin\theta_\mathrm{i}, \quad (2.26)$$

is the same proportionality factor appearing in Eq. 2.21. The polarization factor is still provided by $\sqrt{R(\theta_s)R(\theta_i)}$.

The P_j's and the C_{jm}'s are the physical quantities that affect the intensity and the mutual coherence of the scattered waves, which in turn interfere to build up the XRS diagram. They can be computed by studying the roughness evolution in the multilayer growth process (see Section 10.1.2).

2.6 Consolidated manufacturing techniques for the X-ray telescopes: past, present and near future

The practical manufacturing of X-ray optics is a trade-off of exacting requirements sometimes in contrast with each other. A large mirror mass usually results from a large collecting area, an excellent angular resolution and a good mirror thermo/mechanical stability. A low optical weight usually goes at the expense of the optical performances. The X-ray telescope production method can be classified depending on the mirror production and integration methods. Each method can has its advantages and disadvantages, and usually a specific feature is preferred at the expense of the others, depending on the requirements of the mission.
The mirror production encompasses two methods:

- the production by direct polishing of single mirror shells

- the production by replica of a figured and polished mandrel

There are several optical substrates that have been already successfully used for X-ray mirrors:

- monolithic quartz or Zerodur (direct polishing) for Einstein, ROSAT and Chandra
- electroformed nickel (replica) for Beppo-SAX, XMM, Swift/XRT, eRosita
- thermally slumped aluminum foils (replica) for ASCA, Suzaku, ASTRO-H
- thermally slumped glass foils (replica) for HEFT and NuSTAR.

The mirror integration also comprises two methods:

- integration of monolithic shells
- integration of segmented mirrors

In Table 2.1, the telescopes already existing are compared in manufacturing technology and final performances. The telescopes to be launched in the future are compared in Table 2.3.

Table 2.1: *: Comparison of past and present X-ray telescopes.*

Mission	Einstein	Rosat	ASCA	BeppoSAX	Chandra	XMM	Jet-X	Suzaku	NuSTAR
Launch Year	1978	1990	1993	1996	1999	1999	2004	2005	2012
Configuration	Wolter I.	Wolter I	D. cone	D. cone	Wolter I	Wolter I	Wolter I	D. cone	D. cone
n. modules	1	1	4	3+1	1	3	2	4+1	2
Technology	Dir. pol.	Dir. pol.	Al segm.	Ni replica	Dir. pol.	Ni replica	Ni replica	Al segm.	Slump.glass
Substrate	Glass	Zerodur	Al	Nickel	Zerodur	Nickel	Nickel	Al	Glass
n. shells/mod.	4	4	120	30	4	58	12	175/168	133
Ext. diam.	559 mm	835 mm	345 mm	162 mm	1230 mm	700 mm	350 mm	400 mm	51 mm
Int. diam.	325 mm		120 mm	68 mm	650 mm	306 mm	153 mm	118 mm	191 mm
Ageo./mod.	350 cm^2	1140 cm^2	558 cm^2		1100 cm^2	2000 cm^2		887 cm^2	
E range (keV)	0.1-4	0.1-2	$\leq$ 12	0.1-10	0.1-10	0.1-12	0.2-10	0.2-12	6-79
HEW	2 arcsec	5 arcsec	3.5 arcmin	1arcmin	0.5 arcsec	15 arcsec	18 arcsec	114 arcsec	58 arcsec
Aeff.@0.15 keV/mod.		1020 cm^2							
Aeff.@0.25 keV/mod.	400 cm^2				800 cm^2				
Aeff.@1 keV/mod.				240 cm^2	$\leq$ 300 cm^2				
Aeff.@1.5 keV/mod.			300 cm^2			1430 cm^2	110 cm^2	440 cm^2	
Aeff.@4 keV/mod.	30 cm^2								
Aeff.@5 keV/mod.					400 cm^2				450 cm^2
Focal (m)	3.4	2.4	3.5	1.85	10	7.5	3.5	4.75	10.15
Coating	Ni	Au	Au	Au	Ir	Au		Au	Pt/C W/Si

2.6.1 Direct polishing: Eistein, ROSAT, Chandra

In the direct polishing technology, the substrate of each single monolithic shell is directly polished and figured. The shells are usually in Quartz or Zerodur and their thickness about 20-30 mm, in order to withstand the steps of production and to have the necessary rigidity to not suffer from deformations. With this technique is possible to obtain mirrors of high angular resolution (Einstein: 2 arcsec, ROSAT: 5 arcsec, Chandra: 0.5 arcsec), because the geometrical profiles are controlled with high precision, but the telescope will have a relatively small collecting area, because only few shells can be nested. This type of optics is employed for observations of nearby X-ray sources. Observation of distant sources is also possible, but require a very long observation time (on the order of 1 Msec).

Figure 2.9: *: Chandra telescope at different stages of production. Starting from left: a single raw blank prior to grinding and polishing; polished element; coated element prior to insertion into the mirror holding fixture; the mirrors in their support structure. Credits: [Weisskpft 2012].*

2.6.2 Replication with Nickel: BeppoSAX, XMM, Jet-X, e-ROSITA

Nickel optics are electroformed on a precisely figured mandrel in a Electroless Nickel galvanic bath [Chambure et al. 1996]. The mandrels are made out of initially double conical aluminium blocks coated with Kanigen nickel (selected for its hardness, necessary for good polishing, high adhesion to the aluminium, and low porosity) and then lapped to the exact shape and finally super-polished to a surface roughness better than 0.4 nm. Prior to electroforming, a 250 nm thick layer of gold is deposited on the mandrel and it acts both as a release agent and as reflective coating. Shells obtained with this technique are thinner (typically from 0.2 mm to 1 mm), so many shells can be nested at the advantage of the collecting area. Anyway, this replica process can reach at best 15 arcsec angular resolution, as in the case of XMM (Table 2.1) and e-ROSITA (Table 2.3).

Figure 2.10: *: XMM telescope at different stages of production. Starting from left: the super polished Al mandrels and the Ni mirror shells; Ni shells during the alignment and assembly; the mirrors in their support structure. Credits: ESA*

2.6.3 Replication with slumped aluminum foils: ASCA, Suzaku, ASTRO-H

In this case the mirrors are not monolithically produced: segmented aluminum substrates, with thickness 0.127 mm, are pre-shaped at relatively high temperature, being pressed onto a conical mandrel with air pressure. The mirrors are fabricated by the epoxy-replication method in which a thin reflective layer (Au for ASCA and Suzaku, depth-graded Pt/C and W/Si multilayers for ASTRO-H) is sputtered onto the smooth surface of a glass tube and transferred to a shaped aluminum substrate with epoxy glue. The integration of segmented optics is a critical step. The best resolution obtained with this process is $\sim$ 100 arcsec for Suzaku and ASTRO-H (see Tables 2.1 and 2.3)

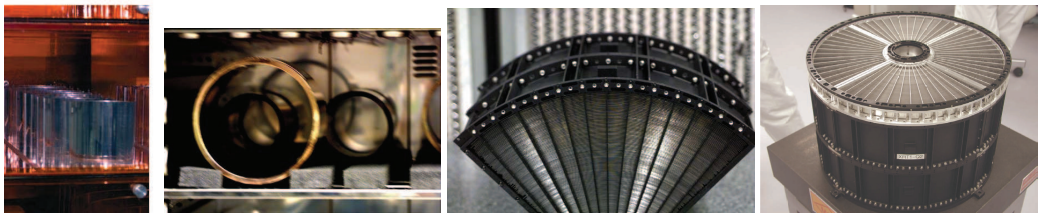

Figure 2.11: *: Suzaku telescope at different stages of production. From left: aluminum foils formed to conical section; coupled foil-mandrel placed in oven for epoxy-curing; one assembled sector of the optic; picture of the Suzaku module XRT-I1. Credits: NASA-JAXA.*

2.6.4 Replication with slumped glass foils: HEFT, NuSTAR

Thin glass foils are thermally formed in a furnace over a forming mandrel. For HEFT and NuSTAR, Schott D263 glass foils, with a thickness of 0.2mm, where used over fused silica forming mandrels [Harrison et al. 2006]. Two different slumping technologies were used: indirect slumping for HEFT and direct slumping for NuSTAR (see chapter 3). In the first case, concave mandrels were used and the foil did not touch the mandrel; in the second instead, convex mandrels were used and the optical side of the glass foil was brought into contact with the mandrel (Fig. 2.12-centre); the mandrels were figured into precise cylinders and then coated with a BN release layer to avoid glass sticking due to the contact between the glass and the Fused Silica mould. The integration of the coated glass foils was performed with glued ribs in grafite, forcing the glass foils to change their shape from cylinder to the adopted double cone configuration. For NuSTAR, the final resolution was $\sim$ 58 arcsec. Considering the slumped glass foils a viable alternative for the optics of the ATHENA telescope (HEW = 5 arcsec), it is clearly necessary to improve the process here described. Several groups are working to this end (see paragraph 2.7.2).

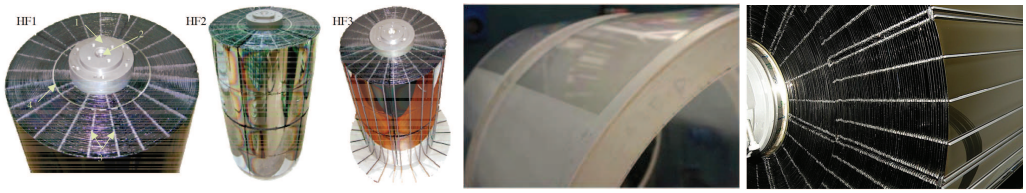

Figure 2.12: *: Letf: HEFT, a view of the three modules. Center: NuSTAR: thin glass foils formed over fused silica mandrels. Right: NuSTAR, a view of the optics module showing the different azimuthal length of the inner and outer segments. Credits: NASA.*

2.7 Manufacturing techniques for the next generation X-ray telescope: ATHENA

ATHENA (Advanced Telescope for High ENergy Astrophysics) comes from the reformulation of the IXO mission on March 2011, when NASA and JAXA abandoned their participations and

ESA, along with the scientific community, started to investigate to what extent a European-led mission could preserve the original science case of IXO, competing with JUICE and NGO to be the first Large-class mission in the ESA's Cosmic Vision 2015-2025. At this time, the original IXO telescope with an effective area of 3 m^2 at 1 keV, already descoped to 2.5 m^2, was reduced to the ATHENA one with effective area of 2 m^2 at 1 keV. The ATHENA's telescope was made by 2 modules (Fig. 2.13) with effective area of 1 m^2 each, focal length of 12 m (to be compared to the 20 m focal length of IXO) and resolution of 10 arcsec, with a goal of 5 arcsec, which was the original IXO's specification. After the selection of JUICE as L1 mission in may 2012, a further reformulation of the ATHENA mission occurred (Fig. 2.14). In spring 2013 the scientific community proposed to ESA the science themes to be addressed by the new ATHENA mission (see par. 1.3). In fall 2013, the "Hot and Energetic Universe" was selected by the ESA SSC. Finally in June 2014, the mission was selected for L2, the second Large class mission in ESA's Cosmic Vision science program, with a launch foreseen in 2028. An Ariane-V class launcher will carry the spacecraft to an L2 orbit with an expected operational lifetime of 5 years.

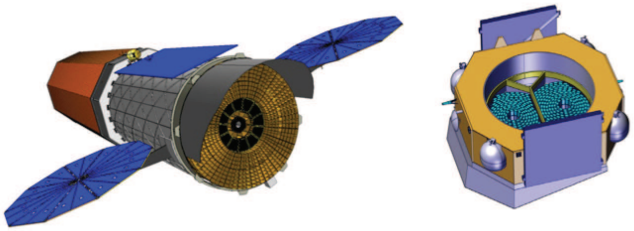

Figure 2.13: *: Left: IXO spacecraft design. Athena-old: schematic view of the telescope structure. Credits: ESA*

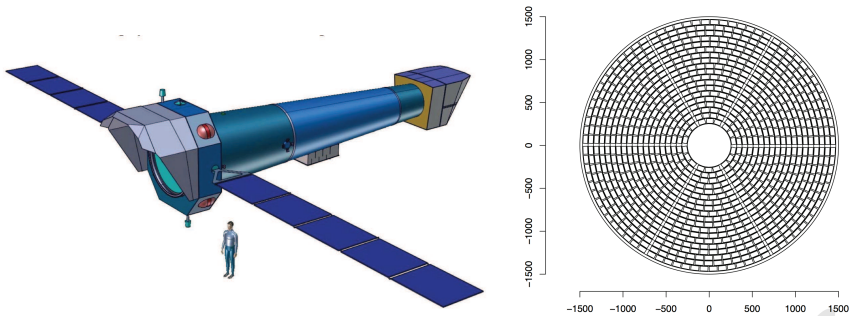

Figure 2.14: *: Athena: on the left the spacecraft design, on the right a schematic view of telescope. Credits: ESA*

A comparative analysis of the telescope performances required for ATHENA and other mission, in term of resolution and effective area, sets the mission in the so-called "Golden Quadrant" (Fig. 2.15): the large effective area reduces the time required to observe distant and faint objects, the high resolution enable to distinguish distant objects often located in crowded fields, providing the breaking leap required to achieve the science goals of ATHENA.

To reach the angular resolution and the effective area required for the ATHENA mission is a challenging goal. To have a mirror with a high angular resolution requires a precise mirror figure and a very smooth surface. The large dimension, necessary to reach the ATHENA requirements,

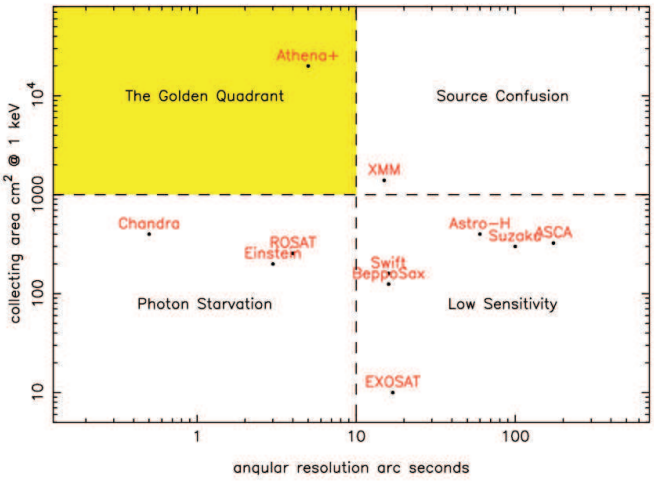

Figure 2.15: *: The performance of X-ray telescope modules. [Credits: Willingale]*

forces the use of a modular approach: in this scheme, the optical module is divided into segments, manufactured individually and lately assembled following a hierarchical principle. Large areas typically require a large mass, hence lightweight optics should be used; moreover, any alignment and integration mechanism would require additional mass and volume to move and assemble mirrors. The challenge is to develop a technology that eventually achieves the requested specifications (Tab. 2.3) while maintaining the low-mass and low-cost characteristics of the technologies used by Suzaku and NuSTAR (Tab. 2.2).

Table 2.2: *: Comparison of key requirements for some X-ray telescopes. Credits: Zhang SPIE 2013.*

Mission	**Mass/Aeff at 1keV** kg/m^2	**HEW** arcsec	**Production cost/Aeff at 1keV** 2013 M$/m^2
Chandra	18000	0.5	9800
XMM-Newton	3200	15	360
Suzaku	400	114	88
NuSTAR	400	58	80
ATHENA	400	5	80

Tab. 2.3 summarises the key technological parameters defined for the ATHENA telescope, compared to other telescopes to be launched in the near future.

Table 2.3: *: Comparison of ATHENA with other near future X-ray telescopes.*

Mission	ASTRO-H Soft X-ray telescopes	ASTRO-H Hard X-ray telescopes	e-Rosita	ATHENA
Launch Year	2016	2016	2017	2028
Configuration	D. cone	D. cone	Wolter I	Wolter-Schwarzschild
n.modules		2+2	7	1
Technology	Al segm.	Al segm.	Ni replica	Si Pore
Substrate	Al	Al	Ni	Si
n.shells/mod.		213	54	
Ext. diam.	450 mm	450 mm	358 mm	1437 mm
Int. diam.		120 mm	76 mm	285 mm
Ageo./mod.		968 cm^2		
Energy range	0.3-12 keV	5-80 keV	0.3-10 keV	0.3-12 keV
HEW	102 arcsec	102 arcsec	15 arcsec	5 arcsec for E $<$ 8keV
Aeff. @ 1 keV	160 cm^2		1365 cm^2	$\geq$ 20000 cm^2
Aeff. @ 5 keV			139 cm^2	
Aeff. @ 6 keV	210 cm^2			$\geq$ 2500 cm^2
Aeff. @ 8 keV		$\geq$ 800 cm^2		
Aeff. @ 30 keV		$\geq$ 300 cm^2		
Aeff. @ 50 keV		$\geq$110 cm^2		
Focal (m)	6	12	1.6	12
Coating	Au	Pt/C	Au	Ir + B_4C

2.7.1 Silicon Pore Optics: SPO

The Silicon Pore Optics (SPO) technology has been under development by ESA and Cosine Measurement Systems (http://cosine.nl) for over a decade [Collon et al. 2014] and was defined as the technology to be used for the production of the ATHENA telescope. This technology was first introduced by Beijersbergen et al. (2004) and subsequently applied to the ESA XEUS mission, [Kraft et al. 2005], and later for IXO [Collon et al. 2009]. SPO utilises commercially available 300 mm Silicon Wafers and 0.775 mm thick [Bavdaz et al. 2010]. The requirements imposed on the surface finish of the latest generation silicon wafers for the electronics industry are very similar to the ones of X-ray optics: the silicon wafers surface roughness corresponds to that required for X-ray optics and the figure errors are within the error budget for a few arc second angular resolution optic [Bavdaz et al. 2010]. Another advantage of crystalline Silicon is its excellent thermal conductivity that rapidly smoothes out thermal gradients in the optic. The technology for the SPO (see also app. A) largely rely on existing and modified processes available in the semiconductor industry: the Silicon wafers are diced, wedged and ribbed on their non-optical side, coated with Iridium (plus an optional layer of B_4C to enhance the low-energy reflectivity) on the reflective side, leaving uncoated strips in correspondence of the ribs, and finally stacked onto a mandrel having the desired curvature to form a building block of the optical module. The contact of the native oxide on the pristine Silicon wafer surface with the oxide used for wedging the ribs ensures a firm adhesion without the use of any glue. Each silicon plate replicates from the mandrel a principal azimuthal curvature determined by its distance from the optical axis, and a secondary parabolic or hyperbolic curvature in the longitudinal direction suitable to focus X-rays. The rectangular apertures left clear by the Silicon membranes and ribs are the pores that enable the propagation of X-rays to the mirror surface. The parabolic and the hyperbolic stacks are subsequently aligned in such a way that X-rays undergo two reflections in sequence - in the widespread Wolter-I optical configuration - and are focused to the focal plane at a 12 m distance.

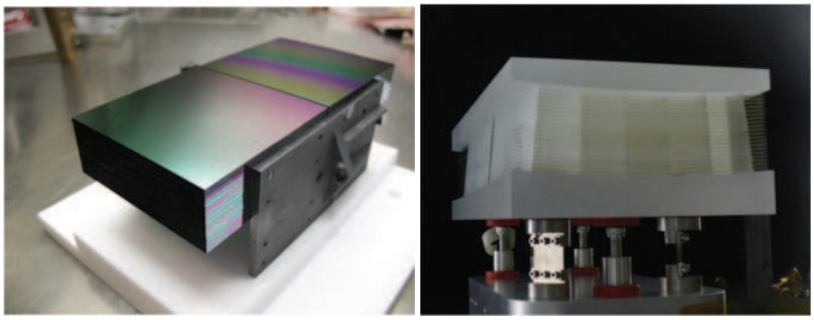

Figure 2.16: *: Left: Silicon Pore Optics module. Credits: ESA. Right: Slumped Glass Optics module produced and integrated at INAF-OAB.*

2.7.2 Slumped Glass Optics: SGO

Beside silicon, thin glass foils are also considered, owing to mechanical properties and low density ($\rho_{Si} = 2.32\text{g/cm}^3$, $\rho_{EagleXG-glass} = 2.38\text{g/cm}^3$). Moreover, thanks to the technological advances in glass foils production (see par. 3.4), the glass surface roughness is approaching the one of the silicon wafers, therefore suitable for X-ray optics. Therefore the Slumped Glass Optics (SGO) technology was also developed as an alternative to SPO for the ATHENA optics.

Thin glass foils are curved by hot slumping process over a mould into a furnace. The slumping can be direct or indirect, the surface in contact with the mould being the optical or the non-optical, respectively. Moreover pressure can be exerted in order to assist the mould replication. The glass foils can be slumped with the final figure profile and a stress free integration is then implemented in order to stack the glass mirrors, or they can be slumped with cylindrical shape and then assembled, with a stress integration concept, to the final configuration.

SGO for X-ray optics is the natural development of the technology already used for HEFT and NuSTAR (Craig et al. 2011), and it is under further development by several groups worldwide: INAF-Osservatorio Astronomico di Brera (OAB, Italy), Max Planck Institut für Extraterrestrische Physik (MPE, Germany), NASA-Goddard laboratories and Columbia University (USA), Harward-Smithsonian Center for Astrphysics (USA), Academy of Science of Prage (Czech Republic). Different approaches and different materials are used in the mentioned research groups. The SGO research at INAF-OAB was supported from 2009 till 2013 by the European Space Agency, as a backup development of the IXO optics [Pareschi et al. 2011, Proserpio et al. 2011, Ghigo et al. 2012]. The main idea is to thermally form 0.4 mm thin glass foils to cylindrical shape, via direct hot slumping assisted by pressure, and integrate them in a Wolter-I configuration into the X-ray optical unit via a cold shaping step [Civitani et al. 2013]. The innovation of the approach followed by OAB has been the introduction of pressure to force the glass foils to replicate the shape of the slumping moulds; moreover the use of Zerodur K20, as material for the slumping mould, avoided the use of an anti-sticking coating. Our slumping process is fully described in chapter 5, together with the process improvements developed during my Ph.D. thesis. The results, in term of expect resolution of the slumped glass foils, are presented in chapter 6, where I show that the goal of 2 arcsec, allocated for the slumped foils in order to have the total resolution of the telescope within 5 arcsec, is almost reached.

CHAPTER 3

Fundamentals of X-ray glass mirror thermal forming

3.1 Introduction

Glass thermal forming is a commonly used technique to produce a glass with a desired shape by replication: instead of figuring each glass object to its final shape by means of expensive processes like grinding and polishing, the glass is formed by a thermal process that impart the final shape to the object and is repeatable for many glass objects. Different techniques can be adopted, depending on the use and the tolerances required by the glass object:

1. Glass blowing is probably the most well-known glass forming process. Numerous objects of practical and artistic value are formed by blowing molten glass. The process has been industrialised to manufacture containers, tubing [Doyle 1994] and light bulbs [Rekhson et al. 1991]. In the glass blowing technique, no mould is required to figure the glass piece.

2. Compression moulding is most frequently used to create precision glass lenses. It is a hot forming method in which a heated raw glass gob is pressed by optically polished moulds to create the finished lens shape (Fig. 3.1). Controlled cooling of the moulded glass is carried out immediately after pressing to keep the stress and thermal shrinkage level below a required value after the molding process. Few technical challenges of this process are well known, which include, for the moulds, curvature compensation, mould design and mould life, and, for the moulded lens, residual stresses, and refractive index deviation after the moulding process [Doyle 1994, Tao et al. 2013].

3. Thermal slumping is a forming process where a piece of glass sheet is placed into an initially cold oven and heated until it is sufficiently fluid to sag under its own weight. If the final shape is sufficiently simple, no mould is needed and the glass is allowed to sag until the desired shape is attained: such slumping is used industrially in the fabrication of windshields and other vehicle components [Daoudi et al. 1994]. However, if the final glass shape requires higher precision, a mould is used to form glass sheets. The process can then be *direct* (the side of the glass in contact with the mould will be the optical one), or *indirect* (the

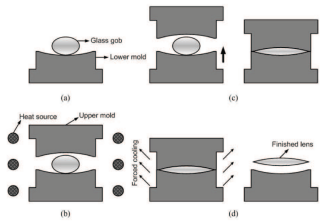

Figure 3.1: *: Schematic illustration of the glass compression moulding: (a) Placing of raw glass gob/ blank material on the lower mold, (b) Heating of the glass and mold assembly to the molding temperature, (c) Pressing (molding) of the glass material between the mold halves and (d) Forced cooling of the lens and mold assembly to near room temperature and lens release. Credits: Jain 2006.*

optical side of the glass is not in contact with the mould surface). Glass thermal slumping utilises similar process conditions as compression moulding, e.g. heating, moulding, and cooling. In glass thermal slumping process, the raw glass sheet and mould are heated up to the working temperature (or soaking temperature) and then slumped by its own weight or vacuum pressure. Controlled cooling of the slumped glass mirror is carried out immediately after slumping is completed, to obtain the mould replication to the required level.

In this thesis, the thermal slumping process is considered. In the following sections I will give an overview of the materials used for thermal slumping: I will describe different glass and mould types, that are most commonly used, together with their main properties and parameters. In section 3.8, I will describe different slumping techniques adopted in different laboratories. In this section, I will also give a description of the different integration method, which can be roughly divided in "stress-free" integration (NASA, MPE approach for the Athena mission) and "stress-based" (as developed for HEFT and NuSTAR, and now adopted in our laboratories). In the first approach, the integration is meant to preserve the glass figure; in the latter, the integration forces the glass to assume a slightly different shape, thus imparting a stress to the glass foil.

3.2 Definition of a glass and its viscosity dependence on temperature

Strictly speaking, glasses are substances that behave as rigid solids, but may act as liquids owing to their amorphous structure. Despite the most commonly used glasses are based on silica, silica is not a required component of a glass. In the recent years, the existence of a vast number of non-silicate glasses was found. In fact, it is know that polymers and metals can also be formed as glasses, as can a large number of non-oxide, inorganic compounds. A correct definition of glass is "an amorphous solid completely lacking in long range, periodic atomic structure, which exhibit a region of glass transformation behaviour" [Shelby 2005].

Figure 3.2-left shows a plot of temperature vs. volume of a liquid being cooled at some finite rate, at constant pressure. At the melting point, a non-glass forming liquid readily freezes into a crystalline solid (line AE). However, in a glass-forming system the melt cools down below its solidification temperature. In the liquid state the viscosity of glass is so low that the structure changes in step with temperature and the equilibrium structure is attained almost instantaneously. As the temperature is lowered further, the viscosity gradually increases along with the time required to attain a new equilibrium configuration. This results in the deviation of the cooling curve from the equilibrium line AB until the structure is finally frozen in a fixed configuration at point C. This state is called the *glassy state*.

Figure 3.2-right shows the typical viscosity of a glass as a function of temperature. It is common use to define some temperatures where the viscosity η of the glass assume fixed values: the *softening* point is defined as the temperature where $\eta = 10^{7.5}$ poises , the *annealing* point is defined as the temperature where $\eta = 10^{13}$ poises and the *strain point* is defined as the temperature

where $\eta = 10^{14.5}$ poises[1]. At these temperatures, the stresses stored in the glass are relieved at different speed according to Table 6.7.

The temperature interval from the strain point (also called the lower annealing point) and the upper annealing point is the glass transformation zone. If we extrapolate the glass (CD) and the liquid (AB) lines of Fig. 3.2-left , they intersect at a temperature defined as the *glass transformation* temperature T_g [Web reference: Britglas, Daoudi et al. 1994].

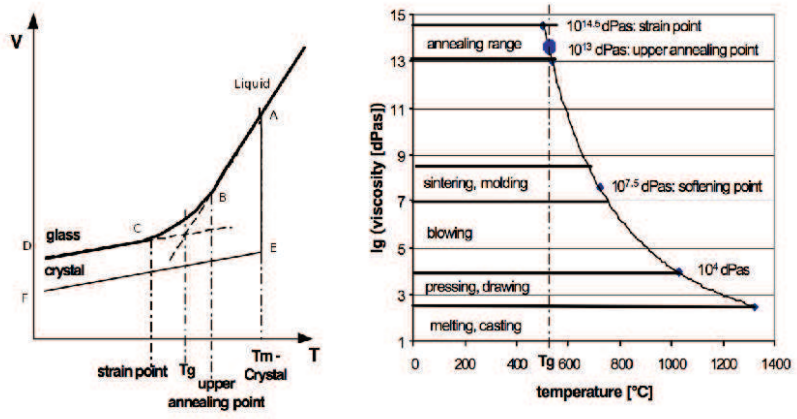

Figure 3.2: *: Left: the Volume/Temperature diagram of a glass showing the transition region from liquid to glass. Right: The viscosity of glass as a function of temperature. Credits: Schott.*

Table 3.1: *: Reference viscosities for glass: the time for stress relaxation changes with viscosity.*

	Viscosity	Description
Strain point	$[10^{14.5}]$ poise	Stress is relieved within several hours
Annealing point	$[10^{13}]$ poise	Stress is relieved within a few minutes
Softening point	$[10^{7.6}]$ poise	Glass deforms under its own weight

Two expressions that have commonly been used to describe the temperature dependence of viscosity for glasses are the Arrhenius equation and Vogel-Fulcher- Tamman (VFT) equation [Shelby 2005]. The expression for the Arrhenius equation is given by:

$$\eta = \eta_0 \exp\left(\frac{\Delta H}{RT}\right), \tag{3.1}$$

where η_0 is a constant, ΔH is the activation energy for viscous flow, R = 8.31 J/(mol K) and T is the temperature (η is given in Pa s, T in K). Arrhenius equation can provide a good fit in the transition temperature range and at high temperature where melts are very fluid [Shelby 2005]. Actually, the activation energy is not constant over the entire viscosity range. A better fit to viscosity data over the entire viscosity range is provided by a modification of Eq. 3.1, which includes a varying activation energy for viscous flow. This expression is usually called the Vogel-Fulcher-Tamman (VFT) equation. The VFT equation adds a third variable T_0 to the Arrhenian expression to account for the variability of the activation energy and replaces the ΔH with the

[1] Note that the CGS unit of viscosity is the poise, while the Pas - Pa · sec - is the MKS unit. The dPas is also commonly used: 1 poise = 0.1 Pas = 1 dPas. The viscosity of liquid water is 0.01 poise.

parameter B:

$$\eta = \eta_0 \exp\left(\frac{B}{T - T_0}\right). \tag{3.2}$$

This expression is most often written in the form actually used by Fulcher [Fulcher 1925]:

$$log_{10}(\eta) = -A + \frac{B}{T - T_0}, \tag{3.3}$$

where A replaces η_0, and T and T_0 are given in °C. A, B and T_0 are constants that are usually obtained from the glass vendor. T_0 for a given glass composition is always considerably lower than the T_g for that composition. If T_0 is equal to zero, the viscosity/temperature curve will exhibit Arrhenian behaviour over the entire viscosity region, with a single value of ΔH. On the other hand, as T_0 approaches T_g, the curvature increases and the difference between ΔH for the fluid melt and in the transformation region becomes large [Shelby 2005].

At large viscosity values, a change in temperature takes a finite time to result in the corresponding change in viscosity, and this time increases as viscosity increases (and temperature decreases). This process is called *relaxation*. Different models have been used to describe relaxation in glasses, as the creeping flow model [Stokes Ph.D. thesis 1998], the Narayanaswamy model [Scherer 1986] and several works at Ohio University [Jain Ph.D. thesis 2006], (Chen & Yi 2008), [Chen 2010]. I have used a model proposed in 2003 by Jimenez-Garate [Jimenez et al. 2003], since it simply describes the origin of the corrugations experimentally observed in the glass foils slumped during my work, typically observed over spatial frequencies of 1-2 cm. This is described in section 3.7.

3.3 Types of glasses

Vitreous silica is the most viscous of all common glass forming melts. The glass transformation temperature of vitreous silica, strongly influenced by OH^- and other impurity concentrations, lies in the range of 1060 to 1200 °C. The viscosity of silica varies very slowly with temperature. Productions of commercial vitreous silica requires processing temperatures in the range of 2200 °C, in order to obtain bubble free-glass. Adding alkali oxides to silica results in formation of non-bridging oxygens and a reduction in the connectivity of the structure. The practical effect is a rapid decrease in viscosity with small additions of alkali oxide to silica, and a reduction of the melting temperature.
For classification purposes, the multitude of glasses can be roughly arranged in groups, according to their oxide composition (percentage of weight) [Web reference: Schott-1].

3.3.1 Soda-lime glass (Alkali alkaline earth silicate glasses)

This is the oldest glass type. It encompasses flat glasses (window glass) and container glasses. Adding of sodium carbonate (Na_2CO_3), known as soda ash, to produce a mixture of 75% silica (SiO_2) and 25% of sodium oxide (Na_2O), reduces the melting temperature to about 800°C. However, a glass of this composition is water-soluble and is known as water glass. In order to give the glass stability, other chemicals like calcium oxide (CaO) and magnesium oxide (MgO) are needed. These are obtained by adding limestone which results in a pure inert glass. Soda-lime glasses contain about 15% alkali (Na_2O), 13-16% alkaline earths (CaO+MgO), 0-2% Al_2O_3 and about 71% of SiO_2. Commercial glass is normally colourless, allowing it to freely transmit light, which is what makes glass ideal for windows and many other uses. Additional chemicals have to be added to produce different colours.

3.3.2 Borosilicate glass

This type of glass, in the form of ovenware and other heat-resisting ware, is better known under the trade name Pyrex. It has a relatively low alkali content and consequently has both excellent chemical durability and thermal shock resistance (i.e does not break when changing temperature quickly). Characteristic of this type is the presence of substantial amounts of silica (SiO_2) and boric oxide ($B_2O_3 > 8$ %) as major elements for glass formation. The amount of boric oxide affects the glass properties in a particular way. Beside the highly resistant varieties (B_2O_3 up to a maximum of 13%), there are others that, due to the different way in which the boric oxide is incorporated into the structural network, have only low chemical resistance (B_2O_3 content over 15%), that is the glass surface can be attacked by chemical agents. Hence, borosilicate glasses are classified in the following subtypes:

1. Non-alkaline earth borosilicate glass: the B_2O_3 content for borosilicate glass is typically 12-13% and the SiO_2 content over 80%. High chemical durability and low thermal expansion (3.3×10^{-6}/K).

2. Alkaline earth borosilicate glasses: in addition to about 75% of SiO_2 and 8-12% of B_2O_3, these glasses contain up to 5% of alkaline earths and alumina (Al_2O_3). They are softer than non-alkaline earth borosilicate glasses, with thermal expansion of between $4.0\text{-}5.0\times10^{-6}$/K. *Schott D263 glass* belongs to this group.

3. High-borate borosilicate glasses: they are glasses containing 15-25% of B_2O_3, 65-70% of SiO_2, and smaller amounts of alkalis and Al_2O_3 as additional components. They have low softening points and low thermal expansion; the increased B_2O_3 content reduces the chemical resistance.

3.3.3 Aluminosilicate glass

A small, but important type of glass, aluminosilicate, contains 20% of aluminium oxide (alumina, Al_2O_3) often including calcium oxide, magnesium oxide and boric oxide in relatively small amounts, but with only very small amounts of soda or potash. It is able to withstand high temperatures and thermal shock and is typically used in combustion tubes, gauge glasses for high-pressure steam boilers, and in halogen-tungsten lamps capable of operating at temperature as high as 750°C. They are further classified as:

1. Alkaline earth aluminosilicate glasses. Characteristically, these glasses are free of alkali oxides and contain 15-25% of Al_2O_3, 52-60% of SiO_2, and about 15% of alkaline earths. They typically have very high transformation temperatures and softening points.

2. Alkali aluminosilicate glasses. The Al_2O_3 content of alkali aluminosilicate glasses is typically 10-25 % and the alkali content over 10 %. The high alkali content prepares the glass for ion exchange with bigger alkali ions in order to improve the surface compressive strength. High transformation temperatures and outstanding mechanical properties, e.g. hardness and scratch behaviour, are characteristic features of this glass type that make them especially suitable for portable electronic devices. *Corning Gorilla* belongs to this class. In paragraph 7.1, I will present my research on Gorilla glass, which is very attractive also for X-ray telescopes, where the substrate must be capable to survive the launch.

3.3.4 Aluminoborosilicate glasses

Alkali-free aluminoborosilicate glasses essentially consist of 55-65% of SiO_2, 15-20% of Al_2O_3, 5-10% of B_2O_3 and about 10 to 15% alkaline earth oxides, without any addition of alkali oxides (typically trace amounts of < 0.05 wt% are present). A low coefficient of thermal expansion, combined with high transformation temperature, and good chemical stability, makes them especially suitable for substrate glasses for flat panel displays. *Schott AF32* and *Corning Eagle* and *Willow* glass belong to this class.

3.4 Methods to produce flat sheet glass

Flat glass foils can be made using a variety of techniques.
In the *float process* (Fig. 3.3) a glass melt is poured from a furnace onto the surface of molten tin, where it floats over. The floated glass melt spreads to form a ribbon with a defined thickness and a smooth surface [Shelby 2005]. The tin melt bath is operated in inert atmosphere to prevent its oxidation. In general, no interaction or diffusion processes takes place between the glass and the tin. However, in practice, tin ions are found up to several micrometer deep inside the glass. In contrast, the opposite glass side is tin free and also very smooth. Each temperature gradient in the cross section of the slit or the tin bath affects the thickness distribution of the sheet; the final thickness of the glass sheet can be adjusted by the speed at which the solidifying glass melt is drawn off from the tin bath. The glass ribbon on the tin bath is drawn by rollers that are located at both edges. Since the glass has cooled sufficiently before leaving the bath, the subsequent contact with the rollers does not produce flaws but minor scratches. This technology is commonly used for thickness values ranging from 25 to 0.4 mm.

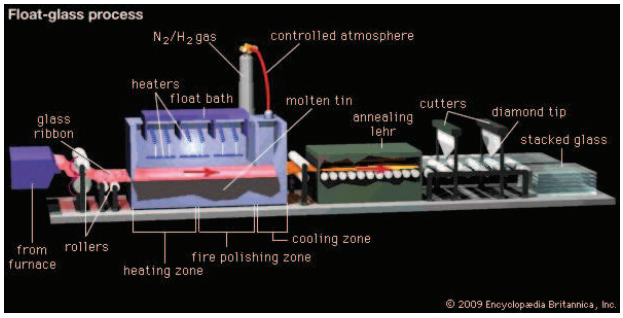

Figure 3.3: *: Schematic of the float process.*

The *down-draw* process (Fig. 3.4-left) is used to manufacture thin and ultra-thin glass. The molten glass is allowed to flow vertically downwards through a defined orifice and is pulled by traction from below, passing between a pair of rotating metal tools to form the sheet. The glass produced in the down-draw process (D263 and AF32) covers the range of thickness from 1.1 mm down to 25 μm [Web reference: Schott-2].

The *fusion-overflow* method was developed by Corning Glass Works. A schematic of the process is shown in figure 3.4-right. In this process a melt stream overfills a platinum vessel (trough) and it is thereby forced over the edges to split into two parts. The melt flows over the trough faces and eventually both stream recombine into a single stream just below the trough. The surfaces of the free falling melt are only in contact with the surrounding atmosphere. The correct choice of the radius on the top edges and of the tip angle at the bottom of the trough are of great importance. This process allows for the fabrication of glass sheets with freely formed, very smooth surfaces, and high thickness uniformity (Eagle, Gorilla, Willow). The thickness of the produced glass sheet is determined by the pull-down rate.

3.5 Physical properties of some glasses

In Table 3.2, the most important properties, for the slumping process, of the glasses used in our laboratories are summarised. The roughness of these glasses are compared in paragraph 6.2.1 where it appears that the glasses produced by Corning with the fusion-overflow process are preferable, most probably because of the non-contact with any solid surface during their production.

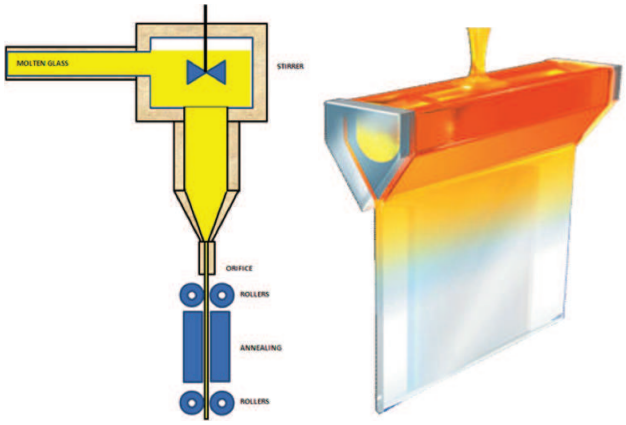

Figure 3.4: *: Left: schematic of the down-drawing process. Right: schematic of the fusion-overflow process*

Table 3.2: *: Some parameters for the type of glasses considered in this work.*

	D263 [Web reference: D263]	**AF32** [Web reference: AF32]	**Eagle XG** [Web reference: Eagle]	**Gorilla2** [Web reference: Gorilla]
Producer	SCHOTT	SCHOTT	Corning	Corning
Type of glass	Borosilicate	Alkali free Alumino-borosilicate	Alkali free Alumino-borosilicate	Alkali Alumino-silicate
Production method	Down-draw	Down-draw	Fusion overflow	Fusion overflow
n @ 589 nm (n_D)	1.523	1.51	1.51	1.505
Softening point [°C]	736	969	971	895
Annealing point [°C]	557	728	722	653
Strain point [°C]	529	686	669	599
Slumping temp. [°C] @ INAF-OAB	570	750		620
Thickness [mm]	0.4	0.4	0.4	0.55
CTE [$10^{-6}/K$]	7.2 (20 - 300 °C)	3.2 (20 - 300 °C)	3.17 (0 - 300 °C)	8 (0 - 300 °C)
Tempering temp. [°C]	Possible	Not possible	Not possible	∼400 °C
Avail. thickness [mm]	0.03-1.1	0.03-1.1	0.3-1.1	0.5-2

3.6 Slumping moulds

3.6.1 Introduction

Slumping moulds have traditionally been separated into four material categories including ceramic, metallic, cermet (composed ceramic and metal) and glass [Fischbach 2010]. The selection is based on the following considerations:

1. non-sticking behaviour with the selected glass at high temperature, otherwise the glass and the mould would fuse together;
2. maximum applicable temperature higher than the glass slumping temperature, to avoid deformation or melting during the slumping cycle;
3. good CTE matching with the selected glass, to reduce the shearing of the glass and mould surface leading to mid frequency errors on the slumped glass foil;
4. good properties of machinability and polishability , to minimise the roughness degradation on the slumped glass foil due to partial replication of the mould roughness;
5. high thermal conductivity, to minimise thermal gradients on the slumping mould, resulting in deviation from the desired shape;
6. hardness of the material, to prevent scratches during the handling.

Unfortunately, these properties are often in conflict with each other: for instance, a material polished to very small roughness will cause more easily glass sticking, and a hard material, therefore more easily handled during the cleaning process, without the risk of scratching it, will be difficult to be polished. As usual, a trade-off between the different requirements has to be defined, depending on the application.

In the industry of lens compression moulding, the most common material for mould is a ceramic composed of approximately 97% Tungsten Carbide (WC) and 3% Cobalt used as a cementer [Fischbach 2010]. Even though ceramics are typically more difficult to machine, their oxidation resistance at high temperatures that prevents sticking, makes them very attractive to be used without antisticking-layers. Metal moulds can also be considered, but high temperatures anyway, materials such as aluminum, stainless steel, and nickel alloys start deteriorating and potentially can stick to the glass. In this case, an antisticking layer has to be applied to the mould. Also in the case of ceramics mould, protective coatings are sometimes applied to their surface to increase the mould tool life by 10 to 50 fold factor. In general there are three types of coatings utilized in the glass moulding industry: noble metal based coatings, ceramic coatings, and carbon based coatings. The most widely used noble metal based coating to be applied to WC is Pt-Ir due to its high chemical inertness with glass even at high temperatures. In reality, a certain degree of diffusion of the Pt-Ir coating was reported with some glasses, depending on their chemical composition [Bobzin et al. 2014]. The high cost of noble metals, anyway, continues to drive the search for alternative coatings. Ceramic coatings such as Silicon Carbide (SiC), Silicon Nitride (Si_3N4), Titanium Nitride (TiN), Chromium Nitride (CrN), Chromium Tungsten Nitride (Cr-W-N) and Ti-Al-N have all been applied for the moulding of optical lenses of inorganic glasses at working temperatures of approximately 550 °C, with varying degrees of success [Fischbach 2010]. However, at higher temperatures, also single phase nitrides and carbides may start sticking, as a result of corrosion and oxide formation. It was also reported that material like TiAlN/ZrN can successfully be used as coating materials to improve the endurance against corrosion and oxidation and thereafter prevent the sticking of the glass [Hock et al. 2003].

For the thermal slumping, the most common material for moulds is Silica: quartz was used for the production of the HEFT glass mirror substrates [Koglin et al. 2004], and Fused Silica was used for NuSTAR [Craig et al. 2011]. Its major drawback is its sticking behaviour when used

for slumping glass foils. While for HEFT the slumping was performed in such a way to avoid contact of the glass with the mould, the technology developed for NuSTAR included the contact of the glass with the mould, hence a Boron Nitride antisticking layer was used. Fused Silica was also used in our laboratories at the beginning of our research, when a trade-off study between INAF-OAB and MPE was performed [Ghigo et al. 2010]. In this case, a Cr-Pt coating was used to prevent sticking. Although more difficult to produce, ceramic material are also employed in the thermal slumping technology, for their antisticking properties: HPC1465, a porous ceramic based on aluminium oxide was used at MPE [Winter et al. 2012] to enable the air suction through the mould surface, and solve the problems of air bubbles entrapped under the glass with the Fused Silica mould (see paragraph 3.8.4); Zerodur K20 was used in our laboratories to solve the problem of Pt-Cr coating degradation after slumping (see paragraph 3.8.5). Other materials have been considered in our laboratories (Aluminium Oxide, Silicon Nitride and Silicon) as well at MPE (Silicon Carbide). At INAF-OAB, the best result have been obtained using Zerodur K20, at least until the time of writing.

3.6.2 Zerodur K20

Zerodur is the trade name of a low thermal expansion glass-ceramic composite material made by Schott Glass. Glass-ceramic composites were discovered at Corning glass in 1952: the material was not transparent and was commercialised as cookware product in 1957 [Web reference: Zerodur-1]. Borosilicate glasses, developed in the late 1800s, were already used in commercial cookware (Pyrex for example) before the discovery of glass-ceramic composites. Schott started the development of glass-ceramic for scientific used in 1966, with a collaboration with the Max Plank Institute for Astronomy. In 1968 the Zerodur was discovered. The composition is reported in Table 3.3. This material have a very low CTE (0.01×10^{-6}/K), as a result of its composite structure: the crystalline phase, with negative CTE, is suspended in a glassy phase ($20-30\%$, [Dohering et al. 2004]), with positive CTE. By controlling the manufacturing process, the resulting CTE is essentially zero. In addition, Zerodur is not corroded by most acids and alkali [Web reference: Zerodur-2], an important consideration from the cleaning point of view.

Table 3.3: *: Left: The chemical composition of Zerodur [Web reference: Zerodur-1]. Right: physical properties of Zerodur and Zerodur K20. Credits: Schott.*

Material	% in weight
SiO_2	52.7
Al_2O_3	25.3
P_2O_5	6.5
Li_2O	3.4
TiO_2	2.3
ZrO_2	1.8
ZnO	1.4
MgO	1.0
As_2O_3	0.5
K_2O	0.4
Na_2O	0.2

	Zerodur	Zerodur K20
CTE [$10^{-6}/K$]	0.01	
CTE (20 °C- 700 °C) [10^{-6}/K]		2.4
CTE (20 °C- 300 °C) [10^{-6}/K]		2.2
CTE (20 °C- 50 °C) [10^{-6}/K]		1.6
Young's modulus E [GPa] @ 20 °C	90.3	84.7
Poisson ration ν	0.24	0.25
Density [g/cm^3]	2.53	2.53
Thermal conductivity @ 20 °C [W/m/K]	1.46	1.63
Knoop hardness	620	620
Max applicable temperature [°C]	600	850
Residual surface roughness	as low as 1 nm	N.A.

Zerodur can be converted, by a Schott proprietary thermal process at temperatures beyond 800 °C, to a non-transparent glass ceramic material named Zerodur K20. This is a low CTE ($\sim 2\times10^{-6}$/K) material, optimised to withstand higher temperatures (850 °C instead than 600 °C) (Tab. 3.3). The material has white color (Fig. 3.5). Being the chemical composition the same as that of Zerodur, the same high chemical resistance applies also to K20.

Unlike Zerodur, polishing the Zerodur K20 is quite challenging. The material was already considered for hot slumping of thin glasses for X-ray application at NASA: Schott prepared the forming mould [Dohering et al. 2004], and Zeiss performed the polishing on the Wolter-I surface [Egle et al. 2004]. They report a surface roughness of 5-8 nm rms, as measured with the Promap

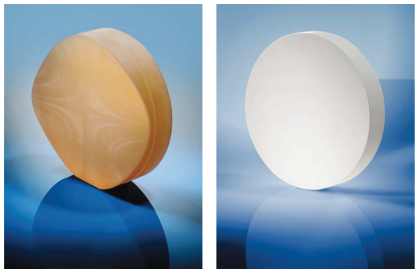

Figure 3.5: *: Zerodur (left) and Zerodur K20 (right) in comparison. Credits Schott.*

512 (no further information was given regarding the exact spatial frequency range). Anyway, no slumping was performed on this material at NASA[1]. For what concerns our K20 cylindirical moulds, we have polished them at Hellma-optics in Germany. The work was performed on a best effort basis: the result was a surface still crowded with points like defects and, in some AFM images, also pores were visible (Fig. 3.6). The defects in ejection are due to the cristalline part of the material. The interpretation of the pores is more puzzling: pores are typically due to the sinterisation process used for ceramics, but Zerodur K20 is a ceramic material obtained from the transformation of a non-porous material. It is anyway possible that the remaining 10% glass phase, contained in the Zerodur K20, could be washed out during the polishing process, leading to structures similar to pores[2]. The roughness of our cylindrical K20 moulds polished at Hellma was found on the order of 15 nm at the AFM scale (Fig. 6.13)

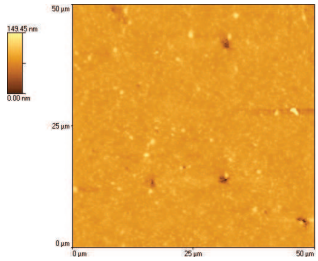

Figure 3.6: *: AFM image (width 50 µm) of a flat Zerodur K20 sample: the image show defects in ejection, due to the crystalline part of the materials, and pores, possibly the result of the polishing process on the 10% glass phase of the material.*

3.6.3 Physical properties of some mould materials

In Table 3.4 the most important physical parameters, of the materials considered for slumping moulds in our laboratory, are compared.

From Table 3.4, it appears that mono-crystalline Silicon is very attractive: it exhibits superb thermal conductivity properties, when compared to Zerodur K20 or Fused Silica. In the hot slumping technology, this represents an advantage because the thermal gradients inside the mould would be minimized, thus leading to better performances of the glass to mould replication. Therefore, we have produced a convex cylindrical Si mould at Hellma-optics in Germany. However, the surface could not be polished to the desired requirements. I have performed a full characterisation [Salmaso IR11-2014] of both Si and Zerodur K20 cylindrical slumping moulds,

[1] Private communication with NASA.
[2] Private communication with Schott.

Table 3.4: *: Physical parameters of different mould materials.*

Material	**Zerodur K20** [Web reference: K20]	**Fused Silica** [Web reference: SiO2]	**Silicon** [Web reference: Si]	**Silicon Nitride** [Web reference: Si3N4]	**Allumina** [Web reference: Al2O3]
Chemical Formula	See Table 3.3	SiO_2	Si	Si_3N_4	Al_2O_3 (99.7%)
CTE ($10^{-6}/K$)	2.2 (20 - 300 ^oC)	0.57 (0 - 200 ^oC)	2.6	2.4 (20 - 400 ^oC)	7.5 (20 - 400 ^oC)
CTE ($10^{-6}/K$)	2.4 (20 - 700 ^oC)			4.3 (20 - 800 ^oC)	8 (20 - 800 ^oC)
Young's Modulus (GPa)	84.7	73	129.5	300	360
Max working temperature (^oC)	850	1100	1400	1300	1650
Thermal Conduct. (W/m/K)	1.63	1.38	148	33	31

produced at Hellma-optics, showing a much higher contribution from mid-frequency in the Si mould: the expected HEW computed form LTP data, after the subtraction of the best fit 4th order polynomial, to evidence mid frequency errors, was computed to be 5.6 arcsec for the Si mould, compared to 0.8 arcsec for the Zerodur K20, thus making this Silicon mould not suitable for the production of a 5 arcsec HEW telescope, as required for ATHENA. However, it is possible that other companies could have better results on polishing mono-crystalline Si curved surfaces.

Fused Silica was used in our laboratories, in the early stage of the hot slumping process development. It was chosen for its properties of good polishability. The main disadvantages anyway was the sticking behaviour with glass at the temperatures required for the slumping. A Cr-Pt antisticking layer was used, but it was found that it was degrading with the slumping cycles. It was therefore replaced by the Zerodur K20, owing its antisticking properties (see paragraph 3.8.5).

I have considered also Silicon Nitride and Alumina, for the slumping of AF32 and Eagle glasses and Gorilla glass respectively (see chapter 7): both materials do not need antisticking layer. The advantage of the Silicon Nitride would be a higher rigidity with respect to the Zerodur K20, a better matching of the CTE with the one of the Eagle glass, and a higher thermal conductivity with respect to the Zerodur K20. The Alumina was instead selected as matching the CTE of the Gorilla glass.

3.7 Ripple relaxation in glass

As anticipated in section 3.2, there are different models to describe relaxation in glasses. In this thesis, I have used a model proposed in 2003 by Jimenez-Garate [Jimenez et al. 2003]. A modification of the model, to account for the pressure exerted in our setup, is described in Section 6.4. The choice of this model lies in the simple description of the origin of the corrugations experimentally observed in the glass foils slumped during my work, typically observed with spatial frequency of 1-2 cm (Fig. 3.7).

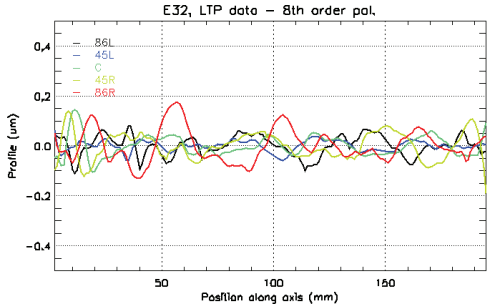

Figure 3.7: *: Typical ripples observed in a slumped glass foil: the graphs are obtained by subtracting the best fit 8th order polynomial to the scans measured with the LTP, on the slumped glass foil.*

3.7.1 The Jimenez-Garate model

During thermal slumping, if the glass and the mould get in contact, ripples in the glass surface are formed, as consequence of the imperfect match of the two materials' CTEs. These ripples would relax in a time dependent, among others, on the glass viscosity; the relaxation time is longer at high viscosity. The Jimenez-Garate model permits us to compute the relaxation time for a ripple present in a glass surface.

Let us consider a sheet of glass with ripples, as pictured in Fig. 3.8, where λ is is the wavelength of the ripple, a is its amplitude (with $a \ll \lambda$), R is the radius of curvature of the ripple, $h = 2a$ is the peak-to-valley of the ripple.

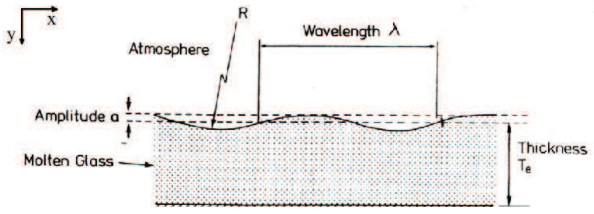

Figure 3.8: *: A glass sheet with ripples on its surface [Jimenez et al. 2003].*

The ripple's profile varies from 0 to $u/2$, where $u(x)$ is given by:

$$u(x) = h \sin\left(\frac{2\pi}{\lambda} x\right). \tag{3.4}$$

Once generated, the ripples tend to relax, under the action of two forces:

1. **Surface tension**: from geometrical considerations, we have $\left(\frac{\lambda}{4}\right)^2 = (2R-a)a \sim 2Ra$, and therefore the radius R of the ripple can be written as $R \sim \frac{\lambda^2}{32a}$. From surface tension theory, we have that there is an increase in pressure beneath the convex ripple equal to S/R, where S the surface tension of the air-glass interface, and a decrease in pressure of the same magnitude beneath the adjacent concave ripple. Thus there is a differential hydrostatic pressure of magnitude $2S/R \sim 64aS/\lambda^2$ acting to move the glass from the thicker to the thinner regions.
2. **Gravity**: between the thicker and the thinner parts of the glass there is a differential hydrostatic pressure of $2\rho g a$, where ρ is the glass density.

These two forces act to reduce the ripple height, with a force for unit area given by

$$\frac{F}{A} = \frac{64aS}{\lambda^2} + 2\rho g a. \tag{3.5}$$

By integration of eq. 3.5 in da, we have the potential energy per unit area:

$$\frac{U}{A}(x) = \int_0^{u/2} \left(\frac{64S}{\lambda^2} + 2\rho g\right) a \mathrm{d}a = \left(\frac{64S}{\lambda^2} + 2\rho g\right) \frac{u^2(x)}{8}. \tag{3.6}$$

The potential energy per unit area, averaged over a sinusoidal period, is:

$$\left\langle \frac{U}{A}(x) \right\rangle = \left(\frac{8S}{\lambda^2} + \frac{\rho g}{4}\right) h^2 \left\langle \sin^2\left(\frac{2\pi}{\lambda}x\right) \right\rangle = \left(\frac{8S}{\lambda^2} + \frac{\rho g}{4}\right) \frac{h^2}{2}. \tag{3.7}$$

The energy stored in the ripple is dissipated via viscosity forces. In most glass forming processes, the glass can be considered a Newtonian fluid [Jain Ph.D. thesis 2006], which means that the viscosity coefficient η is constant. In this case we can write

$$\frac{F_{yx}}{A} = \eta \frac{\mathrm{d}v_y}{\mathrm{d}x}, \tag{3.8}$$

where F_{xy} is a force in the y direction applied on a surface perpendicular to the x direction and v_y is the velocity in the y direction (see Fig. 3.8 for the xy orientations). The dissipated energy per unit area, can be written as:

$$\frac{\mathrm{d}U}{A} = \frac{F_{yx}\mathrm{d}y}{A} = \eta \frac{\mathrm{d}v_y}{\mathrm{d}x}\mathrm{d}y = \eta \frac{\mathrm{d}v_y}{\mathrm{d}x} v_y \mathrm{d}t = \frac{\eta}{2} \frac{\mathrm{d}\left(v_y^2\right)}{\mathrm{d}x} dt = \frac{\mathrm{d}}{\mathrm{d}x}\left(\frac{1}{2}\eta v_y^2\right) \mathrm{d}t. \tag{3.9}$$

Since the relaxation process is extremely slow, we replace the differentials with finite differences: hence we set dt equal to the relaxation time τ, $dx = \lambda$, and $dy = h$, leading to

$$\frac{U}{A} = \frac{\eta h^2}{2\tau\lambda}. \tag{3.10}$$

Equating Eq. 3.10 and Eq. 3.7, provides the relaxation time τ as a function of the viscosity η, of the surface tension S and of the ripple spatial wavelength λ:

$$\tau = \frac{\eta}{8S/\lambda + \rho g \lambda/4}. \tag{3.11}$$

Note that in this model, τ does not depend on the ripple height : this will be no longer true if the pressure is included (Sect. 6.4.2).

In his work, Jimenez reports rippling in AF45 and D263 glass types using steel, graphite and quartz mandrels. In order to apply the model and compute the relaxation time τ, it is essential

to have data for the surface tension $S = S(T)$ and the viscosity $\eta = \eta(T)$. The surface tension was estimated by Jimenez from tabulated numbers that assume a linear dependence on the glass composition: the detailed dependance is $S = S_0 - \delta_0(T - T_0)$, with S_0, δ_0 and T_0 constants given by the supplier [Jimenez et al. 2003]. The value used in the calculation (S = 0.343 J/m^2) is the one obtained at T = 900 °C, while S = 0.325 J/m^2 is obtained at T = 1200 °C; apparently S is only slightly dependent on T. The viscosity dependence on T is instead very large. Its dependence can be computed by fitting the viscosity versus temperature values reported in the data sheet (Table 6.7), with the Vogel-Fulcher-Tammann (VFT) equation 3.3. Fig. 3.9 reports the viscosity dependance upon temperature for the AF45 glass. This glass was slumped, in Jimenez's work, at viscosity of $10^9 - 10^{10}$ Pas.

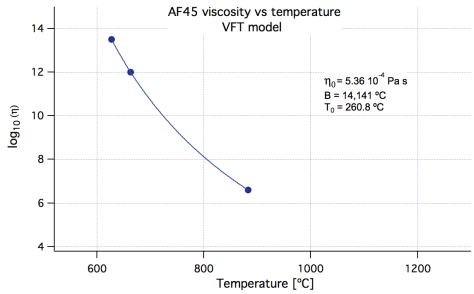

Figure 3.9: *: Viscosity versus temperature for AF45 glass type. The points are taken from the datasheets, while the solid lines are fitted with the VFT equation (Eq. 3.2).*

Using η_0, B and T_0 values found, we have derived τ as a function of λ from Eq. 3.11. Fig. 3.10 shows τ for two different viscosity values, namely $\eta = 10^9$ Pas (the viscosity at the soaking temperature) and $\eta = 10^{12}$ Pas (the viscosity at the annealing temperature). From Fig. 3.10, it can be seen that ripples with wavelength larger than 5 μm are not relaxed during the 15 minute soaking time at 761 °C (η = 10^9 Pas). Indeed, at the upper annealing temperature, where the viscosity takes a value of 10^{12} Pas, relaxation times are much longer. Moreover, there is a critical wavelength of about 2 cm where the relaxation time is maximum: this corresponds to the ripple observed in the slumped glass foils both in Jimenez and my work. For this reason, I have considered Jimenez approach to model the effect of pressure on the ripples seen in my experiments (Sect. 6.4.2).

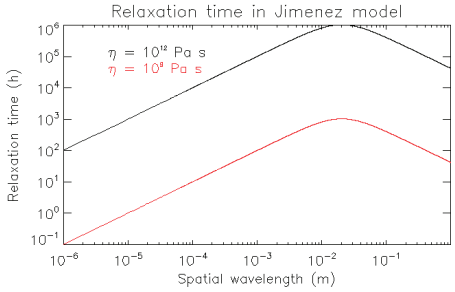

Figure 3.10: *: Predicted relaxation time of surface ripples versus ripple wavelength for the AF45 glass type, at η = 10^9 Pas (T = 761 °C, soaking temperature), and η = 10^{12} Pas (T = 663 °C, annealing temperature).*

3.8 Thermal slumping for X-ray telescopes

Thermally-formed glass optics for X-ray astronomical mirrors were firstly introduced for the small size hard X-ray optics of the HEFT (High Energy Focusing Telescope) balloon experiment [Koglin et al. 2004], and more recently used for the NuSTAR mission [Craig et al. 2011]. Based on these successful applications, glass thermal slumping process was considered to be a promising method for fabricating precision optical components at an affordable cost.

Concerning large size X-ray optics, they were firstly considered by NASA during the development of the Constellation-X optics [Zhang et al. 2007] and then studied again by NASA for the IXO project [Zhang et al. 2010]. In Europe, at first in the content of XEUS [Friedrich et al. 2006, Ghigo et al. 2008] and later in the context of IXO (Pareschi et al. 2011), [Winter et al. 2010] the thin glass approach was also developed, with very promising results. Now the ATHENA mission [Nandra et al. 2014] is approved for the L2 slot in the Cosmic Vision program. At this regard, in addition to the baseline solution based on Silicon Pore Optics (SPO), thin glass foils have also been considered a viable alternative. Finally, thin glass foils with piezo-electric actuators are being developed by a group at SAO/CfA in USA to manufacture the mirrors of the X-ray Surveyor (previously named SMART-X) mission [Reid et al. 2014] and are also studied in Italy for the AXYOM project [Spiga et al. 2014].

Clearly the quality of the optics for these future mission has to be improved, compared to the telescopes in operation, to reach higher angular resolution requirements. Many laboratories, worldwide, are at work to reach this goal, using different thermal slumping approaches. In the following sections, an overview of the historical development of thermal slumping of glass foils for X-ray telescopes is given, pointing out the different techniques adopted. In this section, the different integration methods are also presented: they can be roughly divided in "stress-free" integration (NASA, MPE approach for the ATHENA mission) and "stress-based" integration (as developed for HEFT and NuSTAR, and now adopted in our laboratories). In the first approach, the integration is meant to preserve the glass figure; in the latter, the integration forces the glass to assume a slightly different shape, thus imparting a stress to the glass foil.

3.8.1 The indirect approach at Columbia University: HEFT

Indirect slumping of thin glass foils was the solution adopted to produce the glass mirrors for the HEFT telescope [Koglin et al. 2004, Craig et al. 2000]. Individual glass pieces were thermally formed into a concave half cylinder of quartz (Fig. 3.11-left). In their approach, the temperature was raised in a controlled way to approximately 60 °C above the annealing point of the glass ($\sim$ 620 °C for D263), and gravity was causing the glass to slump onto the cylinder. Just before the glass could touch the mandrel surface, the forming process was terminated by lowering the oven temperature. The formed glass foils, when measured in shape, revealed a nearly cylindrical shape with an error in radius of only a few millimeters, because in the azimuthal direction the glass approximates an hyperbolic cosine profile. The missed contact with the mandrel, however produces large-scale figure errors: less then 0.1 mm in amplitude over the length scale of the piece (200mm), but negligible errors over shorter length scales, and preserving the excellent initial roughness properties of the glass micro-sheet, even without the aid of highly polished and very expensive mandrels.

The slumped glass foils were then mounted forcing the nominal cylinder segments to a conical form (thus removing radial mismatches and some small twists in the glass foils), and stacked on top of each other, starting with a titanium mandrel. In this stress-based process, graphite spacers are first glued (with epoxy glue) to the mandrel and then precisely machined to the correct radius and angle. Next, a layer of glass and a second layer of spacers are glued to the first set of spacers, then machined to the appropriate radius and angle. This process is repeated until the required number of layers are assembled. A key point is that each layer of spacers is machined with respect to the optic axis, and not the last layer of glass. In this way, stack-up errors are avoided

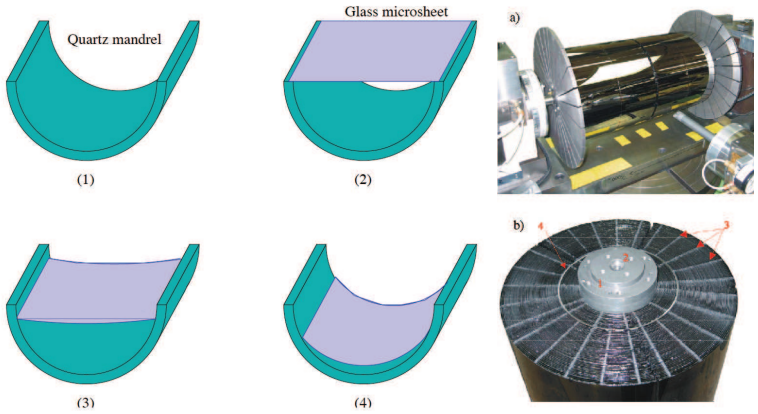

Figure 3.11: *: Left: indirect slumping approach for the HEFT telescope. Right: (a) The second HEFT flight module (HF2). b) An end view of the first HEFT flight module (HF1) with 70 layers of segmented mirrors, with azimuthal length of about 70 degrees. The following details can be noticed: 1) the central titanium mandrel; 2) precision alignment cone that defines the optical axis; 3) stacks of graphite spacers; 4) intermediate mandrel used for structural support when switching between 3 and 5 spacers for each mirror. Credits: Koglin 2004.*

during the telescope fabrication.

The final angular resolution for this telescope was 1.3 arcmin HEW, independent of the energy until 50 keV, with an alignment contribution estimated below 15 arcsec, thus negligible with respect to the final angular resolution achieved [Koglin et al. 2004].

3.8.2 The direct approach at NASA's Goddard Space flight centre: NuSTAR, and ATHENA

The limit of the indirect approach, as described in the previous section, was that the glass did not come in touch with the mandrel, therefore leading to large-scale figure errors, because the cylindrical shape could not be replicated. On the other hand, the contact with the mandrel could not ensure a glass mirror with minor errors, because the thickness variations of the glass foil was transferred to the upper optical surface [Zhang et al. 2003]. Therefore, the slumping approach for NuSTAR was changed to direct; i.e. the slumping was done over convex mandrels (Fig. 3.12-left). This approach exhibited several advantages. First, it ensured the inner surface of the glass to come into contact with the mandrel surface. Second, any thickness variation in the glass sheet did not translate into profiles errors on the optical glass surface. Third, the slumping process is very gradual: as the temperature ramps up, the flat glass sheet gradually leans against the mandrel, unlike the abrupt sagging of the glass foil in the indirect approach that caused "wrinkles" in the optical substrate.

This direct approach was used for the development of the Constellation-X project [Zhang et al. 2003], for the production of the NuSTAR telescopes [Craig et al. 2011] and lately it was also considered for the IXO and finally the ATHENA mission. Constellation-X was a NASA's mission with a high throughput requirement (3 m^2 effective area at 1 keV) and moderate angular resolution (15 arcsec HEW) [Zhang et al. 2003]. The production of its mirror segments (made of 0.4 mm thin D263 glass) was developed starting from an epoxy-based process to an epoxy-free process.

Initially [Zhang et al. 2003], each mirror segment was fabricated using a two-step process: substrate formation and epoxy replication. The glass foils (D263) were slumped onto a convex forming mandrel (Fused Silica with anti-sticking layer) with conical approximation, to form the substrates (Fig. 3.12-left). These substrates had a good large scale figure but a lot of mid-frequency errors. The substrate's inner surface was then sprayed with a layer of epoxy and posi-

tioned onto an Au-coated precision replication mandrel. After the epoxy was cured, the substrate plus the epoxy and the Au coating were separated from the replication mandrel. This process was developed for fabricating the ASTRO-E mirrors (a satellite who was broken during its launch in 2000, and then replicated into the ASTRO-E2, lately called Suzaku), in order to smooth the ripples out and impart the correct sag to the segments.

Lately, Constellation-X mirror developments were focused at producing mirror segments that do not require epoxy replication for various reasons [Petre et al. 2006]:

1. the elimination of the second, expensive set of superpolished mandrels;
2. the removal of undesired mechanical properties introduced by the epoxy layer. Mechanical stress between the epoxy and the substrate introduced by epoxy shrinkage during curing could reveal as another source of low frequency errors. The different CTEs of substrate and epoxy also lead to much tighter temperature ranges for mirror operations;
3. obvious simplification of the segment manufacturing process;
4. the volatile component of the epoxy might cause contamination problems in a space flight environment (Zhang et al. 2003).

NASAs direct technique was therefore developed further on, to improve the quality of the slumped glass foils also in the mid-frequency region, avoiding the use of epoxy. The efforts lead to the production of the NuSTAR mirrors [Craig et al. 2011]. The glass for the optical modules was D263, with a thickness of 0.2 mm. The thermal forming process was done on fused silica mandrels, ground into precise cylinders and then coated with a Boron Nitride (BN) release layer. The slumped glass were then trimmed to the final trapezoidal shape required by NuSTAR and forced into the conical shape by the mounting hardware, using the existing facility developed for HEFT. This process could reach the NuSTAR requirement of 58 arcsec HEW.

Figure 3.12: *: Left: the convex mandrels for the direct slumping approach at NASA. Right: NuSTAR flight optics FM0 with 106 layers on assembly machine. Credits: Hailey 2010.*

In 2008, the IXO mission started its development, as a merger of NASA's Constellation-X and ESA's XEUS mission concepts. NASA continued the research for mirror production in the direct slumping configuration even after they abandoned their participation to the IXO mission in 2011. Hot glass slumping, as a production method for segmented mirrors, is now a stable and mature technology at GSFC consistently producing mirror pairs capable of 6 arcsec HEW in double reflection [Zhang et al. 2014]. D263 glass foils are currently used, with thickness of 0.4 mm, and fused silica mandrels with Wolter-I configuration are adopted.

Regarding the alignment of the mirror segments for the IXO-ATHENA mission, having been the glass foils slumped with Wolter-I configuration, a stress-free integration process was developed at NASA (Fig. 3.13). In this process, called "edge-bonding", a mirror segment with three bonded interface balls is set in the temporary kinematic mount, fixed to a precision alignment

hexapod. Once the mirror segment alignment is achieved through control of the alignment hexapod, the mirror segment is then permanently fixed to the module using the edge-bond process. The edge-bond process uses six bonding pins (three bonding pins per side) that slide into position to bond to the mirror segment edges. After the epoxy under the pins is fully cured, the temporary mirror segment mount is removed as well as the three temporary support balls that provide the interface to the kinematic temporary mount. This alignment process is approaching 10 arcsec HEW optics [Chan et al. 2015], and the overall image is dominated by the quality of the mirror figures. An alternative segment permanent mounting process, called "kinematic permanent mirror mount", to remove mirror distortions caused by epoxy curing for optics to achieve below 5 arcsec HEW has been tested [Biskach et al. 2014]. Both mirrors permanently mounted using edge-bond and kinematic methods survived vibration tests.

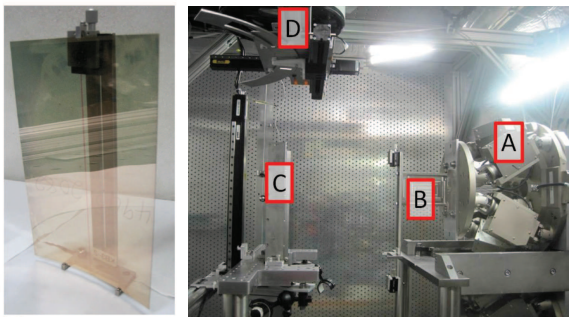

Figure 3.13: *: Left: Three steel balls are temporarily bonded to top and bottom edges of mirror to interface with temporary mount. Right: Attached to precision hexapod manipulators [A] are kinematic temporary mirror mounts [B] that support mirror segments during alignment into a module [C]. Alignment masks [D] mounted between the collimated light source and module allow for Hartmann measurements to be performed on a specified mirror segment or mirror pair. Credits: Biskach 2014.*

3.8.3 The compression approach at Massachusetts Institute of Technology

In the technique developed at NASA GSFC, the mirrors have very good figure, with mirror pairs capable of 6 arcsec HEW angular resolution [Zhang et al. 2014], primarily degraded by mid-range scale spatial frequency errors. These mid-range errors are probably caused by clumping and particulates in the BN coatings used to prevent sticking between mandrel and mirrors. To avoid additionally mid-range errors, the group at Massachusetts Institute of Technology has developed a slumping process where the hot glass substrate floats between a pair of porous air bearing mandrels, through which compressed nitrogen is flown. It is a non-contact approach, just like the one developed at Columbia University for the HEFT substrates, and therefore the glass replicate the desired figure without introducing roughness or mid-frequency errors. Actually, in the Columbia's approach, a repeatability problem was found, because it is difficult to produce profiles independent of initial glass warpage. To solve this problem, the MIT's approach foresees the use of pressure, forcing compressed nitrogen over the top and bottom glass surfaces. The first development of this technique was done during Akilian's PhD thesis [Akilian 2008]. She developed the first air bearing glass shaping tool, shown in Fig. 3.14-left. The glass was hung between two vertical air bearings. The entire assembly was placed in an oven and heated to 600 °C. Since the vertical configuration had repeatability issues due to the method of constraint of the glass, the configuration was set horizontal, essentially rotating the device by 90°, and some form of control was added to avoid the glass sheet sliding out of the bearings (Fig. 3.14-right) [Sung 2013].

Several slumping tests were done, using 100 mm-diameter, 550 μm-thick Schott D263 wafers. While unslumped glass wafers typically have 50-90 μm peak-to-valley (P-V) surface height variation, they found that their air bearing slumping tool, using air gap of 35 μm, yielded repeatable shapes with a P-V of about 10 μm (Fig. 3.15). Tests with smaller gap are planned, as modelling shows that this should produce much lower P-V [Schattenburg et al. 2015]. Anyway, they pro-

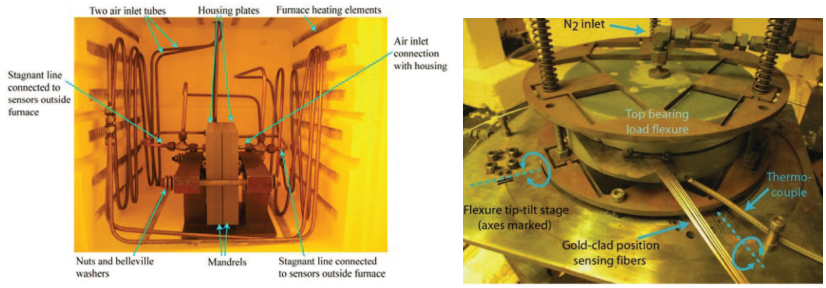

Figure 3.14: *: Left: Akilian's air bearing glass shaping tool (vertical configuration). Credits: Akilian 2008. Right: Horizontal slumping tool. Credits: Schattenburg 2015.*

pose a method to correct residual long-range errors after slumping, using a deterministic figure correction scheme such as ion-implant stress or differential deposition [Schattenburg et al. 2015].

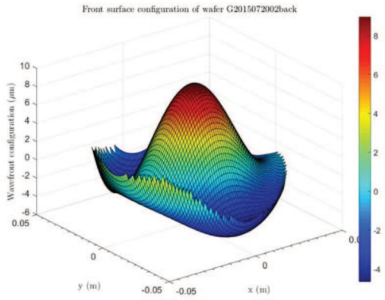

Figure 3.15: *: Topograph for a substrate slumped for 16 hours using a 35 μm bearing gap and a slumping temperature of 550 °C. Credits: Schattenburg 2015.*

Least but not last, this technique enables quick slumping runs and rapid sample changeover, achieving up to three slumping runs per day, an important advantage in the mass production of telescope mirrors. This is to be compared with GSFC's slumping cycles that take several days to achieve the highest accuracy.

Anyway, the technology for slumping flat substrates has still to be extended to curved optics. To this end, they are now developing a test stand for slumping conical mirrors (Fig. 3.16). The prototype tool is - for the moment - designed to test substrate position sensor and control concepts in a cylindrical geometry [Schattenburg et al. 2015].

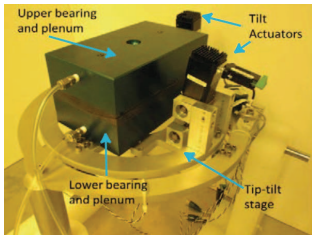

Figure 3.16: *: Conical optic slumping test stand, as of now designed for room temperature tests. Credits: Schattenburg 2015.*

3.8.4 The indirect approach at MPE

The indirect approach is also developed since 2006 at the Max Planck Institüt für Extraterrestrische Physik in Garching (Germany). In 2006 [Friedrich et al. 2006] they produced their first Wolter-I X-ray mirror segment with parabola and hyperbola in one piece (Fig. 3.17-left). The glass was D263 with 0.55 mm thickness, slumped to a size of 200 mm $\times$ 100 mm, where the parabolic and hyperbolic parts are 100 mm $\times$ 100 mm. Aluminium oxide ceramic was selected as slumping mould material, in order to minimise the difference in CTE between the glass and the mould, to minimise the gradients inside the mould improving the heat conduction [Friedrich et al. 2005]. Unlike the indirect approach used for HEFT, the glass foil was fully in contact with the mould during the slumping. Some print-through effect of mould defects over the millimetre scale was therefore observed, fortunately damped by a 10-fold factor [Winter et al. 2010], on the optical side of the glass foil.

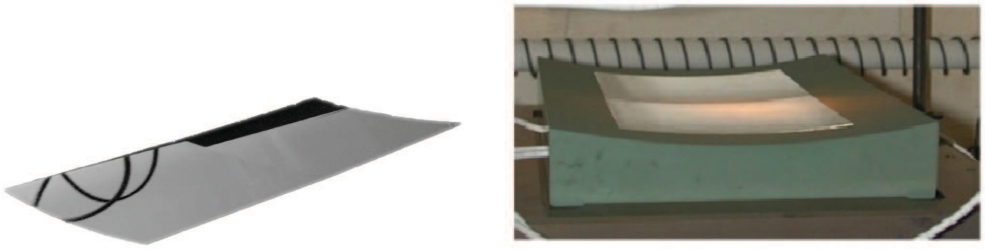

Figure 3.17: *: Left: Slumped mirror segment with the parabolic and hyperbolic parts made in a single piece Credits: Friedrich 2006. Right: The concave mandrel for the indirect slumping approach at MPE. Credits: Proserpio 2015.*

Several different mould materials have been lately tested and the HPC1465, based on aluminium oxide, was chosen, because this is a porous material that allows the application of a vacuum suction through the mould volume, thus leading to a much more homogeneous contact of the glass with the mould and avoiding air entrapping under the glass [Winter et al. 2012]. The best result obtained on this mould was an HEW value from the slumped glass foils of 70-80 arcsec, mainly due to the mould errors, due to the difficult machinability of the material. More recent work has been done to remove the thickness variation on the optical surface of the glass foils, a known problem of the indirect slumping. Despite the great effort in polishing thin glass foils, no major improvement was computed from optical measurements on plane-parallel D263 glass foils with 0.4 mm thickness, slumped over the porous ceramic mould, with respect to previous slumped glass foils [Winter et al. 2013], since the limiting factor is the mould figure error. A slumping mould in CeSiC, a material with a better machinability than HPC1465, was therefore procured to improve the result [Winter et al. 2014]. This mould was polished to Wolter I shape and turned out two orders of magnitude better for wavelength errors below 10 mm, and slightly better than the ceramics in the region above 10 mm, giving an expected HEW of about 20 arcsec. This is to be compared to the 65-70 arcsec of the ceramics mould on 2011 and 120 arcsec of the ceramics mould on 2006. AF32 glass type was then selected, because of a better CTE matching with respect to D263 / CeSiC. Because of problems with air entrapped between the slumped glass foils and the CeSiC mould, the slumping was moved to a heatable vacuum chamber. Neither sticking nor air entrapping problems were reported in the heatable vacuum chamber; nevertheless, waviness on the centimetre scale was reported [Winter et al. 2014].

As for the integration, due to the fact that the glass foils are slumped with ideal Wolter-I configuration, a stress-free integration concept was developed at MPE, with different configurations tested (Fig. 3.18).

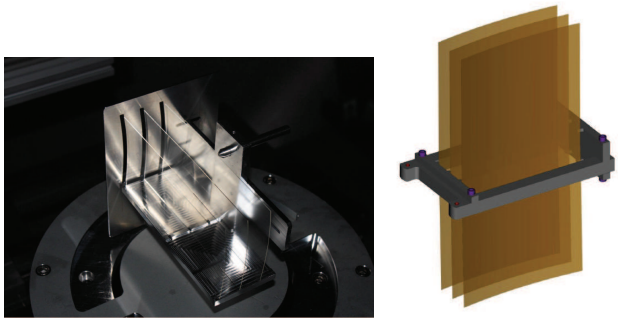

Figure 3.18: *: Left: Mounting scheme adopted on 2012. Credits: Winter 2012. Right: Mechanical model of the mirror module developed on 2015. Credits: Winter 2015.*

3.8.5 The direct approach with pressure application at INAF-OAB

In our laboratories, we have developed a direct slumping approach assisted by pressure, in which the optical side of the glass foil is forced to come into contact with the mould by pressure application.

OAB started working on hot slumping on 2006 in a study for the European Extremely Large Telescope (E-ELT) [Ghigo et al. 2006]. A stainless steel box (hereafter called muffle), hosting the glass and the mould, was used to create a better temperature homogeneity in the slumping environment. At first, small mould and glass samples were used to select the materials. Subsequently, to demonstrate the scalability of the process to large dimensions, a 700 mm diameter mould in Zerodur K20, coupled with a Borofloat glass disk with diameter of 500 mm and thickness of 1.7 mm (Fig. 3.19) was slumped in a stainless steel muffle inside a oven of larger size (see Chapter 4 for more detailed description of the ovens).

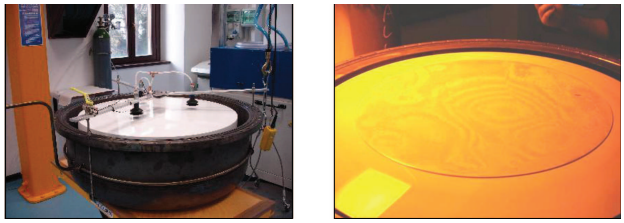

Figure 3.19: *: Left: K20 mould placed inside the muffle during the preparation of the slumping process. Right: A glass disk of 500 mm diameter after the slumping cycle: the interference fringes are seen under sodium light illumination. Credits: Canestrari 2008.*

After this study, the research on hot slumping at INAF-OAB was dedicated to the production of thin glass foils for X-ray telescopes. The research was supported, from September 2009 until June 2013, by the European Space Agency (ESA) and proceeded with the collaboration of several institutes and Italian companies: Max Planck Institut für Extraterrestrische Physik (MPE, Garching, Germany), BCV-Progetti (Milano, Italy), ADS-International (Lecco, Italy), and Media Lario Technologies (Bosisio Parini, Italy). The project, named "The Back-up IXO (former XEUS) optics Technology, Phase 1" was aimed to develop in Europe a process, alternative to the one based on Si pore optics, currently the baseline for the ATHENA telescope. Aim of this study was not only to investigate the thermal slumping technique for the manufacturing of the glass substrate of X-ray telescopes but also to set up of a suitable integration method of the substrates. The study was divided in two phases.

During Phase 1 (September 2009 - September 2010), OAB and MPE carried out a trade-off

between direct and indirect slumping techniques [Ghigo et al. 2010], individuating in the direct one the approach to be followed during Phase 2 (September 2010 - June 2013). Cylindrical moulds in Fused Silica, with a square base of 250 mm x 250 mm, a thickness of 50 mm and a radius of curvature of 1 m, were produced by Hellma Optik (Jena, Germany). The moulds were coated via evaporation with a first layer of Cr of 5 nm thickness and a second layer of Pt of 50 nm thickness: the Pt film, owing to its high melting point (1772 °C) and its very low chemical reactivity, acts as a release and anti-sticking agent between the glass foil and the Fused Silica mould, while the layer of Cr has been added to enhance the adhesion of Pt to the mould surface. Schott D263 borosilicate glass, with thickness of 0.4 mm, was chosen for the glass foils to be thermally slumped. In the previous section, the indirect slumping approach, developed at MPE, has already been described. In the direct approach developed at OAB, a system for pressure application on the glass foil was developed, in order to overcome the frequent problem of air bubbles entrapped under the glass surface and to reduce mid frequency errors of the slumped glass foil. During Phase 1, a stainless steel thin foil was used (Fig. 3.20) to divide the muffle chamber in two parts and enable a vacuum application on the bottom part in order to force the glass foil to replicate the mould figure. The result of the trade-off was that, in the case of direct slumping, low frequency errors (essentially sag errors) were still present in the slumped foils. However, it was demonstrated that they could be corrected during the integration phase by the innovative integration scheme employed (see Fig. 3.23). Regarding the indirect slumping, mid-frequency errors, coming from the nonuniform thickness of the original glass, were present in the slumped foils. Since these errors cannot be corrected by our integration process and could degrade the plates optical performances, the direct method was selected.

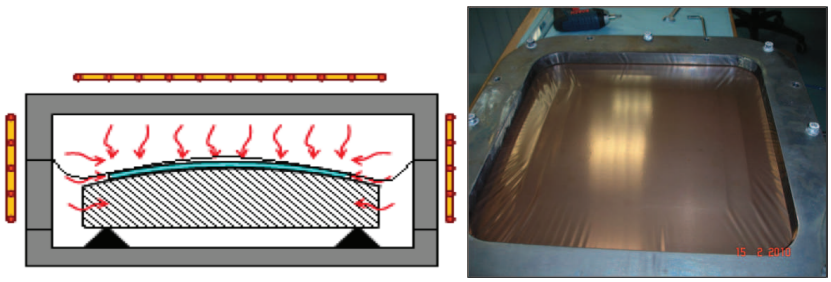

Figure 3.20: *: Left: a sketch of the first slumping configuration: the glass is slumped to its final dimension over a cylindrical mould; a stainless steel foil is used to divide the muffle in two chamber and allow the pressure application. Right: top view of the cover frame of the muffle with the stainless steel foil over the glass.*

Phase 2 was dedicated to the improvement of the direct slumping technology and to the development of the integration process. As for the hot slumping, the mould and glass materials were changed. Fused Silica moulds needed the application of a release layer of Cr+Pt. To improve the adhesion of the bi-layer film to the mould, an annealing thermal cycle (T_{max} = 580°C, holding time of 2 hours and cooling rate of 3 °C/ h) was used, that caused a surface degradation in terms of roughness. A further degradation was also observed after several thermal cycles. Therefore, the mould material was changed to Zerodur K20, a material that does not need a release layer, as already observed during the previous study for E-ELT. The glass foil material was then changed from D263 to AF32, also produced by Schott, to better couple the CTEs (CTE$_{K20}$ = 2.0 10^{-6}/K, CTE$_{D263}$ = 7.2 10^{-6}/K, CTE$_{AF32}$ = 3.2 10^{-6}/K). The good coupling of the CTE of the glass and the mould is, in fact, a key factor for the optical quality of the slumped glass foils, as it avoids the shear of the optical surface on the mould when the temperature is decreased, thereby reducing errors in the centimeter spatial wavelengths. These types of errors are expected to be present on the glass surface, when the glass is in contact with the mould [Jimenez et al. 2003], and they have to be minimized because not corrected by our integration procedure [Parodi et al. 2011]. Finally, also the configuration for pressure application was modified. Since the steel foil, used during

Phase 1 (Fig. 3.20) was damaging the back surface of the glass foil, thus reducing its strength after slumping [Proserpio et al. 2014], the process was modified by using the glass foil itself as a membrane to divide the muffle chamber (Fig. 3.21). This setup has been patented (registered italian patent TO2013A000687, 12/08/2013). In this new configuration, the glass needs then to be trimmed to its final size.

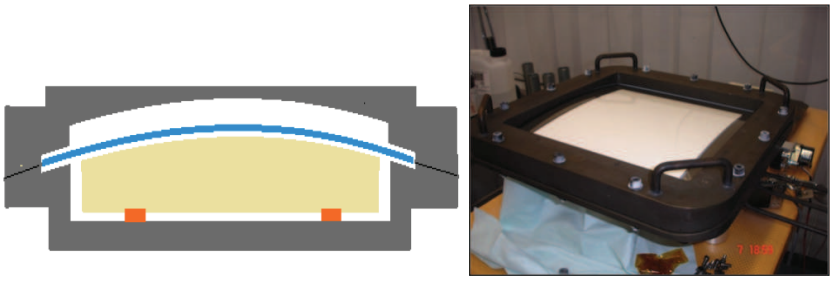

Figure 3.21: *: Left: a sketch of the new slumping configuration: the glass is slumped with dimension lager than the final ones, in order to act itself as a membrane to create two chambers in the muffle. Right: top view of the glass over the slumping mould, closed inside the muffle just before going into the oven.*

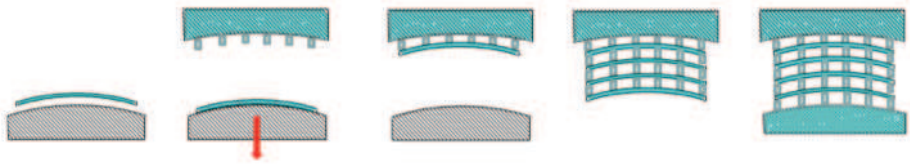

Figure 3.22: *: The integration scheme: the slumped glass foils is forced to the integration mould and glued to glass spacers (called ribs) that endow the structure with more stiffness and freeze into the glasses the Wolter-I profiles of the integration mould, thus correcting for residual low-frequency error profiles.*

Regarding the integration, we have adopted a stress-integration concept, that also employs a vacuum suction to force the mirror foils, slumped with nominal cylindrical shape, to the Wolter-I integration moulds. To freeze the correct shape before releasing the vacuum, the first glass foil is bonded to a stiff structure (e.g., a thick glass backplane) by means of ribs (Fig.3.22). The following mirror plates are successively bonded to the previously integrated plates in the stack. Therefore, the ribs play a structural role, but also a functional one, since they constrain the glass to the correct shape at their locations. In both Phase 1 and Phase 2, BK7 was used for the backplanes and the ribs, to match the CTE with the one of the D263 glass. The selected glue was the low shrinkage Masterbond EP30-2: as a glue layer of 75 μm on average is used, the ribs do not need to have a very accurate profile, because the glue fills profile errors of the ribs up to a few tens of microns, while the optical surface of the glass is forced in correct shape [Civitani et al. 2013].

After the vacuum release, spring-back effects are present due to the elasticity of the glass, and the profile differences between the initial glass plate shape and the integration mould figure. The spring-back is nearly zero at the rib locations and increases for increasing distance from the ribs, so the accuracy of the integrated plate improves as the rib spacing decreases [Civitani et al. 2013]. Finite Element Analysis was carried out in order to compute the correction factors [Parodi et al. 2011] by which we can simulate the integration on the glass foils, assuming perfect integration moulds and no effects due to the glue shrinkage (Section 4.4.1). This simulation will be extensively used in this thesis to compute the expected performances from the slumped glass foils

(Chapter 6).

The corrective properties of the adopted integration scheme have several advantages:

1. since the slumping moulds do not need to be Wolter-I, but cylindrical, it simplifies the slumping moulds procurement and reduce the costs;
2. FEA showed that the same slumping mould can even be adopted to slump 5 consecutive layers plates with different radius of curvature [IXO-BCV-RE-002 2011], with a further cost reduction;
3. residual low frequency errors due to the slumping process can be corrected, even if the capability to correct drops as the errors frequency increases (Section 4.4.1). It was derived that the first harmonic is damped by about 80%.

A dedicated Integration Machine (IMA) was developed with the support of A.D.S International (Fig. 3.23-left) [Civitani et al. 2011]. The IMA has been used to assemble several prototypes of X-ray modules [Civitani et al. 2013], during the Phase 2 of the project. One of these is shown in Fig. 3.23-right. They have been tested in X-rays at PANTER-MPE, showing a continuous improvement in performances, obtained by optimizing the process at various levels [Civitani et al. 2014].

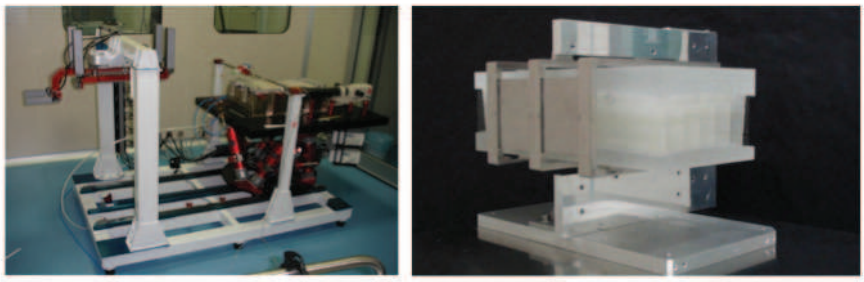

Figure 3.23: *: Left: the Integration Machine (IMA). Right: the X-ray Optical Unit Breadboard (XOU-BB) prototype.*

The first prototype, realized in late 2011, was based on two plate-pairs (PP) integrated in parallel configuration. This Proof of Concept #1 (PoC#1) was particularly useful to perform a test of the IMA behaviour and to debug the associated software and the entire assembly procedure. From the X-ray tests, performed intra-focally, the inferred HEW of the plates were in the range 80-120 arcsec.

The second prototype has been assembled in 2012 (Fig. 3.23-right). It comprised 20 PP (3 optical + 17 dummies) in a fully representative mechanical configuration, including a frame in titanium representing the interface with the satellite structure. It was called XOU-BB (acronym for "X-ray Optical Unit Breadboard"). The PoC#1 and XOU-BB were assembled using integration moulds with low accuracy figure, made of Metapore. Moreover, the slumped foils of D263 glass were characterized by poor optical quality. The measured HEWs at the best focus of each layer of the XOU-BB were observed to be between 48 arcsec and 60 arcsec. Both prototypes were developed following a "parallel" configuration, in which all the PP have the same incidence angle and therefore with no common focus for the system.

A new proof of concept (PoC#2) was realized in early 2013, using new integration moulds in BK7 (figured at Zeeko Ltd to a final HEW of around 3-4 arcsec) and new AF32 slumped glass foils with better optical quality with respect to the previous ones. This third model was based on 4 PP layers (1 dummy pair + 3 optically representative pairs), mounted in co-focal configuration

in order to check the alignment performance of the IMA. X-ray in-focus measurements for the PoC#2 were possible in early 2014: the achieved result with this prototype was 22.1 arcsec in full illumination mode @0.27keV (Chapter 8).

Aim of this thesis is to continue the optimisation of the hot slumping of thin glass foils, to further improve the mirror substrate quality. Since the ESA collaboration stopped on 2013, the work has been done on internal funds.

3.9 Error budget for SGO at INAF-OAB

At early times of the research [Civitani et al. 2010], an error budget has been defined, focusing on the angular resolution performances at 1keV. Since the errors are independent, their contribution is expected to sum in quadrature:

$$HEW_{TOT}(\lambda) = \sqrt{HEW_{Mould}^2 + HEW_{RepProc}^2 + HEW_{Int}^2 + HEW_{GlobEff}^2}. \quad (3.12)$$

For the slumping process, 1.8 arcsec was allocated for the slumping mould realisation errors (HEW_{Mould}); 3.5 arcsec was allocated for the mirror errors in double reflection ($HEW_{RepProc}$), including both figure and roughness errors. For the integration process (HEW_{Int}), a degradation of 1.5 arcsec was considered. Finally, for the integration of the XOU in the bench structure of the FMA, 2.8 arcsec was considered for global effects ($HEW_{GlobEff}$), including mechanical stresses at the mirror module fixation points and mirror module thermal environment during operation.

Since the contribution to the final HEW of the mirror foil is nowadays computed after the simulation of a perfect integration (Section 4.4.1), the two first terms of Eq. 3.12 should be considered the allocated error for the mirror foils $HEW_{Slumping}$, which sets to 3.9 arcsec the total result of their combination, if the quadratic summation is assumed:

$$HEW_{Slumping}(\lambda) = \sqrt{HEW_{Mould}^2 + HEW_{RepProc}^2}. \quad (3.13)$$

It was already pointed out (Section 4.4.3) that there is evidence that the two HEWs, resulting from figure and roughness errors, compose themselves linearly at the focal plane [Raimondi & Spiga 2015]:

$$HEW_{Slumping}(\lambda) = HEW_{Figure} + HEW_{Roughness}(\lambda). \quad (3.14)$$

Considering a maximum roughness contribution to the HEW of 1 arcsec at 1 keV, 2.9 arcsec represents the allocated error for the figure of the mirror foils in double reflection when an ideal integration is considered. Therefore, we can assume 2 arcsec the allocated error for the figure of the mirror foils in *single* reflection when an ideal integration is considered.

CHAPTER 4

Methods for surface characterization of slumped glass mirrors

The instrumentation hereafter described, and present at the INAF-OAB laboratories, was used in this work to characterise the surface of glasses and moulds, both qualitatively and quantitatively. Quantitative metrological data are important to predict the angular resolution of X-ray mirrors. They can be divided into instruments for a deterministic characterization of the surface (e.g. the LTP and the CUP, which measure the mono- and bi-dimensional profiles, respectively) or for a statistical characterization (e.g. the WYKO, the MFT and the AFM, used to measure the roughness of the surface). Different methods exist to compute the optical performance of the surface under test from the metrological data. In this chapter, the instruments used in this Ph.D. activity are described, and the different methods for analysis are introduced.

4.1 Visual inspection: the phase contrast Nomarski microscope

The Nomarski microscope is used to image sample which contain little or no optical contrast when viewed using bright field illumination. It returns images of the surface under test, giving qualitative indication on its topography. It is a fast method to understand the size and origin of defects or periodic patterns. The instrument (Fig. 4.1) produces a polarized white light beam, which is splitted by a modified Wollaston prism, producing two correlated beams with perpendicular polarizations, travelling in slightly different directions. A lens focuses the two beams at two positions on the surface under test, separated by one-micron distance. If a surface defect is present, the two beams will be reflected with two different phase changes. A further polarization plane rotation in the modified Wollaston Prism, recombines the two beams, which can interfere in the image plane. The phase variation result in variable brightness of the image, returning a surface map with a sensitivity of 1 nm. The space resolution is 0.22 μm. Many magnifications are selectable (from 5$\times$ up to 100$\times$) and the phase difference may be shifted in order to highlight the features at the most interesting height. The images show features superposed to spatial frequency ranges of AFM and WYKO instruments (Table 4.1).

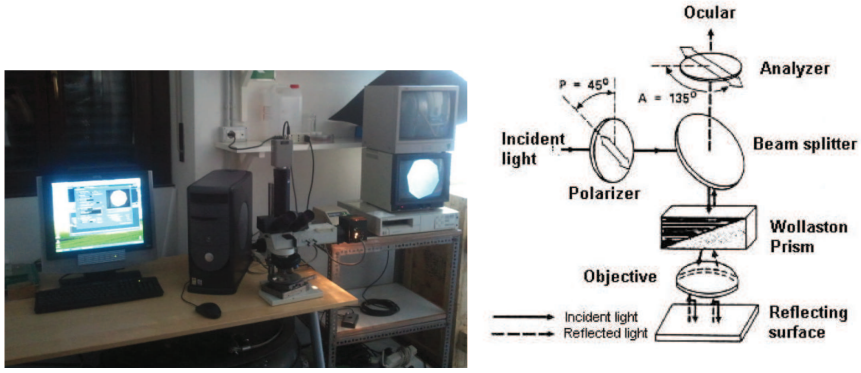

Figure 4.1: *: Left: Photo of the Nomarski phase contrast microscope. Right: Scheme of the Nomarski microscope.*

Table 4.1: *: The images obtainable with the Nomarski microscope visually show the features in the spatial frequency ranges of WYKO and AFM instruments.*

Magnification	5X	10X	20X	50X	100X
Image dim.	750 μm	375 μm	187 μm	75 μm	37 μm
Spatial freq. range	WYKO	WYKO	WYKO/AFM	AFM	AFM

4.2 Shape metrology

4.2.1 1D-profile: the Long Trace Profilometer

The Long Trace Profilometer (LTP) is a non-contact optical profiling instrument, sensitive to slope angles, based on the original concept of the pencil-beam interferometer of Von Bieren [Von Bieren 1983], and developed by P. Takacs et al. [Takacs et al. 1987]. It is designed to measure the absolute figure and mid-frequency errors of flat, spherical and aspherical surfaces up to 1 m in length, with no more than a 10 mrad ($\sim$ 0.57 degree) change in slope along the scan length: this translates into a surface radius of no less than 100 m for a 1 m scan length, or a surface radius of no less than 20 m for a 200 mm scan length.

The LTP system is comprised of an optical head mounted onto an air-bearing carriage that traverses a 1 m long ceramic bar chosen for its dimensional stability. The HeNe laser beam is split into two parts by a cube beamsplitter (Fig. 4.2), which are then laterally displaced by right angle prisms, in order to produce an interference pattern, and increase the resolution by analyzing the dark fringe. The two probe beams are directed down to the test surface and reflected back into beamsplitter, which directs them, through the Fourier transform (FT) lens, to a linear array detector; the beams, before going to the detector, are reflected three times onto a couple of mirrors (not shown in Fig. 4.2) to make the appropriate path length for the software to correlate the displacement on the detector to the correct slope error. Another part of the beam is focused on a reference surface, in order to subtract the tilting and rotation of the optical head. While scanning the surface under test, the reflected beam direction changes according to the local surface slope at that position. The Fourier transform lens converts the angle variation of the reflected beam in a variation of position in its focal plane. The whole instrument is mounted on self-stabilizing, air-suspensions: these are necessary for isolation from the sound waves, propagating from the ground. The LTP repeatability is of a few tenths of nm over a scan of 200 mm, the typical length of a glass mirror produced in this work; the lateral resolution is better than 1 mm. For our instrument, the stability of 200 measurements on a fixed measuring point is about 20 nm; the

difference of two consecutive scans, of 200 mm length, have rms = 20 nm.

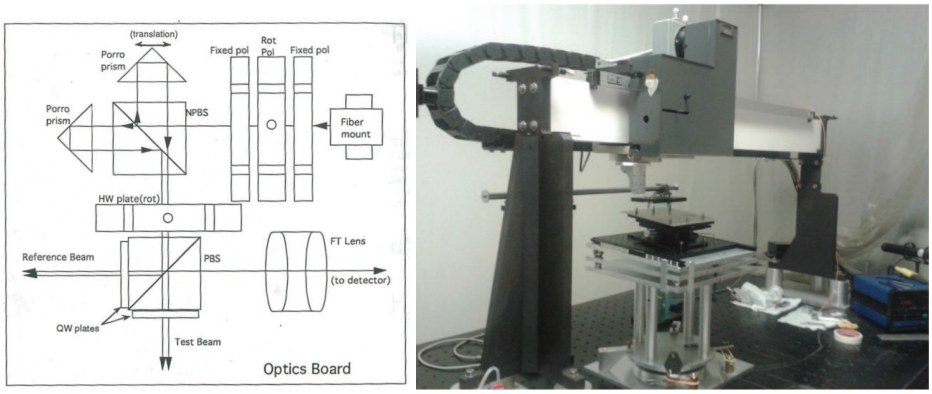

Figure 4.2: *: Left: Optical diagram of the LTP head: NPBS= non polarising beam splitter, PBS = polarising beam splitter; HW = half-wave retardation plate (to adjust the relative intensity between the test and the reference arms), QW = quarter wave retardation plate, FT lens = Fourier transform lens. The rotating polariser (Rot Pol) adjusts total light intensity. One of the Porro prisms translates to adjust the beam spacing and interference fringe position. (right) The LTP at INAF-OAB.*

4.2.2 1D-profile: CHR mounted on LTP

LTP measurements can be done only on specular surfaces, i.e. surfaces that are polished and smooth. Thin glass foils have smooth surfaces, but the presence of the second reflection, from the lower surface, makes the LTP signal unstable (constructive or destructive interference from the reflections of the two surfaces results in a "flickering" signal). A different setup was already developed to enable this kind of measurements (Fig. 4.3) [Spiga IR05-2011]. A CHRocodile optical sensor is mounted on the LTP head. The CHRocodile sensor in use on the LTP (3300 μm) measures distances in the range of 3.3 mm with a 100 nm vertical resolution and 6 μm lateral resolution. CHR can be used in "distance" or "thickness" configuration, the second one enabling the measurement on both glass surfaces. The glass is supported on three bearing points and measured on both concavity. The actual profile of the optical side of the glass is retrieved by subtracting the two scans: this enables removing both gravity and bearing points deformations. A Rodenstock RM600-S sensor is also installed to subtract, in real time, the LTP stage error contribution by measuring a calibrated rod.

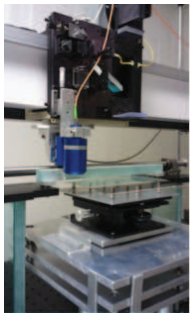

Figure 4.3: *: The CHRocodile 3300 sensor head mounted on the LTP; the Rodestock RM600-S is used to subtract the LTP stage errors by measuring a calibrated rod.*

4.2.3 1D-profile: development of a method to use LTP for thin glass profiles

The CHRocodile setup, described in the previous section, introduces spurious mid-frequency errors in the glass profiles. I clarified this [Salmaso IR12-2013] by comparing the measurements on a slumped glass foil, both with the CHR-LTP setup and with the sole LTP after evaporating a reflective coating on the glass optical surface (Fig. 4.4).

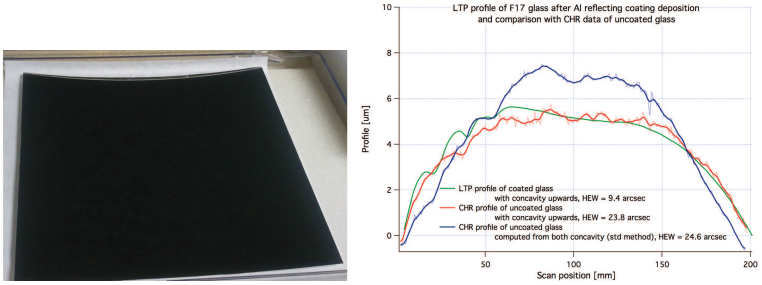

Figure 4.4: *: Left: a slumped glass coated with evaporated Aluminium. Right: Profiles of this glass foil (code F17). The CHR measurements (red and blue) are both in thickness mode and exhibit spurious mid-frequency errors not present in the LTP measurement (green).*

On the other hand, the LTP measurements of the uncoated glass foils, were considered impossible because of the unwanted reflection form the back glass surface. Water was previously considered, to suppress the second reflection, because its index of reflection is very similar to that of the glass, but the measurement of the glass floating of the water surface was not stable; moreover the water surface tightness introduces a significant bending of the surface. I have introduced a new method to measure thin glass foils with the LTP [Salmaso IR12-2013], by painting the back surface with First Contact (Fig. 4.5-left), a polymeric paint usually used to clean the optical surfaces. I have subtracted the distortion due to the gravity and the bearing points by Finite Element Analysis. In this way, I have suppressed the reflection from the lower surface of the glass foils, without causing stress and distortion on the glass: in fact, the measurement performed with the CHR-LTP setup match the ones with the LTP-FEA, with the removal of the spurious mid-frequency errors (Fig. 4.5-right).

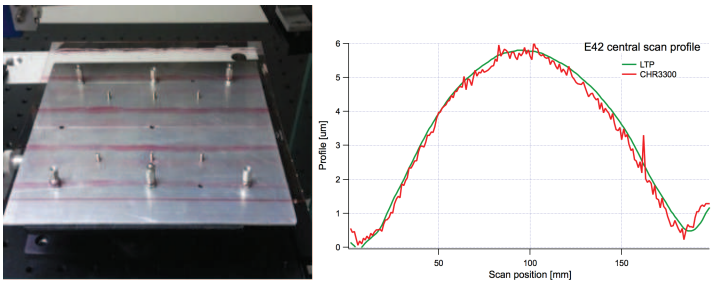

Figure 4.5: *: Left: First contact on the glass back surface, over the scanned lines. Right: central profile of a slumped glass foil (code: E42). The LTP-FEA measurement (green line) matches the CHR-LTP measurement (red line), without introducing spurious mid-frequency errors.*

4.2.4 1D-profile: mounting a cylindrical lens on the LTP to measure cylindrical moulds

Since the mould surface is convex, the laser beam diverges after reflection and would form a broader trace on the LTP detector, decreasing the alignment accuracy. Hence, I make use of a cylindrical lens with 1 m focal length in the optical path of the laser: in this way, the laser spot

size reflected by the mould on the detector is reduced, and therefore the alignment accuracy is improved.

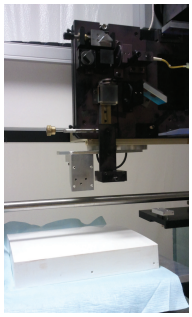

Figure 4.6: *: A cylindrical lens with 1 m focal length is mounted on the LTP head to increase the accuracy of the measurements for slumping mould with 1 m radius of curvature.*

4.2.5 2D-profile: the Characterization Universal Profilometer

The Characterization Universal Profilometer was developed at INAF-OAB during the ESA contract "The Back-up IXO (former XEUS) optics Technology, Phase 1" [Civitani et al. 2010b]. The CUP working principle is based on the measurement of the distance between the surface under test and a reference flat mirror. Two non-contact sensors, the CHRocodile optical sensor and the SIOS triple beam interferometer, are mounted onto a xyz stage and measure the surface under test and the reference mirror, respectively. The CHRocodile sensor in use on the CUP (660 μm) is characterized by 20 nm vertical resolution and 2 μm lateral resolution, with a maximum thickness measurement range of 0.9 mm, sufficient for the 0.4 mm thickness of the glasses used in this thesis. It is used in "null configuration", with the z axis movement of the translational stage keeping the surface continuously in the centre of the measuring range. The x and y movements are used to move the CHRocodile sensor across the sample surface. Due to the short working distance (6.5 mm) the lens aperture is able to collect reflected rays at large angles with respect to the sensor axis (up to +/-30 deg). Consequently, the CHRocodile sensor can perform scans of curved surfaces without the need of tilting its orientation with respect to the optical axis of the lens. Finally, the CUP operates in an ISO6 clean room environment with a temperature control of +/- 0.2 °C.

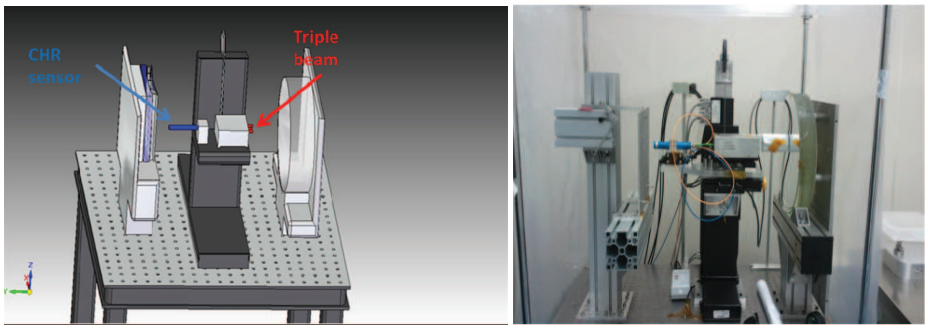

Figure 4.7: *: The Characterization Universal Profilometer (CUP). Layout (left) and photo (right) of the CUP.*

4.2.6 2D/1D-profile: the ZYGO interferometer

The ZYGO CPI-XP is an Fizeau type interferometer. The light source is a HeNe laser, expanded to 100 mm diameter. A transmission element, mounted in front of the aperture, reflects some of the laser light back into the interferometer, thus creating a reference wavefront. The remainder of the laser light passes through the transmission element to the surface under test and is the measurement wavefront (Fig. 4.8-left). Inside the interferometer, the reflected wavefront is recombined with the reference wavefront, producing interference. The ZYGO CPI-XP is equipped with two transmitting elements, one for flat and another for spherical surfaces: in these cases, 2D measurements can be acquired. For cylindrical surfaces, instead, only 1D scans can be measured. The accuracy of the instrument is $\lambda/100$ (= 6 nm); the rms repeatability is $\lambda/2000$ at 2σ (= 3 Å).

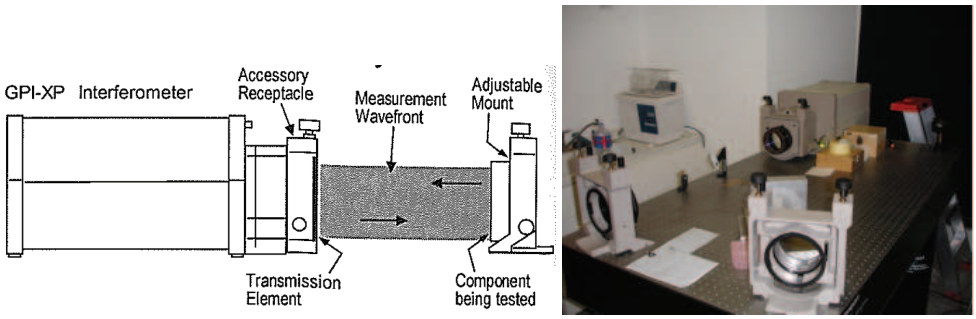

Figure 4.8: *: The ZYGO CPI-XP interferometer. Layout (left) and photo (right) of the ZYGO interferometer.*

4.2.7 About the HEWs computed from LTP vs CUP

LTP and CUP measurements return a good agreement in the long-scale defects, but a substantial discrepancy in the mid-frequency region, especially at azimuthal coordinates distant from the centre, both for glass foils and moulds. This difference in turn yields a different result in terms of expected HEW (Section 4.4.6 describes how HEW values are computed from profile data). To decide between the results, I have used a third instrument, the ZYGO interferometer. The interferometric measurements on glass foils are more difficult, because the samples are sensitive to vibrations, hence the Zerodur K20 MK20-20B slumping mould (see Section 6.2.4 for the full mould characterisation) was measured with the ZYGO, the LTP and the CUP. The ZYGO was used with a flat null lens of 100 mm diameter, therefore returning only mono-dimensional profiles of 100 mm maximum length of the cylindrical surface. The MK20-20B slumping mould was measured on three positions: the center, 80 mm right off-center, 80 mm left off-center. Fig. 4.9 shows one of the three profiles, obtained after the subtraction of the best fit 8th order polynomial: the LTP and ZYGO measurements are in very good agreement; the small differences of about 10 nm are due to:

1. alignment errors: small deviation from the azimuthal coordinate would result in a comparison of slightly different profiles with differences in mid frequency height contribution;
2. better stability and repeatability of the ZYGO over the LTP (repeatability over 100 mm at 1 sigma: rms-LTP = 5 nm, rms-ZYGO=1nm).

In Table 4.2, the expected HEW values, computed for the three scans, are presented: the results of the LTP and ZYGO data are in substantial agreement with each other and anyway much smaller than the one computed with the CUP at position 80 mm off-center ($\text{HEW}_{CUP} \sim 8$ arcsec). Hence the HEW values computed from the LTP are considered to give a more accurate description of the glass foils and slumping moulds quality, over the CUP ones.

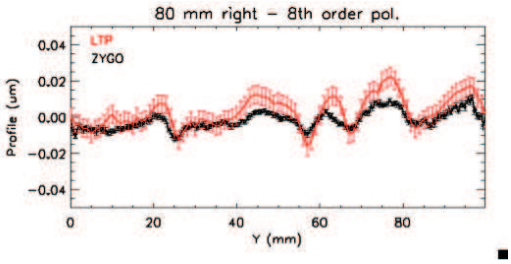

Figure 4.9: *: Comparison between the LTP (red curve) and ZYGO (black curve) scans of the MK20-20B after annealing: the profile shown was taken at 80 mm right from the center, and it is the residual after the subtraction of the best-fit 8th order polynomial.*

Table 4.2: *: HEW values computed with physical optics from the LTP and ZYGO scans of the MK20-20B mould after the annealing, after the subtraction of the best fit 8th order polynomial.*

	LTP	ZYGO
80L	0.13	0.13
C	0.36	0.13
80R	1.4	0.13

For this reason, all the expected HEW values are presented, in this thesis, from data taken with the LTP. Fig. 4.10 show the typical five scans (green dashed lines) taken with the LTP, superimposed to the CUP map after the simulation of the integration. The six pink lines represent the ribs. On the right side of Fig. 4.10, the HEW value computed from physical optics from the LTP scans, after the simulation of a perfect integration, are reported.

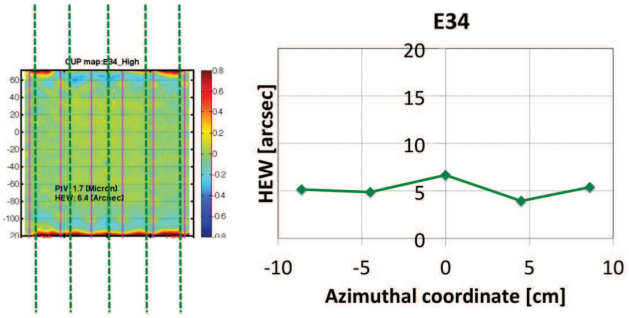

Figure 4.10: *: Left: CUP map of a slumped glass foil (code: E34) after the simulation of a perfect integration. The six pink lines represent the ribs. The six green dashed lines represent the LTP scans. Right: the HEW computed, from physical optics, for the 5 LTP scans after integration.*

4.3 Roughness metrology

The direct measurements of roughness at INAF-OAB are mainly performed using:

1. the WYKO TOPO-2D optical profilometer, which is sensitive, with different objectives, in the range 1 - 5300 μm of spatial wavelengths;
2. the MFT optical profilometer, sensitive, with different objectives, in the range 0.2 - 1800 μm of spatial wavelengths;

3. the AFM, sensitive to higher frequencies, corresponding to a spatial wavelength range 0.01 - 100 μm;
4. the BEDE-D1 diffractometer: if operated at the X-ray energy of 8.045 keV = 1.541 Å, the Cu Kα_1 fluorescence line, with incidence angle θ_i = 500 arcsec, a detector scan at scattering angles $\theta_s \in [\sim 0 \div 4000]$ arcsec, corresponds (through Eq. 2.22) to spatial wavelengths between 50 μm and 0.8 μm, i.e. the ones in the sensitivity window of the AFM.

4.3.1 The WYKO TOPO-2D interferometer

The WYKO TOPO-2D (Fig. 4.11) is a non-contact profilometer, which uses the technique of phase-shifting interferometry. The interference between the light reflected from the surface under test and the light reflected form an internal reference surface is imaged onto a one-dimensional detector array. Two objectives are available: 20× and 2.5×, which uses the Mirau and the Michelson [1] interferometer respectively (Fig. 4.11-left). The scan widths are of 660 μm and 5.3 mm, the maximum surface heights are 3.1 μm and 7.9 μm, and the maximum detectable surface slopes are 10.7 degree and 1.3 degree, respectively. Being the WYKO scans of 1024 points, the lowest spatial wavelength that can be measured is about 1 μm (Nyquist's limits). The instrumental noise, however, limits the effective lowest wavelength to 3 μm. The vertical resolution is of few angstrom. A fitting of the profile is necessary to subtract the misalignment of sample and the profile error, hence obtaining the intrinsic sample roughness: a typical detrend of the 4th order best fit polynomial is applied.

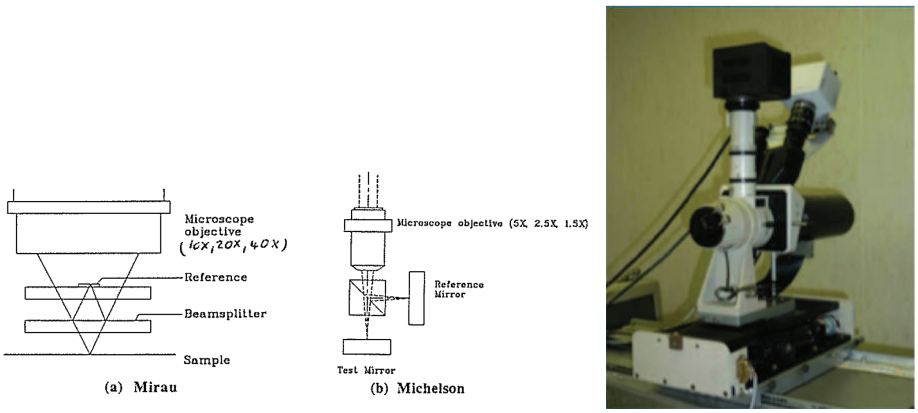

Figure 4.11: *: The WYKO TOPO-2D. Layout (left) and photo (right) of the WYKO TOPO-2D.*

4.3.2 The Micro Finish Topographer

The Micro Finish Topographer (MFT), as the WYKO TOPO-2D, is a phase shift interferometer, but returns 2D maps. It uses a Point Source Microscope (PSM) mounted with different interferometric objectives: 2.5× and 5× Michelson interferometers, and 10×, 50× and 100× Mirau interferometers. The lowest spatial wavelength that can be measured is about 0.2 μm. With the 10× objective, the residual error between two consecutive measurements, resulting of a average of 16, have rms = 0.6 nm; the result can be improved if a 3 points smoothing is performed, giving rms = 0.2 nm.

[1] Reference mirror errors can always be subtracted. Anyway, Michelson interferometer is more sensitive to temperature variations because the arm movement is larger. From this point of view, Mirau configuration is preferable for super polished surfaces with roughness less than 1 Å.

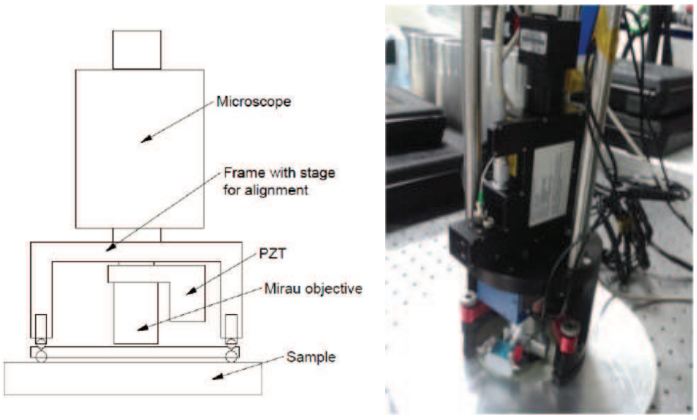

Figure 4.12: *: The Micro Finish Topographer (MFT). Layout (left) and photo (right) of the MFT.*

4.3.3 The Atomic Force Microscope

The Atomic Force Microscope (AFM) (Fig. 4.13) is a type of Scanning Probe Microsope (SPM), where a sharp tip (made with Antimony-doped Silicon) is brought in close proximity to the surface under test. Van Der Waals forces, between the atoms of the tip and those of the surface, cause a deflection of the cantilever where the tip is mounted on. At each height change, the tip changes distance/oscillation frequency and phase, and this change may be monitored by a laser lever that amplifies the oscillation. The AFM can work either in "contact mode" (the interaction of the tip to the surface is stronger and the instrument has a better resolution but the tip surface can be damaged) or in "non-contact" (tapping) mode. We typically operate it in tapping mode. Two types of scanners can be used: tripod scanner (for scan width from 100 μm to 10 μm, with z range of 10 μm) and tube scanner (for scan width of 1 μm, with z range of 0.8 μm). Since the scan covers a 512 $\times$ 512 pixel matrix, the scan resolution varies between 0.2 μm and 20 Å.

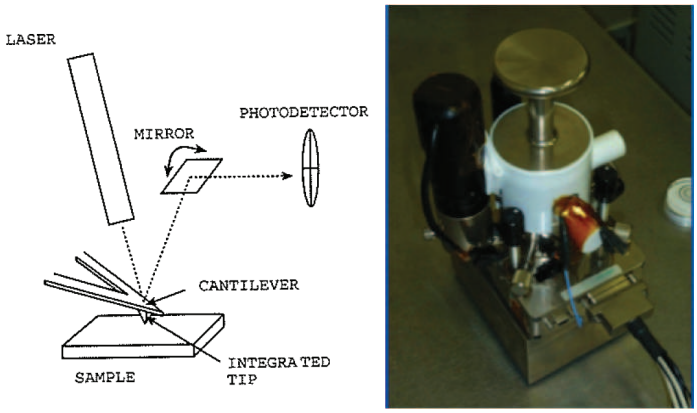

Figure 4.13: *: The Atomic Force Microscope (AFM). Layout (left) and photo (right) of the AFM.*

4.3.4 The BEDE-D1 diffractometer

The BEDE-D1 is a general purpose X-ray diffractometer: it allows X-ray diffraction (XRD), reflectance (XRR: X-Ray Reflectivity), and scattering (XRS: X-Ray Scattering) measurements.

X-ray reflectivity provides informations about the thickness of the materials deposited onto the substrate, the diffuseness of the deposited layers, the optical constants and density of the materials used for the coatings. On the other hand, the X-ray scattering provides indirect highly representative information about the roughness of the surface under test (Eq. 2.21).

An X-ray tube (typically equipped with a copper anode) generates a bremsstrahlung spectrum, superposed to characteristic fluorescence lines of Cu. In particular the $K\alpha 1$ line (8.05 keV, 1.541 Å) is selected because of its intensity and sharpness (typically it has a 1 eV equivalent width). The line intensity may be changed by external power controls. The X-ray tube is easily removable in order to change the target anode to Molybdenum, in case measurements in harder X-rays are required. The Cu or Mo fluorescence line are then filtered by a Si crystal monochromator, and collimated. The emerging beam incides on the sample, mounted on a precise (1 arcsec) goniometer. The reflected/scattered rays are collected by a scintillation detector, equipped with a photomultiplier (Fig. 4.14).

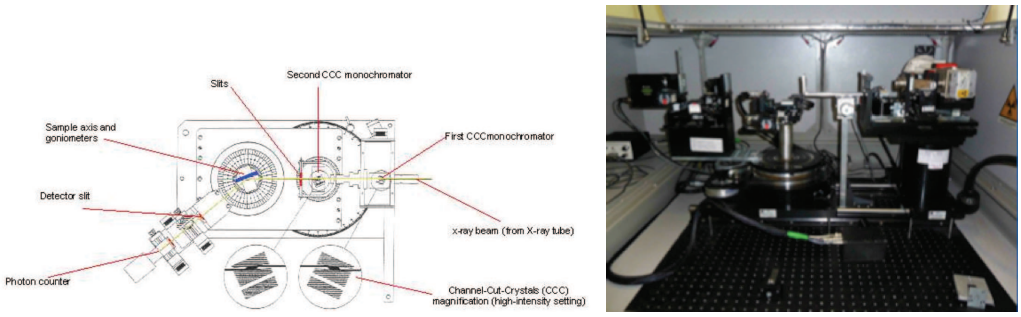

Figure 4.14: *: The BEDE-D1 X-ray diffractometer. Layout (left) and photo (right) of the BEDE-D1.*

The measurements can be divided into two groups:

1. theta/2theta scans for XRR measurements: the sample under test, illuminated with a monochromatic beam, is rotated under different grazing incidence angles (with incident angle = theta). The reflected beam is followed and measured by a co-rotating detector (at angle = 2 theta to detect the reflected beam). The measurement resolution is determined by the incident beam divergence, which can be controlled using a system of microslits. The reflectivity in the specular direction is related to the surface/interfacial roughness, but it does not allow a complete characterization of the surface (Eq. 2.20);

2. detector scans for XRS measurements: in this case the incidence angle is constant and the detector measures the scattered light around the reflection angle. An exhaustive description of the surface roughness is given by the non-specular reflectance, that is, the scattering in directions other than the specular one, being related to the PSD of the surface (Eq. 2.21).

4.4 Methods for data analysis

The metrological data, gathered with the previously listed instruments, are used to predict the optical performance of X-ray mirrors. This is essential in order to optimise the mirror production process. The imaging degradation of a X-ray telescope is mainly caused by:

1. integration errors;
2. "profile" errors, i.e. deviation from the desired figure, typically in the $>$ 10 cm lateral range;
3. "mid-frequency" errors, in the centimeter spatial wavelength range;
4. roughness: high frequency errors, from 1 mm spatial wavelength downwards.

The first one is not treated in this work, since a perfect integration is considered, nor will errors from the integration moulds or from the glue shrinkage be treated. The other errors can be directly measured with the instruments described in the previous sections. The methodology adopted are listen hereafter. We notice that the discrimination of these different ranges is purely operational. The difference is simply related to the measurement technique (either deterministic or statistical), but the impact in terms of PSF can be determined regardless of this separation (Section 4.4.6).

4.4.1 The shape measurements of slumped glass foils: raw data and simulation of a perfect integration

The shape of the glass foils and moulds is routinely characterized in our laboratories with the LTP for 1-D profiles and with the CUP for 2-D maps. Both measurements have advantages and disadvantages. The CUP gives a full characterisation of the mirror, both in longitudinal and azimuthal directions, but the measurements have to be filtered above 5 mm, to remove the noise of the system at higher frequencies. The central azimuthal part of the glass foils is accurately measured, but, in the lateral part of the glass foils, the carriages introduce errors that are only partially corrected. The LTP is giving mid-frequency measurements more accurate then the CUP (see Section 4.2.7), but only longitudinal profiles can be measured, since, in the azimuthal direction, the slope variation is outside the dynamic range of the instrument. Owing the better accuracy of the LTP with respect to the CUP in the mid-frequency range, I consider the LTP the best measuring tool to predict the optical performance of slumped glass mirrors. All the slumped glass mirrors were sampled on five longitudinal scans: the central scan, the scans 45 mm off the centre, in the left and right direction, and the scans 86 mm off the centre, again in left and right directions. These particular positions were chosen because they are at different distance from the integration ribs, hence representative for different damping during the integration. Fig. 4.15 shows the CUP and LTP measurements of one slumped glass foil. The central sag error is ~ 10 μm. Fig. 4.17 show the same data after the simulation of a perfect integration: in this case, the central sag error is reduced to ~ 2 μm. The concept of this simulation is described hereafter.

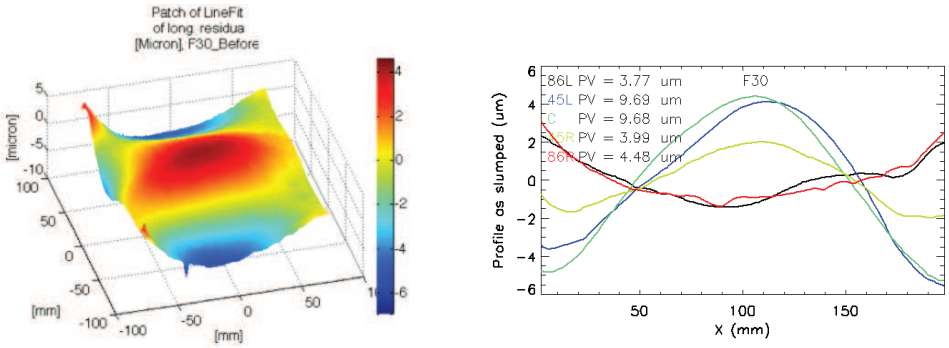

Figure 4.15: *: Shape measurement of a slumped glass foil (code: F30). Left: the CUP map. Right: the five LTP profiles, whose position whose chosen because they are at different distance from the integration ribs, hence representative for different damping effect during the integration.*

As described in Section 3.8.5, our integration concept foresees the use of two integration moulds with Wolter I profile, whose shape has to be replicated by the cylindrical slumped glass foils. Six ribs are used to freeze the shape of the cylindrical slumped glass foil to the Wolter I configuration. Due to the elasticity of the glass, the glass replicate the Wolter I profile only under the ribs, while the spring-back increases for increasing distance form the ribs. FEA was carried out in order to compute the factors by which a sinusoidal profile, with a given amplitude, is damped [Parodi et al. 2011]. The attenuation coefficients are shown in Fig. 4.16. Each curve represents the degree of attenuation for the harmonics of a profile scan at a particular distance

from the central longitudinal scan: the scan at 20 mm off the centre is the closest to a rib and therefore is the most attenuated, while the scan at 40 mm off the centre is the closest to a anti-rib position and therefore is attenuated to the smallest extent.

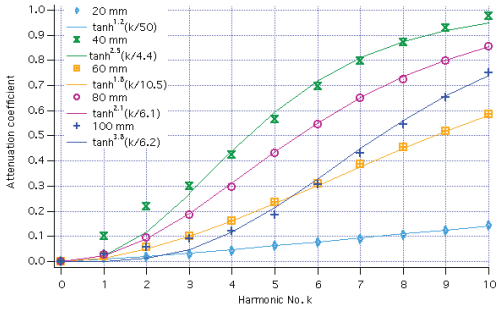

Figure 4.16: *: Attenuation coefficients for the harmonic components of profiles at different distance from the central longitudinal scan. Each curve represents the degree of attenuation for the harmonics of a profile scan at a particular distance from the central longitudinal scan: the scan at 20 mm off the centre is the closest to a rib and therefore is the most attenuated, while the scan at 40 mm off the centre is the closest to a anti-rib position and therefore is the less attenuated.*

The damping result of the integration can be visualised in Fig. 4.17, both for the CUP and LTP measurements. The ribs pattern is clearly visible in the CUP map; the region in between the ribs is the one where the shape deviation from the nominal Wolter is maximal. For the glass foil considered in Figs. 4.15 and 4.17, the central sag error of ~ 10 μm of the slumped glass foil, is reduced to ~ 2 μm after the simulated integration.

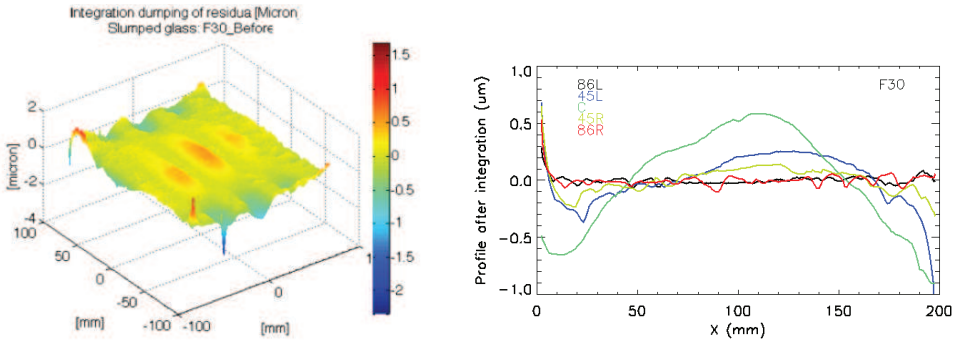

Figure 4.17: *: Simulation of a perfect integration of a slumped glass foil (code: F30). The CUP map (left) and the LTP profiles (right) are damped with the coefficient reported in Fig. 4.16. The central sag error of ~ 10 μm of the slumped glass foil, is reduced to ~ 2 μm after the simulated integration.*

4.4.2 The roughness measurements of slumped glass foils: PSD computation from roughness data

The instruments for roughness characterisation, described in the previous sections, provide a description of the surface under test in the different spatial wavelength ranges, depending on the sampling length and the sampling interval. From these measurements, the Power Spectral Density (PSD) distribution of the surface, can be computed as the square module of the Fourier transform of the profile $z(x, y)$:

$$\hat{z}(f_x, f_y) = \frac{1}{L_1 L_2} \int_{-\frac{L_1}{2}}^{+\frac{L_1}{2}} \int_{-\frac{L_2}{2}}^{+\frac{L_2}{2}} e^{-2\pi i(f_x x + f_y y)} z(x,y) \mathrm{d}x\mathrm{d}y, \tag{4.1}$$

$$\mathrm{PSD}(f_x, f_y) = L_1 L_2 \left|\hat{z}(f_x, f_y)\right|^2, \tag{4.2}$$

being f_x and f_y the spatial frequencies along x and y respectively, L_1 and L_2 the dimension of the sampled surface.

By integrating P on f_x or f_y, it can be shown that the mono dimensional PSD can be written as:

$$\mathrm{PSD}(f_y) = \int_{-\infty}^{+\infty} PSD(f_x, f_y)\mathrm{d}f_x = \frac{1}{L_1}\int_{-\infty}^{+\infty} dx \frac{1}{L_2}\int_{-\infty}^{+\infty} z(x,y) e^{-2\pi i f_y y}\mathrm{d}y, \tag{4.3}$$

$$\mathrm{PSD}(f_x) = \int_{-\infty}^{+\infty} PSD(f_x, f_y)\mathrm{d}f_y = \frac{1}{L_2}\int_{-\infty}^{+\infty} dy \frac{1}{L_1}\int_{-\infty}^{+\infty} z(x,y) e^{-2\pi i f_x x}\mathrm{d}x, \tag{4.4}$$

with PSD(f_x,f_y) having the dimensions of the fourth power of a length (usually nm^4), whereas those of PSD(f_x) and PSD(f_y) are a length at the third power (usually nm^3).

Finally, from the PSD it is possible to compute the rms of the surface:

$$\sigma^2 = \int_{-\infty}^{+\infty} \mathrm{d}f_x \int_{-\infty}^{+\infty} \mathrm{d}f_y PSD(f_x, f_y) = \int_{-\infty}^{+\infty} PSD(f_x)\mathrm{d}f_x = \int_{-\infty}^{+\infty} PSD(f_y)\mathrm{d}f_y. \tag{4.5}$$

The treatment of the roughness data is performed separately for all the instruments mentioned in the previous sections. The PSD can be computed for each instrument, therefore giving a contribution covering a different frequency range: the minimum spatial frequency, $1/(2d)$, is dictated by the pixel size, d, while the maximum, $1/L$, by the length of the scan, L. Fig. 4.18 shows the superposition and mutual agreement of PSDs, computed from several instruments, for a D263 slumped glass foil.

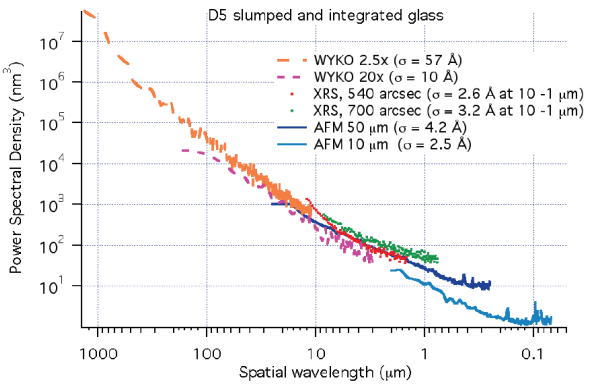

Figure 4.18: *: Overall PSD of a glass foil (code: D5). The WYKO, the BEDE-D1 and the AFM were used.*

4.4.3 The expected angular resolution of slumped glass foils: an overview

To compute the expected angular resolution of the slumped glass foils, the low, mid and high-frequency errors have to be considered. The traditional approach is to use geometrical optics for the treatment of the shape errors, using the ray-tracing formalism (Section 4.4.4). Roughness data are traditionally treated with the first-order scattering theory (Sections 4.4.2 and 4.4.5). In this context, the limit where to change from one treatment to the other is not defined a priori. Moreover, the way the two resulting HEWs compose themselves at the focal plane, to the final mirror HEW, is not completely clear: the traditional approach is to sum them in quadrature, but there is evidence that this approach is incorrect, in general. A novel approach has been developed at INAF-OAB during the Ph.D. thesis of Lorenzo Raimondi [Raimondi & Spiga 2010], [Raimondi & Spiga 2015] (Section 4.4.6). I have extensively used this approach to compute the HEWs from the mirror produced during my work. For all the slumped glass foils, I have been computing with physical optics, the expected angular resolution from:

1. the LTP raw profiles, at 1 keV. This data gives an indication of the mould replication in the low-frequency range.
2. the LTP profiles after the simulation of a perfect integration, at 1 keV. This represents the glass quality in terms of profile errors.
3. the LTP profiles, after the simulation of a perfect integration, and the roughness data, at 1 keV. This represents the glass quality in terms of profile and roughness errors, and it it therefore dependent on the energy.
4. the LTP profiles, after the simulation of a perfect integration, and the roughness data, at 1.5 keV. In this phase of the research, the scattering contribution is only considered up to 1.5 keV.

In the following sections, the methods to derive the expected angular resolution from slumped glass foils are described.

4.4.4 Ray tracing for figure and errors analysis

Ray tracing is a geometrical method to calculate the path of the light impinging on a mirror. It was introduced for the first time by Whitted [Whitted 1980]. The ray is reflected on the mirror surface with an angle equal to the incident one. The equation that describes the behaviour of a ray of light after a single reflection is:

$$\overrightarrow{k_1} = \overrightarrow{k_0} - 2\left(\overrightarrow{k_0} \cdot \overrightarrow{n}\right)\overrightarrow{n} \tag{4.6}$$

where $\overrightarrow{k_0}$ is the direction of the incoming ray, $\overrightarrow{n}$ is the unit vector normal to the surface in the point where the ray impinges and $\overrightarrow{k_1}$ is the direction of the reflected ray. The normal to the surface can be computed numerically from the surface map, either measured or simulated.

The ray is then propogated to the subsequent reflection. After the last reflection, the final position on the detector plane is computed. If (x_0,z_0) are the coordinates of the point where the ray impinges on the mirror, the coordinates (x_f,z_f) of the point where the ray arrives at the focal plane, are given by:

$$x_f = x_0 + \frac{z_f - z_0}{k_{1z}} k_{1x} \qquad\qquad z_f = z_0 + \frac{x_f - x_0}{k_{1x}} k_{1z} \tag{4.7}$$

After a number of rays traced, the Point Spread Function (PSF) can be computed. The HEW is the angular diameter, in the focal plane, which include the 50% of the focused rays.

The limit of this method is that it is reliable only as long as geometrical optic can be applied, and does not take into account the wave nature of light, so the aperture diffraction and the surface scattering are not considered.

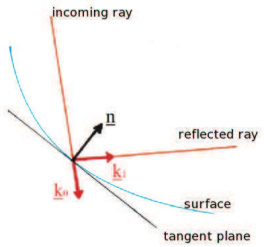

Figure 4.19: *: Geometry of the reflected ray.*

4.4.5 X-ray scattering from a rough surface: an analytical method to compute the roughness contribution to HEW

In section 2.4.2 I have already described how the rays distribution in the focal plane can be retrieved by using the PSD computed from roughness data: the formalism uses the first order perturbation theory in the smooth-surface condition. Let us re-write it here, for clarity reasons:

$$\frac{1}{I_0}\frac{\mathrm{d}I_\mathrm{s}}{\mathrm{d}\theta_\mathrm{s}} = \frac{16\pi^2}{\lambda^3} Q_\mathrm{is}\, \sin^2\theta_\mathrm{s} \sin\theta_\mathrm{i} \mathrm{PSD}(f). \tag{4.8}$$

Of course, also the reverse holds: if one measures the scattering from a surface (as can be done by the BEDE-D1 diffractometer), the PSD can be computed as a function of the spatial wavelength, given by

$$\frac{1}{f} = \frac{\lambda}{|\cos\theta_\mathrm{i} - \cos\theta_\mathrm{s}|}. \tag{4.9}$$

In [Spiga 2007] a method is described to derive the HEW from the surface PSD. It is therein shown that the HEW, in radians, can be written as:

$$\mathrm{HEW}\,(\lambda) = \frac{2\lambda f_0}{\sin\theta_i}, \tag{4.10}$$

where λ is the wavelength of the incident beam, θ_i is the incident angle, and f_0 is defined by the integral equation

$$\int_{f_0}^{\frac{2}{\lambda}} \mathrm{PSD}(f)df = \frac{\lambda^2 \ln\left(\frac{2N}{2N-1}\right)}{16\pi^2 \sin^2\theta_i}. \tag{4.11}$$

where N is the number of reflections at the grazing angle θ_i. The limit of this method is that it is reliable only if the smooth-surface condition is applicable, and if $\mathrm{HEW}(\lambda) \ll \theta_\mathrm{i}$.

4.4.6 PSF computation from Fresnel diffraction

This method was developed during the Ph.D. thesis of Lorenzo Raimondi [Raimondi & Spiga 2010], (Spiga & Raimondi 2014), [Raimondi & Spiga 2015]. It is based on the Huygens-Fresnel principle for computing the diffracted intensity from the grazing-incidence mirror: it accounts simultaneously for profile, roughness, and aperture diffraction, providing analytical formulae that are valid at any light wavelength, for computing the PSF of an X-ray mirror shell from the measured longitudinal profiles and the roughness power spectral density, without distinguishing spectral ranges with different treatments. In the case of a point-like and isotropic source on the optical

axis of a axially-symmetric grazing-incidence mirror, the PSF for single-reflection can be written as [Raimondi & Spiga 2015]:

$$\mathrm{PSF}(x) = \frac{\Delta R_1}{L_1^2 \lambda R_0} \left| \int_f^{f+L_1} \sqrt{\frac{x_1}{\bar{d}_{2,0}}} e^{-\frac{2\pi i}{\lambda}\left[\bar{d}_{2,0} - z_1 + \frac{x_1^2}{2(S-z_1)}\right]} \mathrm{d}z_1 \right|^2 , \tag{4.12}$$

where $x_1(z_1)$ is the radial profile along the z axis, which is the longitudinal telescope axis, L_1 is the mirror length, λ is the radiation wavelength, R_0 is the radius of the mirror at the axial position closer to the focal point, S is the source position, ΔR_1 is the radial amplitude of the mirror's entrance pupil seen from the source and defined as $\Delta R_1 \simeq L_1 \sin\theta_i$, and $\bar{d}_{2,0}$ is defined as $\bar{d}_{2,0} = \sqrt{(x_1 - x)^2 + z_1^2}$.

The longitudinal mirror profile is composed of three terms:

$$x_1(z_1) = x_{n1}(z_1) + x_{meas1}(z_1) + x_{PSD1}(z_1), \tag{4.13}$$

where x_{n1} is the nominal mirror profile, x_{meas1} is the measured profile error along the entire profile length L_1, and x_{PSD1} is one of the infinitely possible profiles of length L_1, computed from the PSD. Using a combination of Eqs. 4.13 and 4.12, the PSF can be computed from LTP/CUP and roughness measurements.

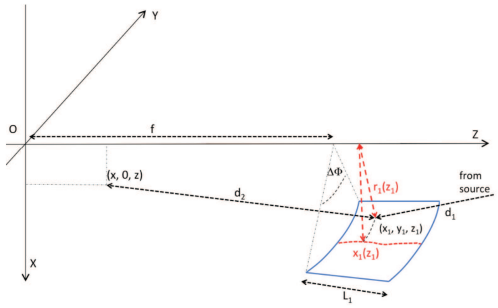

Figure 4.20: *: Reference frame used to compute the diffracted field from a grazing-incidence mirror. Credits (RaimondiSpiga 2015)*

The method has been extensively used in this thesis to compute the PSF expected in single reflection from the glass mirror foils produced with different processes. Profiles and roughness data were acquired for each mirror and the expected PSF was computed using an IDL code developed to implement Eq. 4.12.

CHAPTER 5

Description of the hot slumping process assisted by pressure

5.1 The setup

INAF-OAB has developed an innovative technique to produce thin glass foils for X-ray telescopes with a replica process. The technique combines a thermal cycle to curve the glass foil on a slumping mould, with the application of pressure to help the mould shape replication. Each individual glass foil, whith characteristic thickness of 0.4 mm, is curved in a furnace with a thermal cycle that enables a tolerable surface roughness and a proper curvature. In brief, the glass foil is positioned over a mould, whose shape has to be replicated in negative, and closed inside a muffle. The glass is slumped with dimension larger than the mould, as it also acts as membrane to divide the muffle chamber in two parts: the pressure is exerted by vacuum suction from the lower part. This setup has been patented (TO2013A000687, 12/08/2013). At the end of the process, the slumped glass has to be trimmed to the final dimension, 200 x 200 mm^2. In the following paragraphs I describe the process setup.

5.1.1 The furnaces at INAF-OAB

All thermal slumping tests in this research were conducted in the thermal furnaces installed at INAF-OAB. Three furnaces are available (Fig. 5.1), from Teknokilns: one small for tests and two identical of larger size (SN079770 purchased in 2009, named oven A, and SN120723 purchased in 2012, named oven B).

The small oven (model VV00) has an internal volume of 0.5 m $\times$ 0.5 m $\times$ 0.3 m. It can reach a max temperature of 950 °C, using two sets of resistors located at the top and at the bottom of the oven cavity. The maximum power used by the oven is 6 kW. A single internal thermocouple controls the temperature inside the oven.

The big oven (model 140/60) has an internal size of 1.3 m $\times$ 1.3 m $\times$ 0.6 m. It can reach a maximum temperature of 950 °C, using five different heating zones, each one equipped with its own K-type[1] thermocouple. The maximum power used by the oven is 50 kW, divided among the

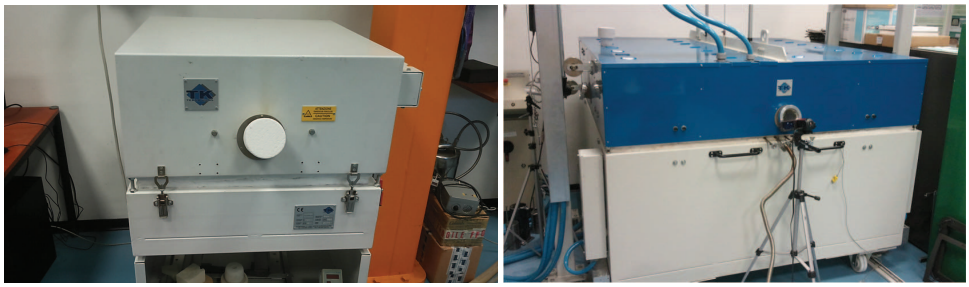

Figure 5.1: *: The types of furnaces operated at INAF-OAB. Left: The small furnace. Right: One of the two large furnaces.*

different heating zones. A sector consists of the lateral electrical resistors (supplied with power of 17 kW) and the other sectors are represented by the upper and lower resistors, both composed by two separate heating elements, a central one (supplied with power of 9 kW) and a lateral one (supplied with power of 7.5 kW) following the perimeter of the oven. The heating zones can be switched on and off separately, depending on the thermal cycle adopted: this can be set on the oven controller (model TC-M2). The Bentrup WinControl program is then used to supervise the oven process on a PC.

5.1.2 The thermal cycle

A thermal cycle for slumping is typically divided into a heating time, to reach a maximum temperature called *slumping temperature* or *soaking temperature* (somewhat higher than the annealing temperature); a holding time at the soaking temperature, a cooling time at controlled speed down to the strain temperature, and finally a faster cooling time down to room temperature. The thermal cycle has to be set in such a way to reduce the temperature gradient present in the mould, especially during the cooling down phase, when the glass foil freezes its shape. In the cooling phase however, the edges of the mould cool down faster than its centre. Having been all the cylindrical slumping cycles carried out in the big ovens, FEA was previously performed [Proserpio Ph.D. thesis 2011] to define the best use of the different heating zones during the thermal cycle. It was therefore defined that the central top and bottom resistors should be used during the heating and holding time, while the lateral resistors is preferable during the cooling time, below the annealing temperature. Table 5.1 reports the thermal cycle, as optimised during this thesis. Compared to the previous one [Proserpio Ph.D. thesis 2011], the soaking time was set 2 h longer to reduce the sag error, the cooling cycle was divided into two steps of different cooling rate, before and after the strain temperature, and the cooling rate was lowered from 9.6 °C/h to 2.5 °C/h in the region from the annealing to the strain temperature. The latter was found to reduce the mid frequency errors, as in this region the cooling ramp has to be sufficiently slow to let the glass foil to relax and release internal stresses.

5.1.3 Temperature monitoring inside the muffle

The big oven is equipped with five internal thermocouples, positioned very close to the oven resistors. During Proserpio's Ph.D. thesis, the temperatures values of the internal thermocouples were routinely recorded together with the image of the interference fringes between the glass foil and the mould (see paragraph 5.2). Actually, the temperature inside the muffle can be different, and gradients among the different parts of the mould can be present. In Proserpio's Ph.D. work, tests were carried out with external thermocouples positioned at the bottom and lateral side of the

[1] A K-type thermocouple uses the junction of Ni-Cr and Ni-Al to measure in the temperature interval -200 ÷ 1260 °C.

Table 5.1: *: The final thermal cycle, after the entire optimisation carried out in this thesis.*

Step	Temperature [°C]	Time	Speed [°C/h]	Heating zone ON
1	to 750	11 h	66.4	central top and bottom
2	@ 750	4 h		central top and bottom
3	to 722	4 h	7	central top and bottom
4	@ 722	2 h		central top and bottom
5	@ 722	10 min		lateral
6	to 670	21 h	2.5	lateral
7	to 600	8 h	8.8	lateral
free cooling				

mould, but only on a flat K20 sample (and a flat muffle). These measurements were used to tune the thermal cycle, and to define that the lateral resistors should be used during the cooling cycle below 722 °C. This setting was unchanged during my research (Table 5.1). Nevertheless, after this test, the mould temperature was never measured on the cylindrical K20 used for the production of the curved glass foils. Fig. 5.2 plots the values registered by the internal thermocouples T0 (blue curve) and T4 (green curve), measuring the temperature of the top central resistors and the lateral one respectively, during a typical cycle for the production of the cylindrical glass mirrors. A drop in the recorded value for T0 appears in the cooling phase below the annealing temperature, where the central top resistors is switched off and the lateral resistors starts driving the cooling cycle. To clarify the effect of this drop at the level of the cylindrical mould I have modified the cylindrical muffle to house the heads of two thermocouples, and measure the temperature of the mould at the bottom and lateral sides (Fig. 5.3).

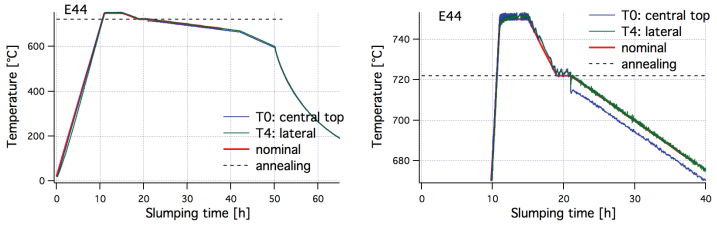

Figure 5.2: *: Temperature values registered by the oven internal thermocouples during the slumping of the E44 glass foil in oven-A: T0 (blue curve) is the temperature registered by the bottom thermocouple, and T4 (green curve) the temperature of the lateral thermocouple. The red curve represent the nominal temperature. Left: the entire cycle. Right: a zoom near the reach of the annealing temperature. From this graph we can see that a temperature difference of about 5 °C is registered in the oven.*

The thermocouples were calibrated to give the same temperature value when being at the same temperature: to this end, I have inserted them in a stainless steel block with two holes to host the thermocouple'e heads and I have measured their reading during a thermal cycle identical to the one used for the glass slumping. Fig. 5.3-right shows that the maximum temperature gradient inside the muffle is $\sim$ 2-3 °C during the soaking time and the first part of the cooling time, until the reaching of the annealing temperature. During this period, the lateral part of the mould is colder than the bottom part, consistently with the fact that the driving resistors are the top and bottom ones. In the cooling phase, below the annealing temperature, the driving resistors is set to be the lateral one, to heat the lateral side of the mould while this would cool faster than the core part. The reading of the two external thermocouples gets equal, showing that no gradients are presents in the mould in most critical part of the cycle, when the cylindrical shape of the glass foil will be frozen. This clarify that the difference of about 5 °C, between the internal thermocouples T0-bottom and T4-lateral (Fig. 5.2), is not an issue, giving confirmation to the setting adopted in Proserpio's work. Anyway, the presence of the external thermocouples is essential when using different ovens, whose internal thermocouples may be differently calibrated. Preliminary tests,

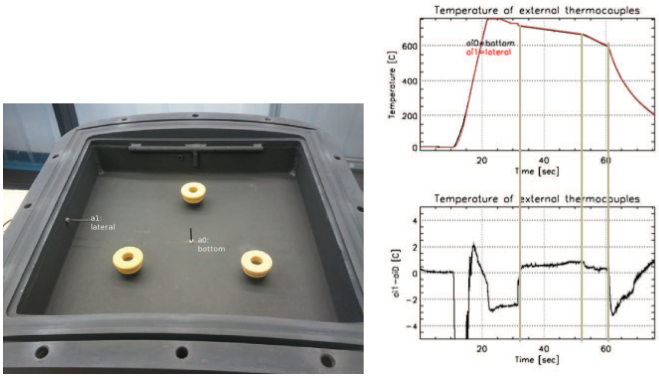

Figure 5.3: *: Left: The external thermocouple heads, entering the muffle, to measure the temperature of the bottom (ai0) of lateral part (ai1) of the mould. Right: The thermal cycle of the glass foil E44, as measured by the external thermocouples ai1 and ai0, together with the plot of their difference. This graph shows that the temperature difference between the bottom and lateral part of the mould is almost zero in the cooling region from 722 to 600 °C, very different from the 5 °C difference registered by the oven thermocouples. This value is registered on a slumping with a closed muffle configuration, in particular with the thick closed cover (see paragraph 5.2.1).*

using the second oven (oven-B) installed at INAF-OAB, showed that the slumping results are different, even when using the same parameters, due to small differences in the calibration of the ovens. Precise calibration with external thermocouples is therefore essential to transfer the process to different ovens.

5.1.4 The pressure control system: open and closed loop

To force the glass foil to come in contact with the mould, a differential pressure is applied in the two chambers of the muffle. A rotative vacuum pump is connected to the lower chamber of the muffle and the vacuum pressure is controlled, either in open or closed-loop system (Fig. 5.4). A capacitance-based manometer (Baratron valve 626B) is inserted in the air flow: this system measures changes of pressure/vacuum as changes in capacitance between the sensor's diaphragm and an adjacent electrode disk. It works in the range from 1000 Torr (1360 g/cm^2) to 0.10 Torr (0.14 g/cm^2). It provides a 0-10 VDC analog output, linear with pressure, with a 0.25% accuracy. Its signal is fed to a pressure control module from MKS (MKS-205E): it can keep the desired pressure constant, by feedback to the control valve MKS-248, thus enabling a controlled gas flow (closed-loop configuration).

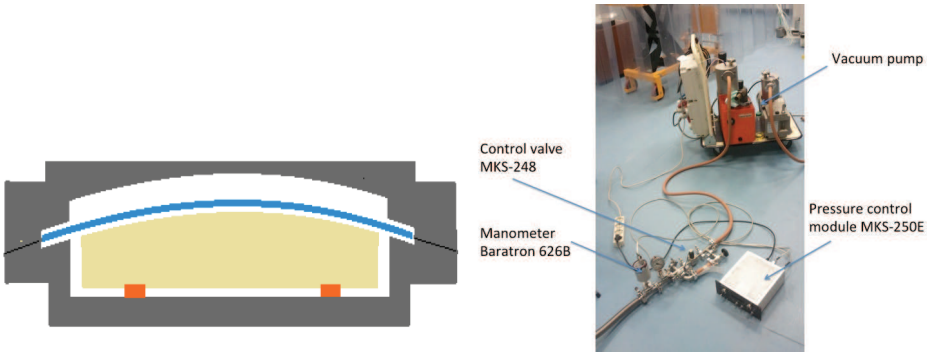

Figure 5.4: *: Left: A flat glass foil is positioned over a cylindrical mould, inside a stainless steel muffle. With this setup, the glass itself can act as a membrane that allows the pressure application. Right: The pressure control system.*

Before my work, the pressure control was always kept in closed-loop, but no signal was recorded from the control module. Actually, it was noted that the pressure value was used to decrease during the cooling cycle. In order to better understand this behaviour, in early 2015 I have connected the control module 205E to the 9205 module from National Instrument, and the external thermocouples to the NI-9211 module: data acquisition were performed with the DaQ system. From these measurements, I have recognised that the pressure system was not operating in closed loop, as the pressure decreased just after the start of the cooling cycle (Fig. 5.5).

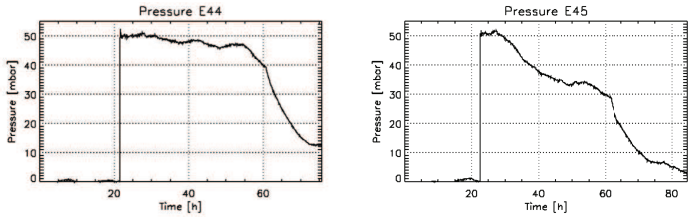

Figure 5.5: *: Pressure value reading during the glass slumping, before the maintenance performed in early 2015. The two slumping cycles were performed in nominal closed loop with P = 50 g/cm^2, but clearly the pressure was not maintained constant. Left: E44. Right: E45.*

To solve the problem, in early 2015 I did an accurate maintenance of the system:

1. all tubes, valves and connectors were dismounted and cleaned with alcohol, the tap connector was provided with a better sealing and all the o-rings were greased with vacuum grease. This maintenance considerably reduced the leakage of the system: I have opened the vacuum suction going from 990 mbar to 8 mbar, and, after closing the tap I have measured this level of vacuum maintained for almost 5 h, compared to few seconds before the maintenance.

2. the capacitance manometer was mounted more distant from the air flow in order to be less sensitive to the air temperature. The manometer, in fact, is affected by the temperature. Since no pressure change were measured when starting the thermal cycle and reaching the 750 °C inside the furnace, I concluded that the temperature dependence has a little impact on the pressure measurement.

3. the company "Gambetti srl" was commissioned to do a cleaning and recalibration of the MKS-248 valve.

After this maintenance, the pressure value were correctly maintained as set (Fig. 5.6 and 5.7). Note that the pressure reading for E52, slumped in open loop after the maintenance performed, is very similar to the one of E44, slumped in closed loop before the maintenance: this is a confirmation that the pressure system was not correctly functioning before this work.

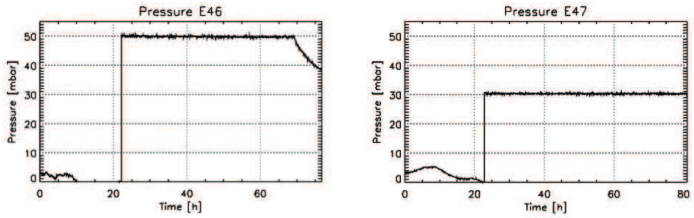

Figure 5.6: *: Pressure value reading during the glass slumping, after the maintenance performed. Left: E46 was slumped with P = 50 g/cm^2 in closed loop. Right: E47 was slumped with P = 30 g/cm^2 in closed loop. These graphs show that the closed loop is efficiently maintaining the pressure value constant.*

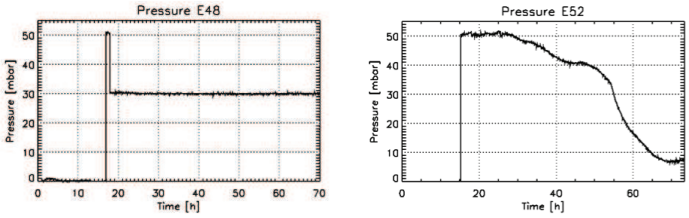

Figure 5.7: *: Pressure value reading during the glass slumping, after the maintenance performed. Left: E48 was slumped with P = 50 g/cm^2 in closed loop for 1 h and P = 30 g/cm^2 in closed loop for the following time. The pressure is kept constantly equal to the setting. Right: E52 was slumped with P = 50 g/cm^2 in open loop. The pressure behaviour is very similar to the one shown in Fig. 5.5, performed in closed loop before the maintenance, confirming that the pressure system was not working properly before the maintenance.*

5.2 The interference fringes recording during the slumping

The evolution of interference fringes in the glass-to-mould gap during the thermal cycle is an efficient monitor of the slumping behaviour. This possibility was already developed in Proserpio's work. Two out of the three furnaces are equipped with windows to illuminate and inspect the furnace inside and collect the relative images during the thermal cycle (Fig. 5.1). To this end, the muffle is kept open, with only a thin cover to shield the direct heat of the resistors to the glass (Fig. 5.9-left). During my research, I used this configuration for many thermal cycles, in order to harvest as information as possible on the effect of a parameter change. A selection from the interference fringes images of the glass foil E5, during the slumping, is reported in Fig. 5.8. The E5 glass foil was slumped on a old K20 mould (MK20-10), whose surface was damaged from previous slumping tests: the consequence is the presence of a pattern in the interference fringes, witnessing mid-frequency errors in the final glass shape. Nevertheless, from the images it clearly appears that a soaking time longer than 2 h was needed in order to bring the glass foil into full contact with the mould (see paragraph 5.1.2). Another interesting information acquired from these images is the reappearance of the interference fringes during the cooling cycle around 690 °C, which denotes the retrieving of the glass rigidity close to the strain point. For this reason, the cooling rate was diminished from 9.4 °C/h to 2.5 °C/h until the strain temperature 670 °C. (see Table 5.1)

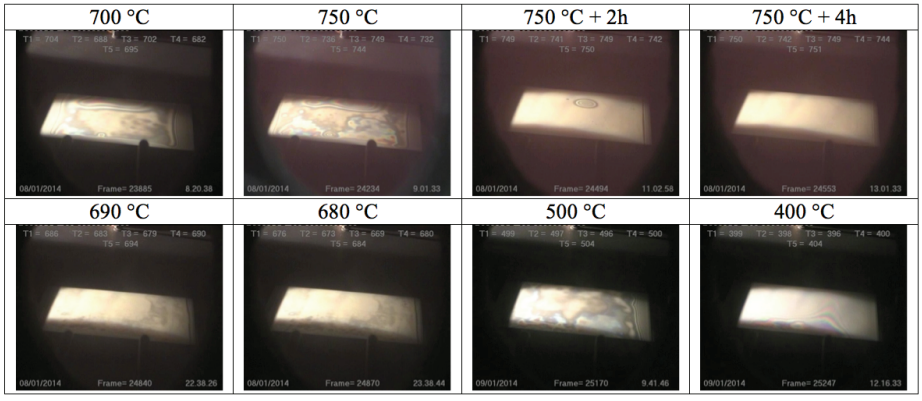

Figure 5.8: *: Interference fringes between the glass and the mould, recorded during the slumping cycle of the E5 glass foil, slumped with mould height h = 2.5 mm.*

5.2.1 The muffle: thick-close or thin-open cover

The muffle, made of AISI 310 stainless steel, is placed in the middle of the furnace, to contain the mould and the glass foil. It enables the pressure application by using the glass foil as a membrane to divide the muffle in two chambers (Fig. 5.4-left). It also has the effect to create a clean and uniform environment for the slumping. Clearly, a closed muffle would be preferable to minimise the thermal gradients. Nevertheless, an open muffle is necessary to monitor the glass during the slumping with the interference fringes (paragraph 5.2). Three different muffle configurations were used during my Ph.D. work. The first one (Fig. 5.9-left) includes a thin open cover, to protect the glass foils from the direct heat from the resistors: it was used during Proserpio's work and the first part of my research. The other two configurations (centre and right of Fig. 5.9), where the muffle is closed, are meant to minimise the thermal gradients inside the muffle. The central one uses a thick cylindrical cover, the right one the same thin cover used in the open configuration (after cutting its corners in order to fit into the space created by the handles). The advantage of the thick cylindrical cover is a better gradient minimisation, due to both the larger thickness and the inner cylindrical profile. The disadvantage is a more critical procedure in the setup preparation, when the glass foil has to be kept in place for the First Contact peeling; this was anyway solved by minor modifications in the setup preparation. Therefore, the last configuration, with the thin closed cover, was used only as intermediate solution before solving the small problems created by the middle configuration, judged to be the optimal.

Figure 5.9: *: The muffle inside the large oven. Left: open configuration to enable the interference fringes recording; only a shield is present. The glass is clamped with a cylindrical frame, visible under the thin shield. Center: the muffle is closed with its own cylindrical cover. Right: the muffle is closed with a cylindrical frame and a thin flat cover.*

In paragraph 6.6.3, the results of the slumping with these three configurations are compared.

5.3 Glass and mould preparation before the slumping

A good replication of the mould shape onto the glass foil can be realised only if the two surfaces are accurately cleaned from any possible contaminant. Two cleaning actions are performed: first, cleaning with solutions to remove organic contaminations and/or residuals from the previous run, then stripping of a peeling layer to remove the dust.

5.3.1 Cleaning of the mould and glass foil

The glass foils and the mould surfaces were routinely cleaned already in Proserpio's work, before their insertion into the furnace for the slumping cycle: a detergent was used (Amber Clean GC95L) to remove organic contaminations, and distilled water was used for the rinse. While this was enough on the glass side, I have found that this was not sufficient to remove the residuals left on the mould by the previous slumping cycle. In fact, in any slumping cycle the glass and mould surfaces are painted with a First Contact coating, to be stripped just before bringing the glass into contact with the mould inside the muffle, hence removing the dust present on the two surfaces.

The First Contact is guaranteed to be a residual-free paint [Web reference: FirstContact] and we have proven this on the smooth surface of the glass foil. Anyway, on the mould side, several peaks are present [Salmaso et al. 2014] which make the First Contact more difficult to be stripped

without residuals. Therefore, after the slumping, the mould surface needs to be cleaned more efficiently than with the sole detergent. With the introduction of the moulds MK20-20 and MK20-20B, with surface more homogeneous than the old MK20-10, I could define a cleaning protocol effective at removing the residuals entrapped into the rough mould surface: the protocol foresees cleaning with Amber Clean, acetic acid and hydrogen peroxide [Salmaso IR15-2014], [Salmaso et al. 2015]. Fig. 5.10 shows the PSD obtained from AFM measurements done on the mould, to compare the surface after the annealing cycle (blue curve), before any slumping, and after the slumping of a glass foil: the measurements taken on the un-cleaned (red curve) and cleaned (green curve) mould surface show that my cleaning protocol is effective at returning the pristine surface quality.

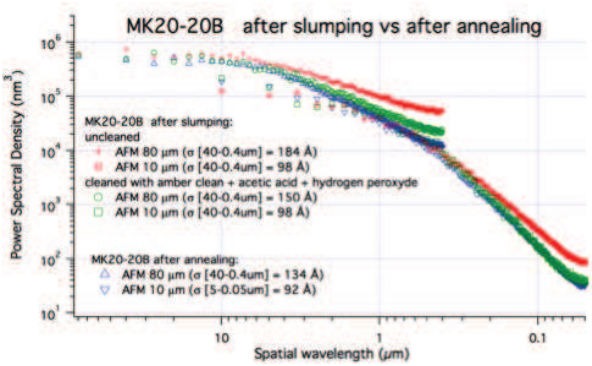

Figure 5.10: *: PSD from AFM 80 and 10 μm scans on MK20-20B. The blue curve is the PSD for the mould after the annealing, that is before any slumping and any use of First Contact; the red curve is the PSD after a glass foil slumping cycle but without the cleaning protocol; the green curve is the PSD after the slumping and after the cleaning protocol. This last PSD matches the PSD of the pristine mould, proving that the cleaning is effective at removing residuals.*

This cleaning protocol was found effective at removing, residuals entrapped in the mould surface, which were seen as repetitive defects in consecutively slumped glass foils, when the sole Amber Clean was used (Fig. 5.11 a and b).

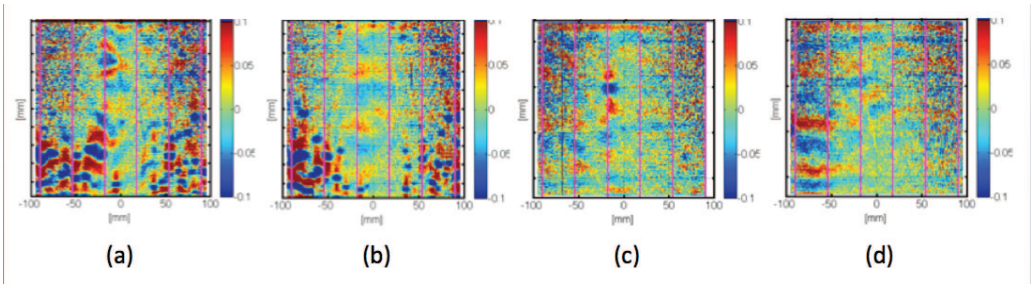

Figure 5.11: *: CUP maps of consecutively slumped glass foils, after removing the Legendre polynomials up to the 8th order. a) and b): foils slumped on MK20-20, before the introduction of the new mould cleaning protocol; c) and d): foils slumped on MK20-20B, after the introduction of the new mould cleaning protocol. Credits: CUP maps by M. Civitani.*

5.3.2 First Contact application and stripping

Dust contamination, trapped within the glass and the mould during the slumping, is a very serious problem, since it prevents the close contact foil/mould and so affects the final optical performance. To avoid this risk, the preparation of the muffle enclosing the mould and the foil for the

slumping is performed inside a ISO5 clean room. Moreover, in order to remove the dust from the glass and mould surfaces, a polymeric film (First Contact by Photonic) is applied on both. A peeling machine, realised at INAF-OAB for this purpose, is inserted in between the two surfaces to remove the films just before drawing the glass into contact with the mould (Fig. 5.12).

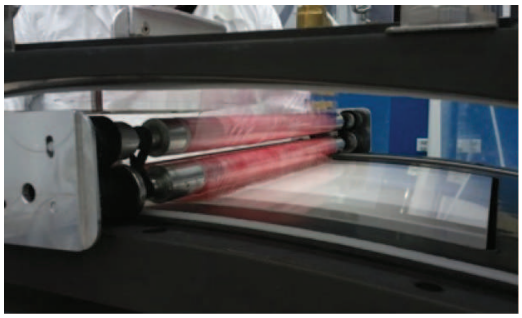

Figure 5.12: *: The peeling machine is inserted between the mould (bottom surface) and the glass (top surface) to remove the dust trapped in the paint film. This procedure is done just before drawing the glass in contact with the mould*

5.4 The cutting of a curved glass foil

After the slumping, the glass foil has to be cut from a 340 mm $\times$ 340 mm size to 200 mm $\times$ 200 mm. To this end, the glass foil is positioned over a convex cylindrical cutting mandrel. A preliminary cut is performed to a 230 mm $\times$ 230 mm size. Our cutting tool is a MDI patented scribing wheel, named Penett, which creates a grove of 80%, and more, of the glass thickness (Fig. 5.13-left). After the preliminary cut, the glass can be clamped on a cylindrical template (Fig. 5.13-right). The same MDI tool is used to perform the final cut to 200 mm $\times$ 200 mm.

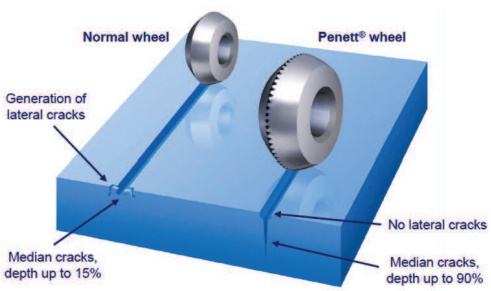

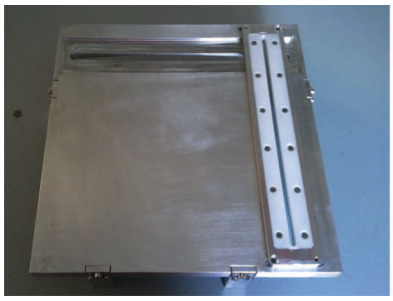

Figure 5.13: *: Left: The MDI Pennet's wheel, credits: MDI. Right: a cylindrical template, realised at OAB - workshop, during Proserpio's Ph.D. thesis.*

5.5 Glass foil cleaning after the slumping

After the slumping and the cutting, the glass has to be cleaned. This is requested as residuals on the glass optical side may cause diffraction of soft X-rays and affect the results of the X-ray tests. During Proserpio's Ph.D. work, the cleaning post-slumping was performed only using a detergent (Amber clean). Anyway, I have found that the AFM measurements were strongly affected by the presence of residuals that could not be removed with acetone or alcohol (Fig. 5.14-left). They probably are First Contact residuals left on the mould surface and entrapped in the glass surface during the slumping: they could not be removed by mechanical action with our standard cleaning

procedure (optical paper soaked with amber clean, rinsed with distilled water, and dried via an optical paper soaked with acetone). First Contact is claimed to be a residual free paint. I have verified that this is correct on a glass surface, by inspection with the AFM. The same test is difficult to be performed on the Zerodur K20 mould, as the typical peaks on the semi-cristalline structure of the keatite make difficult to distinguish the K20 peaks form the possibly remaining First Contact residuals. Anyway, the PSD shown in Fig. 5.10 shows that some residuals are probably left on the mould surface. The residuals on the slumped glasses, are mostly seen as peaks in the AFM scan of 10 μm range (Fig. 5.14), and thereby affecting the roughness in the high spatial frequency range. The heights of these residues ranged 5 to 40 nm, variable from foil to foil; as of now, the reason that determines the difference in heights is unknown. To remove these residuals, I have carried out a test campaign, resulting in the definition of a glass cleaning protocol after slumping with hot hydrogen peroxide SalmasoIR012013.

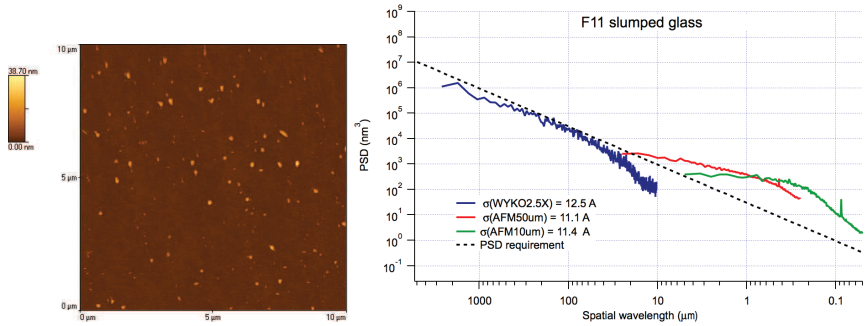

Figure 5.14: *: Left: a 10 μm AFM image of a AF32 slumped glass, namely the F11 glass, shows the residues present on the optical surface after the slumping. The residuals height is up to 40 nm in this case. Right: The PSD of the F11 slumped glass shows that the effect of these residuals is to bring the surface PSD out of specification in the high frequency region.*

The developed cleaning protocol was applied to the F11 slumped glass, whose surface was contaminated by residuals with heights up to 40 nm. It was dipped for 1 h in a hot 35 % solution of H_2O_2, then rinsed in distilled water and dried for 1 h in laminar airflow. The AFM images were recorded before and after the H_2O_2 treatment (Figs. 5.14 and 5.15). Some residual were still detected on the glass, but they could easily be removed by mechanical action with an optical paper soaked with acetone.

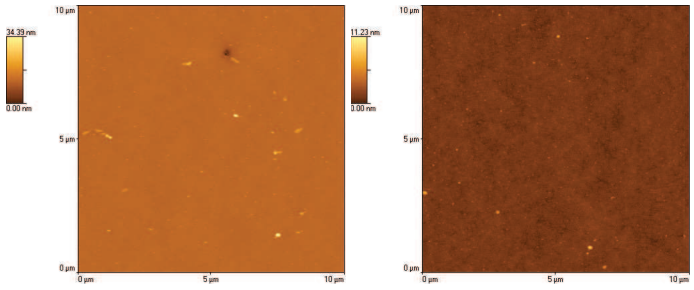

Figure 5.15: *: AFM scans of the F11 slumped glass foil after (left) cleaning treatment in hot H_2O_2. Mechanical action with an optical paper soaked with acetone (right) was also necessary after H_2O_2. The final result is a surface completely free from contaminations.*

The PSD of the F11 slumped glass, before and after cleaning, is shown in Fig. 5.16, compared with the results achieved on the 1 $\times$ 1 cm slumped test sample, with code F2. These data show that the removal of contamination operated by the etching action of the H_2O_2 has brought the

roughness back to the one of the brand new glass foil and close to the PSD specification. This protocol was routinely applied for all the glass foils.

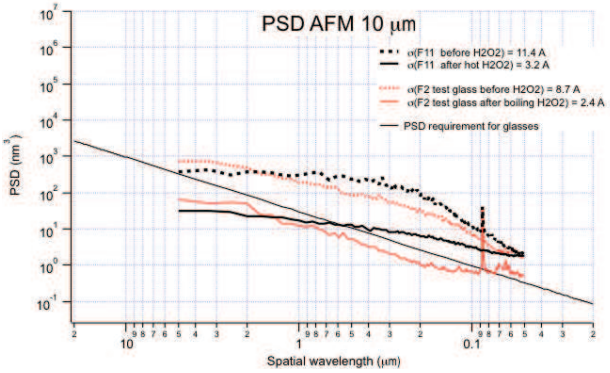

Figure 5.16: *: PSD comparison of the F11 slumped glass and F2 slumped sample (1 × 1 cm) before cleaning and after cleaning with hot H_2O_2 respectively. After cleaning, the surface topography is back within the PSD tolerance.*

CHAPTER 6

Experimental results: hot slumping of thin glass foils on Zerodur K20

6.1 Introduction: a brief summary of the experimental work with Eagle glass foils

As described in Section 3.8.5, different glass and mould materials were used during this research. Fused Silica slumping moulds were changed to Zerodur K20 for its property of not sticking to the glass during the thermal cycle. The glass type used in the first experiments was the Schott D263, the same used for HEFT [Koglin et al. 2004] and NuSTAR [Craig et al. 2011]. Anyway, the change to Zerodur K20 drove also the change of the glass type to the Schott AF32, which better matches the CTE of the slumping mould material (see Sec. 3.8.5). A prototype, the POC#2, was realised in early 2013 using these slumping materials (Zerodur K20 and AF32). Newly procured BK7 integration moulds, with much more accurate Wolter-I profiles with respect to the previous Metapore moulds, were used for the integration of these glass foils. The module was tested in X-ray at the PANTER facility in Munich, and the achieved result was $\sim$ 22 arcsec HEW, measured with full illumination in-focus at 0.27 keV [Civitani et al. 2014].

To improve this result, I have modified various parameters, including the glass material, the thermal cycle, the pressure setting and the muffle configuration; all the experiments were performed using the Zerodur K20 as slumping mould material. Nevertheless, three different slumping moulds were used, in order to improve the performance of the slumped glass foils, especially in terms of roughness and mid-frequency errors. They are hereafter named:

- MK20-10: this is the mould used for the production of the POC#2. Its surface was damaged by several thermal cycles (Fig. 6.4). Also POC#4 was produced with glass foils slumped on this mould.
- MK20-20 with good surface quality. The POC#3 was produced using this mould.
- MK20-20B, also with good surface quality. The glass foils with the best quality were produced using this mould; some of them will be integrated into the next prototype, POC#5.

This Ph.D. research can be divided into six steps, with different glass-to-mould combinations and slumping parameters. These steps are described in the following sections:

1. AF32 on MK20-10: section 6.3, from AF32 to Eagle XG
2. Eagle on MK20-10: section 6.3, from AF32 to Eagle XG
3. Eagle on MK20-20: section 6.5, glass foils for the POC#3
4. Eagle on MK20-10: section 6.6, glass foils for the POC#4
5. Eagle on MK20-20B: section 6.7, glass foils for the POC#5
6. Eagle on MK20-20B: section 6.8, glass foils with lower roughness

In Section 6.9, I summarise the results obtained in each step, highlighting the positive trend of the key parameters adopted to measure the glass foils quality.

Hereafter, a brief summary of the research is presented.

After the production of the POC#2, I have changed the glass material to Corning Eagle XG, increased the soaking time, and modified the mould height to start the glass-to-mould contact at room temperature (Sect. 6.3). I have found that these conditions were effective at reducing the PV and the profile variability from glass to glass. While optimizing the process with MK20-10, the newly polished MK20-20 was produced by Hellma Optics (Jena, Germany). Unfortunately, the optimised slumping process could not be transferred directly from MK20-10 to MK20-20, as the different shear of the glass foil on the rough (MK20-10) or smooth (MK20-20) surface generated different technical issues to be solved (Sect. 6.5). In particular, starting the glass-to-mould contact at room temperature, optimal with the rough mould surface of MK20-10, was found to cause air bubble entrapping with the smooth mould surface of MK20-20, because the higher glass-to-mould contact left a smaller gap for the air to flow out of the contact area during the slumping cycle. To avoid air bubbles, I have applied the pressure at room temperature instead of at the slumping temperature: while this is effective at avoiding air bubbles, this led to an increase in PV with respect to the improved results already obtained on MK20-10 after the POC#2, because the PV of the slumped glass foils integrated into the POC#3 was comparable with the one of the POC#2 glass foils [Civitani et al. 2014]. The overall HEW of the POC#3, however, was found to be higher than the POC#2 ($HEW_{POC\#3}$ = 30 arcsec, $HEW_{POC\#2}$ = 22 arcsec): this was most likely due to asymmetric deformations of the K20, due to preliminary slumping cycles that suffered from air entrapping in the central region [Salmaso et al. ICSO2014] and from some deformations in the slumped glass foils due to entrapped dust during the slumping. Nevertheless, the best HEW value, in a portion of the module, was 5.5 arcsec at 0.27 keV [Civitani et al. 2014], thanks to the use of the new K20. Moreover, the impact of the roughness in the 0.27-1.49 keV range was considerably reduced with respect to the previous prototypes, thanks to the better surface roughness of the MK20-20.

The lesson learnt from the POC#3 was that a further work was necessary to reduce the PV of the slumped glass foils. I have therefore increased the soaking time over the 4 h, used for the POC#3 glass foils production. Before reaching the necessary decrease in PV, a glass foil stuck onto the K20 surface. Despite the problem, this gave a further insight into the K20 properties, stating an upper limit of working conditions to avoid the mould degradation. A rework of the MK20-20 mould was necessary indeed. The re-polished mould was named MK20-20B. While the MK20-20 was re-worked, a thorough slumping process optimization was carried out on the MK20-10 mould, to the aim of reducing the PV, the mid-frequencies and the roughness (Sect. 6.6). The mould height was optimized via Finite Element Analysis and experimental validation; the muffle was closed to reduce the thermal gradients; the cooling rate was decreased; a new protocol for cleaning the mould surface before slumping was introduced, in order to avoid repetitive spots at subsequent slumping cycles. The best glass foils produced on the MK20-10 during this research activity were integrated into the prototype POC#4. Unfortunately, this prototype suffered from an integration error: we expected an HEW of about 15 arcsec from metrological data, but the result in X-ray was much worse [Civitani et al. 2015].

Before producing the slumped glass foils for the last prototype, POC#5, I have performed a thorough optimisation of the pressure system (see Sect. 5.1.4). Ten glasses were slumped in the best process conditions defined so far (Sect. 6.7): the HEW expected from metrological data, after a simulation of a perfect integration, are between 2 and 3 arcsec, very close to the 2 arcsec value allocated for the slumped glass foils (Section 3.9). This result has to be compared with the ~ 7 arcsec computed in the same way for the glass foils of the POC#2. Height of these glass foils will soon be integrated into the POC#5, and the prototype will be tested in X-ray at the PANTER facility, as soon as a measurement slot will be available (at the moment PANTER is very busy with the final calibration of e-ROSITA, to be launched soon). A group of glass foils was also selected for the X-ray Surveyor test at SAO/CfA (Section 9.3).

Finally, the most recent success is the development of a process able to maintain a low roughness of the optical surface of the slumped glass foils, while preserving the result already obtained in terms of mid-frequency (Sect. 6.8).

6.2 Materials characterization

6.2.1 Roughness characterisation of the as delivered glass foils

In my Ph.D. research different types of glass foils were used, produced by different companies and with different processes (see Sect. 3.5). Schott uses the down-draw forming process, while Corning adopted the fusion forming process. A better thickness uniformity is reported for the fusion process, because the glass surface is formed contactless, while rollers are used in the down-draw process [Milillo 2012]. This difference can be inspected via interference fringes under sodium light (Fig. 6.1). I have also measured a more isotropic roughness over the mm scale with the WYKO interferometer for the Corning glass types: the measurements in orthogonal directions give different rms for the Schott glasses, while they are very similar for the Corning glasses (Fig. 6.2). In order to avoid the formation of longitudinal mid-frequencies errors caused by thickness non-uniformities, it is a common procedure to position the glass with the direction of smaller thickness variation, parallel to the optical axis.

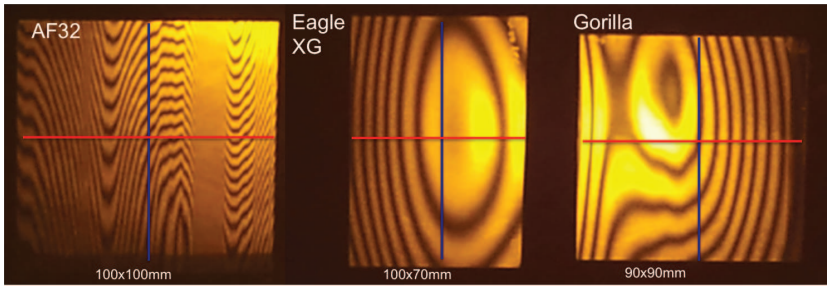

Figure 6.1: *: Interference fringes seen in sodium light for the Schott AF32 and Corning Eagle XG and Gorilla glasses. The blue vertical and red horizontal lines correspond to the direction of the WYKO scans in Fig. 6.2. Corning glasses exhibit more spaced fringes, hence more uniform glass thickness (each fringe equals $\lambda/2n$ in thickness variation). All these glass types have approximately the same roughness.*

In Fig. 6.3, the roughness of various glass types, as measured with the WYKO interferometer and the AFM, is compared: the WYKO measurements were always taken in the direction of minimum thickness variation. All measured PSDs are compared with two reference PSDs, shown as dashed lines. The dashed black line in Fig. 6.3 is derived from the demand that the HEW degradation caused by X-ray scattering at 1 keV and 0.7 deg incident angle is below 1 arcsec. This PSD requirement function was computed using the analytical model described in Sect. 4.4.5 [Spiga 2007]. Using this formalism, one is able to derive the tolerable PSD of a surface to not exceed a given HEW. The dashed pink line in Fig. 6.3, in contrast, represents the model PSD of

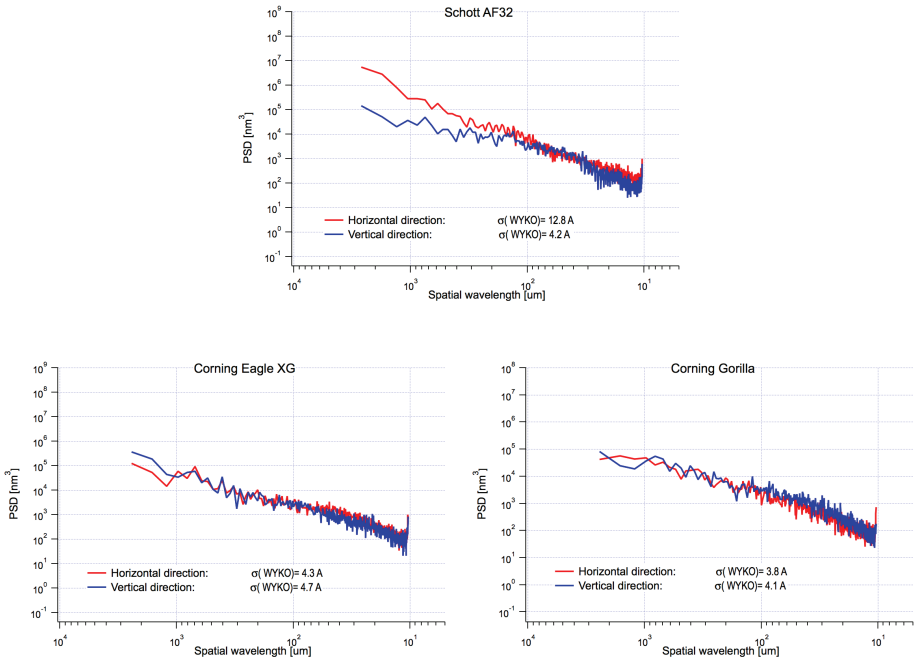

Figure 6.2: *: PSD from the WYKO data taken in the horizontal and vertical directions shown in Fig. 6.1. These graphs show that Corning fusion process produces glasses with more isotropic surfaces.*

brand new glass foils (computed by averaging the roughness data of the glass foils), compliant with a HEW degradation $\leq$ 1 arcsec up to 6 keV, as requested in the ATHENA case.

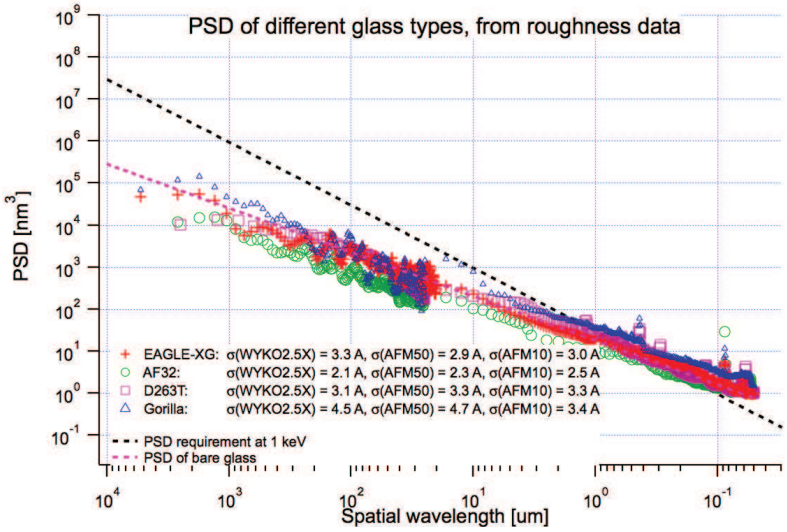

Figure 6.3: *: PSD from WYKO and AFM data for Schott AF32, Schott D263, Corning Eagle XG, and Corning Gorilla. WYKO data are taken in the direction of minimum thickness variation.*

6.2.2 Comparison of Zerodur K20 moulds

In my Ph.D. activity, three different slumping moulds made of Zerodur K20 were used: MK20-10, MK20-20, MK20-20B. The poor surface quality of MK20-10 and the good one of MK20-20 and MK20-20B can be compared in Fig. 6.4. A reflectivity variation is seen for the MK20-10, affecting the slumped glass foils in the millimetre spatial frequencies range. The reduction of these errors in the slumped glass foils could be reached only with the MK20-20 and 20B.

Figure 6.4: *: Visual comparison of the surface roughness of the MK20-10 and MK20-20/20B (size 250 mm × 250 mm). Left) the MK20-10 shows the optical part (200mm × 200mm) with lower reflectivity due to a damaged surface. A damaged texture is also visible on the surface. Right) the MK20-20/20B with uniform, highly reflective surface.*

The characterisation of the as-delivered MK20-20 and MK20-20B is hereafter reported. A full description of the in-coming characterization is reported in [Salmaso IR01-2014] and [Salmaso IR03-2015], respectively.

6.2.3 MK20-20 characterisation

The profiles of the MK20-20 were measured with the LTP. A cylindrical lens, with focal length of 1 m, was inserted in the optical path of the laser, to match the mould curvature and the laser wavefront, improving the alignment accuracy (Paragraph 4.2.4). The measured profiles (shown in Fig. 6.5-left) have amplitude of less than 0.8 μm over 250 mm, with an estimated HEW of 2 arcsec (Fig. 6.5-right), as computed with physical optics [Raimondi & Spiga 2015].

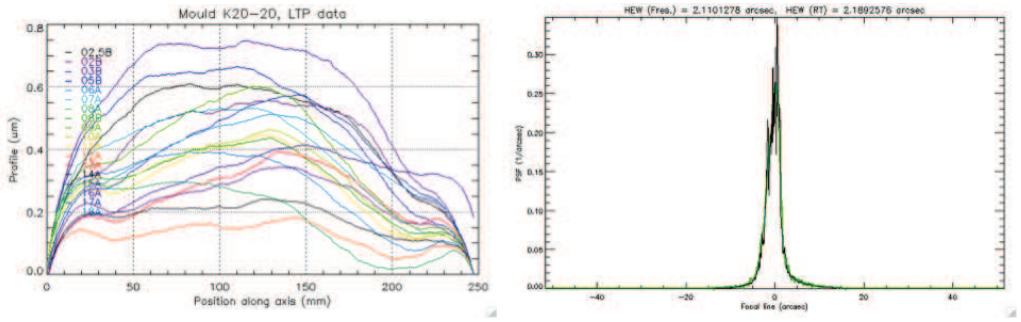

Figure 6.5: *: Profiles characterisation of the as delivered MK20-20. Left: axial profiles measured in OAB with the LTP. Right: expected PSF from the measured profiles: HEW = 2.0 arcsec.*

The roughness was measured with the AFM, available at OAB laboratories (area 10 μm and 100 μm), and the Taylor Hobson interferometer (hereafter named CCI) with the 10× and 50× Mirau objectives, available at MLT (scan area side: 1.5 mm and 0.33 mm respectively). In Fig. 6.6, two AFM scans are presented, showing the typical peaks of the semi-cristalline structure of the K20 material.

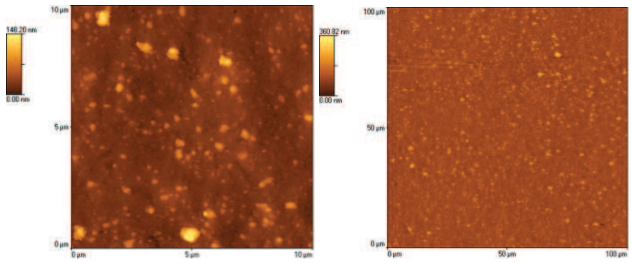

Figure 6.6: *: AFM scans on the MK20-20 mould. Left: 10 × 10 μm scan, rms = 135 Å. Left: 100 × 100 μm scan, rms = 187 Å.*

In Fig. 6.7, the PSDs obtained from all the roughness data are presented, including the roughness measurement performed at Hellma, with a ZYGO interferometer. This graph show that the K20 peaks, visible in AFM scans, were not seen by Hellma, whereas measurements performed with the light interferometer CCI at MLT completely confirm the topography seen by the AFM. As a possible explanation, even if the scan size is very similar (100 μm for AFM vs. 150 μm for the ZYGO 50x), one of the limits of the optical interferometry is the light diffraction, which hides details smaller than $\Delta x = 1.2 f\# \lambda$, where f# = f/D of the objective used (f: focal length, D: diameter of lens). In the present case, the defects seen by the AFM would be completely smoothed out if seen by an objective with $f\# > 8$, yielding an effective image resolution worse than 5 μm.

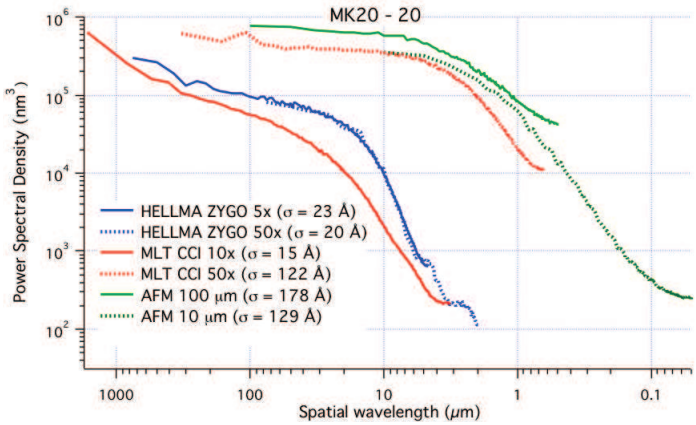

Figure 6.7: *: Roughness characterisation of the as delivered MK20-20. Notice the substantial agreement of the two AFM magnifications and the CCI at the highest magnification. The 10× magnification of the CCI is in quite good accord with the ZYGO 5× of HELLMA. The 50× magnification of ZYGO is in complete contrast with the CCI 50x.*

In Fig. 6.8, the images of the CCI 50× were degraded to a much poorer angular resolution (4.5 μm) than it actually has (0.7 μm). This has been done by convolving a quarter of a true CCI 50× image with the aperture diffraction figure from a circular objective with - hypothetically - f# ≈ 9: the size and the height of the defects is reduced to a very similar value to the one present in the ZYGO 50× images. Also the rms is reduced to a 21 Å, very close to the rms measured with the ZYGO 50× by HELLMA. Finally, the PSD obtained from the degraded image fits nicely the one obtained from HELLMA measurements (Fig. 6.9).

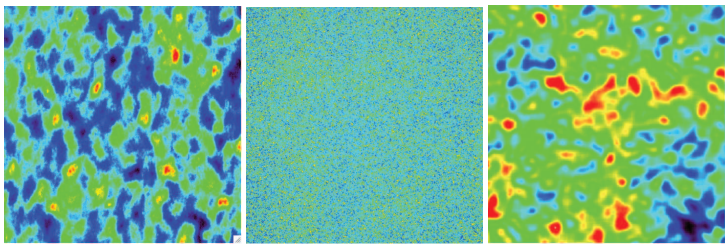

Figure 6.8: *: Roughness scans on the MK20-20 mould. Left: 150 μm scan, taken with the ZYGO 50× Mirau interferometer at Hellma, rms = 22 Å. Center: 330 μm scan, taken with the CCI 50× Mirau interferometer at MLT, rms = 184 Å. Right: one quadrant of the original CCI 50 × image, degraded to a 4.5 μm spatial resolution, rms = 21 Å, to be compared with the image provided by HELLMA.*

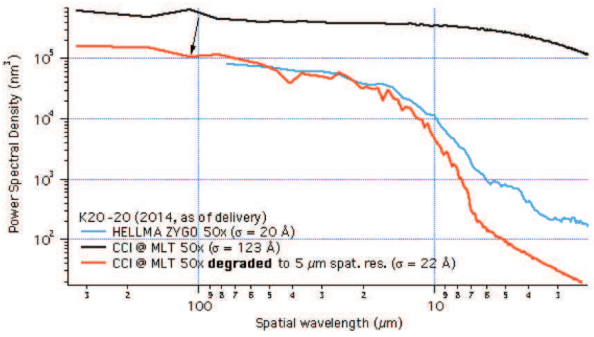

Figure 6.9: *: Degrading a CCI 50× image (black line) to a 5 μm spatial resolution brings the PSD to values (orange line) close to the ones derived from the ZYGO 50× measured by HELLMA (blue line).*

6.2.4 MK20-20B characterisation

The MK20-20B mould was produced by removing the glass stuck onto the MK20-20 (Fig. 6.37), and a ceramic layer 3 mm thick. The polishing was quite difficult and several attempts were done, from September 2014 to April 2015, in order to get results as good as for the MK20-20, delivered in early 2014. Despite the efforts, the mould turned out to be worse in shape, mid-frequencies, and roughness, with respect to the MK20-20. Nevertheless, the mould was received to have the opportunity to implement all the slumping process parameters optimized on the MK20-10, and to produce better performing glass foils in terms of mid-frequencies and roughness.

In Fig. 6.10, the shape characterisation of the MK20-20B is shown. The measured LTP profiles (shown in Fig. 6.10-left) have amplitude up to 1.6 μm over 250 mm, with an estimated HEW of 6.7 arcsec (Fig. 6.10-right), as computed with physical optics [Raimondi & Spiga 2015].

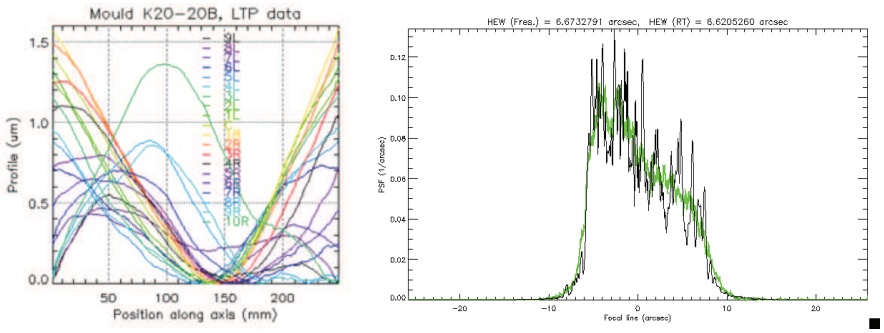

Figure 6.10: *: Profiles characterisation of the as delivered MK20-20B. Left: axial profiles measured in OAB with the LTP. Right: expected PSF from the measured profiles: HEW = 6.7 arcsec. The polishing result of the MK20-20B is of lower quality with respect to the MK20-20 (Fig. 6.5).*

In order to understand the impact of the low- and mid-frequency errors, the HEWs were computed with physical optics as a function of the lateral coordinate of the profiles, both for the LTP profiles (blue curve of Fig. 6.11), and the same profiles obtained after the subtraction of the best fit 8th order polynomial in order to evidence mid-frequency errors (red curve of Fig. 6.11). The results are compared in Fig. 6.11 for the two moulds MK20-20 and MK20-20B. The more recent mould exhibits a much higher contribution from the low-frequency error (blue curves) and a slightly higher contribution from mid-frequency errors (red curves). The two red curves are compared in Fig. 6.12 to expanded Y-scale.

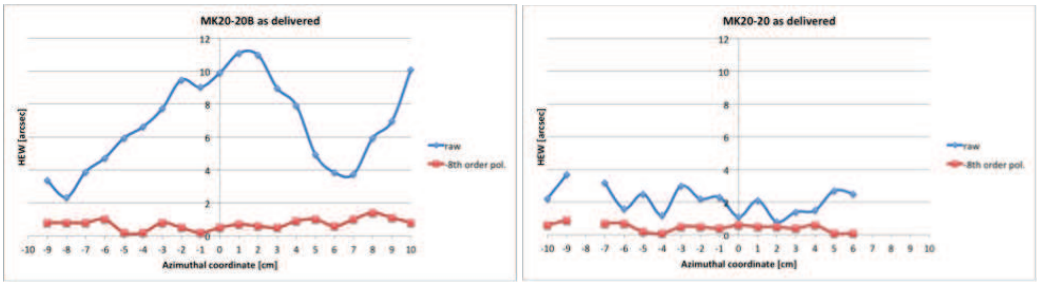

Figure 6.11: *: HEW computed for the MK20-20B (left) and MK20-20 (right) as delivered. The blue curve is for the raw LTP profiles. The red curve is for the LTP profiles after the subtraction of the 8th order best fit polynomial to evidence mid-frequency errors. The more recent mould exhibits a much higher contribution from the low-frequency errors. Mid frequency errors are compared in Fig. 6.12 to expanded Y-scale.*

In principle, the worse low-frequency errors of the MK20-20B would affect on the final quality of slumped glasses. Fortunately low-frequency errors are efficiently corrected with our integration

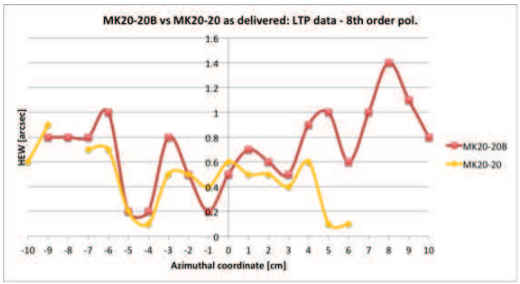

Figure 6.12: *: HEW computed for the MK20-20B (red curve) and MK20-20 (yellow) as delivered: for both curves, the 8th order best fit polynomial was subtracted to see the impact of mid-frequency errors. The more recent mould exhibits a slightly higher contribution from mid-frequency errors.*

method [Parodi et al. 2011]. As for mid-frequency errors, only a slight increment can be observed for the MK20-20B. Assuming a glass foil perfectly replicating the mould surface and integrated with 6 ribs, the resulting HEW (as computed from physical optics on 10 LTP scans) would be 0.4 arcsec, with a maximum value at its central position of 1 arcsec. Hence, the degradation of MK20-20B could be neglected.

The roughness of the MK20-20B was measured with the WYKO, AFM, and MFT at OAB laboratories, and the CCI, in MLT. From Fig. 6.13-left, it appears that the WYKO, the MFT, and the CCI 10× underestimate the surface roughness at high-frequencies: this is in line with what observed for the MK20-20, and it is most probably a consequence of the diffraction limit of the objectives. Rather, the CCI 50× result is in line with the AFM data. Moreover, the WYKO is sensitive to some extent to the mid-frequency errors, being its scan length the largest among the instruments used for surface roughness characterization.

The roughness data of the two moulds as delivered, MK20-20B (red curve) and MK20-20 (green curve), are compared in Fig. 6.13-right. This graph shows a roughness decrease from MK20-20 to MK20-20B of about 30% in the AFM range, but an increase of about 30% at lower wavelengths.

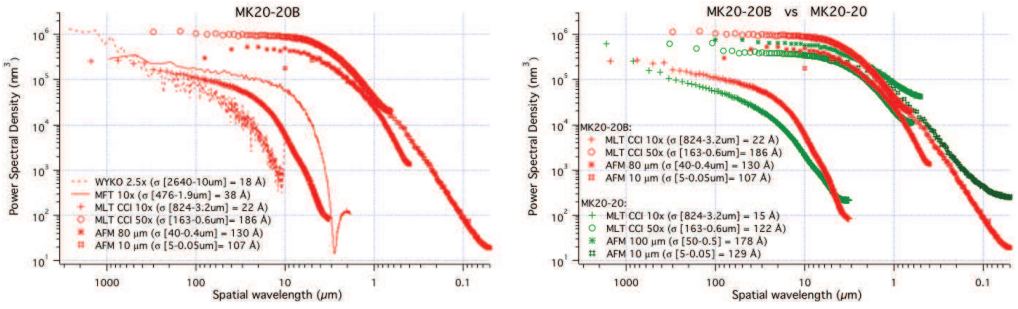

Figure 6.13: *: Left: PSD comparison for the roughness data of the MK20-20B, obtained with several microtopography instruments. Right: PSD comparison for the roughness data of the MK20-20B and MK20-20. This graph shows a roughness decrease from MK20-20 to MK20-20B of about 30% in the AFM range, but an increase of about 30% at lower wavelengths.*

6.2.5 Roughness replication during slumping

Fig. 6.14 displays the roughness of a glass foil, slumped on the new MK20-20B. An important result is that the roughness of the mould is replicated only partly by the glass surface. In fact, only

the high peaks leave an imprint in the mirror topography, and the PSD of the glass foil remains far below the one of the mould in the same range Fig. 6.15.

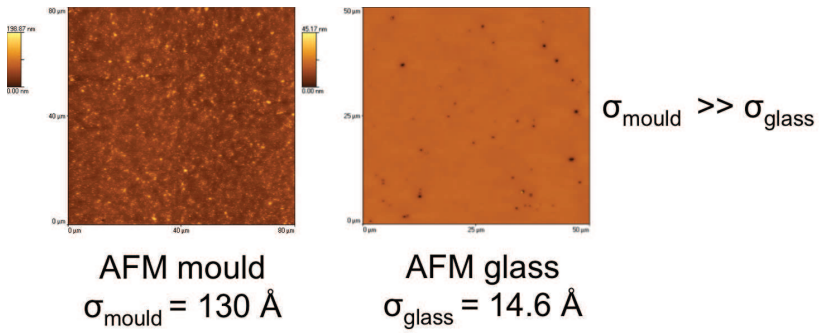

Figure 6.14: *: Comparison of AFM images for the K20 mould (left) and a slumped glass foil (right). The high peaks of the mould leave an imprint on the slumped glass foil, but the roughness is indeed much smaller on the glass foil.*

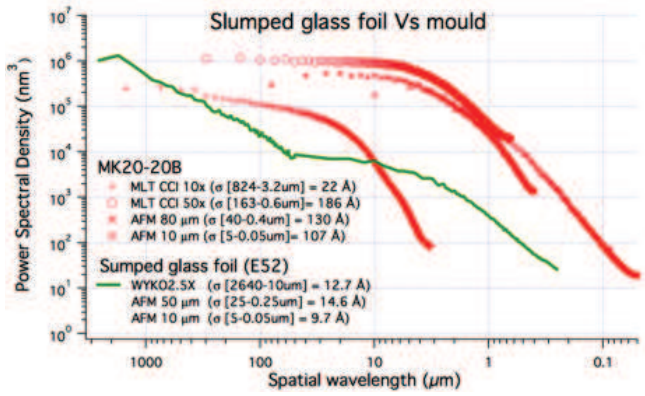

Figure 6.15: *: PSD from roughness data obtained for the MK20-20B slumping mould (red line) and one Eagle glass foil slumped on it (green line, glass code E52). The PSD of the glass foil remains far below the one of the mould.*

The degree of replication depends on the slumping process: with the process described in Section 6.7, the roughness of the slumped glass foils in the 50 μm AFM scan range is σ_{Glass} = 14.6 Å, while the roughness of the mould is σ_{Mould} = 130 Å (σ_{Mould} = 130 Å in the range 40-0.4 μm and 127 Å in the range 25-0.4 μm to be compared with the one of the glass foil) (Fig. 6.14). This value of glass roughness guarantees a HEW degradation less then 1 arcsec at 1 keV and 0.7 deg incident angle: this can be computed using the analytical model described in Section 4.4.5 [Spiga 2007]. From this model it can be derived that the spatial frequency involved in the AFM measurements are not affecting the X-ray scattering up to 1keV: therefore the larger roughness measured in the 50 μm AFM scan is not an issue for energies up to 1keV. Anyway, in order to decrease the scattering contribution at higher energies, both the WYKO and AFM roughness should be improved. Some result in this direction were obtained in the very last part of this research and are outlined in Section 6.8.

Other possible ways to improved the roughness of the slumped glass foils are

1. improve the polishing of the K20 surface. A research is now on going with another company, specialised on the production of large cylindrical optics, to ascertain the final roughness on a K20 test mould, with their polishing process;

2. use the indirect slumping approach: I have investigated this possibility in Section 7.5;
3. use the dip coating technique: this in described in Section 7.4.

6.2.6 The Zerodur K20 deformation: protocol definition

During the production of the POC#2 prototype, we have noticed that the longitudinal profiles of the cylindrical K20 surface (the MK20-10 at the time of POC#2) changed with respect to the profiles measured on the as-delivered mould. Therefore, I have started a campaign of measurements on the newly polished MK20-20, checking for deformation after a preliminary annealing cycle, and the subsequent slumping cycles. I had to wait for the second re-work and the new measurements on MK20-20B, to define a protocol to stabilize the K20 surface from deformations. The conclusion of these measurements is that the K20 changes profiles with the sole thermal cycle, i.e. without the application of pressure. Nevertheless, a thermal cycle suitable to prevent further deformation during the subsequent slumpings with pressure could be defined.

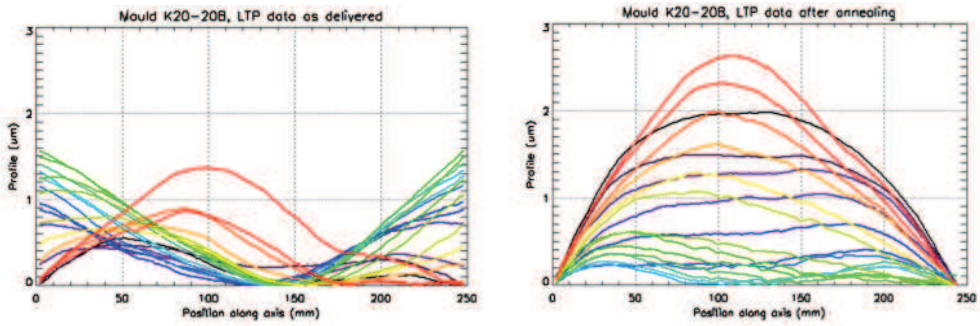

Figure 6.16: *: LTP profiles of the MK20-20B, taken with steps of 1 mm in the longitudinal direction and every cm in the azimuthal direction. Left graph shows the as delivered mould: PV_{center} = 1.4 μm concave, $PV_{90\mathrm{mm-left}}$ = 0.6 μm concave, $PV_{90\mathrm{mm-right}}$ = 0.9 μm convex. Right graph shows the mould after the annealing for comparison: PV_{center} = 0.3 μm concave, $PV_{90\mathrm{mm-left}}$ = 2.1 μm convex, $PV_{90\mathrm{mm-right}}$ = 2.5 μm convex. A large change is experienced in the K20 profiles after the first thermal cycle, but the process conditions where effective in stabilizing the material for the following thermal cycle with pressure (Fig. 6.17-right).*

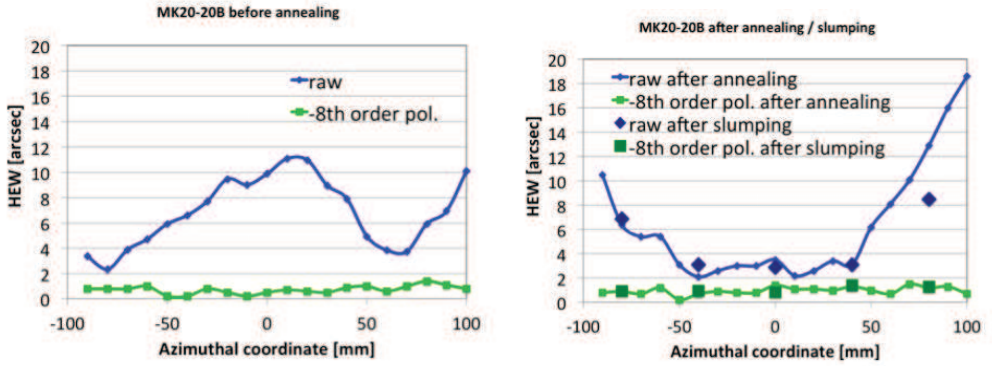

Figure 6.17: *: HEW computed with physical optics from the profiles shown in Fig. 6.16. Both the LTP raw data (blue curve) and the residual after the subtraction of the 8th order best fit polynomial (red curve) are shown. Left is for the as delivered mould, right is for the mould after the annealing. On the right graph the HEWs computed from the LTP data after the first slumping with pressure (glass code E46) are over-plotted, showing no relevant difference.*

Even if the repeatability of the protocol could not be proven on different moulds, the shape stability after several slumping cycles with pressure was proven on MK20-20B. In Fig. 6.16, the

LTP longitudinal profiles of the MK20-20B mould are shown: the measurements were made with steps of 1 mm in the longitudinal direction and 1 cm in the azimuthal direction. The profiles obtained from the brand new mould are compared to the ones measured after the annealing cycle, showing important changes in low-frequencies. Since our integration procedure efficiently damps low frequency errors [Parodi et al. 2011], this change of shape is not critical for our Slumped Glass Optics technology. On the other hand, no relevant changes were measured in the mid-frequencies. This can be seen in Fig. 6.17 where the HEWs, computed from physical optics, are shown both for the raw data and for the data after the subtraction of the 8th order best fit polynomial, in order to highlight the impact of mid-frequency errors. In Fig. 6.17-right, the HEWs computed from the LTP data after the first slumping with pressure (glass code E46) are over plotted. The variation is irrelevant.

Even though the K20 deformation is not critical for our technology, it would be preferable to avoid profile changes of the K20 with the first thermal cycle. This would be essential for those technologies that use a stress-free integration concept and therefore need to produce slumped glass foils with precisely figured Wolter I profiles (Section 3.8.2). The production of our K20 moulds was obtained after polishing cycles following the grinding phase. I suggested the possibility to perform an annealing cycle just before starting the polishing phase: the idea is to stabilize the K20 surface before starting the fine figuring of the mould. Alternatively, I suggested the use of Silicon Nitride as slumping mould material (Section 7.2.2). I have already performed several tests on Si_3N_4 flat slumping mould: no deformation was detected and no sticking ever occurred with different temperatures and pressures around the nominal ones, proving this material to be a good candidate for the slumping technique [Salmaso et al. ICSO2014].

6.3 From Schott AF32 to Corning Eagle XG on MK20-10

AF32 glass has been used to produce the POC#2 optic prototype with hot slumping [Civitani et al. 2013], and the glass foils were slumped on the Zerodur K20 mould MK20-10. A great improvement was obtained with respect to the D263 glass type, owing to the better matching of the CTE of the two materials (CTE_{K20} = 2.0 10^{-6}/K, CTE_{D263} = 7.2 10^{-6}/K, CTE_{AF32} = 3.2 10^{-6}/K). Nevertheless, we had to foresee a change in the glass type, because Schott discontinued the production of AF32 in the dimensions necessary for our setup, namely the 340 $\times$ 340 mm ones. We therefore decided to use the Eagle XG glass, produced by Corning, for the following reasons:

1. it has a CTE very similar to the one of the AF32 ($CTE_{EagleXG}$ = 3.17 10^{-6}/K), as well as very similar characteristic temperatures (see Table 3.2),

2. it has a better thickness uniformity, owing to a dedicated production method (see Figs. 6.1 and 6.2),

3. it is compatible with the active mirror technology developed for the SMART-X project: in fact, the adopted piezoelectric film (PZT), applied after the slumping process, requires a thermal cycle that reaches T = 550 °C. Early works at SAO showed that the D263 glass deformed during the PZT thermal cycle (Fig. 9.5): in fact, the annealing temperature of the glass (T_{D263} = 557 °C) was too close to the crystallization temperature of the PZT. For this reason the Eagle XG, with a higher annealing temperature (T_{Eagle} = 722 °C) was chosen [Cotroneo et al. 2011].

The work performed in this phase can be divided in two parts:

1. Metrology:
   I have defined a method to reliably measure the low- and, most important, the mid-frequency errors of the slumped glass foils (see Sect. 4.2.3, [Salmaso IR12-2013]). I have proven that the previous method for 1D profile characterization (using the CHRocodile sensor installed on the LTP) was introducing spurious mid-frequency errors in the glass profiles. Moreover, the 2D profiles measured with the CUP are also affected by mid-frequency errors and noise that needs to be removed by filtering the data from 1 to 5 mm in spatial wavelengths. The CUP setup was proven to have a good repeatability with an intrinsic HEW error of 5-6 arcsec [Civitani et al. 2010b]. For more accurate characterisation, I have developed a new method, using the pure LTP and painting the back surface of the glass foils with First Contact to suppress the reflection on the back side: this gives reliable profile measurements to characterise the mid-frequency errors down to 1 mm. Finally, to compare the new LTP method with the CUP measurements, I have proven the LTP data to match to the ZYGO interferometer data within 1 arcsec, while the CUP which returned HEW between 5 and 8 arcsec (see Sect. 4.2.7) [Salmaso IR04-2015].

2. Process optimization:
   I have defined two process parameters as key factors to reach a first quality improvement in the slumped glass foil: the soaking time and the mould height inside the muffle. Therefore, I made few a slumping cycle with the AF32 glass foils, in order to compare the results obtained with these process changes on the AF32. Finally, I have started using Eagle glass foils, using the best parameters defined in the preliminary work, and so improving the process for Eagle glass changing few other process parameters. Those parameters are fully described in the following sections. The letter "F" denotes AF32 glass and "E" Eagle glass.

This work is reported in detail in [Salmaso IR12-2013], [Salmaso IR14-2013], [Salmaso IR02-2014].

6.3.1 Slumped glass foils process parameters

The AF32 glass foils, integrated in the POC#2, were slumped with the parameters reported in Table 6.1. Also the glass foil with code F18 was slumped with these parameters: therefore, I assumed this glass as a reference to assess the improvements in mirror quality in the first phase of my work. F18 was discarded during the selection for the POC#2, and therefore it represents a pessimistic test with respect to the glass foils integrated in the POC#2. Nevertheless, it is one of the possible results, because a large variability from glass to glass was reported with the process.

Table 6.1: *: The thermal cycle used for the production of the glass foils integrated in the POC#2.*

Step	Temperature [°C]	Time	Speed [°C/h]	Heating zone ON
1	to 750	11 h	66.4	central top and bottom
2	@ 750	2 h		central top and bottom
3	to 728	4 h	7	central top and bottom
4	@ 728	2 h		central top and bottom
5	@ 728	10 min		lateral
6	to 600	13 h	9.4	lateral
free cooling				

1. AF32
   In the preliminary work with the AF32 glass type, with respect to the reference thermal cycle only the soaking time (time spent at 750 °C) was modified, while in a second phase, with Eagle glass, also the cooling rate was changed (Section 6.6). In details, the soaking time was increased from 2 h to 4 h, and later also to 8 h. Moreover, in this first phase the mould height inside the muffle was modified, from the same height as the muffle, to a height of 2.5 mm above the muffle level. This modification brought the mould to glass contact to start at room temperature, instead of at close to the soaking temperature; the idea was to test the result with a start condition similar to the one used at GSFS (Sect. 3.8.2). A mould rotation of 180 deg was used for two glass foils (F31 and F32), to check if the mid-frequency errors on the slumped glass foils were replicated from the mould. Finally, as for the pressure, it was exerted at the reaching of 750 °C. Few tests were performed to define if the pressure application could be stopped at an early time, in order to reduce the mould roughness replication on the slumped glass foil: for one glass foil (F24) the pressure was alternately switched off/on over the 4 hours at 750 °C, in order to see if the release of the pressure was not affecting the glass-to-mould contact. Another glass foil (F33) was produced stopping the pressure application after the soaking time.

2. Eagle
   For the Eagle glass, the adopted thermal cycle was almost unchanged with respect to the slumping of the AF32 glasses, with the sole difference of the holding temperature during the cooling cycle, because the annealing temperature is 722 °C for the Eagle XG and 728 °C for the AF32. The starting parameters were derived from the F30 glass foil. To further improve the process, different pressure values were used, namely 20 and 80 g/cm^2, beside the standard 50 g/cm^2). The lower pressure was tested to check if the mould roughness replication could be reduced, maintaining a proper shape. The higher pressure was instead used to check how much would the glass roughness be degraded in order to improve the result in terms of shape replication. The Jimenez model (see Section 3.7), modified to include the pressure, was compared to the data obtained from these glasses. Finally, preliminary check to apply the pressure at room temperature, instead of at the reaching of the soaking temperature, were performed in order to avoid air bubbles entrapping problems.

For all these glass foils, the muffle configuration was open with the thin cover, as described in Section 5.2.1.

Table 6.2: *: Process parameters of the AF32 slumped glass foils. For all the glass foils: P = 50 g/cm^2, pressure application starts at 750 °C.*

	Soaking time	Mould height	Mould rotation	P. application end
F18	2 h	0 mm	0	at 200 °C
F24	4 h	0 mm	0	off/on along the 4 h at 750 °C stop at 200 °C
F29	4 h	0 mm	0	at 200 °C
F30	4 h	2.5 mm	0	at 200 °C
F31	4 h	2.5 mm	180	at 200 °C
F32	4 h	2.5 mm	180	at 200 °C
F33	4 h	2.5 mm	0	after the soaking time
F34	8 h	2.5 mm	0	at 200 °C

Table 6.3: *: Process parameters of the Eagle slumped glass foils. For all the glass foils: t_{soak} = 4 h, mould-height = 2.5 mm, mould-rotation = 0, pressure application ends at 200 °C, as for the F30 glass foil.*

	Pressure value [g/cm^2]	P. application start	cooling
E5	50	at 750 °C	13 h from 722 to 600 °C
E6	50	at 20 °C	13 h from 722 to 600 °C
E7	50	at 750 °C	13 h from 722 to 600 °C
E8	50	at 750 °C	13 h from 722 to 600 °C
E9	50	at 750 °C	13 h from 722 to 600 °C
E11	20	at 750 °C	13 h from 722 to 600 °C
E12	20	at 750 °C	13 h from 722 to 600 °C + 3 h from 600 to 510 °C
E17	80	at 750 °C	13 h from 722 to 600 °C

6.3.2 Comparison of results: shape, roughness and expected HEW

After developing a reliable and accurate method for shape characterisation (see Sect. 4.2.3, [Salmaso IR12-2013]), an AF32 glass foil (glass code F18), slumped on the same process condition of the ones integrated into the POC#2, was measured as reference starting point. This glass foil was characterised on five longitudinal scans, named C = central scan, 45R= scan 45 mm off the centre in the right direction, 86R= scan 86 mm off the centre in the right direction, 45L= scan 45 mm off the centre in the left direction, 86L= scan 86 mm off the centre in the left direction. These positions are chosen at different distances from the 6 ribs, and therefore affected by different shape dampings during the integration (see Sect. 3.8.5). Considering a inter-ribs distance of 36 mm and a rib width of 2.5 mm, the C, 45 and 86 scans have a scale distance from the ribs of 16.75, 7.75 and 2.75 mm respectively. The 86 scan is the one with the most efficient correction, being the closest one to the rib. In Fig. 6.18, the five F18 longitudinal profiles are shown: the two methods are compared, the CHR+RD installed on the LTP (Sect. 4.2.2) and the method explained in Sect. 4.2.3. In Fig. 6.19 the same profiles, after the simulation of a prefect integration with 6 ribs, are presented. Figure 6.19 clearly shows the improvement reached, discriminating between real and spurious mid-frequency errors. Using the two dataset, I have computed the PSF via physical optics [Raimondi & Spiga 2015], and the correspondent HEW values (Table 6.4): the HEW estimated with the CHR-RD method is 13 arcsec, while the value obtained with the LTP-FEA, free from spurious oscillations, is 6.8 arcsec.

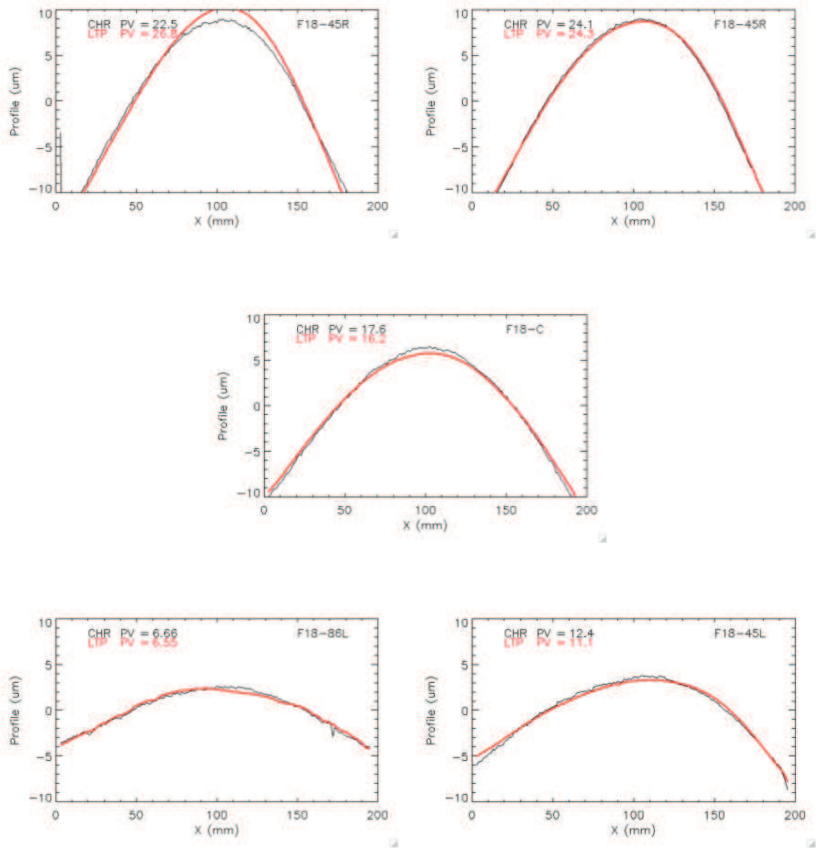

Figure 6.18: *: F18 profiles: in black the profiles derived from the standard CHR+RD measurements, in red the profiles derived from the new LTP measurements (Sect. 4.2.3). The two measurements are in substantial agreement on the low-frequency range.*

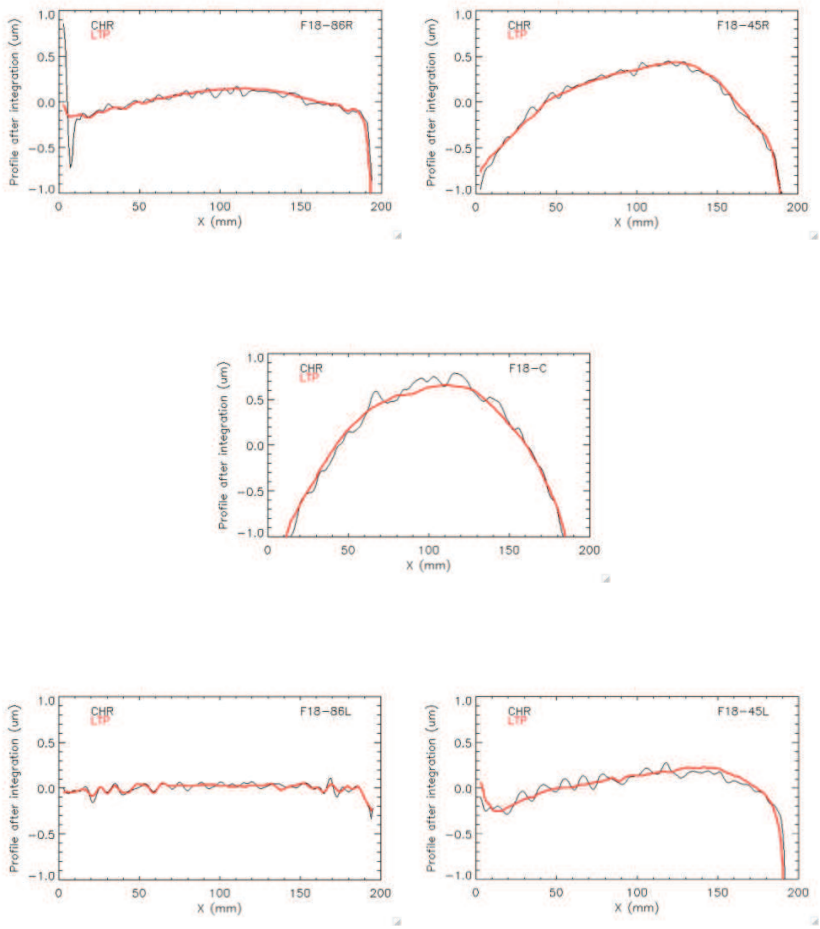

Figure 6.19: *: The same profiles of Fig. 6.18 after a simulated integration: in black the profiles derived from the standard CHR+RD measurements, in red the profiles derived from the new LTP measurements. The new method is free from spurious oscillations (Sect. 4.2.3).*

Table 6.4: *: HEW computed for the F18 glass foil, with the standard CHR+RD method and with the new LTP method. These data show the net improvement obtained by the new measuring method (Sect. 4.2.3).*

Profile	**HEW from LTP-FEA**	**HEW from CHR-RD**
86L	7.1 arcsec	9.8 arcsec
45L	4.4 arcsec	16.8 arcsec
C	16.2 arcsec	20.2 arcsec
45R	8.8 arcsec	12.6 arcsec
86R	4 arcsec	9 arcsec
all	6.8 arcsec	13 arcsec

The roughness of the F18 glass foil was characterised with the WYKO interferometer and the resulting PSD is shown in Fig. 6.20. A 4th order polynomial fit was subtracted from the data (Section 4.3.1).

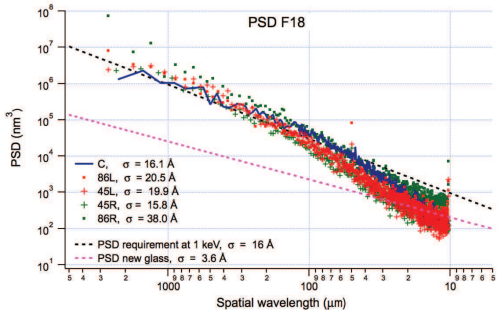

Figure 6.20: *: PSD from WYKO data for the F18 glass. A 4rd order, best-fit polynomial was subtracted from the profile data. This roughness represents the reference starting point of my work.*

From these data, we can see a large PV (for the central scan $PV_C \sim 17$ μm: this scan is the most critical), large mid-frequencies ($\sim$ 200 nm height in the 86L scan, over 1-2 cm spatial wavelengths), and roughness values above the tolerance.

To improve this result, few parameters were at first modified with the AF32 glass type. Table 6.2 presents the process parameters of the slumped glass foils. The process conditions adopted and the results obtained for each glass foil are shortly listed hereafter:

1. F24: the pressure was alternately switched off/on over the 4 hours at 750 °C to determine whether the release of the pressure could be done at early times to reduce the mould roughness replication on the glass foil, but keeping a glass-to-mould contact. This was indeed impossible. As soon as the pressure was released, the interference fringes started to increase in number, meaning that the gap glass-to-mould was increasing. The final result was a glass foil with high roughness due to the shear of the two surfaces.
2. F29: the first glass foil slumped after the Gorilla campaign (see Section 7.1). The MK20-10 surface had been further degraded by these tests: as a result, F29 presented a higher mid-frequency and roughness content.
3. F30: the first test starting with glass-to-mould contact at room temperature, obtained by changing the mould height. This produced a decrease in the PV, resulting in an improved HEW computed from the raw data (HEW as-slumped in Table 6.5).
4. F31: the mould was rotated to 180° to determine whether the mid-frequency errors on the slumped glass foils were copied from the mould. A problem occurred with the felt, and a lot of dust was entrapped. The glass was deformed over the centimetre scale.
5. F32: the same as F31 but without the felt misplacement. The test proved that mid-frequency errors are at least partially inherited from the mould, as some of them are present both in F30 and F32 profiles. Nevertheless, we understood that two types of mid-frequency errors are present on the slumped glass foils: some replicate the mould errors, others arise from the interaction of the glass and the mould surface (see Jimenez model in Section 3.7).
6. F34; the longer soaking time resulted in a better replication of the mould in the low-frequency scale, but an increase in mid-frequency and roughness. This can be explained as a tighter replication of the rough mould surface. The increase of soaking time can be better tested with a slumping mould with lower roughness.

For all the mentioned glass foils, I have computed the PSF, from LTP and WYKO data, via physical optics [Raimondi & Spiga 2015], and the corresponding HEW values in four cases:

- for the glass foil before the integration (as-slumped) at 1 keV: this data gives an indication of the mould replication in the low-frequency range;
- for the slumped glass foil after the simulation of the integration at 1 keV: this represents the glass quality in terms of profile errors;
- for the slumped glass foil after integration, plus the roughness, at 1 keV and 1.5 keV: this represents the glass quality in terms of profile and roughness errors, and it it therefore dependent on the energy. Only energies up to 1.5 keV are considered at this phase of the research.

The results are shown in Table 6.5.

Table 6.5: *: : Results from the AF32 glass foils of Table 6.2. The PV of the central scan is shown in the first column, while, in the others, the HEW values computed from physical optics are shown, both before integration (as slumped) and after the simulation of the integration.*

	PV [μm] of C scan	HEW [arcsec] as slumped	HEW [arcsec] predicted after integration		
			only profile	profile + roughness at 1 keV	profile + roughness at 1.5 keV
F18	17.6	120	6.8	7.4	8.9
F24	10.7	45	7.4	20.5	35.8
F29	11.6	66.3	6.3	6.9	8.0
F30	9.8	43.3	6.6	7.0	7.5
F31	5.7	30.1	8.4	8.8	9.4
F32	6.7	47.9	5.9	6.2	7.5
F34	4.6	30.4	6.3	7.1	8.1

Eagle glass foils were then considered. The starting point is the same process condition of the F30 glass foil, the best result so far (Table 6.5). The process conditions adopted and the results obtained for each glass foil are shortly listed hereafter:

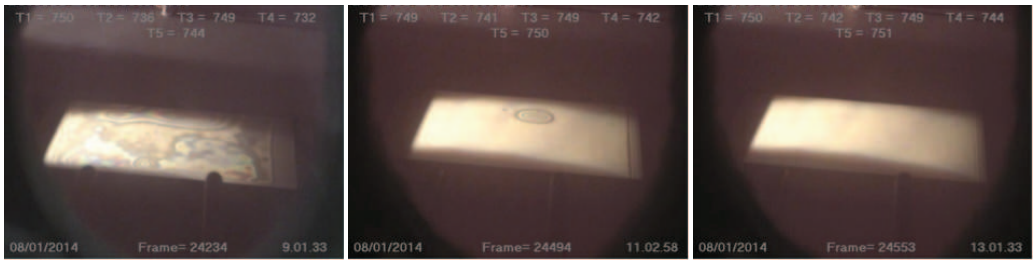

Figure 6.21: *: The interference fringes from the E5 glass foil and the mould surface during the slumping process: from the left at 750 °C, at 750 °C+2h, at 750 °C+ 4h. These images show that the 4 h soaking time is beneficial, as the glass foil is not completely relaxed after 2 h.*

1. E5: it was slumped with the same process condition as the ones adopted for the F30 glass, with the exception of the holding temperature during the cooling cycle. This was done because the annealing temperature is 722 °C for the Eagle XG vs. 728 °C for the AF32. The adoption of a 4 h soaking time resulted appropriate, as some interference fringes were still seen after 2 h, showing that the glass foil was not in full contact yet with the mould (Fig. 6.29) [Salmaso IR02-2014].

2. E6: the pressure application was started at the very beginning of the thermal cycle, in order to check whether the initial contact of the glass could produce better results and avoid air bubble entrapping. Anyway, going from 20 to 750 °C with the pressure valve at fixed aperture, the pressure was observed to increase from 50 to 180 g/cm^2. A possible reason is the transformation of the felt at high temperature into a non-porous material. The thermal cycle was switched off, to avoid possible sticking of the glass, caused by the very high pressure. Anyway, no sticking was observed, and no relevant mould deformation was detected with the Zeiss profilometer [Salmaso IR02-2014].
3. E7: the glass foil was broken during the preliminary cutting phase with the hot tip, in particular during the initiation of the cutting line. From this glass on, the hot tip procedure was abandoned and the glass was preliminary cut with the MDI cutter to a 220 mm × 220 mm size.
4. E8: as for the F31, also for this glass there was a problem of felt misplacement during the closure of the muffle. It resulted in enhanced mid-frequency errors visible in the LTP scans, and therefore worse HEW values (Table 6.3).
5. E9: to reduce the problem of felt misplacements, the felt was not prepared in four independent segments, but it was cut out as a frame. Anyway, after few slumping tests, no relevant difference was observed and the previous methods of felt preparation was re-adopted. The low-frequency shape of the E9 was very similar to the E5, but the mid-frequencies were higher. For a long time, the E5 glass foil remain the best slumped glass foil.
6. E10: the glass was found broken inside the muffle after the slumping, because of an accidental misplacement of the felt.
7. E11: the pressure was set to 20 g/cm^2. The result of this test was a reduction of the central PV (Table 6.3), an increase in mid-frequency errors (Fig. 6.22-left), a reduction in the roughness replication (Fig. 6.22-right): the conclusion is that the pressure value is anti-correlated with the mid-frequency amplitude (Table 6.6).
8. E12: just like E11, the pressure was set to 20 g/cm^2, but the cooling was controlled for a longer time before starting the free cooling, to test mid-frequency relaxation (Table 6.3). Normally, the cooling is controlled down to 600 °C, while for E12 it was controlled down to 510 °C. No visible improvement in mid-frequencies was observed with respect to E11. The explanation is that the shape of the glass is frozen at 690 °C: we understood this later from the interference fringes (see Section 6.6), and also proved it by the unchanged shape of the slumped glass below 600 °C(Section 9.4).
9. E17: the pressure was set to 80 g/cm^2 to check how much would the glass roughness be degraded in order to improve the result in terms of shape replication (Fig. 6.22).

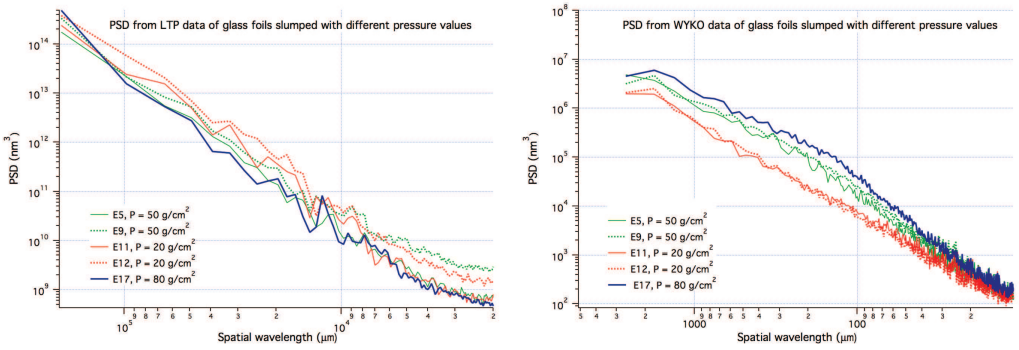

Figure 6.22: *: Eagle glass foils slumped at different pressure values. Left: PSD from LTP data. Right: PSD from WYKO data. The figure proves that the roughness increases with the pressure, while the shape improves with increasing pressure.*

As previously done, for all the mentioned Eagle glass foils, I have computed the PSF, from LTP and WYKO data, and the correspondent HEW values.

Table 6.6: *: Results from the Eagle glass foils of Table 6.2. The PV value of the central scan is shown in the first column, while, in the others, the HEW values computed from physical optics are shown, both before integration (as slumped) and after the simulation of the integration.*

	PV [μm]	HEW [arcsec]	HEW [arcsec] predicted after integration		
	of C scan	as slumped	only profile	profile + roughness at 1 keV	profile + roughness at 1.5 keV
E5	5	25.3	5	5.4	5.8
E8	7.8	29.4	7.5	9.9	13.4
E9	8.1	33	7.3	7.8	8.5
E11	3.8	34.4	9.4	9.6	9.9
E12	3.8	31.2	9.9	10.1	10.3
E17	6.6	36.1	6.1	7	

Finally, to summarise the result of both AF32 and Eagle glass foils, slumped in this first part of the work, the HEW values expected from profiles and the rms computed from roughness data, are reported in Fig. 6.23 and Fig. 6.24, resolved by scan.

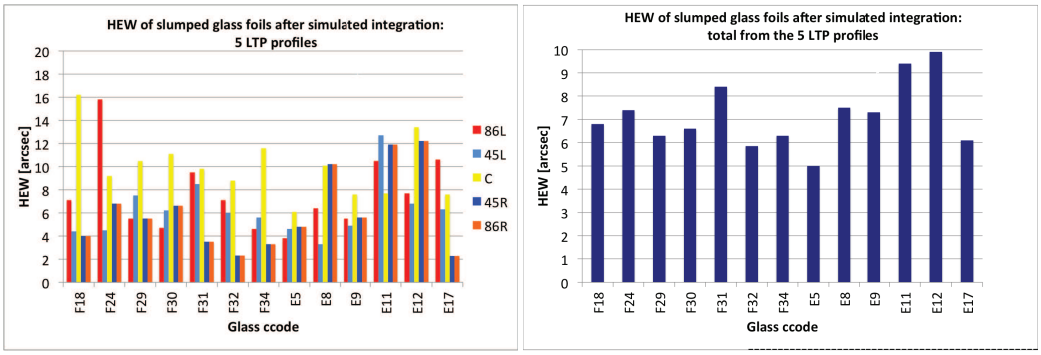

Figure 6.23: *: HEW values as computed from LTP data after the simulation of a perfect integration. Left: the 5 scans are shown separately. Right: the total HEW value computed from the 5 scans. The roughness effect is not included.*

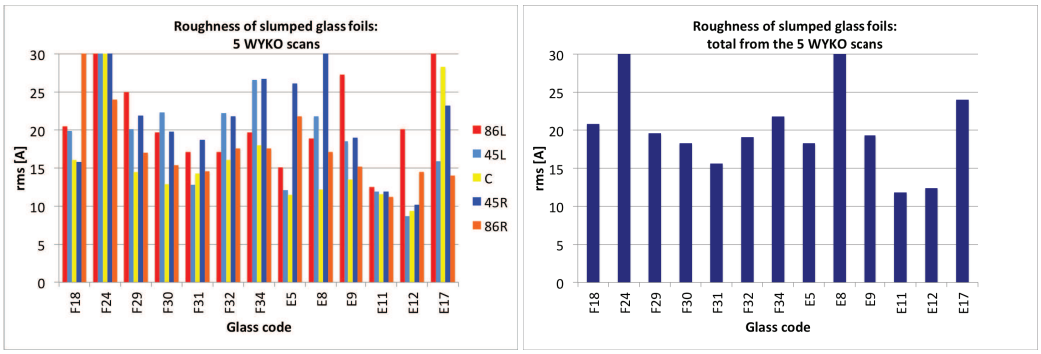

Figure 6.24: *: Rms values as computed from WYKO data. Left: the 5 scans are shown separately. Right: the average result from the 5 scans.*

6.3.3 Conclusions

The main conclusions are:

1. a relevant improvement in the slumped profile PV is obtained by increasing the slumping time from 2 h to 4 h (from F24 on), and by increasing the mould height with respect to the muffle level (from F30 on) (Table 6.5);
2. a further increase of the slumping time to 8 h (F34) degrades the roughness, but as of now the problem can be avoided on the new K20 mould. Tests at increased slumping time were planned on MK20-20 (Section 6.5);
3. the change from AF32 to Eagle does not change substantially the results (Fig. 6.23). The first slumped Eagle glass foil has been the one with the best optical quality so far (Table 6.5);
4. decreasing the pressure from 50 to 20 g/cm^2 (E11 and E12) yields to higher mid-frequency errors and lower roughness. The opposite occurs when increasing the pressure to 80 g/cm^2 (Figs. 6.22, 6.23, 6.24);
5. two kinds of mid-frequency errors are present on the glass: I) replicated from the mould errors, II) from the interaction of glass and mould surfaces. While a parameter change that enables a better copy of the mould profile (increased pressure or slumping time) increases the mid-frequencies of the 1st species and the roughness on the glass, the same actions decreases the mid-frequency of the 2nd species;
6. the use of a K20 mould with a better surface quality is essential to improve the result in terms of roughness and mid-frequencies.

6.4 The modified Jimenez-Garate model: from theory to experiments

6.4.1 The modified Jimenez-Garate model, including pressure

In section 3.7, a model was presented, introduced by Jimenez in 2003 to describe the origin of the ripples experimentally observed in the slumped glass foils, when the glass and the mould surfaces come in contact during the slumping. Here the modification of this model is presented, to include the application of pressure to reduce the ripple height. This modification was introduced by Brizzolari [Brizzolari 2015] and myself.

The application of a pressure P leads to a modification of Eq. 3.5 to

$$\frac{F}{A} = \frac{64aS}{\lambda^2} + 2\rho g a + P, \tag{6.1}$$

from which, by integration, we obtain the potential energy stored in a ripple:

$$\frac{U}{A} = \frac{8Sh^2}{\lambda^2} + \frac{(\rho + 2P/gh)gh^2}{4}. \tag{6.2}$$

From Eq. 6.2 we see that the pressure can be mathematically treated by introducing an effective density $\rho_{\text{eff}} = \rho + 2P/gh$. The ripple relaxation time of Eq. 3.11 thus changes to:

$$\tau = \frac{\eta}{8S/\lambda + \rho g\lambda/4 + P\lambda/2h}, \tag{6.3}$$

where we see that the ripple relaxation time now becomes dependent on the ripple height h and the applied pressure P, and that the application of pressure reduces the relaxation time.

6.4.2 The application of Jimenez model, with and without pressure

As already pointed out in Section 3.7, in order to apply the model and compute the relaxation time τ, it is necessary to have data for the surface tension $S = S(T)$ and the viscosity $\eta = \eta(T)$. For the Eagle glass, the S value was supplied by Corning (private communication): S = 0.328 J/m^2 at T =1400 °C. Due to the weak dependence of S on T (Sect. 3.7), I have used this value in the computation of the relaxation time (using lower values, as the one reported by Jimenez for AF45 at lower temperature, did not change the result substantially).

Table 6.7: *: Comparison of some key parameters of the AF45 and Eagle glass foils, used by Jimenez and in my work, respectively.*

	Density	Softening Point	Annealing Point
Strain Point	**Surface Tension**		
		($10^{6.6}$ Pas)	(10^{12} Pas)
($10^{13.5}$ Pas)			
AF45	2.72 g/cm^2	883 °C	663 °C
627 °C	0.343 J/m^2		
Eagle	2.38 g/cm^2	971 °C	722 °C
669 °C	0.328 J/m^2		

The viscosity dependence on T is instead very large. Its dependence can be computed by fitting the viscosity versus temperature values reported in the data sheet (Table 6.7), with the Vogel-Fulcher-Tammann (VFT) equation (Eq. 3.3). Fig. 6.25 reports the viscosity dependence on temperature for the Eagle glass. The same curve for the AF45 glass was reported in Fig. 3.9.

Once we have derived the surface tension and the viscosity data, it is possible to compute the relaxation time dependence on the spatial wavelength for the model without pressure [Jimenez et

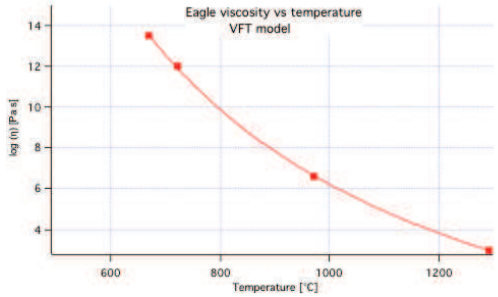

Figure 6.25: *: Viscosity versus temperature for Eagle XG glass. The points are taken from the datasheets, while the solid lines are fitted with the VFT equation (Eq. 3.3).*

al. 2003] and for the model with pressure [Brizzolari 2015].
First, the two models are applied to the AF45 glass: in Jimenez work, slumping is performed at viscosity values of 10^9-10^{10} Pas. From Fig. 6.26-left it can be seen that, considering typical ripple heights of 200 nm, ripples with wavelengths larger than 3 μm are not relaxed during the 15 minute soaking time at 761 °C ($\eta = 10^9$ Pas). Moreover, there is a critical wavelength of about 2 cm where the relaxation time is maximum and the amount of residual ripple height is maximum: this corresponds to the ripple observed in the slumped glass foils both in Jimenez and in my work. The application of pressure drastically reduces the relaxation time, and would completely relax the amplitudes if a soaking time of 1 h were adopted. At the upper annealing temperature instead, where the viscosity takes on a value of 10^{12} Pas, relaxation times are much longer: the use of pressure for 1 h at this temperature would only relax wavelengths longer than 2-3 cm.

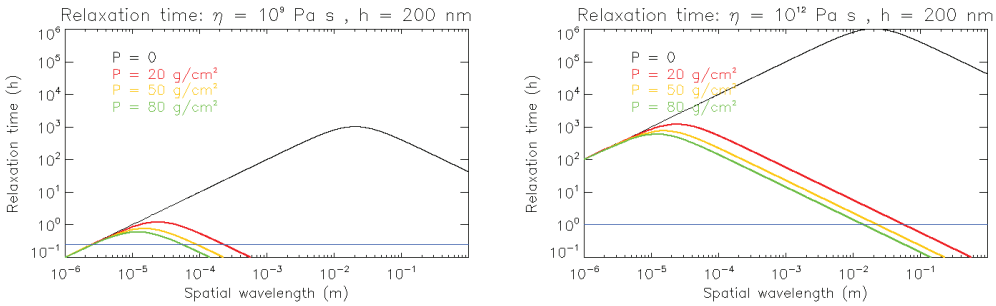

Figure 6.26: *: Predicted relaxation time of surface ripples versus ripple wavelength for the AF45 glass: ripple height of 200 nm are considered. Left: $\eta = 10^9$ Pas corresponds to the soaking temperature T = 761 °C. The blue line corresponds to a 15 min soaking time, used in Jimenez work. The graph shows that the ripples in the centimetre spatial wavelength range are relaxed by the application of pressure. Right: $\eta = 10^{12}$ Pas corresponds to the annealing temperature T = 663 °C. The blue line corresponds to 1 h annealing time. The ripples in the centimetre spatial wavelength range, created in the annealing region, are critical also with the pressure.*

We now consider the case of Eagle glass, where a soaking temperature of 750 °C was used, which actually corresponds to higher viscosity values ($\eta = 10^{10.95}$ Pas), and 4 h soaking time. This is an intermediate case with respect to the ones previously considered in Fig. 6.26. Comparison of Figs. 6.26-right and 6.27-right shows the negligible dependence of the relaxation time on ρ and S. Fig. 6.27-left shows that the ripples with spatial wavelength of 2-3 cm and height 200 nm, would be easily relaxed by the pressure during the 4 h soaking time. On the contrary, if ripples are formed at higher viscosity, for instance around the annealing temperature, their relaxation would be critical, even with the application of pressure. This justified the need of a very slow cooling, as the one adopted in this thesis (Table 5.1).

Profile measurements of Eagle glass foils, slumped at different pressures (E5-E11-E17, in

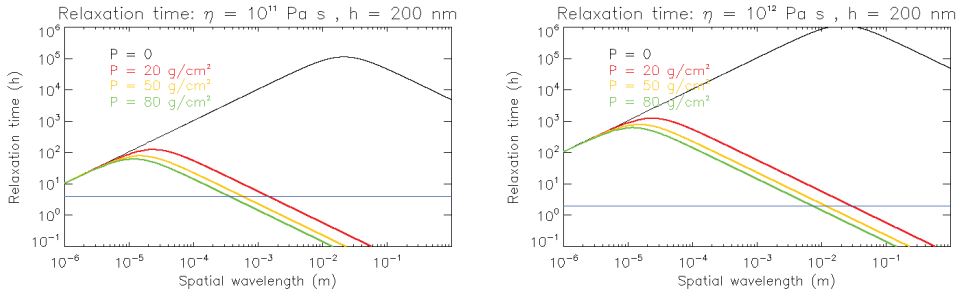

Figure 6.27: *: Predicted relaxation time of surface ripples versus ripple wavelength for Eagle glass: ripple height of 200 nm are considered. Left: $\eta = 10^{11}$ Pas (T_{soak} = 750 °C). The blue line corresponds to the soaking time of 4 h. Right: $\eta = 10^{12}$ Pas (T_{anneal} = 722 °C). The blue line corresponds to an annealing time of 2 h. As for the AF45, the ripples in the centimetre spatial wavelength range, created in the annealing region, are critical also with the pressure. This justified the need of a very slow cooling, as the one adopted in this thesis.*

Section 6.3), are consistent with the prediction of the models (see Fig. 6.28), showing profiles measurements with decreased PSD with increasing pressure. For a deeper comparison of the model with the experiments, it is necessary to repeat the test at variable pressure on a better polished mould, in order to avoid the replication of mid-frequency errors of the slumping mould, as explained in Section 6.3.3.

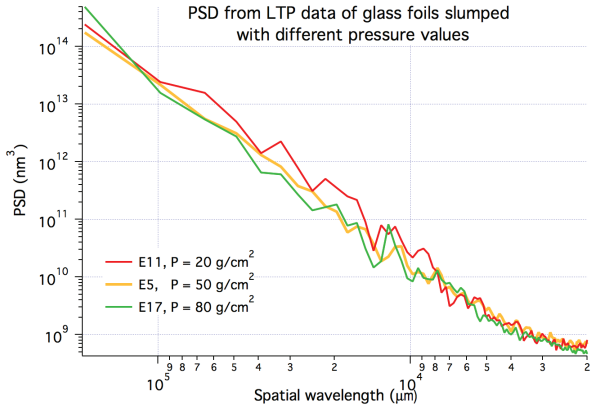

Figure 6.28: *: PSD from LTP data for Eagle glass foils slumped at different pressure values. The experimental result is consistent with the prediction of the models (see Fig. 6.27), showing profiles measurements with decreased PSD when increasing pressure.*

6.5 Eagle XG on MK20-20: the glass foils for POC#3

The process parameters, so far optimised for the MK20-10 mould, could not be directly transferred to the newly polished mould MK20-20. In fact, the different shear of the glass foil on the rough/smooth surface produces different technical issues to be solved. In the previous section, I have shown the improvement, obtained in terms of mould shape replication, when the mould was positioned 2.5 mm higher than the muffle level: in this configuration, the glass foil is already in contact with the mould at room temperature. This condition caused air bubbles to get entrapped on the smooth mould surface of MK20-20, because the higher glass-to-mould contact had left less room for the air to flow out of the contact area during the slumping cycle. This led to the production of deformed glass foils in the first runs on MK20-20, and a asymmetric deformation of the MK20-20 [Salmaso et al. ICSO2014]. To maintain the defined mould height and to avoid the inclusion of air bubbles, the pressure was applied at room temperature instead of after reaching the slumping temperature: while effective in avoiding air bubbles, this led to an increase in PV with respect to the improved results already obtained on MK20-10 after the POC#2. In fact, the PV of the slumped glass foils integrated into the POC#3 was approximately the same as the one of the POC#2 glass foils [Civitani et al. 2014]. Nevertheless, the improvement obtained by the use of a smoother mould surface was seen in the X-ray calibration of the prototype produced with glass foils slumped in this phase of the project: in fact, the best HEW value, in a small portion of the POC#3 module, was 5.5 arcsec at 0.27 keV [Civitani et al. 2014].

6.5.1 Slumped glass foils process parameters

In this phase of the project, the same parameters used for the best AF32 slumped glass (F30) and the best Eagle slumped glass (E5), produced on the old MK20-10, were at first maintained. Since this caused air bubbles entrapping (E13-E14), the pressure application time was moved from the soaking temperature to room temperature. In this way, the glass keeps the contact with the mould for all the duration of the thermal cycle, preventing air in between the two surfaces (E16-E18). These two glass foils were integrated in the POC#3 to verify in X-rays the improvement obtained by the new slumping mould. Tests were then started to reduce the PV, increasing the soaking time: this was already suggested by the previous test campaign (see section 6.3), and E19 and E20 were slumped with 8 h soaking time. To further improve the result, the 8 h soaking time was splitted into 4 h to ramp up from 722 to 750 °C for a better thermalisation of the mould, and 4 h of real soaking time (E21). Since no improvement was observed from E20 to E21, the soaking time was brought to 24 h, to stress the soaking time parameter, for E22 (broken accidentally) and again for E23. E23 was also slumped with a new mould cleaning protocol to prevent repetitive spots throughout consecutive slumping cycles (see section 5.3.1). E23 suffered from various problems, therefore different process conditions were tested. Moreover, the oven passed a major maintenance, therefore a cycle (E24) was repeated with the same parameters of the previous E21. The result was totally different, hence another trial was done with soaking time of 24 h, this time changing the mould height back to the muffle level. However, the preparation of E25 for this test caused the glass to break. E26 was repeated with the same idea, but at the end a serious glass sticking problem was observed, due to the combination of the long soaking time and the 0 mm mould height, as explained later (see section 6.5.3).

For all these glass foils, the muffle configuration was open with the thin cover, as described in Section 5.2.1. The process parameters are listed in Table 6.8.

6.5.2 Comparison of results: shape, roughness and expected HEW

The process conditions adopted and the results obtained for the Eagle glass foils slumped on MK20-20 are shortly listed hereafter. The starting point was the same process of the E5 glass foil.

1. E13: same process as for the E5 glass foil. Air bubbles were entrapped between the glass and the mould. Fig. 6.29 compares the interference fringes seen after 4 h soaking time:

Table 6.8: *: Process parameters of the Eagle glass foils slumped on MK20-20. For all the glass foils: mould-rotation = 0, P = 50 g/cm^2, ramp down from 722 to 600 °C in 11h, P application end at 200 °C. The Table does not report the parameters for the E15 and E25 glass foils, because they went broke down during the preparation.*

	P. application start	Ramp up °C	Soaking time	Mould height	Mould cleaning
E13	at 750 °C	11 h from 20 to 750	4 h	2.5 mm	old
E14	at 750 °C	11 h from 20 to 750	4 h	2.5 mm	old
E16	at R.T.	11 h from 20 to 750	4 h	2.5 mm	old
E18	at R.T.	11 h from 20 to 750	4 h	2.5 mm	old
E19	at R.T.	11 h from 20 to 750	8 h	2.5 mm	old
E20	at R.T.	11 h from 20 to 750	8 h	2.5 mm	old
E21	at R.T.	11 h from 20 to 722 + 4 h from 722 to 750	4 h	2.5 mm	old
E22	at R.T.	11 h from 20 to 722	24 h	2.5 mm	old
E23	at R.T.	11 h from 20 to 722	24 h	2.5 mm	new
E24	at R.T.	11 h from 20 to 722 + 4 h from 722 to 750	4 h	2.5 mm	new
E26	at R.T.	11 h from 20 to 722	24 h	0 mm	new

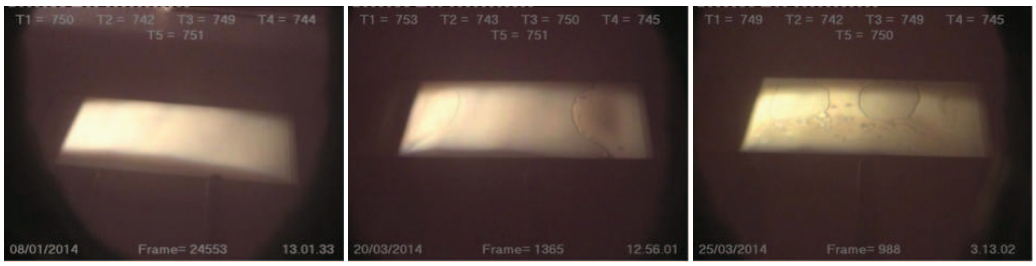

Figure 6.29: *: The interference fringes at 750 °C+ 4h. From left: E5, E13 and E14 glass foils. These images prove that entrapped air was deforming the E14-E15, slumped on the smooth MK20-20, and not the E5, slumped on the rough MK20-10, with the same parameters.*

while no interference is visible for the E5 glass foil, because the glass was completely in contact with the mould, E13 show a pattern caused by the missed contact.

2. E14: repeating the same condition of E13 caused the same problem of entrapped air. The different pattern is due to a slightly increased mould height.
3. E16 was slumped applying the pressure at room temperature to force the glass foil to maintain a contact with the mould and avoid air inlet. Actually, a glass was already slumped with pressure applied at room temperature, namely the E6 glass on the old MK20-10 (see Section 6.3). In this configuration, a large pressure increase was recorded when the temperature was increased from T = 20 °C (P = 50 g/cm^2) to T = 750 °C (P = 180 g/cm^2), as per the gas law, while the pressure value was meant to be kept constant at its initial value. The reason is in the gauge controller installed as of now (MKS type 250 with vacuum transducer MKS type 626B) that does not properly work in this wide range of temperatures. To avoid this problem, the valve was manually closed while the temperature was increasing, keeping the pressure stable to the value of P = 50 g/cm^2: on average, I had to intervene every 30 min for the 11 h ramp up. This operation succeeded to avert any air entrapping. Nevertheless, it produced a higher PV. Finally, dust problems were encountered for this glass foil, close to the 86L scan (Fig. 6.30). This was due to an accidental problem when the muffle was sealed. In Fig. 6.31 the interference fringes at 500 °C, during the cooling of the glass foils E16 and E5, are compared: they exhibit clear evidences of remaining mid-frequencies on the slumped glasses, much reduced on E16 owing to the use of the smoother MK20-20.
4. E18 was slumped with the same parameter used for the E16 glass foil.
5. E19 was slumped with the same parameters of the E16-E18 glass foils, but a soaking time of 8 h instead than 4 h. This was aimed at a reduction of the glass foil PV (up to 13 μm for the central scan of the E18 glass foil), hence a better replication of the mould profile (measured PV value of 4 to 5 μm, after the E18 run, Fig. 6.32). The pattern recorded with the CUP map (Fig. 6.33) is similar (with smaller amplitude) to the pattern registered for the E24 glass foil, slumped just after the E23 glass foil with a 24 h soaking time (Fig. 6.36), and to the glass sticking pattern of the E26 foil (Fig. 6.37). The 8 h soaking time can be set an upper limit in order to preserve the mould integrity.
6. E20 was processed with the same parameters of the E19 glass foil. The central PV was measured smaller for this run, but this was not consistent with the previous glass foil, which was also slumped with 8 h soaking time (PV_{E16-4h} = 10.7 μm, PV_{E18-4h} = 12.7 μm, PV_{E19-8h} = 11 μm, PV_{E20-8h} = 8.9 m). It is possible, however, that the K20 shape changes are transferred to the glass foils.
7. E21: a different heating cycle was used to have a lower heating rate near the soaking temperature, i.e. a better mould thermalisation. Instead of a 8 h soaking time, as for the E19 and E20 glass foils, a 4 h ramp up + a 4 h soaking time was adopted. Relevant improvements were not observed for either the PV or the mid-frequency errors, with respect to the E20 case.
8. E22 was slumped with a direct ramp up to 750 °C, as for the E19 and E20 glass foils, but was broken accidentally.
9. E23: as for the E22 glass foil, it was slumped with a direct ramp to 750 °C, but with a soaking time of 24 h, to the aim of investigating the influence of this parameter on the PV. In fact, at the time of this slumping, no clear evidence was found that the 8 h soaking time was already an upper limit. The E23 glass foil was not better at replicating the mould surface in the low-frequency range, but the mid-frequency errors content was instead very low (Fig. 6.34). This was also due to the newly introduced cleaning protocol (see Section 5.3.1), to remove the contamination present and reduce mid-frequency errors visible on the bottom part of the CUP maps of Fig. 6.34. From the roughness point of view, higher values than usual were found both for the WYKO and the AFM. Several attempt in cleaning the glass

with the standard H_2O_2 method did not improve the result. Therefore, a plasma etch was performed at Gambetti laboratories with a reactive plasma etching (O_2) and a kinetic etching (Ar). This was found to be effective at removing the residuals (Fig. 6.35).

10. E24 was slumped with the same parameters of the E21: a 4 h ramp up + a 4 h soaking time. This run followed a major maintenance on the Bentrup furnace controller, and therefore was repeating the parameters of E21 for comparison. Nevertheless, the result was totally different. The glass foil resulted highly deformed (Fig. 6.36). Moreover, the same pattern of the E19 glass foil (Fig. 6.33) was measured (Fig. 6.36), with higher amplitude. The conclusion is that the mould shape was damaged.

11. E25: the soaking time of 24 h was used, but the glass broke down during the preparation.

12. E26 was slumped with soaking time of 24 h, this time changing the mould height back to the muffle level. A serious glass sticking problem was observed (Fig. 6.37), due to the combination of the long soaking time and the 0 mm mould height. This required a re-working of the mould.

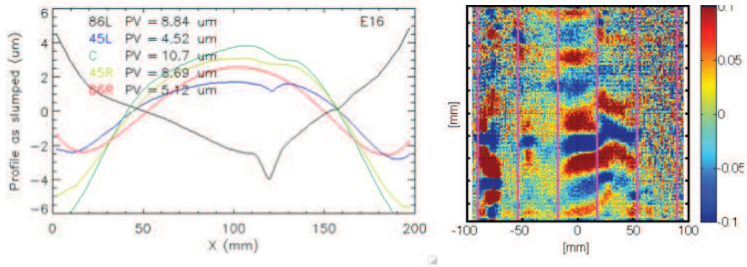

Figure 6.30: *: E16 shape characterisation. Left: the profiles derived from the LTP-FEA. Right: CUP map, after removing the Legendre polynomials up to the 8th order. Two types of problems are visible in both measurements: one in the central region due to the deformation of the mould after the previous slumping cycles, the other in the left region, where dust was entrapped during the preparation of the run. Credits: CUP maps by M. Civitani.*

Figure 6.31: *: Comparison of MK20-10 and MK20-20, from the interference fringes between glass and mould, recorded during the cooling down phase at T = 500 °C. The images show the remaining mid-frequency errors, much reduced on E16 (left), owing to the use of the smoother MK20-20, compared to E5 (right). The problem reported in Fig. 6.30 in the central region is also visible from the interference fringes of the left figure.*

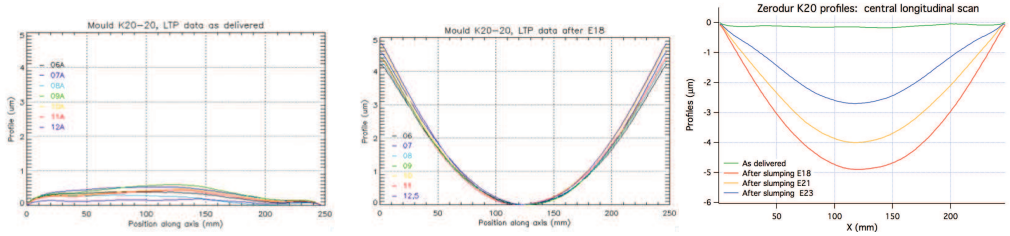

Figure 6.32: *: LTP profiles of the MK20-20 mould. From left: as delivered, after E18, only the central scan compared at different stages. The problem of K20 deformation with slumping cycles was solved with an appropriate preliminary annealing cycle (Section 6.2.6).*

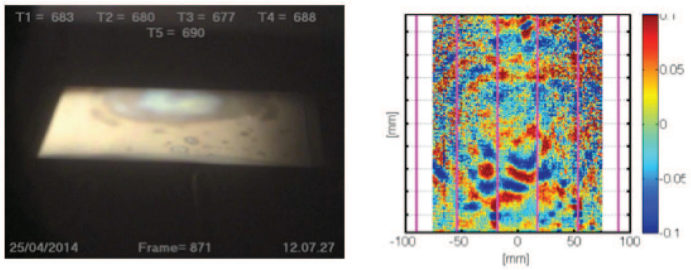

Figure 6.33: *: E19 slumped with 8 h soaking time. The interference fringes, recorded during the cooling down phase at T = 690 °C (left), show a pattern that was after measured also by the CUP (right). These pictures, together with the ones shown in Fig. 6.36, set 8 h as an upper limit for the soaking time in order to preserve the mould integrity. Credits: CUP maps by M. Civitani.*

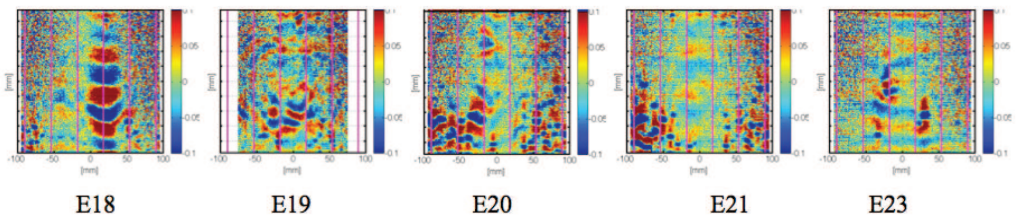

Figure 6.34: *: CUP maps of consecutive slumped glass foils, after removing the Legendre polynomials up to the 8th order. These maps show that the new cleaning protocol, introduced with the E23 run, removes the persistent contaminations on the bottom side. Credits: CUP maps by M. Civitani.*

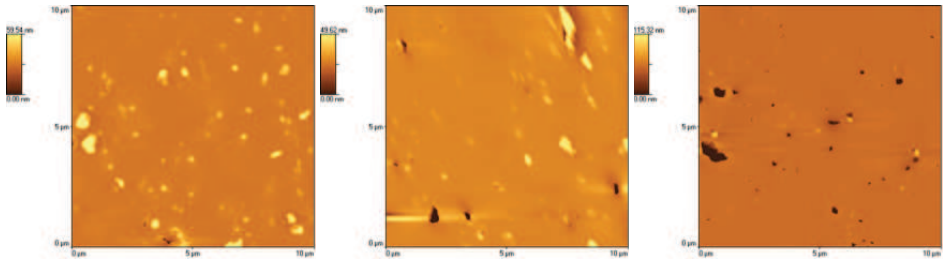

Figure 6.35: *: AFM images (10 μm wide) of the slumped E23, taken at the central position of the glass foil. From left: after 1 h in H_2O_2 (σ = 43 Å, PV = 90 nm); after a second step of 1 h in H_2O_2 (σ = 50 Å, PV = 181 nm); after the plasma etch (σ = 73 Å, PV = 214 nm). These data show that the plasma etch is effective at removing the residuals.*

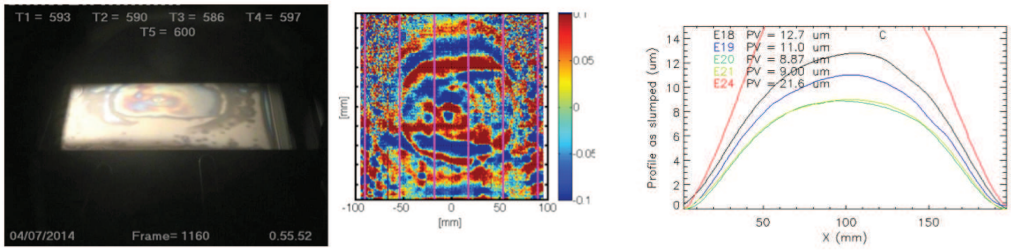

Figure 6.36: *: E24 slumped with 4+4 h soaking time. From left: the interference fringes, recorded during the cooling down phase at T=600 °C; the residual CUP map after the subtraction of Legendre polynomial up to the 8th order, showing a similar map to the interference fringes; the LTP central profile of the E24 glass foil, compared to other glass foils previously slumped on the MK20-20. The conclusion is that the mould precise figuring had been damaged. Credits: CUP maps by M. Civitani.*

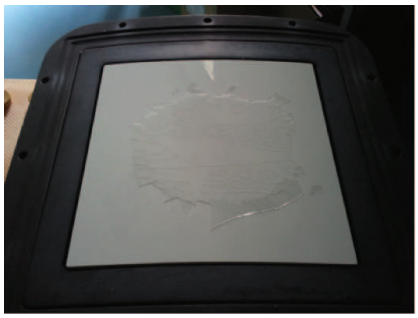

Figure 6.37: *: The glass E26 stuck on the mould. This problems occurred with the combination of a soaking time of 24 h and a mould height of 0 mm with respect to the muffle. We note a pattern similar to the one observed on glass foils E19 and E24.*

For all the mentioned Eagle glass foils, I have computed the PSF, from LTP and WYKO data, and the correspondent HEW values. The results presented in Table 6.9 show the improvement obtained from the new slumping mould, in terms of HEW expected after integration. This corresponds to reduced mid- and high-frequency contribution from the slumping mould. The Table also shows the higher PV obtained in these glass foils, and consequently the higher expected HEW from the raw data (as slumped).

Table 6.9: *: Results from the Eagle glass foils of Table 6.8. The PV of the central scan, and the HEW values computed from physical optics are shown, both before integration (as slumped) and after the simulation of the integration.*

	PV [μm] of C scan	HEW [arcsec] as slumped	HEW [arcsec] predicted after integration		
			only profile	profile + roughness at 1 keV	profile + roughness at 1.5 keV
E16	10.7	56	3.9	4.1	4.4
E18	12.7	51	3.3	3.4	3.7
E19	11	55.4	3.6	3.8	4
E20	8.9	41.6	3.4	3.5	3.9
E21	9	40	3.6	3.7	3.7
E23	10.6	82	5.4	5.7	6.5
E24	12.6	84.3	11.9	12.5	12.7

Finally, to summarise the result of Eagle glass foils, slumped on MK20-20, the HEW values expected from profiles and the rms computed from roughness data, resolved by scan in order to visualise the glass foil dis-uniformity and cumulated for the entire glass, are reported in Fig. 6.38 and Fig. 6.39, respectively.

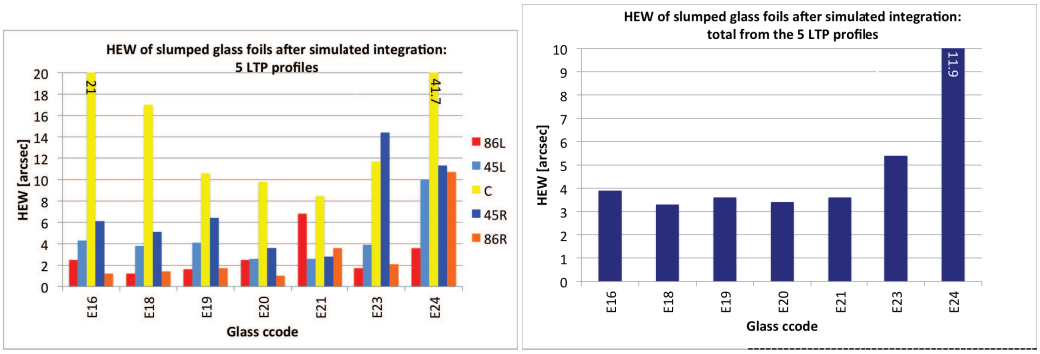

Figure 6.38: *: HEW values as computed from LTP data after the simulation of a perfect integration. Left: the 5 scans are shown separately. Right: the total HEW value computed from the 5 scans. The roughness effect is not included.*

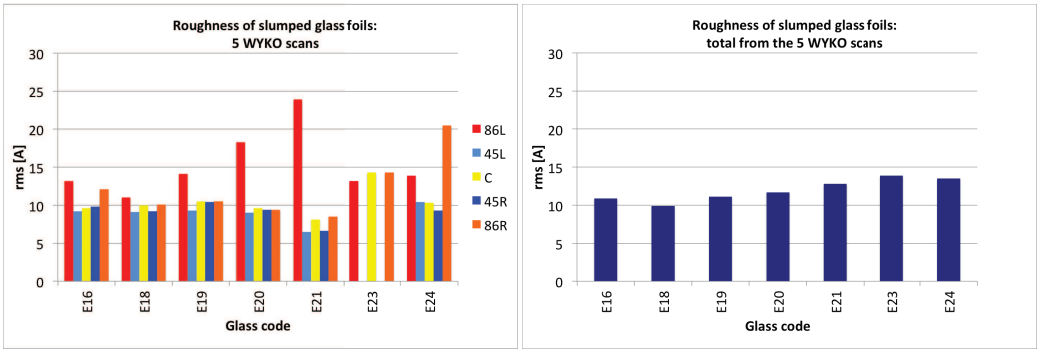

Figure 6.39: *: Rms values as computed from WYKO data. Left: the 5 scans are shown separately. Right: the average result over the scans.*

6.5.3 The glass-to-mould sticking problem

After the sticking of the Eagle glass E26 on the MK20-20 slumping mould, several hypothesis were considered:

1. the presence of H_2O_2 traces, as a possible oxidant agent, might have caused the glass sticking. However, the chemical composition of Zerodur shows a material already fully oxidized (see K20 composition in Section 3.6.2).
2. the presence of First Contact residuals, entrapped in the glass or in the mould surface by the longer soaking time, might be a possible gluing factor. This was considered because of the more abundant residuals seen on the E23 slumped glass (Fig. 6.35).
3. finally, the soaking time prolonged to 24 h to reduce the glass PV, might have been another possible cause.

I have carried out an experiment with a small flat K20 mould, half-painted with First Contact, with a 24 h soaking time and a standard pressure of 50 g/cm^2, without the cleaning with H_2O_2. Although destructive, this experiment clarifies that neither the H_2O_2 nor the First Contact were the cause of glass sticking on the K20 mould. The cause is therefore believed to be the soaking time prolonged to 24 h.

Figure 6.40: *: K20 flat mould used for the failure analysis of the sticking problem. From left: the mould half-painted with First Contact; the muffle ready for slumping; the glass stuck on the mould after a slumping of 24 h, on both half regions. This proves that the 24 h soaking time is the root cause of the glass sticking.*

We note that 24 h soaking time was also used for the E23 run, without sticking problems. Nevertheless, the geometry of the setup was different, because the mould was 2.5 mm higher than the muffle for the E23, and at the same level for the E26 (Fig. 6.41). This higher levelling yielded a lift of the central portion of the glass for E23 that prevented the glass from sticking. A damage of the mould surface surely occurred during the E23 run, as the subsequent glass (the E24) had an unusual CUP map (Fig. 6.36). The damage could be similar to the one observed by the Nomarsky analysis on the mould, after the glass E26 was stuck, close to the sticking area (Fig. 6.42).

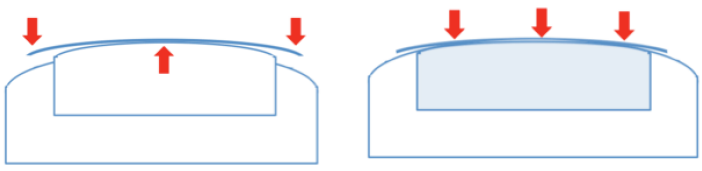

Figure 6.41: *: Geometrical setup of the mould inside the muffle. Left: the setup used for all Eagle glass foils of this phase, excepting the E26. Right: the setup used for the E26 glass (identical to the setup used for the POC#2 glass foils). In the left configuration, the pressure application produce a reduce pressure in the central area, sufficient to avoid the sticking.*

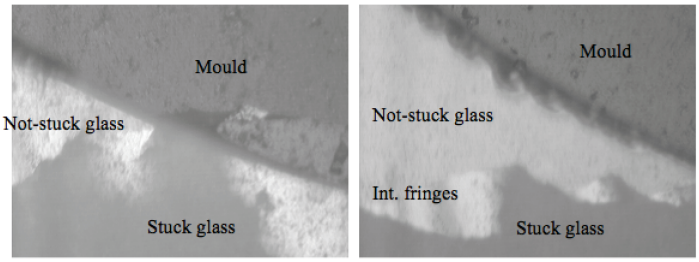

Figure 6.42: *: Nomarski image of the glass stuck onto the mould: the mould appears to be damaged also in the proximity of the glass.*

For completeness, I have considered the possibility to increase the soaking temperature, instead of increasing the soaking time. I have therefore performed a slumping test, on the second side of the flat K20. The glass foil was cut to circular shape and the cycle was done on the small oven. It was slumped at 760 °C, 10 °C higher than the usual, in order to check for margin if the soaking temperature had been increased by few degrees on the MK20-10 mould. Also in this case, the glass was found stuck onto the mould (Fig. 6.43).

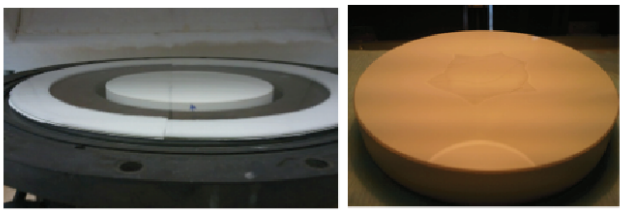

Figure 6.43: *: A soaking time of 4 h at 760 °C also triggers glass sticking. Left: the circular glass on the flat Zerodur K20 mould, inside the muffle. Right: the glass stuck on the K20 mould after the slumping.*

6.5.4 Conclusions

Some problems were encountered when transferring the process from the old to the new K20 mould, owing to some air entrapped in between the mould and the glass foil surfaces during the heating cycle. In order to solve this problem, the pressure application was changed from being applied at 750 °C to room temperature. Somehow, while this action had solved the air problem, it returned slumped glass foils with higher PV values in the longitudinal direction. Despite this problem, the mid- and high-frequency errors of the glass foils first slumped with this new setup (E16-E18) were actually improved with respect to the old K20 mould by a factor of two. In order to reduce the PV of the slumped glass foils, several actions were undertaken:

- the soaking time was increased from 4 to 8 h (E19-E20)
- the heating cycle was modified in order to reach the soaking temperature with a lower heating rate - thus reducing the thermal gradients (E21, E24)
- the soaking time was increased to 24 h with different mould elevations (E23 mould height = 2.5 mm, E26 mould height = 0 mm) leading however to the sticking of the E26 glass foil.

Despite the failure, this research was very useful to cast key points of the slumping process:

1. the soaking time should be kept below 8 h to avoid the mould damage (with Eagle on K20);

2. no margin is available to reduce the PV either by increasing the slumping time or the slumping temperature (with Eagle on K20);
3. the glass-to-mould contact at room temperature should be avoided on smooth mould as the brand-new K20, because it entails the pressure application at room temperature to avoid the entrapping of air bubbles during the heating cycle. This results in a higher glass PV in the longitudinal direction;
4. the residuals present on the optical side of the glass foil slumped with 24 h soaking time are much more than usual and cannot be removed with the standard H_2O_2 cleaning procedure. Rather, a reactive plasma etching (O_2) and a kinetic etching (Ar) can remove the residuals;
5. if no other care is taken before using the K20 material for slumping (as the protocol described in section 6.2.6), the deformation of the K20 is still on going after 10 slumping cycles with a pressure of 50 g/cm^2, introducing a concave longitudinal profiles of amplitude as large as 5 μm, which was reduced to 2.8 μm after 10 slumping cycles.

6.6 Fine tuning of Eagle XG on MK20-10: the glass foils for POC#4

During the re-working of the K20 slumping mould, several tests on the old MK20-10 mould were carried on, aiming at defining the best process starting with no contact (just like the POC#2 glass foils), but keeping the mould higher than the muffle level (differently from POC#2), as the muffle level position was found to be less performing from the mould replication point of view (Section 6.3).

The very first work was to determine, by Finite Element Analysis (FEA) and experiments, the best mould height. A campaign, to reduce the temperature gradients inside the mould and to reduce the ripple formation with a slow cooling cycle, was subsequently conducted.

This section reports the results obtained from this process tuning on the old MK20-10. Six out of the height glass mirror foils of the POC#4 were selected from glass foils slumped during this work.

6.6.1 Optimizing glass-to-mould distance with FEA

The scope of this work was to define the best mould height as the one allowing the smaller stress in the 200 $\times$ 200 mm^2 area of a glass foil curved to cylinder, bonded to the muffle and subject to pressure, as in our configuration. The problem was addressed in two simplified steps: the analysis was first carried out at room temperature in order to understand the stresses induced by the pressure for different mould heights. Small differences in the radius of curvature of the glass foils bonded to the muffle were also considered, to account for errors in the radius of curvature of the muffle. Then the temperature was introduced by computing the expansion of the muffle at 750 °C, and the shrinkage of the felts to determine the glass position with respect to the mould at 750 °C. We have so derived the height the mould should have at room temperature, in order to reach at 750 °C the optimal position.

Fig. 6.44-left shows the setup where the glass, curved to cylinder over the mould, is clamped into the muffle frame, with the felts in between (zoom in the orange circle). In the FEA analysis, a glass with thickness 0.4 mm and size 340 $\times$ 340 mm^2 was considered. The mould dimension was 250 $\times$ 250 mm^2, and the mould radius of curvature 1 m. Fig. 6.44-right shows the different glass regions in the FEA analysis: the elements outside the orange path are fixed to the muffle, corresponding to the part of the glass clamped into the muffle. The elements inside the yellow path go against the mould when the contact occurs, the elements between the two paths are not supported by anything and free to move. In the FEA calculations, the following parameters were considered: E = 70 GPa for the Young modulus, ν = 0.3 for the Poisson ratio, ρ = 3 g/cm^3 for the glass density.

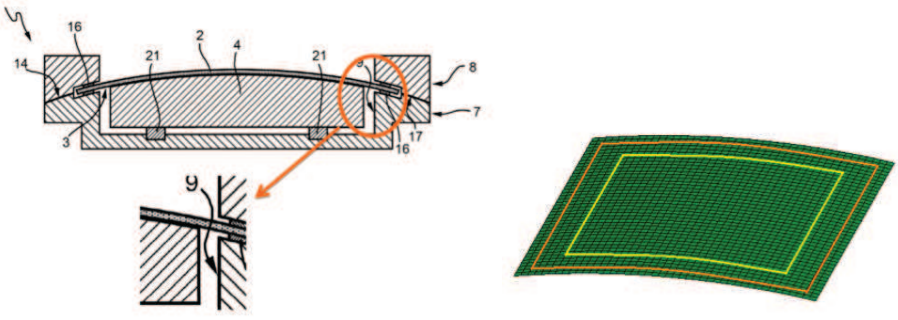

Figure 6.44: *: Left: the slumping setup, showing the muffle, the mould, the glass foil and the felts (in between the glass and the muffle in the enlarged picture). Right: the glass in the FEA analysis; the elements outside the orange path are fixed to the muffle as corresponding to the part of the glass clamped into the muffle, the elements inside the yellow path lean against the mould when the contact occurs. The elements between the two paths are not supported anyway and free to move.*

Different mould-to-glass foil distance where considered, ranging from 0.2 to 2 mm. Three muffle radii, and consequently glass foil radii, around the correct 1 m value, were considered. In fact, the glass radius of curvature is >1 m, as the glass-to-mould contact at room temperature is central when pushing the mould towards the glass foil. The first principal stress stored in the total glass foils surface and the glass-to-mould contact were computed, when pressure value of P = 50 and 20 g/cm^2 were applied. The results of the calculations are plotted in Figs. 6.45 and 6.46.

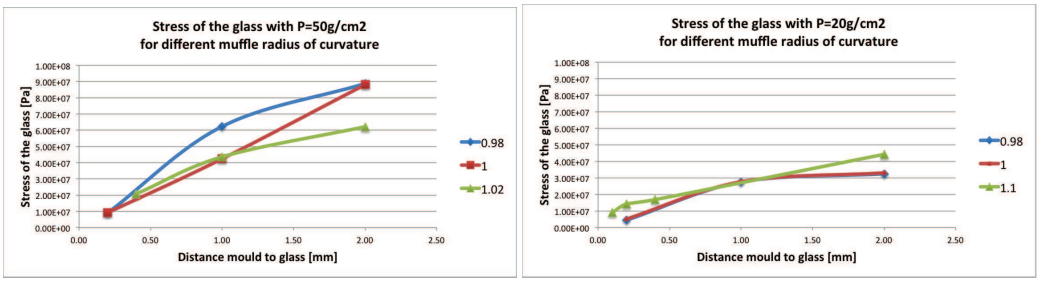

Figure 6.45: *: The stress stored in the total glass foil surface. A minimum glass-to-mould distance has to be set, in order to minimize the stress in the glass.*

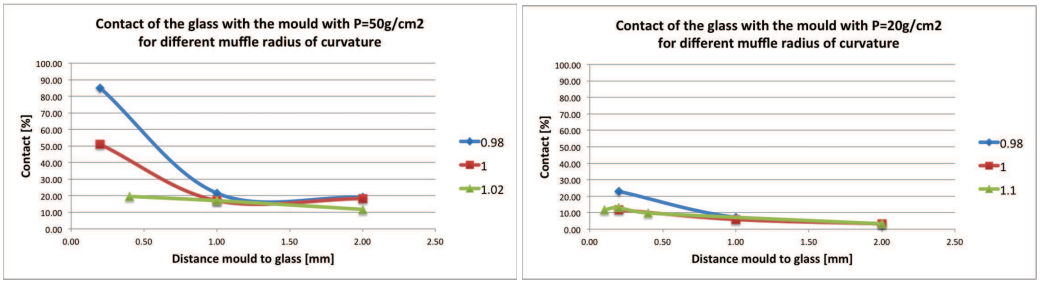

Figure 6.46: *: Glass-to-mould contact. The contact is reduced by reducing the pressure and increasing the glass-to-mould distance.*

From this analysis we conclude that:

1. in order to minimize the stress in the glass, a minimal glass-to-mould distance has to be set (Fig. 6.45 left);

2. the stress in the glass foil is reduced, if a reduce pressure is applied (Fig. 6.45), but the glass-to-mould contact is also much reduced (Fig. 6.46);

3. when the glass-to-mould distance is small (0.2 mm) the stress in the glass foil increases from 4.5 to 9 MPa, if the pressure is increased from 20 to 50 g/cm^2;

4. when the pressure is 50 g/cm^2, the stress in the glass foil increases from 9 to 89 MPa, if the glass-to-mould distance is increased from 0.2 to 2 mm. Considering that 10 MPa is the maximum stress for a glass before breaking down Parodi2011, this explains why the breakage occurred for the E25 glass foil when applying a 50 g/cm^2 pressure at room temperature (Sect. 6.5). The E25 glass foil was prepared with mould height of 0 mm with respect to the muffle, hence the mould-to-glass distance was about 2 mm, determined by the felt thickness. In contrast, the glass foils from the E16 to the E24 were prepared with mould height of 2.5 mm, hence the glass foil was in contact with the mould, and the pressure could be set to 50 g/cm^2 at room temperature, without any glass breakage.

To understand where the stress is located, the stress stored in the whole glass foil surface and in the sole 200 × 200 mm^2 surface was computed, with P = 20 g/cm^2 and glass-to-mould distance of 0.2 mm. Fig. 6.47 shows that the maximum stress value is located near the edge of the mould or near the frame constrained by the muffle.

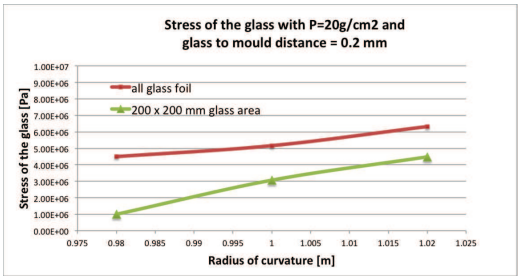

Figure 6.47: *: Stress stored in different glass areas. The maximum stress value is located near the edge of the mould or near the frame constrained by the muffle.*

Finally, the muffle expansion with the temperature was taken into account, resulting in an increased glass-to-mould distance when the temperature is increased. In this case, the vertical displacement of the nodes of the frame welded to the muffle are fixed to a value corresponding to the CTE difference of the material multiplied by ΔT. The simulation was performed for the muffle height of 7 cm (the real value), but considering the expansion at 600 °C, which was the soaking temperature typical for the D263 glass type. This would cause a glass-to-mould increased distance of 0 42 mm. Therefore, the glass-to-mould distance was decreased at room temperature of 0.42 mm in order to reach the closest configuration at 600 °C. A linear behaviour can be assumed and the data rescaled to the 750 soaking temperature of the Eagle glass type, thus giving a glass-to-mould increased distance of 0.52 mm.

Fig. 6.49 presents the stress stored in the 200 × 200 mm^2 glass area, at different pressures. The glass-to-mould distance was set equal to the minimal corresponding gap left for different radius of curvature of the glass foil (Fig. 6.48 , gap = 0.16 mm for glass radius of curvature of 0.98 m, gap = 0 mm for glass radius of curvature of 1.0 and 1.02 m). From Fig. 6.49 we can conclude that if the pressure is increased beyond 30 g/cm^2, leading to more than 50% contact in the central 200 × 200 mm^2 area (Fig. 6.49-right), then all the stress is confined outside the 200 × 200 mm^2 glass area (Fig. 6.49-left).

From this analysis we can conclude that:

1. the glass-to-mould distance should be nearly zero at the reaching of the soaking temperature;

2. to minimise the stresses in the 200 × 200 mm^2 glass area, a pressure of at least 30 g/cm^2 should be used: this also minimises the mid-frequency errors present in the glass foil. In fact, both internal stresses and structural modifications have typical relaxation times Scherer1986 that can be reduced with the application of pressure as described in Section 6.4;

3. the different muffle radii of curvature have small influence when the glass-to-mould distance is minimized.

In order to minimise the glass-to-mould distance at the reaching of the soaking temperature, an expansion in vertical direction of 0.52 mm for the muffle was considered, and the shrinkage of the felts thickness from 2.5 to 1 mm, as measured after the slumping cycles, was included. Measuring a glass-to-mould contact at room temperature at mould height of 1.8 mm, I conclude that 1.8+0.52-1 mm $\sim$ 1.3 mm should be the correct mould height. Experiments around this value were performed, to check the result (Section 6.6.3).

Figure 6.48: *: Glass-to-mould gap, when smaller and bigger glass radius of curvature is considered.*

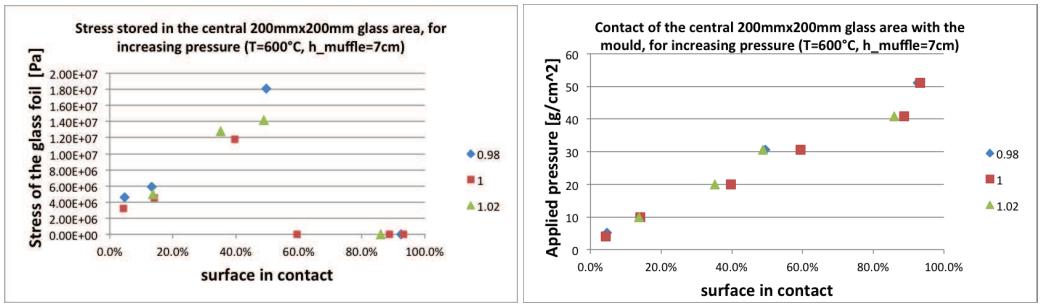

Figure 6.49: *: Left: stress stored in the 200 × 200 mm^2 glass foil surface versus surface in contact, for different glass radius of curvature. Right: the increase of surface in contact when the pressure is increased. These graphs show that if the pressure is increased beyond 30 g/cm^2, leading to more than 50% contact in the central 200 × 200 mm^2 area (right), then all the stress is confined outside the 200 × 200 mm^2 glass area (left).*

6.6.2 Slumped glass foils process parameters

The first part of the research was directed to perform slumping tests around the best FEA height, to determine the best experimental height (E27-E28-E29-E30). Then, to decrease the thermal gradients in the glass-to-mould interface, the muffle was closed (described in Section 5.2.1), at the cost of preventing the video recording of the interference fringes movie during the slumping (from E31). Because of some problems during the preparation with the thick closed muffle, also the thin closed cover was tested (Section 5.2.1). The cooling rate was decreased around the point where the interference fringes reappear, as clear evidence of the glass viscosity transition, to reduce the ripple formation (from E32 on, with different cooling rates). The pressure value was lowered to 20 g/cm^2 (E39) to test the mid-frequency relaxation at lower pressure and lower cooling rate: this increases the mid-frequency defects but reduces the roughness. A longer annealing time was tested (4 h instead of the standard 2 h) to check for possible decreases of mid-frequency (E41). The furnace B was tested with E42-E43. Finally, two glass foils were produced on MK20-10 with the best defined parameters (E44-E45).

6.6.3 Comparison of results: shape, roughness and expected HEW

The process conditions and results from the Eagle glass foils slumped on MK20-10, in this phase of the research, are summarised hereafter:

1. E27: the mould height was set to 1.1 ± 0.5 mm. The different pattern of the interference fringes, when the glass contacts the mould, is shown in Fig.6.50. The pressure was started at 750 °C. No air was creeping in between the glass-to-mould interface during the heating cycle. The glass-to-mould contact is maintained until room temperature for E27, and until 420 °C for E5. Mid- and high-frequency errors are reduced for E27 with respect to E5. PV is still slightly better for E5. In general, the HEW values expected from E27 are smaller than for E5 (Table 6.11).

Table 6.10: *: Process parameters of the Eagle glass foils slumped on MK20-10. For all the glass foils: mould-rotation = 0, soaking time = 4 h, P application start at 750 °C, P application end at 200 °C, new protocol for mould cleaning.*

	Mould height [mm]	Muffle cover	Pressure g/cm^2	Anneal. time [h]	cooling rate 722-670 °C	cooling rate 670-600 °C	Furnace
E27	1.1	thin open	50	2	9.4 °C/h	9.4 °C/h	A
E28	1.3	thin open	50	2	9.4 °C/h	9.4 °C/h	A
E29	1.5	thin open	50	2	9.4 °C/h	9.4 °C/h	A
E30	1.1	thin open	50	2	9.4 °C/h	9.4 °C/h	A
E31	1.1	thick closed	50	2	9.4 °C/h	9.4 °C/h	A
E32	1.1	thick closed	50	2	4 °C/h	8.8 °C/h	A
E33	1.1	thick closed	50	2	4 °C/h	8.8 °C/h	A
E34	1.1	thick closed	50	2	2.5 °C/h	8.8 °C/h	A
E35	1.1	thin closed	50	2	4 °C/h	8.8 °C/h	A
E36	1.1	thin closed	50	2	4 °C/h	8.8 °C/h	A
E39	1.1	thin closed	20	2	2.5 °C/h	8.8 °C/h	A
E40	1.1	thin closed	50	2	4 °C/h	8.8 °C/h	A
E41	1.1	thin closed	50	4	4 °C/h	8.8 °C/h	A
E42	1.1	thin closed	50	2	4 °C/h	8.8 °C/h	B
E43	1.1	thick closed	50	2	4 °C/h	8.8 °C/h	B
E44	1.1	thick closed	50	2	2.5 °C/h	8.8 °C/h	A
E45	1.1	thick closed	50	2	2.5 °C/h	8.8 °C/h	A

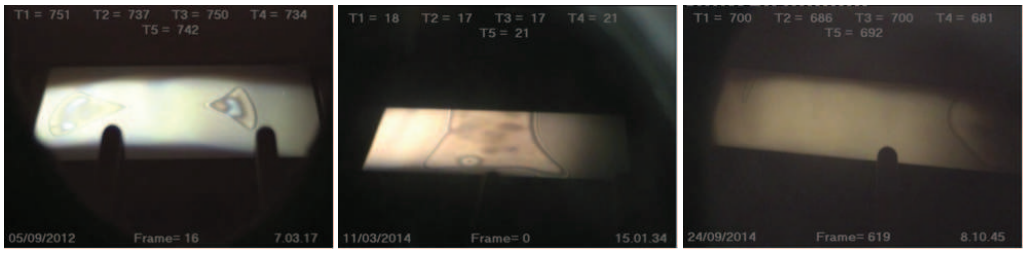

Figure 6.50: *: The interference fringes of the moment when the initial glass-to-mould contact occurs: Left: F6 (POC#2 like glass foil), h = 0 mm and contact just before 750 °C; Center: E5, h = 2.5 mm and contact at room temperature; Right: E27, h = 1.1 mm contact at 690 °C.*

2. E28: the mould height was set to 1.3 mm. The glass resulted slightly degraded by the presence of dust entrapped during the preparation. Anyway, it could be concluded that the result was not improved with respect to the E27.
3. E29: the mould height was set to 1.5 mm. The result was a degradation in terms of PV, mid- and high-frequency, resulting in higher HEWs (Table 6.11).
4. E30 was slumped in the same process conditions as E27, to check the repeatability. The result are comparable with the ones of E27 and E28 (Fig. 6.51).
5. E31: the mould height was ultimately set to 1.1 mm. The closed thick cover of the muffle was used. The preparation of the setup was slightly different and more critical, due to the heavy cover. The set up is shown in Fig. 6.52. The result is a decreased PV, as seen from metrology data (Fig. 6.51) and from the expected HEW values as slumped. Still, a reduction in mid-frequency is needed. This has been done by decreasing the cooling rate.
6. E32: the preliminary step was to define the point where the glass becomes stiffer and set a very slow cooling before that point. This was done by analysing the interference fringes recorded during all the previous slumping tests with the thin open cover (Fig. 6.54). I have found that the fringes start to reappear around 690 °C, with some variability from glass to glass, due to the different process conditions. This temperature is consistent with the strain value given for the Eagle glass (T_{strain} = 669 °C). The cooling rate was therefore lowered from 9.4 to 4 °C/h, going from 722 to 670 °C. The improvement in mid-frequencies is apparent in the CUP maps comparison of E31 and E32 (Fig. 6.54).
7. E33 was slumped in the same process conditions as E32, to check the repeatability. Due to problems during the preparation, E33 resulted with a defect in the central area, due to entrapped dust (Fig. 6.56).
8. E34: a further reduction in cooling rate, 2.5 °C/h from 722 to 670 °C, was used for this glass. The result was a decrease in the central PV ($PV_{central-E30}$ = 6.5 μm, $PV_{central-E31}$ = 4.1 μm, $PV_{central-E32}$ = 2.7 μm, $PV_{central-E34}$ = 1.9 μm), with a larger figure deviation at the corners (Fig. 6.56). The decrease in mid-frequency is evident from the PSD analysis of the data (Fig. 6.57).
9. E35: slumped in the same condition of E32-E33 but with the thin closed cover, to ease the preparation. The result was a glass with a deformed spot in the center due to the presence of an extruding part in the cover.
10. E36: just like E35.
11. E39: the pressure was lowered to 20 g/cm^2 to test whether the mid-frequency errors (increasing with decreasing pressure) could be relaxed at lower cooling rate of 2.5 °C/h. The result was negative.
12. E40: just like E35-E36, removing the extruding part of the thin cover. The result shows that the central PV is anyway higher than with the thick cover, probably due to larger thermal gradients.
13. E41: same configuration and parameters as for the E40, with a longer annealing time, 4 h instead of the usual 2 h: this was done to test whether the longer time allows ripples to relax. A slight improvement was observed, but this was explained by the absence of a central defect present in E40.
14. E42 was slumped in furnace B to check the difference in the two furnaces. A higher PV was observed ($PV_{central-E40}$ = 4.2 μm, $PV_{central-E41}$ = 4.2 μm, $PV_{central-E42}$ = 5.8 μm). Interestingly, the glass foil was almost mid-frequency error free (Fig. 6.58)
15. E43: just like E42 in furnace B. To decrease the PV, the cover was changed from thin-closed to thick-closed. The effect was positive, but the PV was higher than the one of E32, slumped in furnace A, with the same configuration and parameters: $PV_{central-E32}$ =

2.7 μm, $PV_{central-E43}$ = 4.9 μm) (Fig. 6.58). Interestingly, E42 and E43, exhibit a very small contribution of mid-frequency errors (Fig. 6.58). To understand these differences, a thorough calibration of the oven resistance should be done. To this end, I have drilled holes in the cylindrical muffle, to measure, with external thermocouples the temperature in the muffle (Section 5.1.3).

16. E44 was slumped with the best parameters determined so far. The results are $PV_{central-E44}$ = 3.1 μm and expected HEW_{E44} = 4.5 arcsec, computed from profile data after the simulation of a perfect integration.

17. E45: as for E44. The results are $PV_{central-E45}$ = 2.7 μm and HEW_{E45} = 4.1 arcsec.

With the glass foil E45, for the first time, a good combination of small PV and reduced mid-frequency errors was obtained, leading to expected HEW values of less then 5 arcsec in all scans (see Fig. 6.59).

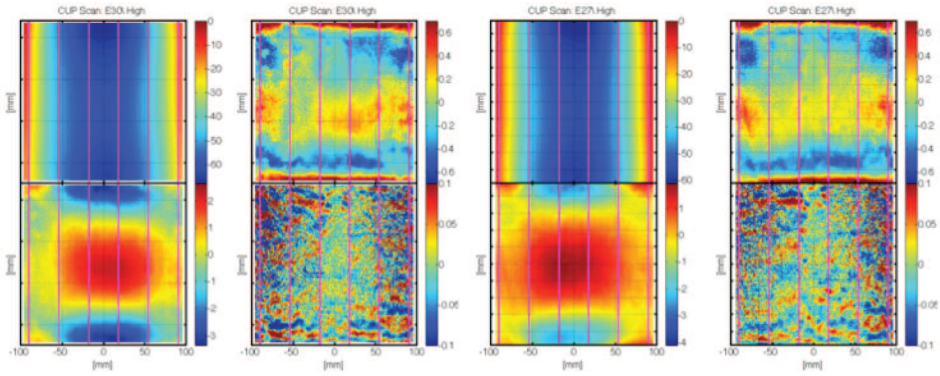

Figure 6.51: *: CUP maps of the E27 and E30 glass foils, slumped in the same process condition. Credits: CUP maps by M. Civitani.*

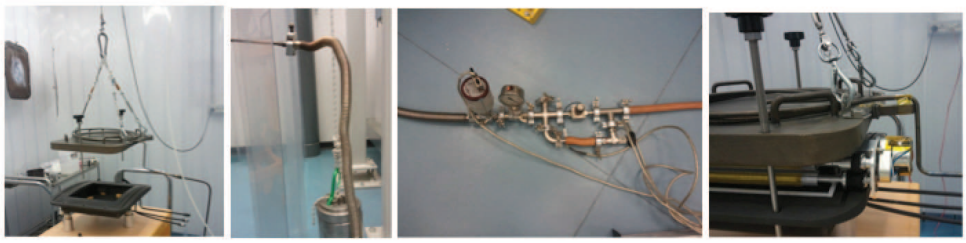

Figure 6.52: *: The setup for holding the glass foil against the muffle cover during the First Contact peeling, by $\sim$ 400 g/cm^2 vacuum suction.*

For all the previous Eagle glass foils, I have computed the PSF, from LTP and WYKO data, and the corresponding HEW values. The results presented in Table 6.11 clearly show the improvement obtained from the optimised mould height, decreased thermal gradients, decreased cooling rate, in terms of expected HEW after integration. All these correspond to decreased low-, mid- and high-frequency errors.

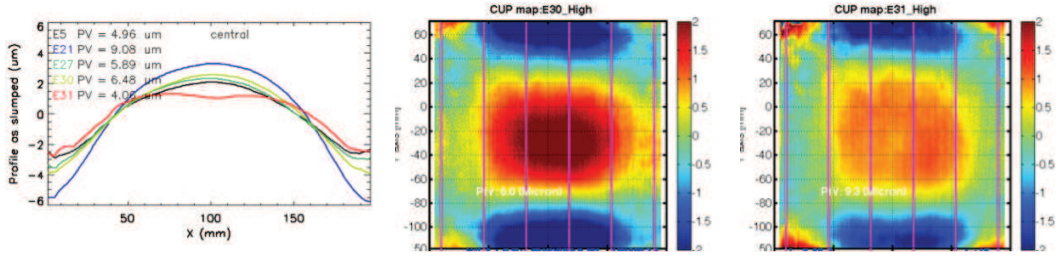

Figure 6.53: *: Shape improvement of E31, slumped with the thick closed cover. Left: comparison of the central scan, as measured with the LTP-FEA, for several glass foils. CUP maps after the subtraction of the nominal cylinder with radius of curvature of 1 m, with a linear detrend for each longitudinal line: E30 (centre), E31 (right). Credits: CUP maps by M. Civitani. The use of the closed cover reduces the central PV.*

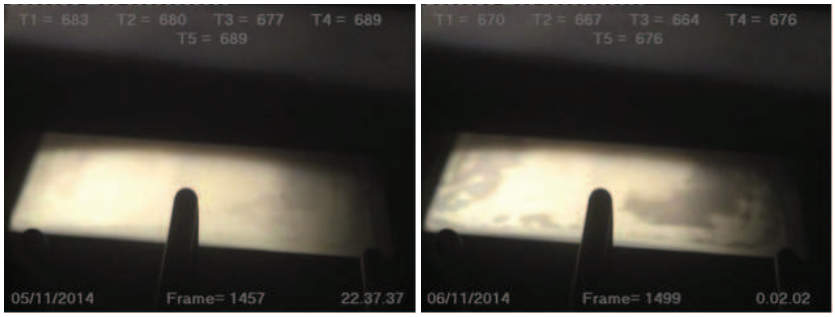

Figure 6.54: *: The re-appearance of the interference fringes during the cooling cycle for E30. Left: at the temperature where the fringes re-appear. Right: some degrees further in the cooling cycle. By comparing the temperature for fringes reappearance on several glass foils, a slower cooling rate was defined around 690 °C.*

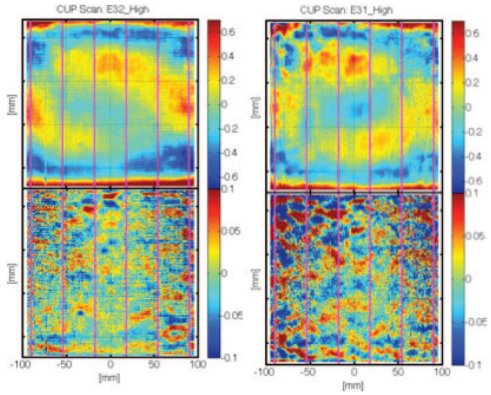

Figure 6.55: *: The effect of the cooling rate reduction: the mid frequency of E32 (left) are reduced with respect to the E31 (right), as can be seen by the CUP maps after the subtraction of the Legendre polynomials up to the 8th order (bottom figures); top figures are subtractd up to the 2nd order Legendre polynomials. Credits: CUP maps by M. Civitani.*

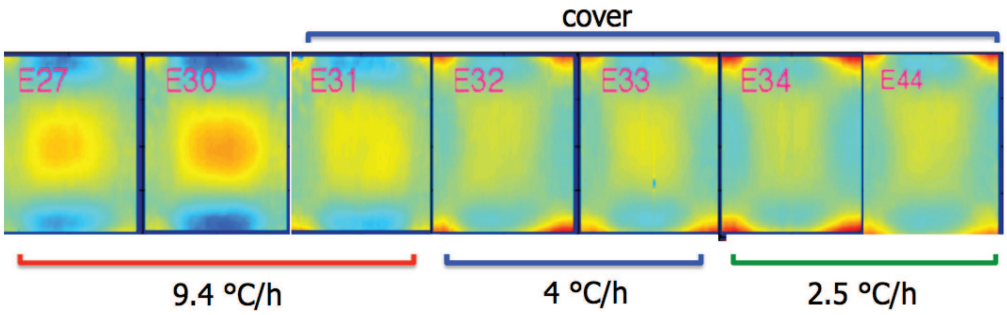

Figure 6.56: *: Central PV reduction with the closing of the muffle (starting from E31) and the reduction of the cooling rate (E32-E33-E34-E44), as seen by the CUP maps after the subtraction of the nominal cylinder with radius of curvature of 1m, and after a linear detrend for each longitudinal line. Credits: CUP maps by M. Civitani.*

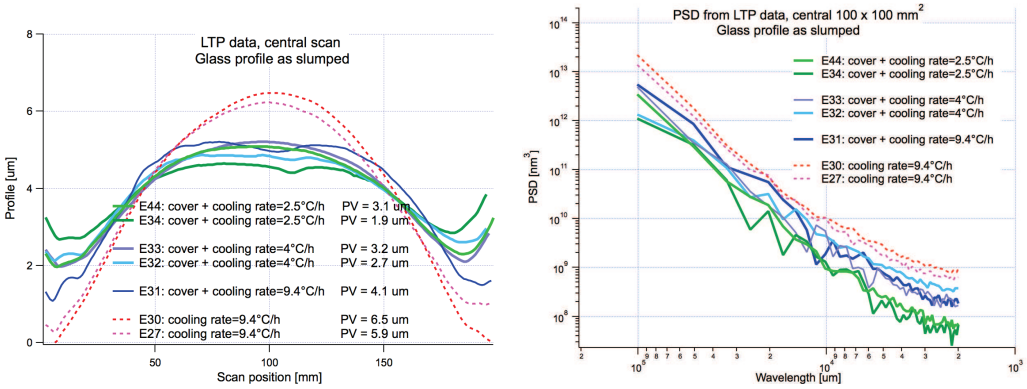

Figure 6.57: *: Central PV reduction (left) and mid-frequency errors reduction (right), as measured with the LTP-FEA, for the glass foils of Fig. 6.56. Note the smaller mid-frequency contribution, in a large frequency range, when decreasing the cooling rate.*

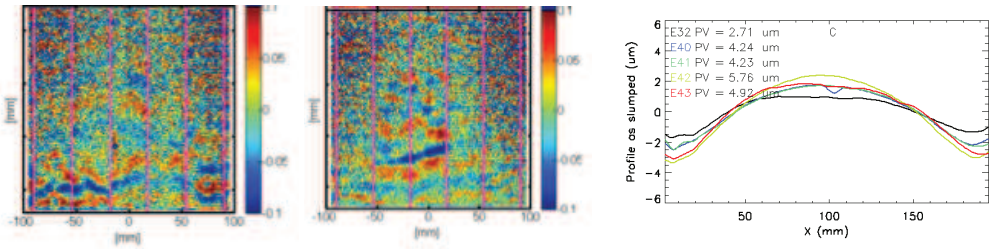

Figure 6.58: *: Two runs done in furnace B, E42 (left) and E43 (centre), interestingly show a very small contribution from mid-frequency errors: this can be seen by the CUP maps after the subtraction of the Legendre polynomials up to the 8nd order. Credits: CUP maps by M. Civitani. Nevertheless, they cannot reach the good result obtained in furnace A, in terms of PV, as can be seen by the central scan comparison of several glass foils, measured with the LTP-FEA (right).*

Table 6.11: *: Results from the Eagle glass foils of Table 6.10. The PV value of the central scan, and the HEW values computed from physical optics are shown, both before integration (as-slumped) and after the simulation of the integration. The data from the E39 glass foil are not reported as highly deformed.*

	PV [μm] of C scan	HEW [arcsec] as slumped	HEW [arcsec] predicted after integration		
			only profile	profile + roughness at 1 keV	profile + roughness at 1.5 keV
E27	5.9	27.7	4.7	4.9	5.3
E28	5.8	25	5.6	5.8	6.1
E29	7.9	45	8.6	9.5	10
E30	6.5	34	5.9	6.3	7.1
E31	4.1	25.9	6.6	6.9	7.3
E32	2.7	21.5	5.0	4.8	5.3
E33	3.2	21.7	5.3	5.4	6.1
E34	1.9	22.4	5.1	5.3	5.7
E35	3.5	25.1	5.3	5.4	5.9
E36	4.8	27	6.0	6.2	6.7
E40	4.3	30.7	5.5	5.7	5.9
E41	4.3	29.5	5.0	5.1	5.6
E42	5.9	29.6	3.9	4.0	4.3
E43	4.9		3.5	3.7	4.4
E44	3.1	22.1	4.5	4.7	5.0
E45	2.7	21.3	4.1	4.2	4.7

Finally, to summarise the result of Eagle glass foils slumped on MK20-20, the HEW values expected from LTP profiles and the rms computed from roughness data, resolved by scan in order to visualise the glass foil dis-uniformity and averaged for the entire glass, are reported in Fig. 6.59 and Fig. 6.60, respectively.

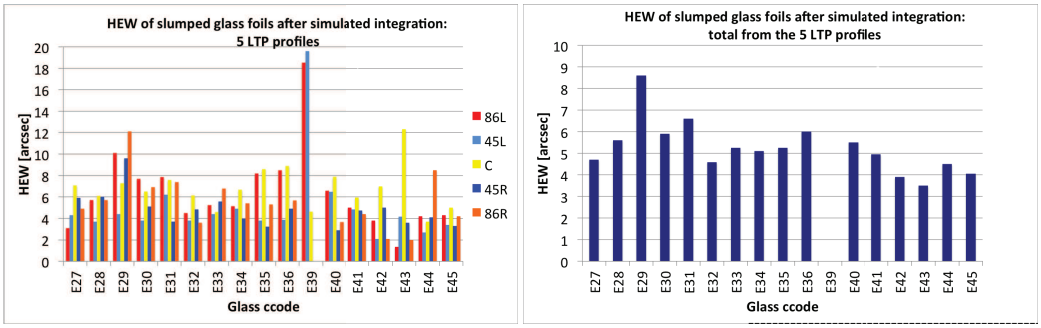

Figure 6.59: *: HEW values as computed from LTP data after the simulation of a perfect integration. Left: the five scans are shown separately. Right: the total HEW value computed from the five scans. The roughness effect is not included.*

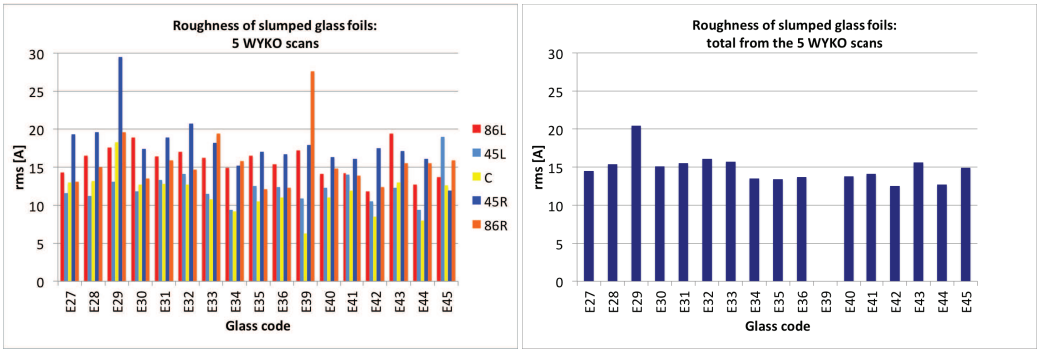

Figure 6.60: *: Rms values as computed from WYKO data. Left: the five scans are shown separately. Right: the average result from the five scans.*

6.6.4 Conclusions

While waiting for the reworking of the MK20-20, I have used the old MK20-10 and considered several parameters to fine tune the shape and roughness of the glass foils towards the goal of 5 arcsec necessary for the ATHENA optics:

1. Finite Element Analysis was carried out, combined with experiments, to define the best mould height: this was set to 1.1 mm higher than the muffle level;
2. a thick closed cover was used to minimise the thermal gradient in the slumping environment, hence reducing the PV and mid-frequency errors;
3. a slower cooling rate around the annealing temperature was used, with the effect of further improve the results. Actually it was found that as the central PV is lower, the more pronounced the foil corner wings become.

The overall improvements, on the glass foils slumped on MK20-10, are:

1. central PV reduction from 7 to 3 μm;
2. HEW computed from the LTP data as slumped from 30 to 12 arcsec;
3. HEW computed from the LTP data after integration from 6 to 5 arcsec;
4. WYKO roughness rms value from 19 to 15 Å (also owing to the new cleaning protocol introduced);

Comparing the results obtained with this work on MK20-10 with the ones obtained on the MK20-20 (used for the production of the POC#3, Section 6.5), we have:

1. central PV reduction from 10 to 3 μm;
2. HEW computed from the LTP data, as-slumped, from 50 to 12 arcsec;
3. HEW computed from the LTP data after integration from 3.5 to 5 arcsec (increase due to higher mid-frequencies on the old mould);
4. WYKO roughness rms value from 11 to 15 Å (increase due to high roughness on the old mould);

Six out of the height glass mirror foils of the POC#4, were selected from glass foils slumped during this work. They were integrated in the Plate Pairs (PP) 1, PP1 and PP2. They are: E27 and E30 in the parabola and hyperbola respectively of the PP2, E32 and E34 in the parabola and hyperbola of the PP1, and E33 and E35 in the parabola and hyperbola of the PP0, the most external layer.

Finally, E45 glass foils combined a small PV to reduced mid-frequency errors, leading to expected HEW less then 5 arcsec in all scans (Fig. 6.59).

6.7 Eagle XG on re-polished MK20-20B: the glass foils for POC#5 and X-ray Surveyor

To further improve the result obtained in section 6.6, the MK20-20, damaged by glass sticking, was re-worked. The new mould was named MK20-20B. The setup for pressure application was also reconditioned, since from the registered pressure values of the E44 and E45 glass foils, the pressure was not maintained constant as it was meant (Fig. 5.5). The mould was used after a proper annealing cycle, which changed the K20 low-frequency shape, but prevented a further deformation with the slumping cycles (Section 6.2.6). Several different pressure values and loops were used, in order to define the best process condition.

6.7.1 Slumped glass foils process parameters

The same parameters used for E44 and E45 were implemented for all the glass foils described in this section: the main difference from case to case is the pressure control system. E46 was slumped with a closed loop at 50 g/cm^2, exactly like E44-E45. Since the setup for pressure application was reconditioned (Section 5.1.4), the result was different, both in terms of maintained pressure values, slumped glass foil shape and roughness. Even if this required a further fine tuning of some parameters, it was essential to understand and control the pressure system.

Table 6.12: *: Process parameters of the Eagle glass foils slumped on MK20-20B. For all the glass foils: mould height = 1.1 mm, mould rotation = 0, soaking time = 4 h, P application start at 750 °C, P application end at 200 °C, annealing time = 2 h, cooling rate = 2.5 °C/h from 722 to 670 °C, new protocol for mould cleaning.*

	Pressure loop [mm]	Pressure value g/cm^2	Muffle cover
E46	closed	50	thick closed
E47	closed	30	thick closed
E48	closed	50 for 1h, then 30	thin open
E49	closed	50 for 1h, then 30	thick closed
E50	closed	first 500, 50 for 1h, then 30	thick closed
E51	closed	50 for 1h, then 30	thick closed
E52	open	50	thick closed
E53	open	50	thick closed
E54	open	50	thick closed
E55	open	50	thick closed
E56	closed	50 for 1h, then 30	thick closed
E57	closed	50 for 1h, then 30	thick closed
E58	open	50	thick closed
E59	open	50	thick closed
E60	open	50	thick closed
E61	open	50	thick closed
E62	open	50	thick closed
E63	open	50	thick closed
E64	open	50	thick closed

6.7.2 Comparison of results: shape, roughness and expected HEW

The process conditions and results from the Eagle glass foils slumped in this phase are hereafter described:

1. E46 was slumped with the same parameters of E44-E45, after reconditioning the pressure control setup (Section 5.1.4 and Fig. 6.61). E46 resulted with a large PV (Fig. 6.62), but very small mid-frequency errors. The expected HEW was therefore much improved in the lateral scans (due to the use of the new MK20-20B) if compared to the E44 (Fig. 6.63). Several

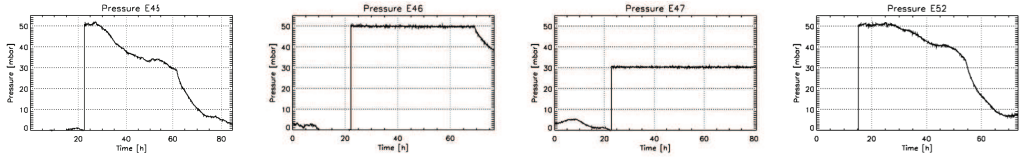

Figure 6.61: *: Pressure reading during the slumping of several glass foils. Before the pressure system reconditioning: E45 with closed loop at 50 g/cm^2. After the pressure system reconditioning: E46 with closed loop at 50 g/cm^2; E47 with closed loop at 30 g/cm^2; E52 with open loop at 50 g/cm^2. Note that E45, processed in closed loop before the reconditioning of the pressure setup, have pressure behaviour very similar to the one of E52, slumped with an open loop after the maintenance: this is a clear evidence of a malfunctioning before the reconditioning.*

residuals were also found from the AFM analysis: as they could not be removed with the standard hydrogen peroxide protocol, some test was performed with plasma etch, as for E23. Due to problems occurred during the etching process, the results were not satisfactory. No further investigation was carried out on the etching.

2. E47: 30 g/cm^2 were applied in closed loop. The rationale was that the mid-frequencies, previsouly observed when decreasing the pressure (E11-E12-E39), could be due to the uncontrolled pressure system. Therefore a controlled lower pressure was tested. The glass was deformed by the presence of entrapped air. To understand the reason of this result, the following foil was processed.
3. E48 was slumped with the thin open cover to access the interference fringes and understand how to treat the air problem observed with E47. 1 h of pressure at 50 g/cm^2 was defined to be sufficient to remove the air. Therefore the pressure was, after 1 h, decreased to 30 g/cm^2, successfully. A relatively high PV was anyway observed, due to the open cover configuration. Therefore, E49 was slumped with the same parameters of E48, but with the thick closed cover.
4. E49: this slumping with closed loop, 1 h at 50 g/cm^2 and the rest at 30 g/cm^2, with the closed muffle, returned the very good result of $PV_{central-E49}$ = 3 μm (Fig. 6.64), and expected HEW = 2.4 arcsec (Table 6.13).
5. E50: just like E49 to check the process repeatability. Actually, an operational error resulted in a very high pressure (around 500 g/cm^2), for a very short time at the beginning of the pressure application. This caused deformations both in the slumped glass and in the slumping mould. The annealing protocol, defined to prevent further deformation of the K20 during the slumping process with standard pressure, is therefore insufficient for such high pressure values.
6. E51: just like E49 to check the process repeatability. The result of E49 could not be reproduced, however (Fig. 6.65). I have so repeated again the setting for E56-E57;
7. E52: it was slumped with the same parameters of E44-E45-E46, but with an open loop. The pressure was observed to decrease with the cooling, as per the gas law. The result was $PV_{central-E49}$ = 3.4 μm, with an expected HEW = 2.7 arcsec. After E52, all the glass foils were slumped with the same process conditions, in order to widely check the process repeatability and also produce height glass foils to be integrated into the next prototype. The CUP maps for the first set of 4 foils can be seen in Fig. 6.67.
8. E53: just like E52 (Fig. 6.67). Fig. 6.68 shows the partial replication of the mould mid-frequency errors.
9. E54: just like E52 (Fig. 6.67).
10. E55: just like E52 (Fig. 6.67). The slightly different result is within the statistical variability of the process.

11. E56 was slumped in closed loop, as for E49-E51, but the system appeared not working properly, as the pressure could not be maintained constant (Fig. 6.66). A scheduled maintenance has to be defined for the future if the system has to be used in closed loop.
12. E57: just like E56, with the same conclusions.
13. E58: just like E52 (Fig. 6.69).
14. E59: just like E52 (Fig. 6.69).
15. E60: just like E52 (Fig. 6.69). This is the best glass foil so far slumped on MK20-20B: Fig. 6.70 displays the high difference in mid-frequency content of this glass foil with respect to E45, the best glass foil slumped on MK20-10.
16. E61: just like E52. Due to dust entrapping in the setup preparation, the glass foils resulted with many dimples.
17. E62: just like E52 (Fig. 6.69).
18. E63: just like E52 (Fig. 6.69).
19. E64: just like E52 (Fig. 6.69).

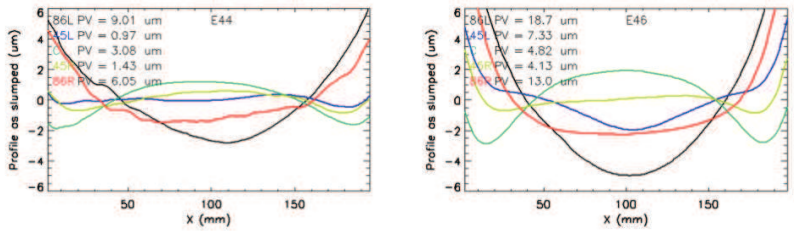

Figure 6.62: *: The effect of the pressure system reconditioning on the profiles measured with the LTP-FEA, on two glass foils slumped with P = 50 g/cm^2 nominally in closed loop. Left: E44 slumped on MK20-10 before the maintenance. Right: E46 slumped on MK20-20B with a reconditioned pressure system.*

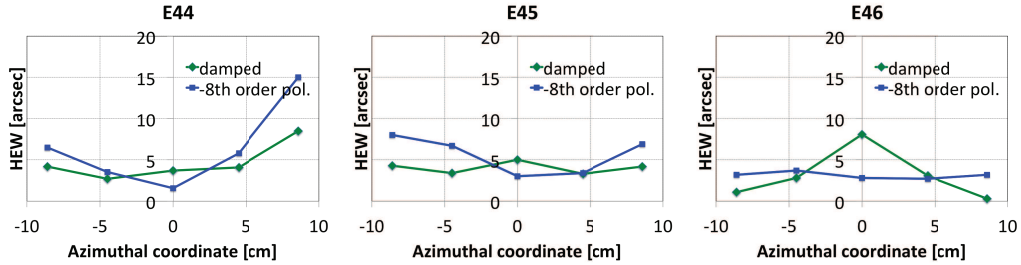

Figure 6.63: *: The effect of the new mould and the pressure system reconditioning on the HEW values computed from the five LTP scans, after the simulation of the ideal integration (green line), and after the subtraction of the best fit 8th order polynomial (blue line). E44 (left) and E45 (center) are slumped on the old MK20-10 before the maintenance, E46 (right) on the new MK20-20B after the maintenance. The improvement obtained with the new MK20-20B on the E46 is evident in the later scans. The central scan value is higher due to the low order deformations introduced by the real closed loop configuration.*

For all the previous Eagle glass foils, I have computed the PSF, from LTP and WYKO data, and the corresponding HEW values. The results presented in Table 6.13 shows the improvement obtained by the use of the MK20-20B, after having solved the problem encountered on MK20-20 and understanding the best pressure setting to be used. The HEW expected from metrological data, after a simulation of a perfect integration, are between 2 and 3 arcsec, very close to the 2

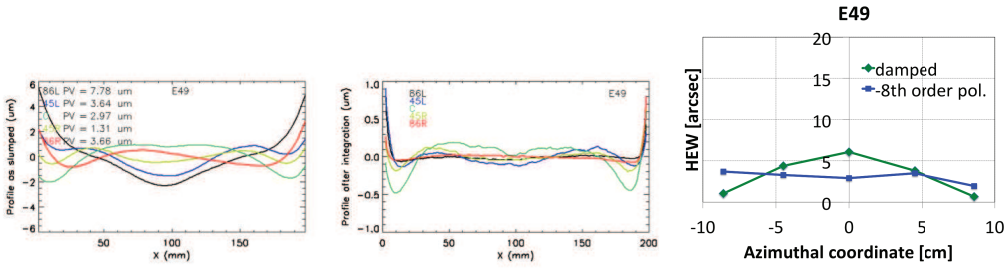

Figure 6.64: *: E49 slumped on the new MK20-20B with a lower pressure, resulted on a lower central PV (left) and lower mid frequency errors (centre: LTP scans after simulated integration). The HEW values computed from the five LTP scans (right), after the simulation of the ideal integration (green line), and after the subtraction of the best-fit 8th order polynomial, show the improved result on this foil with respect to the E46.*

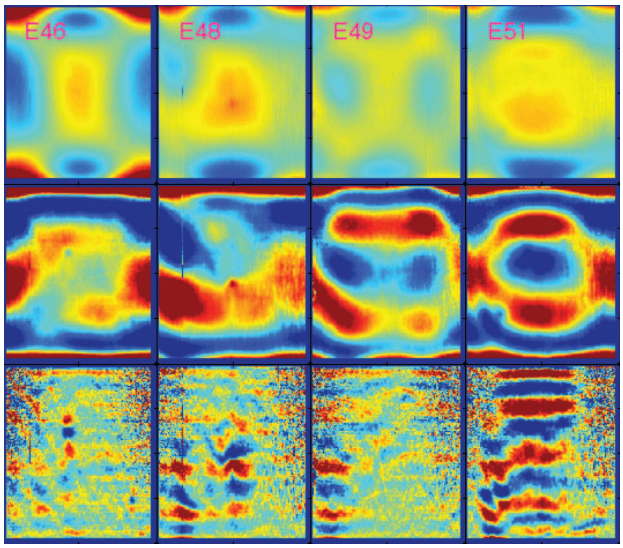

Figure 6.65: *: Different closed loop configurations: E46 with P = 50 g/cm^2, E48-E49-E51 with P = 50 g/cm^2 for the first hour and then P = 30 g/cm^2. The idea was to maintain the low mid-frequency errors of E46 and improve the low-frequency error by reducing the pressure. E48 was slumped with the thin open cover in order to have access to the interference fringes informations. E49 and E51 are slumped in the same nominal conditions, but returned different result. The process conditions were then repeated for E56-E57, but the closed loop pressure system was again not properly working (Fig. 6.66) . From top: CUP maps, after removing the nominal cylinder with radius of curvature of 1 m, with a linear detrend for each longitudinal line; CUP maps, after the subtraction of the Legendre polynomials up to the 2nd order; CUP maps, after the subtraction of the Legendre polynomials up to the 8th order. Credits: CUP maps by M. Civitani.*

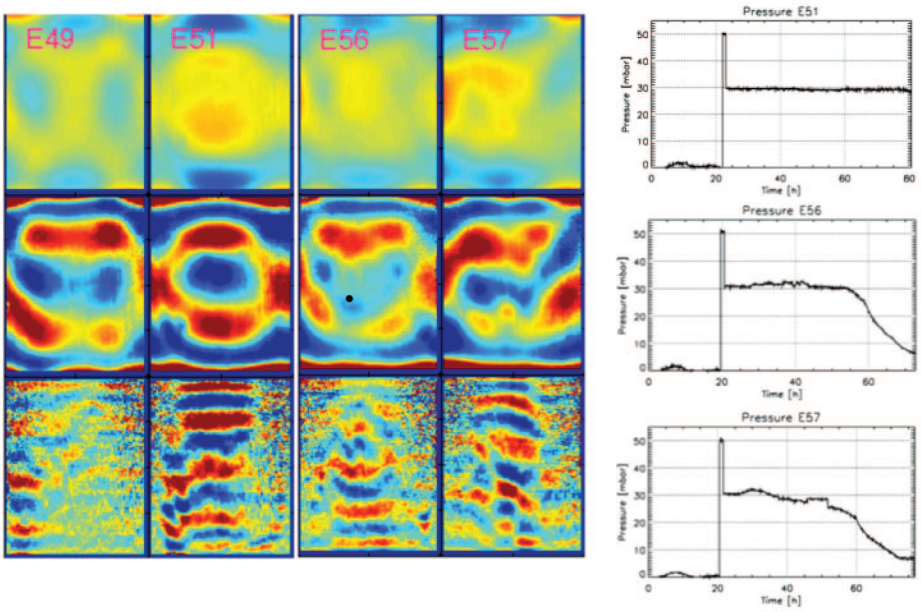

Figure 6.66: *: Foils slumped with in closed loop configuration, with nominally identical process parameters: P = 50 g/cm^2 for the first hour and then P = 30 g/cm^2. The pressure system appeared not working properly for E56 and E57, as the pressure could not be maintained constant. A scheduled maintenance has to be defined if the system has to be used in closed loop. From top: CUP maps, after removing the cylinder with radius of curvature of 1 m, with a linear detrend for each longitudinal line; CUP maps, after the subtraction of the Legendre polynomials up to the 2nd order; CUP maps, after the subtraction of the Legendre polynomials up to the 8th order. Credits: CUP maps by M. Civitani.*

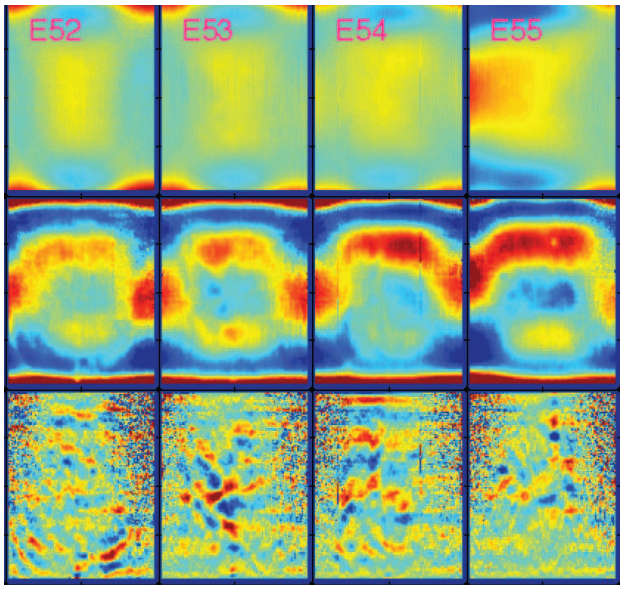

Figure 6.67: *: Foils slumped with P = 50 g/cm^2 in open loop configuration, with identical process parameters. These foils, together with the ones shown in Fig. 6.69, represent the best result of this thesis. The differences are to be read as process statistical variability, most probably attributed to slight differences in the setup. From top: CUP maps, after removing the cylinder with radius of curvature of 1 m, with a linear detrend for each longitudinal line; CUP maps, after the subtraction of the Legendre polynomials up to the 2nd order; CUP maps, after the subtraction of the Legendre polynomials up to the 8th order. Credits: CUP maps by M. Civitani. These data show the great improvement in mid-frequency reduction, obtained with the new process and the new mould.*

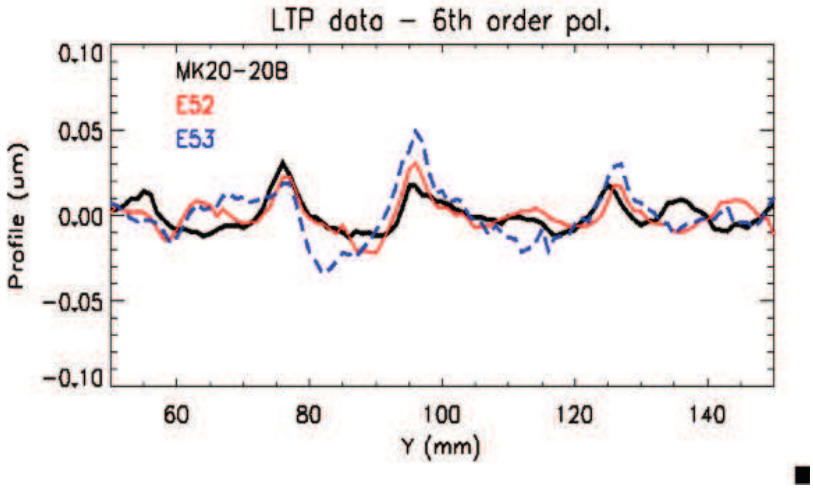

Figure 6.68: *: Mid-frequency errors of the MK20-20B mould replicated on the slumped glass E52 and E53. LTP scans at the same location (45 mm right from the centre), after the subtraction of the 6th order best fit polynomial. The graphs shows that, after the optimisation of the slumping process, we can evidence the smaller mid-frequency contribution from the mould replication.*

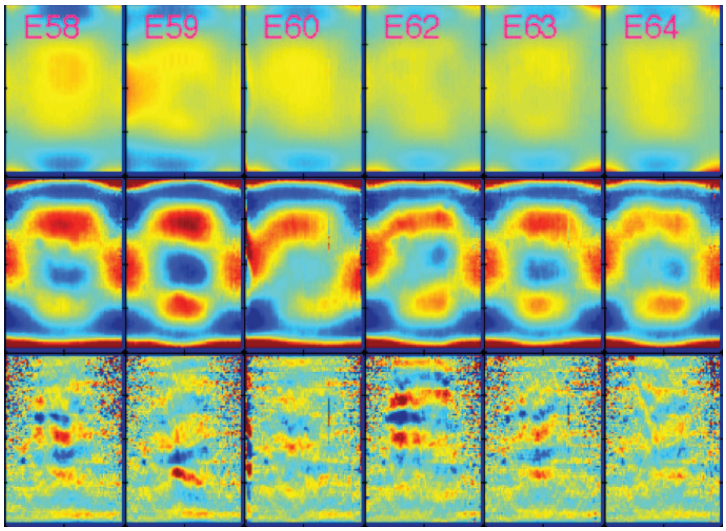

Figure 6.69: *: Foils slumped with P = 50 g/cm^2 in open loop configuration, with identical process parameters as E52-E53-E54-E55. These foils, together with the ones shown in Fig. 6.67 represent the best result of this thesis. The differences are to be read as process statistical variability, most probably attributed to slight differences in the setup. From top: CUP maps, after removing the cylinder with radius of curvature of 1 m, with a linear detrend for each longitudinal line; CUP maps, after the subtraction of the Legendre polynomials up to the 2nd order; CUP maps, after the subtraction of the Legendre polynomials up to the 8th order. Credits: CUP maps by M. Civitani.*

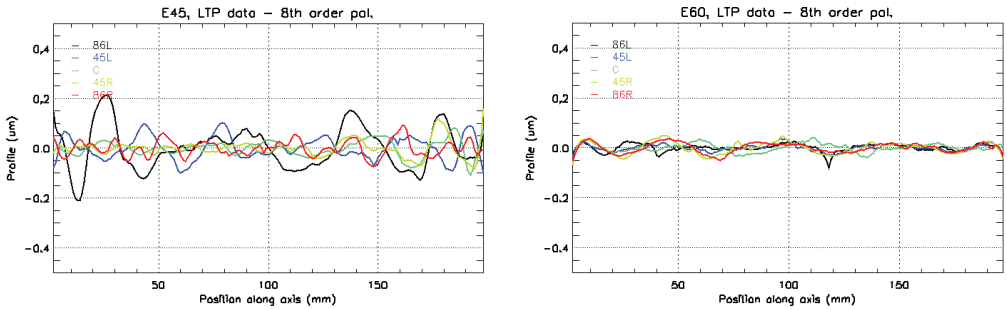

Figure 6.70: *: Mid-frequency content comparison of E45 (the best glass foil slumped on MK20-10) and E60 (the best glass foil slumped on MK20-20B). The graphs are obtained from raw LTP data after the subtraction of the best fit 8th order polynomials. They show the great reduction of mid-frequency errors in the last foils.*

arcsec value allocated for the slumped glass foils (Section 3.9). This result has to be compared with the ~ 7 arcsec computed in the same way for the glass foils of the POC#2.

Table 6.13: *: Results from the Eagle glass foils of Table 6.12. The PV of the central scan and the HEW values computed from physical optics are shown, both before integration (as slumped) and after the simulation of the integration.*

	PV [μm] of C scan	HEW [arcsec] as slumped	HEW [arcsec] predicted after integration		
			only profile	profile + roughness at 1 keV	profile + roughness at 1.5 keV
E46	4.8	38.3	2.2	2.2	2.7
E48	5.7	32.3	2.1	2.2	2.4
E49	2.9	27	2.4	2.4	3.0
E50	5.3	27.3	4.5	N.A.	N.A.
E51	5.4	27.4	2.9	3.0	3.5
E52	3.4	20.7	2.8	2.8	3.2
E53	2.9	22.4	1.9	2.1	2.7
E54	2.7	19.1	1.9	2.1	2.7
E55	3.6	20.7	2.3	2.5	3.2
E56	3.6	21.4	2.4	2.5	2.8
E57	3.8	23.7	2.9	N.A.	N.A.
E58	4.9	23.7	2.5	2.5	3.2
E59	3.8	14.4	2.2	2.2	2.5
E60	3.7	21	2.1	2.2	2.5
E62	3.2	17	2.2	2.4	2.7
E63	3.1	13	2.4	2.4	2.8
E64	3.6	15	2.0	2.0	2.1

As previously done, to summarise the results of Eagle glass foils slumped on MK20-20B, the HEW values expected from LTP profiles and the rms computed from roughness data, resolved by scan in order to highlight the glass foil dis-uniformity and averaged for the entire glass, are reported in Fig. 6.71 and Fig. 6.72.

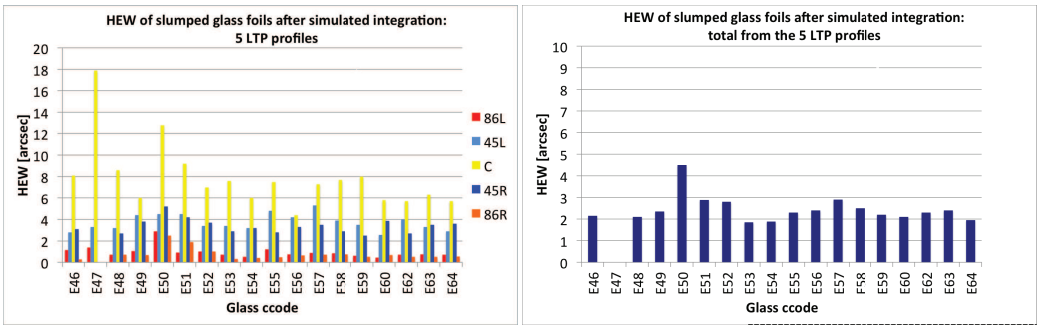

Figure 6.71: *: HEW values as computed from LTP data after the simulation of a perfect integration. Left: the five scans are shown separately. Right: the total HEW value computed from the five scans. The roughness effect is not included.*

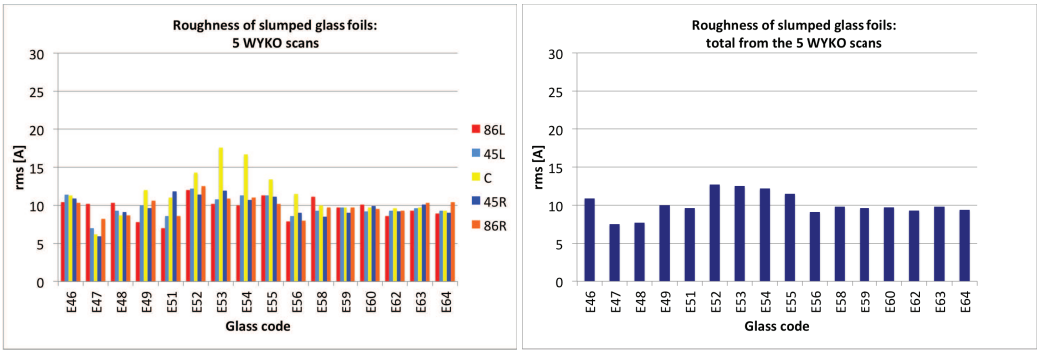

Figure 6.72: *: Rms values as computed from WYKO data. Left: the five scans are shown separately. Right: the averaged result from the five scans.*

6.7.3 Conclusions

The slumping activity with the re-figured mould MK20-20B was carried out with a refurbished pressure control system. The pressure could be maintained constant by a closed loop control, properly working. Anyway, few tests clarified that the best result could be obtained with 50 g/cm^2 in open loop. The process parameters were set as the ones of E44-E45, the best glass foils out of the previous fine tuning on MK20-10. The measured applied pressure, in open loop, was in line with the one of the E44-E45 slumping. Ten glass foils were slumped with these best process parameters, in order to produce the mirrors to be integrated into the next prototype, and to check for process repeatability (Section 6.7).

The improvements on these glass foils are:

1. central PV = 3.5 $\pm$ 0.6 μm, to be compared with 3 μm for E44-E45.
2. HEW computed from the LTP data, as-slumped = 18.7 $\pm$ 3.6 arcsec, to be compared with 22 arcsec for E44-E45.
3. HEW computed from the LTP data after simulated integration = 2.2 $\pm$ 0.3 arcsec, to be compared with 4.3 arcsec for E44-E45. The angular resolution expected from metrology has been improved by a factor of two.
4. WYKO roughness rms = 10.7 $\pm$ 1.4 Å, to be compared with 13.8 Å for E44-E45, and with 16 Å tolerance (Section 6.2.1).

The improved results are due to the use of the new MK20-20B, since E44-E45 were slumped on the old MK20-10, with a surface with poor quality: both mid- and high-frequency errors were reduced using MK20-20B.

With respect to the result previously obtained on MK20-20, the modified mould height solved the problem of entrapped air, which forced the use of pressure starting at room temperature and resulted in a higher PV of the slumped glass foils. Moreover, the reduced thermal gradients and the lower cooling rate could further decrease the low- and mid-frequency errors. The introduction of a new mould cleaning protocol also reduced the high-frequency errors.

With the improved mould replication, for the first time we partially inherit the mid-frequency features on the mould. These errors account for about 1 arcsec in the final HEW of the slumped glass foil. Therefore, the mid-frequency term of the HEW is related to the mould quality. Work is going on at OAB to improve the moulds figure by IBF (Ion Beam Figuring).

6.8 A further step forward: lower roughness and lower mid-frequency errors

The roughness of the slumped glass foils should be kept as low as possible, preserving if possible the original surface of the bare glass foil (rms = 3.6 Å in the WYKO range), in order to minimise the contribution from the scattering to the final HEW of the mirror. It was already shown (Eq. 2.21) that the scattering increases with the increasing roughness, and this is enhanced at high X-ray energy and high incident angles. During all the work in this thesis, I have considered a roughness tolerance of 16 Å in the WYKO frequency range, as a limit in order to have a contribution from roughness not exceeding 1 arcsec at 1 keV and 0.7 deg incidence angle. During this work, the roughness of the slumped glass foils was shown to have been reduced from about 20 Å for the POC#2-like foils to 10.7 Å for the last foils slumped on MK20-20B. Attempts to further lower this value, by decreasing the pressure (from 50 to 20 g/cm^2) in order to have a smaller replication of the mould roughness (rms-mould $\sim$ 130 Å in the WYKO range, Fig. 6.15), always resulted in an increase in mid-frequency errors (glass foils E11-E12 in Section 6.3, E39 in Section 6.6, E47 in Section 6.7). Some foils were slumped with a pressure value of 50 g/cm^2 for 1 h, then 30 g/cm^2 for the rest of the cycle, but the roughness was not improved significantly (glass foils E48-E49-E50-E51-E56-E57 in Section 6.7).

A different approach was found to be effective at reducing both mid- and high- frequency errors (E65 and E67). The pressure was maintained at value of 50 g/cm^2, but the thermal cycle and the pressure application time were changed.

1. Thermal cycle:
   - the temperature ramp up now goes from 20 to 722 °C (and not 750 °C) in 11 h with an heating rate of 63.8 °C/h, and from 722 to 750 °C in 4 h with an heating rate of 7 °C/h. The lower heating rate close to the soaking temperature is aimed at reducing the temperature gradients.
   - E66 was slumped with the standard 4 h holding time at the soaking temperature. E65 and E67 were slumped without an holding time at the soaking temperature
2. Pressure application time:
   - the standard pressure application time is at the reach of the soaking temperature, 750 °C
   - for E66 the pressure of 50 g/cm^2 was applied at the reach of the soaking temperature. For E65 and E67, the pressure was applied after 1 h of the second ramp up branch, that is at 729 °C

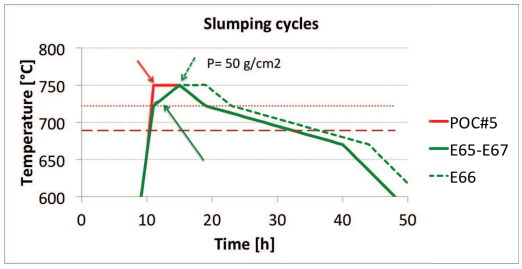

Figure 6.73: *: Thermal cycles comparison. The arrows represent the moment for the pressure application. The red line represents the thermal cycle of the glass foils that will be integrated into the POC#5 (Fig.s 6.67 and 6.69). The green solid line line is the cycle used for E65 and E67, which resulted in a lower mid- and high-frequency errors. The green dashed line is for E66, which resulted deformed by entrapped air bubbles.*

The improved result with the new process is shown in Fig. 6.74 for the roughness and Fig. 6.75 for the expected HEW. The shorter time spent at higher temperature is responsible for the lower roughness value. The pressure application at 729 °C allows mid-frequency to be small, i.e. comparable to the glass foils slumped in the previous experiments (the ten glass foils for the POC#5). On the contrary, the pressure application at 750 °C for E66 resulted in air bubbles entrapped during the slow heating from 722 to 750 °C, caused by a partial slumping of the glass foil.

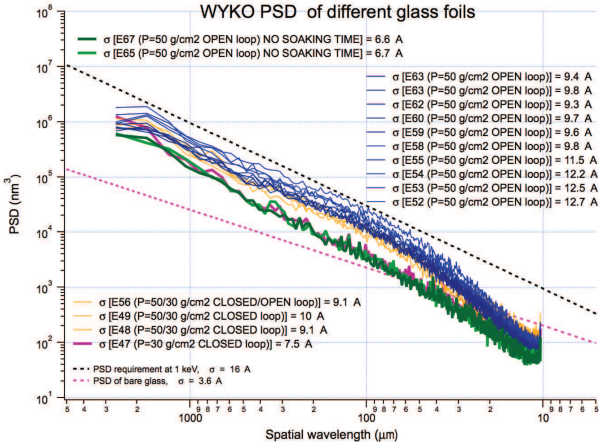

Figure 6.74: *: PSD from WYKO data of various slumped glass foils. Green lines correspond to E65 and E67 glass foils, slumped with the new process. Blue lines corresponds to the ten glass foils slumped for the POC#5 (Section 6.8). Yellow lines represent the PSD of glass foils slumped at pressure values of 50 g/cm^2 during the first hour, and the rest at 30 g/cm^2. Pink line denotes E47, slumped at a pressure value of 30 g/cm^2, but resulted deformed.*

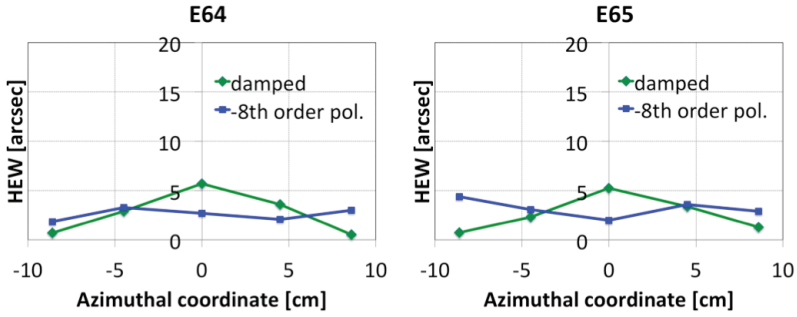

Figure 6.75: *: Comparison of expected HEW values for E64 slumped with the previous process, and E65 slumped with the new process described in this section. The figure shows comparable results for the two processes, but for E65 the roughness is much lower.*

6.9 Final remarks on the quality of the slumped glass foils

This Ph.D. research was divided into six steps: in each step, few parameters were modified to improve the quality of the slumped glass foils. While some resulted in a real improvement, others did not improve the result, but increased the understanding of the process (pressure value, pressure application time, annealing time, etc.). The reference starting point was the F18, a Schott AF32 glass foil, slumped on MK20-10 with the same parameters of the glass foils integrated into the POC#2.

In the following scheme, I summarize the glass-to-mould combination and the effective parameters, modified in each step:

1. AF32 on MK20-10. Effective parameters: mould height from 0 to 2.5 mm, soaking time from 2 to 4 h;
2. Eagle on MK20-10. Effective parameters: even the sole glass type change has been effective at improving the process;
3. Eagle on MK20-20. Effective parameters: pressure application at room temperature. This was modified in the next step, since it was increasing the PV even if solving the air bubble problems;
4. Eagle on MK20-10. Effective parameters: mould height optimisation by FEA and experiments to 1.1 mm, thermal gradients reduction, cooling rate reduction from 9.4 to 2.5 °C/h in the temperature range from 722 to 670 °C;
5. Eagle on MK20-20B. All the effective parameters were implemented for the new slumping mould MK20-20B.
6. Eagle on MK20-20B. Slower heating from $T_{annealing}$ to T_{soak}, pressure application before T_{soak}, and no time spent at T_{soak}

Table 6.14 summarizes the major improvements obtained in these thesis, in terms of quality of the slumped glass foils.

Table 6.14: *: Improvements of the most important parameters, which measure the quality of the slumped glass foils: peak to valley of the central LTP scan, expected HEW from the raw LTP data (as-slumped), expected HEW from LTP data after the simulation of a perfect integration, rms roughness from WYKO data. I have divided my Ph.D. research into six steps, each one characterised by the improvement of some particular parameters.*

Step	Description	Best glass	PV [μm] of C scan	HEW [arcsec] as slumped	HEW [arcsec] predicted after integr.	WYKO rms [Å]
Ref.	POC#2 like	F18	17.6	120	6.8	20.8
1	AF32 on MK20-10	F30	9.8	43.3	6.6	18.3
2	Eagle on MK20-10	E5	5.0	25.3	5.3	18.3
3	Eagle on MK20-20	E21	9.0	40	3.6	12.8
4	Eagle on MK20-10	E45	2.7	21.3	4.1	14.9
5	Eagle on MK20-20B	10 glasses	3.5 ± 0.6	18.7 ± 3.6	2.2 ± 0.3	10.7 ± 1.4
6	Eagle on MK20-20B	E65	2.5	25.7	2.4	6.7

The ten glass foils slumped with the same process parameters evidence a stable process. The HEW value predicted from LTP data, after the simulation of a perfect integration, is almost in line with the error budget allocated for the slumped glass foils (2 arcsec, Section 3.9). Approximately 1 arcsec is due to replication of the mid-frequency errors in the slumping mould, which are for the first time, owing the improved result in the slumping, partially replicated on the slumped glass foil. From the point of view of roughness, the main part of the work has been carried out keeping the roughness contribution to the final HEW less then 1 arcsec at 1 keV and 0.7 deg incidence

angle (Section 6.2.5). The roughness was decreased from 20.8 to 10.7 Å measured on the ten slumped glass foils produced during step 5 of the research. Going to higher X-ray energies or higher incidence angles required a further lowering of the roughness. This was reached in the last part of this thesis (step 6), with the development of a new process capable to maintain the low amplitude of the mid-frequency errors, and reduce the roughness replication from the mould onto the slumped glass foils. This result makes the technology attractive for telescopes sensitive also in the hard X-ray band.

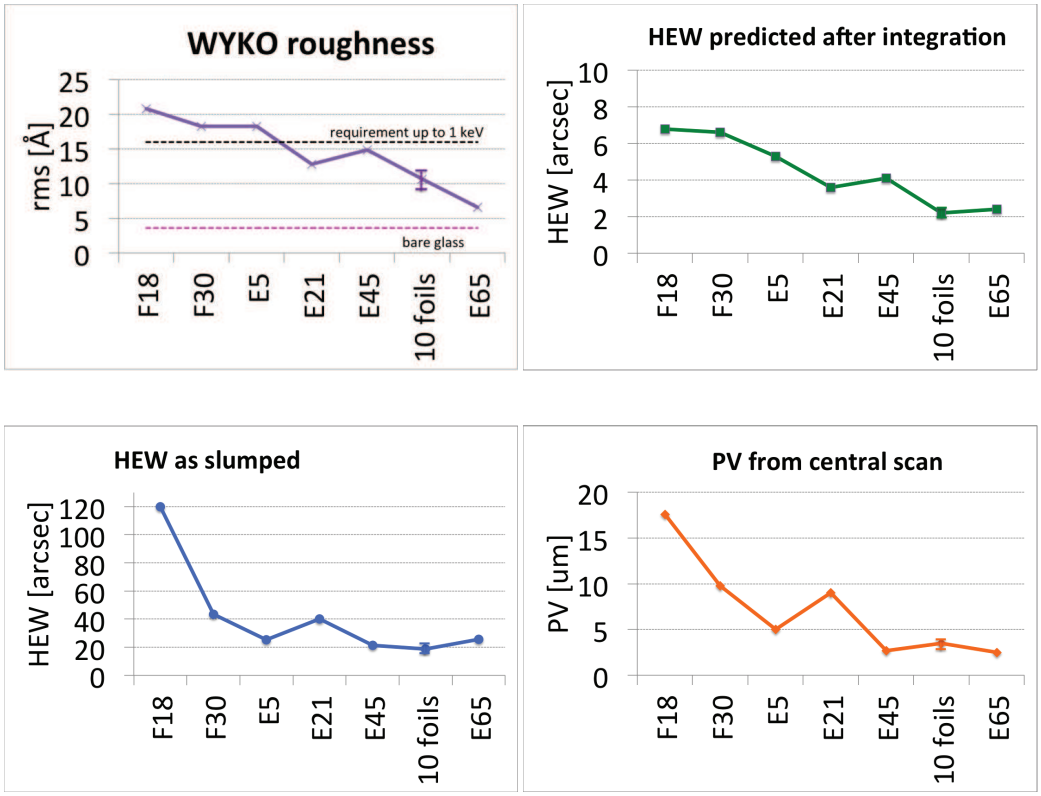

Figure 6.76: *: Trend of the results obtained in the six phases of this Ph.D. thesis. Top left: Roughness from WYKO data. Top right: HEW computed from LTP data after the simulation of a perfect integration. Bottom left: HEW computed from raw LTP data. Bottom right: PV of the central scan, the most critical as the less corrected during the integration.*

CHAPTER 7

Alternative materials and processes

After demonstrating the capabilities of the SGO technology for high-resolution X-ray space telescopes, I have considered the possibility to improve the performances bypassing the limits of our setup. Several aspects were considered:

1. reduced strength of the glass foils after the slumping: use of Gorilla® glass
2. mismatched CTE of the Gorilla® glass and K20 mould: use of Al_2O_3 for Gorilla®
3. Zerodur K20 deformation: use of Si_3N_4 for Eagle XG
4. dust released by our insulating felt: use of alternative felts
5. degradation of the optical surface in the direct slumping: use of dip coating
6. degradation of the optical surface in the direct slumping: use of indirect slumping

7.1 Corning Gorilla® glass

7.1.1 Scientific motivation

The thermal cycle and the contact of the glass with the mould might affect the strength of the glasses, hence our group carried out an intensive study to check the effect of the slumping process on the strength of the glasses [Proserpio et al. 2013, Proserpio et al. 2014]. This work was committed by the European Space Agency during the contract "The Back-up IXO (former XEUS) optics Technology, Phase 1". Due to the large number of IXO glass mirror segments (16.560), the problem required a statistical approach (Weibull statistics). Two reference values for the reliability of the whole mirror assembly were provided by ESA, the stricter being 99.99% and the looser 99.00%. These numbers represent the probability to avoid any "catastrophic" breakage, defined to be when causing the detachment of a large number of glass fragments, floating in the spacecraft and leading to the complete mission failure [IXO-BCV-RE-002 2011]. Due to the

large number of the IXO mirror foils, and considered that the usual glass strength distributions exhibit a broad statistical distribution, the evaluation of the Weibull parameters characterizing the full mirror foil population required a very large number of specimens. To this aim, more than 200 samples of Schott D263 glass were used to perform double-ring destructive tests. As a main result of the study, it has been found that the minimum tensile stress at measured breaking point was 82 MPa for curved glasses, just slightly smaller if compared to the 117 MPa for the as-delivered flat glasses before slumping. The reduction of the glass strength by the slumping process could ensure a survival probability of 99.00% for the IXO telescope, while the more conservative survival level of 99.99% could not be reached. These requirements appears very strict, especially when compared with the NuSTAR telescope, that is also based on the same technology. The NuSTAR flight optics successfully survived vibration tests [Craig et al. 2011]. Moreover, more than 400 representative witness coupons were produced to test the NuSTAR manufacturing process: the bondings, rather than the glass foils themselves, were defined as the primary mode of failure. Nevertheless, we have to consider that the number of the IXO glass foils is much larger (16.560) than the one for NuSTAR (2.376 foils for each of the two optics) increasing the probability than one single foil would break. Moreover, the NuSTAR entrance and exit apertures of the optics modules are protected with thermal covers [Craig et al. 2011], that would also prevent possible glass fragments to float in the spacecraft in case of breaks. The comparison of the loads that the two optics had-should sustain is not trivial. Equivalent static loads at launch of $\pm$ 70 g in the longitudinal and $\pm$ 55 g in the lateral direction where considered for IXO to compute the survival probability [Parodi et al. 2011]: these values were obtained rounding the algebraic sum of the quasi-static transient loads (longitudinal = 18 g, lateral = 4 g), provided by ESA, and random vibrations effects managed as equivalent static loads (longitudinal = $\pm$ 50 g, lateral = $\pm$ 50 g). No equivalent numbers are reported in the literature for NuSTAR, to our knowledge. Anyway, since the telescope structures are totally different, the loads on the telescope would also be different. Based on the numbers obtained in our research, possible solutions to increase the survival probability of the mirror assembly were studied. A natural choice is to re-enhance the slumped glass strength with a step of chemical tempering after slumping. The chemical tempering, in fact, changes the surface properties of the glass introducing a compressive layer that enormously strengthens the glass. As the increase in strength is strongly dependent on the glass type, Corning® Gorilla® glass was selected, a glass renowed for its capability to develop high compressive strength.

7.1.2 Gorilla® glass versus other glass types

As the glass is a brittle material and the telescope have to withstand the intense stresses experienced during the launch, the strength of the glasses must be carefully considered. If the glass surface were flawless, the strength would approach the theoretical value of 20 GPa (Holloway 1973), as computed from the bonding energies of silicon and oxygen. Indeed, the glass surfaces are subject to damage during manufacturing, leading to increased stress near the flaws according to Eq. 7.1 [Inglis 1913, Griffith 1924, Kulp Master thesis 2012]:

$$\sigma = 2\sigma_A \left(\frac{l}{r}\right)^{\frac{1}{2}} \tag{7.1}$$

where σ_A is the applied stress, σ the stress on the flaw tip, l the flaw length, r the flaw tip radius, assumed to be equal to the interatomic distance ($\sim$ 1 Å). When the applied stress causes σ to exceed the theoretical strength, a failure will occur. Typical defects occurring on the glasses have l ranging from 1 to 100 μm, returning maximum applicable stresses from 100 to 10 MPa, respectively. A further slight damage is introduced by the hot slumping process, contributing to a reduction of the glass foil resistance, as already demonstrated with D263 glass foils (Proserpio 2014). Therefore, we have considered the possibility to re-enhance the glass strength after the slumping. There are several techniques to improve the glass strength, one of which is chemical

strengthening. In this method, the glass is dipped in a molten salt bath (Uhlmann 1980), with temperature ranging from 350 to 550 °C. During the process, at the interface between the glass and the molten salt, two types of alkali ions exchange places with each other [Adamson & Gast 1997], for example a sodium ion from the glass will exchange places with a potassium ion from the bath. The ion exchange is temperature and time dependent. As the potassium ion occupies a larger volume than sodium, a compressive stress will be developed in the part of the glass where the ion exchange process occurred. One of the most important parameters is the depth at which this process occurs, because the strengthening process effectiveness increases with the depth. In addition to time and temperature, the composition of the glass and the ion exchange species play an important role in the ion exchange process. It has been shown [Uhlmann et al. 1980], that alkali-alumina-silicate glasses (like the Gorilla® glass) are the most receptive to the ion exchange process. Borosilicate glasses (like D263 glass) instead have been shown to be a less desirable composition. Although the process can still be carried out using this composition, it occurs at a slower rate, and yields lower strengths and exchange depths. Table 3.2 presents a comparison of some key parameters of the Gorilla® glass with other glass kinds used in our laboratories for the slumping technology development for X-ray telescopes. Note that neither Eagle nor AF32 glass are suitable for chemical tempering as they are alkali-free glass.

The Gorilla® glass was selected for this investigation among three available aluminosilicate thin glasses (Corning® Gorilla® glass, SCHOTT XensationTM Cover glass and AGC DragontrailTM) because of the particular Corning® forming process (fusion for the Gorilla® glass, microfloat for the SCHOTT XensationTM and float for the AGC DragontrailTM), which, in my experience, gives the best results in terms of microroughness. The Gorilla® glass generation 2 was used because it exhibits the same resistance characteristics as the generation 1, even if it is thinner by 25%. The used thickness was 0.55 mm, the thinnest at the time of the research. It is reported (Corning spec, Gorilla 2), that this glass, after tempering, develops a compressive stress beyond 800 MPa with a Depth Of Layer (DOF) larger than 40μm, to be compared to typical values of minimum tensile stress at breaking point ranging from 100 to 150 MPa for non-tempered glasses [Kulp Master thesis 2012].

In order to ascertain if the surface roughness of the tempered Gorilla® glasses does not degrade the high angular resolution required to slumped glass mirrors, I have measured a flat tempered Gorilla® glass with the WYKO interferometer. The Power Spectral Density (PSD), computed from these measurements, was compared with the ones of the brand new glasses that we are evaluating for the production of X-ray optics, namely D263, AF32 and Eagle XG glasses. The result was already presented in Fig. 6.3. The measurements show that the chemical tempering does not introduce any degradation on the glass surface micro-roughness with respect to non-tempered glass foils.

7.1.3 Slumping of the Gorilla® glass

The mould used for the slumping of the Gorilla® glass foils was the same used for the production of the prototypes POC#2 and POC#4 (Section 6), that is the cylindrical mould in Zerodur K20, MK20-10. The CTE is mismatched with respect to the Gorilla® glass foils ($CTE_{Gorilla}$ = 8.1 10^{-6}/K, CTE_{K20} = 2.2 10^{-6}/K), but the mould was anyway used to the sole aim of investigating the effect of chemical tempering. In section 7.2 preliminary slumping tests of Gorilla® on Alumina are presented (CTE_{Al2O3} = 7.5 10^{-6}/K; hence Alumina better matches the Gorilla).

In order to assure the non-sticking behavior of the Zerodur K20 with the Gorilla® glass, preliminary slumping tests were performed on small flat Zerodur K20 sample moulds. Different combinations of temperatures (600 to 650 °C) and pressure (0 to 50 g/cm^2) were tested and the final thermal cycle was defined (Table 7.1) with a pressure application of 50 g/cm^2, starting just after reaching the soaking temperature 620 °C, and ending at temperature below 200 °C, in cooling-down phase. Four Gorilla® glass foils were slumped on the cylindrical Zerodur K20 using the thermal cycle described in Table 7.1.

Table 7.1: *: Thermal cycle for the slumping of the Gorilla® glass*

Step	Temperature [°C]	Time [h]
1	25 → 620	10
2	Hold at 620	2
3	620 → 602	4
4	Hold at 602	2
5	602 → 530	10
6	530 → 450	5

7.1.4 Cutting and tempering

The glass foils, slumped to size of 340 × 340 mm^2, were preliminarily cut to approx. 230 × 230 mm^2. The cut was done propagating an initial crack in the glass foil by means of a hot tip. The glass foils were then cut by CO_2 laser at MDI-Schott in Germany in four 100 × 100 mm^2 foils (Fig. 7.1). This was done to increase the statistic of the result. The CO_2 laser was used because it is reported to be the best cutting process to avoid edges micro-cracking and chipping [Coherent Inc. Application report 2008]: defects introduced by the cutting process are reported to reduce the strength of the glass and therefore also the survival probability of the glass foils during the tempering process. The chemical tempering of these slumped glass foils was done at EuropTec (Switzerland) in their standard production baths. None of the glass foils broke down during the tempering process.

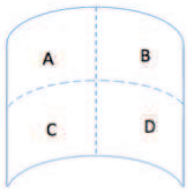

Figure 7.1: *: The slumped glass foils were cut into four 100 × 100 mm^2 glasses by CO_2 laser.*

7.1.5 Roughness and shape characterization

The four slumped foils have been measured in shape, prior the CO_2 laser cutting, with the CHR mounted on the LTP to evaluate the glass profile deviation from the mould. Due to the glass and mould mismatched CTE, only one glass foil (named G7) was considered appropriate for the study. The surface roughness of the slumped and tempered Gorilla® glass sub-foils, obtained form the G7 foil, were measured with the WYKO interferometer on their central axis, and the results were compared to the surface roughness measurements obtained from the flat tempered Gorilla® glass foil. The measurements show (Fig. 7.2) that the entire process of slumping and tempering does not introduce any degradation on the glass surface micro-roughness, and it is therefore suitable for the production of X-ray glass mirrors.

The four samples, obtained from the G7 glass foil, were characterised in shape before and after the chemical tempering, using both the CHR - LTP (mono-dimensional profiles) and the CUP (bi-dimensional surface map). Three profiles were measured with the CHR - LTP before and after chemical tempering: the actual profiles are derived from the difference of the measurements with concavity up and down, in order to subtract the gravity and the bearing deformations. The scans are at the central position (denoted as C), and 30 mm left and right of the foil center (denoted as 30R and 30L). Fig. 7.3 shows that the chemical tempering reverses the concavity of the profile error in the longitudinal direction, with a reduction of the peak-to-valley (PV). Even

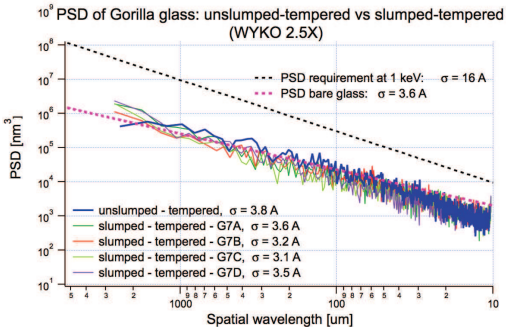

Figure 7.2: *: PSD of the slumped and tempered Gorilla® glass foils G7A, G7B, G7C and G7D, compared to the PSD of the flat tempered Gorilla® glass foil.*

though the integration procedure acts as a damping of the low-frequency errors (Parodi 2011), the remaining amplitude of the low-frequency error still represents a contribution to the angular resolution degradation. To understand whether the mid-frequency errors are real profile features or metrology artefacts, the LTP was used in its usual slope-detecting configuration, combined with the used of First Contact® (by Photonic Cleaning) to suppress the reflection of the back surface of the glass, and FEA to subtract the gravity and bearing point deformation (Section 4.2.3). This method was used only for the slumped and tempered samples. For the glass foils before slumping, this solution had not been found yet at the measurement time, and the LTP-CHR setup was adopted. Fig. 7.4 compares the LTP-CHR and the LTP measure of the G7-D central scan. Incidentally, this confirms that the mid-frequency errors detected with the LTP-CHR are spurious.

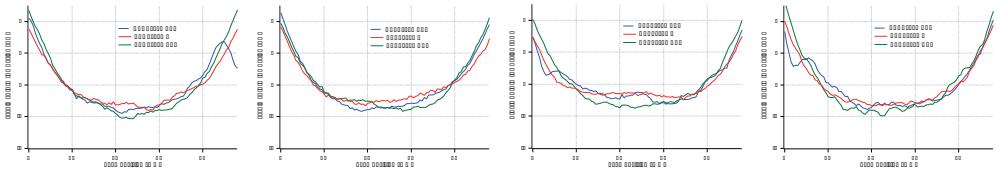

Bi-dimensional surface maps were also measured with the CUP. Fig. 7.5 shows the figure errors, with respect to the nominal cylindrical surface, of the four samples before and after tempering. The characteristic parameter values (Peak-to-Valley: PV, rms, for the entire map and along the sole longitudinal direction) of these measurements are summarised in Tab. 7.2 for each glass foil.

Tab. 7.2 shows high PV values in the entire maps, indicating that the radius of curvature of the four glass foils, after the slumping and the cutting, is rather different from the actual radius of the cylinder of the slumping mould. The main reason is the imperfect CTE matching between the glass and the mould material. Also the pressure setting has still to be optimised in the slumping

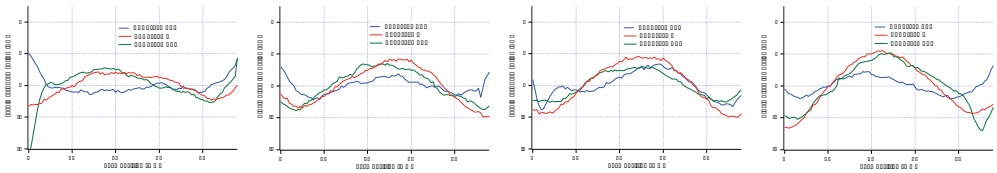

Figure 7.3: *: Profiles computed from up-down CHR measurements of the slumped Gorilla® glasses. (top) profiles before tempering; (bottom) profiles after tempering. From left to right: the samples A, B, C and D.*

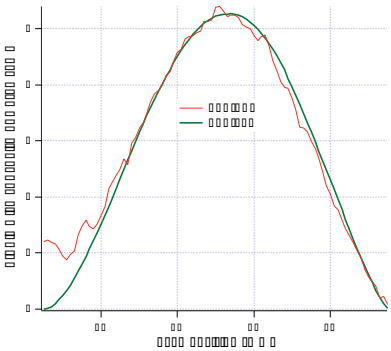

Figure 7.4: *: Profiles of the G7-D sample after tempering, measured with the sole concavity upwards: in red the CHR scan, in green the LTP scan.*

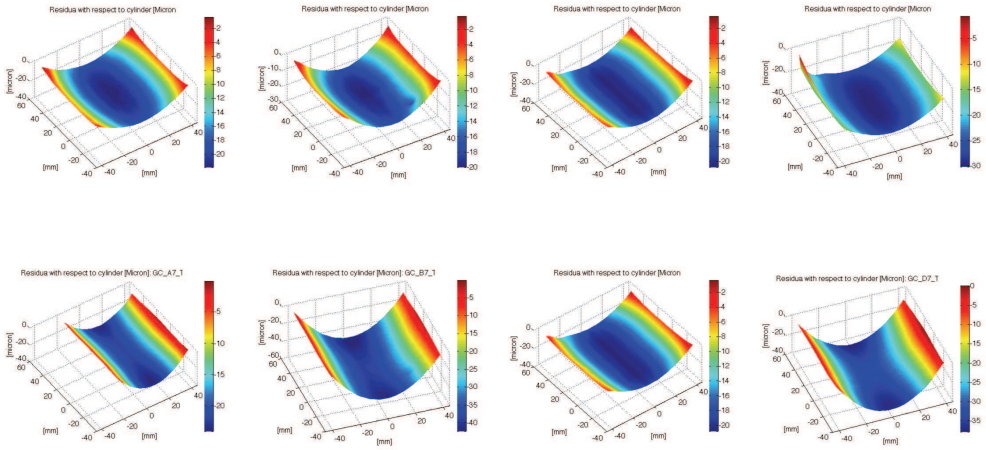

Figure 7.5: *: Deviation of the measured surface from the nominal cylinder of the slumped Gorilla® glasses, as measured with the CUP: (top) the foils before tempering, (bottom) tempered glasses. From left to right: samples A, B, C and D. Credits: CUP maps by M. Civitani.*

Table 7.2: *: PV and rms, calculated on residual errors after the subtraction of a cylinder with radius of curvature of 1 m, before and after chemical tempering. Both values on the entire map and on the longitudinal axis are listed.*

	BEFORE				AFTER			
	All		Longitudinal		All		Longitudinal	
sample	PV	rms	PV	rms	PV	rms	PV	rms
	$[\mu m]$	$[\mu m]$	$[\mu m]$	$[\mu m]$	$[\mu m]$	$[\mu m]$	$[\mu m]$	$[\mu m]$
A	15.2	3.2	6.0	1.2	24.3	6.6	3.9	0.5
B	19.6	4.5	5.7	1.1	40.1	11	4.1	0.8
C	17.6	4.1	4.8	0.8	35.4	9.5	4.6	1.1
D	20.4	4.6	6.1	1.1	35.9	9.8	5.1	1.2

process for a better mould replication. At the moment, anyway, the different radius of curvature is irrelevant for our purposes, since our integration procedure corrects azimuthal low frequency errors [Parodi et al. 2011]. Tab. 7.2 also shows the relevant information in the longitudinal direction, the most critical for our integration procedure. As we already noticed in the 1D measurement (Fig. 7.3), the chemical tempering reverses the longitudinal concavity with a reduction of the PV value.
In order to highlight the differences possibly introduced by the tempering process, the measurements before and after tempering were subtracted. The results are shown in Fig. 7.6. The top figures of Fig. 7.6 show the difference between the maps, obtained before and after tempering, evidencing the saddle introduced by the tempering. The bottom panels of Fig. 7.6 show the difference of the residual maps, obtained before and after tempering, after the application of a linear detrend.

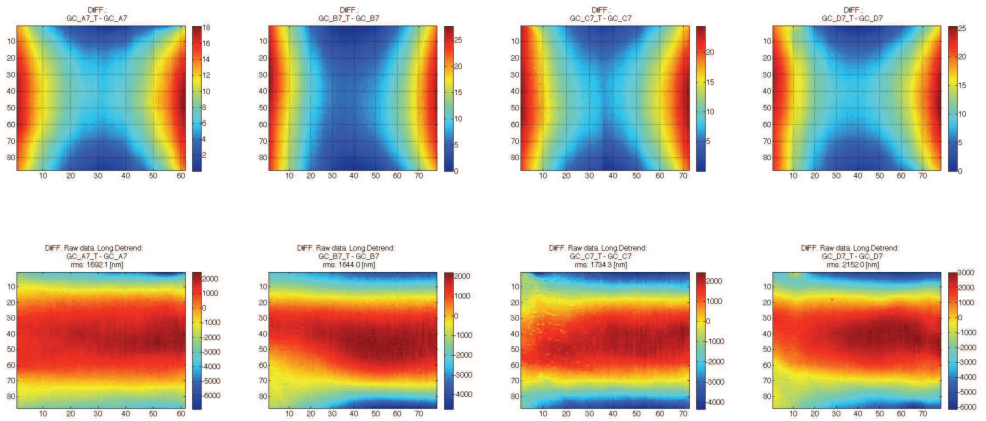

Figure 7.6: *: Results for the A-B-C-D samples. Difference of the maps shown in Fig. 7.5, before and after tempering. The bottom figures are obtained after a line-by-line detrend of the maps shown on the top. The z-scale is in microns for the top figures and nanometers for the bottom figures. Credits: CUP maps by M. Civitani.*

From this analysis we conclude that:

1. the results for the four samples are similar in shape and amplitude (Figs. 7.5-7.6);
2. a saddle shape of about 20 μm is introduced during the tempering process (Fig. 7.6), with the largest deformation in the azimuthal direction, not critical for our integration;
3. along the longitudinal scans, a change in concavity with an amplitude of about 7-8 μm appears (Fig. 7.6);
4. the overall effect on the longitudinal scans is an amplitude reduction of about 1 μm (Table 7.2).

7.1.6 Expected HEW after integration

In order to evaluate this result in terms of final performances for an X-ray telescope, we have simulated the integration of these glass foils: four equally-spaced ribs were considered for the 100×100 mm^2 glass foils. In Fig.7.7 we report the integrated map of the B sample, as computed from the CUP measurement, taken before and after the tempering process. The resulting HEW is computed for single reflection with incidence angle of 0.7 deg. The value does not significantly change, going from 6.2 arcsec for the un-tempered glass foil to 6.6 arcsec for the tempered one. For the C sample, the quality of the glass before the tempering was better, giving a value of 5.4 arcsec (Fig. 7.8). Unlike the B sample, the effect of the chemical tempering on the C sample is

a substantial degradation the HEW, giving a value after tempering of 8.2 arcsec. The expected HEW values after integration for all the samples are reported in Tab. 7.3.

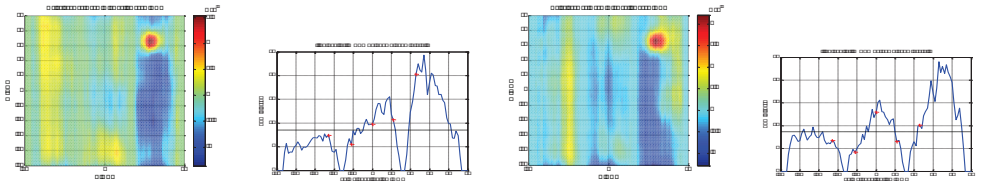

Figure 7.7: *: Simulation of the integration with 4 ribs for the G7B glass foil, before tempering (left), and after tempering (right). For each case, two graphs are shown: at the left, the displacements due to the spring-back of the integrated glass foil, and the expected HEW value, as a function of the x coordinate, computed for single reflection with incidence angle of 0.7 deg. Credits: S. Basso.*

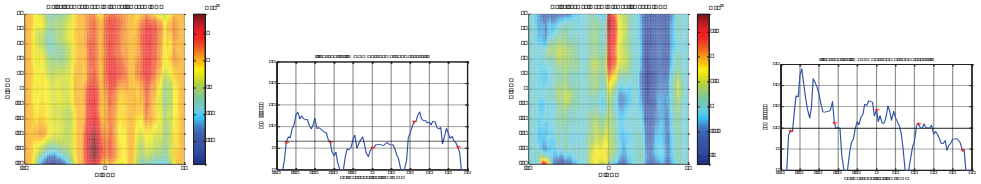

Figure 7.8: *: Simulation of the integration with 4 ribs for the G7C glass foil, before tempering (left), and after tempering (right). For each case, two graphs are shown: at the left, the displacements due to the spring-back of the integrated glass foil, and the expected HEW value, as a function of the x coordinate, computed for single reflection with incidence angle of 0.7 deg. Credits: S. Basso.*

Table 7.3: *: HEW values expected after integration with 4 ribs.*

Sample	HEW [arcsec] before tempering	HEW [arcsec] after tempering
G7A	5.5	5.8
G7B	6.2	6.6
G7C	5.4	8.2
G7D	7.7	6.6
Mean $\pm\sigma$	6.2 $\pm$1.1	6.8 $\pm$1.0

Table 7.3 shows that the chemical tempering is expected to contribute with about 1 arcsec to the degradation of the quality of the X-ray mirrors, computed in single reflection with incidence angle of 0.7 deg. The actual result on integrated glass foils has still to be proven: for the moment we base the work on the correction capability of our integration process, demonstrated with 200 $\times$ 200 mm^2 glass foils and 6 ribs [Civitani et al. 2014].

7.1.7 Conclusions

Corning® Gorilla® glasses were selected, for strength reasons, as a viable option for future X-ray telescopes with large effective area and high spatial resolution. They were curved in our laboratories by hot slumping with pressure assistance on a cylindrical mould made of Zerodur K20. Despite the mismatched CTE of the glass and the mould, it was possible to obtain a 200 $\times$ 200 mm^2 slumped glass with profiles suitable for the test. The glass was cut by CO_2 laser into four 100 $\times$ 100 mm^2 samples to improve the statistics. They were characterized in shape with 1D and 2D profilometers, both before and after chemical tempering. Most of the difference in the maps, measured before and after tempering, is due to change in the azimuthal direction, which

is not critical for our integration, as we efficiently correct in this direction (this was previously proven by X-ray tests on our prototypes, integrated on 200 $\times$ 200 mm^2 size with 6 ribs). In the longitudinal direction, the chemical tempering yields a reduction of the PV value of the measured profiles. From the simulation of the integration with 4 ribs, we could compute the expected HEW, at 1 keV and single reflection at 0.7 deg incidence angle on the integrated glass foil. The results of the computation returns only a small change of the expected HEW in three cases: G7A, G7B and G7D samples. For the sample G7B, for instance, 6.2 arcsec HEW is expected after integration and before the tempering process, changing to 6.6 arcsec after the tempering. In one case, the sample G7C, a higher change in the expected HEW after integration is observed, going from 5.4 to 8.2 arcsec. Finally, the roughness of the tempered Gorilla® glasses was shown to be in line with the roughness of other non-tempered glasses used in our laboratories, and within the prescribed tolerances. A possible development of this research would be to quantify the shape deformations after chemical tempering for 200 $\times$ 200 mm^2 cylindrical samples of Gorilla® glass foils, as of today the size used in our laboratories for the production of the X-ray telescopes segment prototypes. The repeatability of the results with several glass foils has still to be tested. To improve the slumping result, Al_2O_3 material might be used for the slumping mould, owing to its better CTE matching with the Gorilla® glass and to the not-sticking property already proven by our preliminary tests on small flat samples (section 7.2). Destructive tests might be done on slumped Gorilla® samples, comparing the results obtained from tempered and un-tempered samples to quantify the strength improvement after the tempering on our specific slumping process. Finally, X-ray tests on the 200 $\times$ 200 mm^2 integrated glass foils should be done to assess the performances of slumped and tempered Gorilla® glass for X-ray telescopes.

7.2 Alternative mould materials

7.2.1 Scientific motivation

In section 3.6, the main considerations to motivate the selection of the material for the slumping moulds were presented. Among the others, two are considered critical for the Zerodur K20, used in the previous work both for the slumping of the Eagle and the Gorilla® glass:

1. the maximum applicable temperature for the Zerodur K20 is reported to be 850 °C by the vendor (Table 3.3), but in this research the material was found to deform already with a thermal cycle at 750 °C;
2. since a good CTE matching between glass and mould is essential to reduce the mid-frequency errors on the slumped glass foil, Zerodur K20 is not the best selection for slumping Gorilla® glasses.

To solve these issues, two other mould materials were considered, and preliminary tests have been performed in this thesis.

1. Si_3N_4 for Eagle XG;
2. Al_2O_3 for Gorilla®.

7.2.2 Si_3N_4 for Eagle XG

In Table 3.4, the main parameters of Si_3N_4 are reported, compared with other materials selected in our laboratory for the slumping moulds. The research on Silicon Nitride was driven by three key points:

1. a higher rigidity with respect to the Zerodur K20 (Young's Modulus for Si_3N_4 = 300 GPa, for K20 = 84.7 GPa);
2. a higher thermal conductivity (k) with respect to the Zerodur K20 (k_{Si3N4} = 33 W/m/K, k_{K20} =1.63 W/m/K);
3. a better matching of the CTE with the one of the glass ($CTE_{Si3N4} = 3.4\times 10^{-6}$/K, $CTE_{Eagle} = 3.17\times 10^{-6}$/K).

Silicon Nitride flat samples, with diameter 100 mm, were purchased by Bettini srl (Monte Marenzo, Italy).

As a first step, the antisticking property of the Si_3N_4 was proven by several slumping tests, with increasing temperature and pressure up to values of T_{soak} = 750 °C and P = 50 g/cm^2. The setup is shown in Fig. 7.9. No sticking ever occurred, proving this material as a good candidate for the slumping technique.

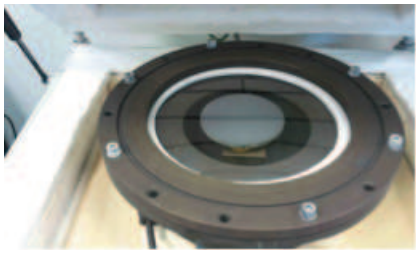

Figure 7.9: *: The setup for the slumping of Eagle glass on the flat Si_3N_4 sample mould: the glass was cut to circular shape with diameter suitable for the application of pressure.*

The higher stiffness of this material makes also possible to produce a cylindrical slumping mould thinner than the mould in K20, thus reducing the cost of the mould production: FEA

showed that a negligible deformation for a cylindrical mould with dimension 250 × 250 mm and radius of curvature of 1 m, in our working conditions, can be obtained with mould thickness of 50 mm for the K20, Vs. only 32 mm for the Si_3N_4.

Unlike K20, Si_3N_4 does not deform under the slumping cycles. Profiles measurements on the diameter of the Si_3N_4 flat sample, before and after the slumping with standard process parameters, show no deformation, whilst they are commonly seen with Zerodur K20 (Fig. 7.10).

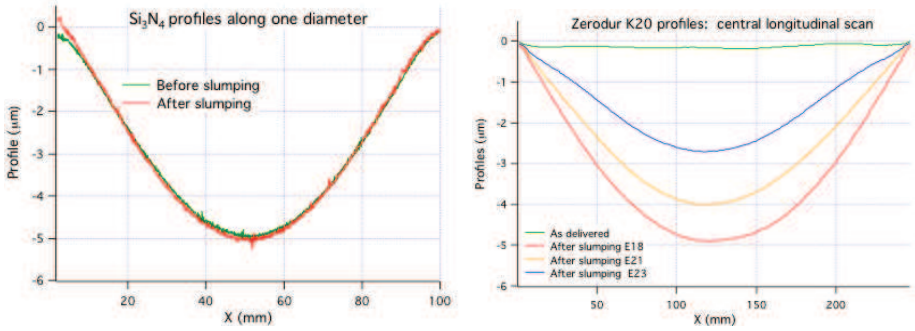

Figure 7.10: *: Shape stability with thermal cycle of Si_3N_4 compared to the deformation of the Zerodur K20. Left: the Si_3N_4 profiles along a diameter, as measured with the Zeiss contact profilometer before and after the slumping. Right: the K20 profiles along the central longitudinal scan, as measured with the LTP after several slumping cycles.*

From the roughness point of view, the Silicon Nitride sample moulds were very rough, with rms[WYKO] = 207 Å (Fig. 7.12), as no special attention was paid to the polishing of the mould in this first phase of the research. The surface was crowded with peaks (Fig. 7.11-right) and this entails a very poor quality of the slumped glass surface in contact with the mould (Fig. 7.11-left). The slumped glass rear surface, not in contact with the mould (indirect approach), is almost comparable to the pristine glass (Fig. 7.11-center). In Fig. 7.12, the roughness of the Si_3N_4 slumping mould, and the ones of the slumped Eagle glass, considering both direct and indirect approaches are compared.

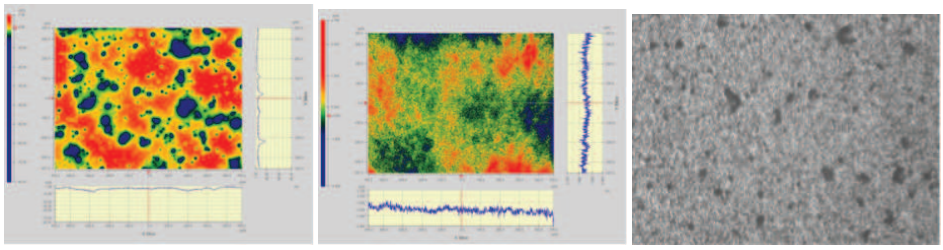

Figure 7.11: *: Surface maps of an Eagle glass slumped on Si_3N_4 mould (left and centre) compared to the Si_3N_4 mould surface (right). Left: a MFT image of the slumped Eagle glass on the surface in contact with the mould, rms = 4.1 nm, PV = 87.8 nm. Center: a MFT image of the slumped Eagle glass on the surface NOT in contact with the mould, rms = 0.5 nm, PV = 5.3 nm. Right: an image of the Si_3N_4 surface, taken with the Nomarski microscope with approximately the same field of view of the MFT images (∼ 1 mm).*

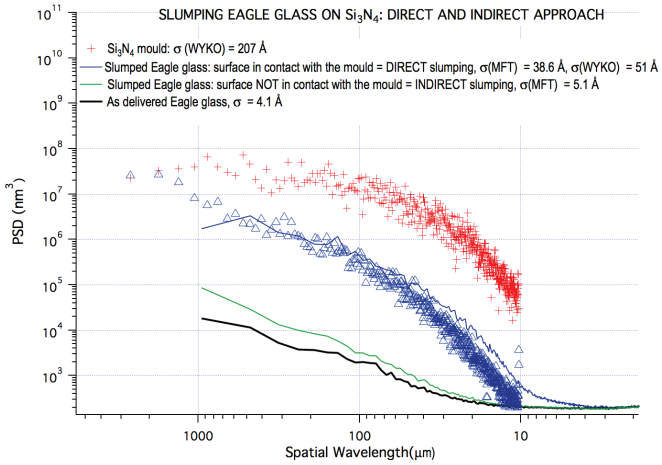

Figure 7.12: *: PSD comparison of the Si_3N_4 mould and an Eagle slumped glass. Red curve: the Si_3N_4 mould measured with the WYKO. Blue curves: the slumped glass, surface in contact with the mould, measured both with the WYKO and the MFT. Green: the slumped glass, surface NOT in contact with the mould, measured with the MFT. Black: un-slumped glass, measured with the MFT. The PSD are computed as average of 5 measurements. Solid lines are from MFT, lines with markers are from WYKO.*

7.2.3 Al_2O_3 for Gorilla®

In Table 3.4, the main parameters of Al_2O_3 are reported, compared with other materials selected in our laboratory for the slumping moulds. This material was chosen owing its better CTE matching with the one of the Gorilla® glass ($CTE_{Al2O3} = 7.8\times 10^{-6}$/K, $CTE_{K20} = 2.3\times 10^{-6}$/K, $CTE_{Gorilla} = 8\times 10^{-6}$/K).

Alumina flat samples, with diameter 100 mm, were purchased by Bettini srl (Monte Marenzo, Italy) (Fig. 7.13).

A small sample of Alumina, also produced by Bettini, of dimension 63 × 63 mm and thickness = 5mm, was used for preliminary sticking tests (Fig. 7.13-right). The thermal cycle was set as defined by the slumping tests of Gorilla® glass on Zerodur K20 mould (Tab. 7.1) and the slumping was performed in the small TK oven. The anti-sticking property of the couple Al_2O_3/Gorilla® was proven by several slumping tests, with increasing temperature and pressure up to values of T_{soak} = 620 °C and P = 100 g/cm^2. The setup is shown in Fig. 7.9. No sticking ever occurred, proving this material as a good candidate for the slumping of the Gorilla® glass.

Figure 7.13: *: Left: Al_2O_3 flat samples from Bettini srl. Right: the circular Gorilla® glass on the Al_2O_3 63 × 63 mm mould, inside the circular muffle before closing it with the frame, as in Fig. 7.9.*

The surface of the brand new sample was first observed by the Nomarski microscope and the AFM (Fig. 7.14). The surface shows voids, typical of a sinterization process.

The polishing capability of the Al_2O_3 was tested at Laboratorio Ottico Colombo (Rovagnate, Italy). The preliminary analysis showed Al_2O_3 is harder to polish than K20, and the roughness

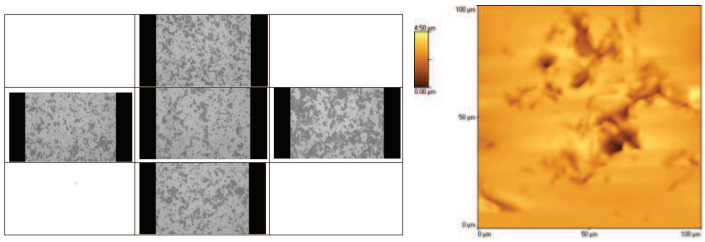

Figure 7.14: *: Images of a Al_2O_3 sample, as delivered by Bettini. Left: 10 × Nomarski. Right: 100 µm AFM image.*

of Al_2O_3 after polishing is also higher.

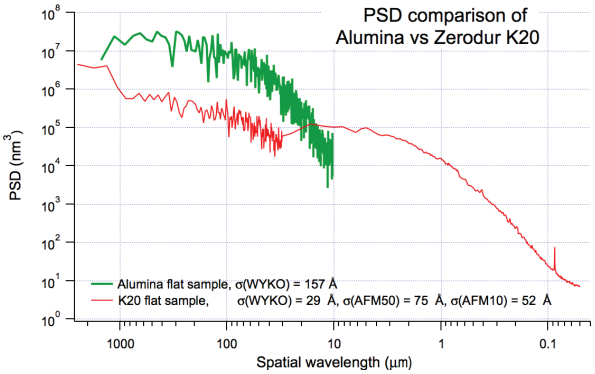

Figure 7.15: *: PSD comparison of the Al_2O_3 (green line) and Zerodur K20 (red line) flat moulds, as polished at Laboratorio Ottico Colombo.*

7.2.4 Conclusions

Si_3N_4 and Al_2O_3 flat samples were purchased at Bettini srl (Monte Marenzo, Italy). They were both produced with a sinterization process, typical of many ceramic materials. Their surface is therefore crowded with pores.

Si_3N_4 was shown to be a very promising candidate material for slumping mould, since no sticking ever occurred in the typical working condition of our slumping process. Unlike K20, the Si_3N_4 was proven to remain unchanged under the thermal cycles. Since the tests, in this preliminary phase, were done on a very rough Si_3N_4 surface, the slumped glass foil resulted with a high roughness on the side in contact with the mould. However, the side not in contact with the mould (indirect slumping) has a roughness equivalent to the one of the pristine glass. The higher thermal conductivity, with respect to K20, would reduce the thermal gradients, providing a better environment for the minimization of mid-frequency errors. A follow up of this research foresees the investigation on the polishing capability on the Si_3N_4.

Al_2O_3 was also shown not to need anti-sticking layer for the slumping of the Gorilla® glass. Preliminary polishing tests on this surface were done at Laboratorio Ottico Colombo. The surface could not be polished to the same level than the K20 surface, most probably for the presence of the pores. A coating could be considered to fill the pores, and to be polished afterwards. At the moment, no preferable candidate materials for the coating could be selected.

7.3 Vacuum sealing materials

7.3.1 Scientific motivation

Our setup for slumping foresees the use of felts between the glass and the muffle, both in the upper and the lower part. The upper felts enable the vacuum holding of the glass during the First Contact stripping (Fig. 5.12); the lower felts enable the pressure application during the thermal process. The material has to be soft to fill the gap between the muffle chamber and the glass, and it has to be a good sealing material. Moreover, it has to be stable at the high temperatures used during the slumping cycle. The Superwool 607 HT was selected at early times of the process development as it satisfies both requirements. However, it is a very dusty material and may release dust between the glass foil and the mould during the setup preparation, especially if some problems occurs during the muffle closure. The final effect is a deformation on the slumped glass foil as shown in Fig. 7.16. Therefore, dust-free materials with low content in silica were searched for.

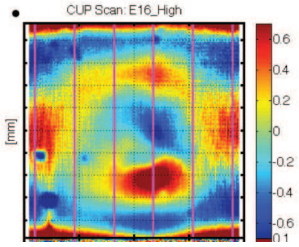

Figure 7.16: *: CUP map of the E16 slumped glass foil showing, on the bottom left corner, a deformation due to some dust particles entrapped during the setup preparation.*

7.3.2 Materials comparison

The tested alternative materials have a common characteristics to be ceramic textiles, i.e. they are obtained by sinterization processes. They are all made of fibers with diameter ranging from 4 to 12 μm, depending on the material. The length of the fibers is small, except for Nextel, which can be produced in continuos filaments. The filaments are usually kept together by an organic binder, which burns at relatively high temperature: only Nextel and Zirconia do not contains organic binder. Table 7.4 reports the main characteristics of the selected materials.

1. Superwool 607 is a alkaline-earth silicate (AES) consisting of SiO_2, CaO and MgO, and traces of other oxides. Superwool is a high-temperature insulating wool composed of vitreous silicate fibres. It is obtained by hot pressing of the fibres with an organic binder. Since the binder begins to burn out at 180°C, the felts results very fragile after a typical slumping cycle. It is available in different grades: 607 for application up to 1100°C, 607 HT for application up to 1300°C, and Plus, an improved version of the 607 grade, for application up to 1200°C. The 607 HT grade is no longer supplied and it is substituted by the Plus grade for environmental reasons.

2. Thermatex 850 was specifically developed as replacement for asbestos paper. With respect to Superwool 607, it has a lower content of silica compensated by the presence of alumina. It can be used up to temperature of 850°C. Just like Superwool 607, it contains an organic binder.

3. Zirconia Felt Types ZYF-100 is composed of 100% yttria-stabilized zirconia fibers which are mechanically interlocked. Designed for use in extremely corrosive environments and

high temperatures, these felts are 100% inorganic fibers and contain no binders. They undergo no phase transitions on temperature cycling and are very effective thermal insulators, capable of use at temperatures in excess of 1930°C.

4. S1600 is a material composed of almost pure alumina, stabilised by 6% of silica. It contains a binder. It is used in the quartz fabrication industry. It can be used up to temperature of 1600°C.

5. Nextel is a material that can be produced in continuous filaments and textiles. During the manufacturing the fibers are coated with organic sizing and finishes which serve as aids in textile processing. They can be removed by heat cleaning. It can be used up to temperature of 1200°C.

Table 7.4: *: Comparison of different insulating materials.*

Type	**Superwool 607 HT**	**Thermatex 850**	**Zirconia ZYF-100**	**S1600**	**Nextel 312**
Supplier	Thermal Ceramics	Thermal Ceramics	Zircar Zirconia	Insultecno	Insultecno
Wt%	SiO_2 : 70-80 CaO + MgO : 18-25 Others < 3	SiO_2 : 40 CaO + MgO : 25 Al2O_3 : 21 Iron oxide: 6 Others: 8	ZrO_2 +Y_2O_3: 99+ $Al_2O_3 < 0.01$ $SiO_2 < 0.02$	Al_2O_3 : 94 SiO_2 : 6	Al_2O_3 : 62 SiO_2: 24 B2O_3: 14
Binder	YES	YES	NO	YES	NO
Max T	1300 °C	1930 °C	850 °C	1600 °C	1200 °C

7.3.3 Preliminary tests

The different fibers were observed under the Nomarski microscope. Some images are reported in Fig. 7.17. The peculiar aspect of the long Nextel filaments is visible.

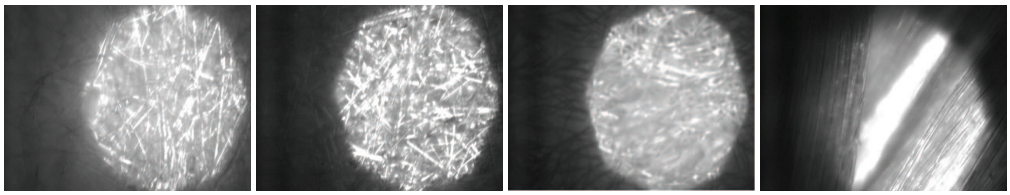

Figure 7.17: *: Nomarski 5x images of some insulating materials. From left: Superwool 607, Thermatex 850, Zirconia ZYF-100, Nextel 312.*

All the materials where easily cut with a stander cutter. No residuals were left on the cardboard used, with the exception of the Zirconia ZYF-100 (Fig. 7.18), probably caused by the absence of the binder.

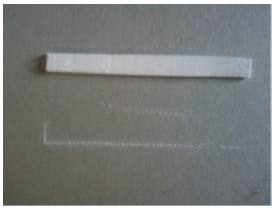

Figure 7.18: *: Residuals left on cardboard when cutting a strip of Zirconia ZYF/100.*

Residuals from the different materials were also tested by pressing a strip of felt between two glass foils. Also in this case, the Zirconia ZYF-100 showed to be the one with more residuals left on the glass substrates. For this reason, the Zirconia ZYF-100 was discarded in this preliminary test.

Felt stability at high temperature was tested by simulating the standard configuration of the felts inside the muffle (Fig. 7.19): a small glass foil was positioned between two strips of felt, inside the muffle, with cover pressing from the top. The smaller amount of residuals were found with the S1600.

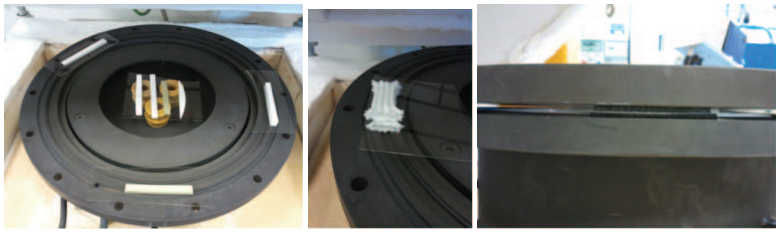

Figure 7.19: *: Testing the felts inside the oven. Left: at the centre of the muffle, a flat glass holds some felts of different material to check their conditions after a thermal cycle. At the border, a small glass foil was positioned between two strips of felt of different material, before the positioning of the cover. Center: same as left figure for the Nextel. Right: the cover pressing on the felts.*

After the thermal cycle, the thickness and the integrity of the felts were tested. The thickness reduction of the felts was found as:

1. SuperwoolPlus: from 2 mm to 0.7 mm = 65%;
2. Thermatex850: from 2 mm to 1.1 mm = 45%;
3. S1600 : from 3 mm to 1.5 mm = 50%;
4. Nextel 312: no reduction.

As for the integrity after the thermal cycle, the worst was of the Superwool Plus, that was found very brittle and difficult to handle without breaking. Thermatex850 and S1600 were quite similar, as it has been possible to handle the felt strip without breaking it. The best was the Nextel 312 that was found unchanged after the thermal cycle, therefore giving the possibility to be reused.

Nextel 312 was therefore selected as possible alternative to the Superwool 607:

1. it is made of continuous filaments, hence less prone to produce dust when closing the muffle;
2. it does not contain an organic binder that burns at our operative temperature;
3. it has a lower content in silica, thereby reducing the production of dust that woul be incorporated into the mould.

7.3.4 Slumping test

A roll of Nextel 312 with appropriate dimensions (diameter of 3.2 mm (Fig 7.20)) for our slumping setup was purchased. After cutting, the strip length was unstable, changing length as the strip was stretched. Moreover, after the cutting, to prevent an excessive spread of the filaments at the cut ends, the ends were terminated by a Nextel wire. (Fig 7.20).

The first slumped glass foils was found with a high content of mid-frequency errors, already visible by the interference fringes, most probably due to the imperfect sealing at the strip corners (Fig 7.21-left). The Nextel strips were therefore bound together by a Nextel wire. The result was a hard point that broke the glass foil at the closure of the muffle.

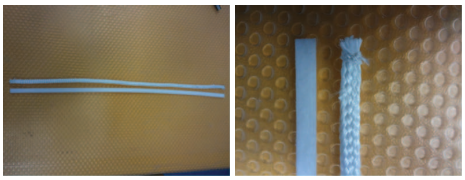

Figure 7.20: *: Left: comparison of the strip of Nextel (top) and Superwool 607 (bottom). Right: comparison of the ends of the strip of Nextel (right, terminated with a Nextel wire) and Superwool 607 (left).*

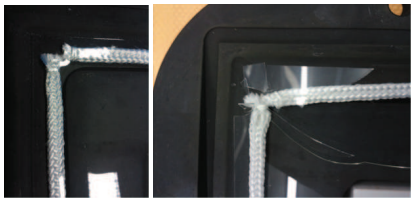

Figure 7.21: *: Left: corners imperfectly aligned due to elasticity of the strips. Right: the corners, bound together with a Nextel wire, created a critical point that broke the glass foils at the closure of the muffle*

7.3.5 Conclusions

Even if Nextel appears a dust-free material, it was found to be not suitable as sealing material during the slumping tests. A proposed alternative could be Mica, another dust-free material, but very expensive.

7.4 Dip coating

7.4.1 Scientific motivation

A key aspect is to improve the high-energy response of the telescope by improving the micro-roughness of the slumped glass foil. The surface micro-relief is affected by the presence of pores in the glass, owing to the partial replication of the forming mould surface topography during the slumping under pressure (Fig. fig=MK20-20B-roughnessreplication). Considering the high number of glass segments to be produced for a telescope like the one foreseen for the ATHENA mission, we need a low-cost technique to fill the pores and planarize the surface, such as the dip coating technique. An advantage of this coating technique, compared to other planarization methods, is that the coating is applied on both foil sides, thus preventing the glass profile from stress deformations. The glass type selected is the Schott AF32, the one used at the time of this activity. The glass foils have been coated at Lenti srl (Brembate di Sopra, Italy), an Italian enterprise whose core business is the molding and coating of surfaces for glasses and visors. The coating characterization was performed at the INAF-OAB laboratories and at Politecnico of Milano.

7.4.2 The dip coating technology

The basic idea is to find a suitable material and a process to smooth out the defects of the glass surface after slumping, by application of a thin coating. Possible ways of coating are spin, spray, roll or flow coating. While the first one is definitely not applicable to curved surfaces, such as those used in X-ray astronomy, the others can be investigated. I have concentrated the research to the dip coating technology, because it is a low-cost technology, firmly developed for lenses, where the substrate is formed to the desired shape and a coating is applied as anti-reflecting, scratch resistant or anti-fog layer. In this process, the substrate is dipped in the coating liquid and extracted at controlled speed; as the solvent evaporates, a coating thin film remains on the substrate.

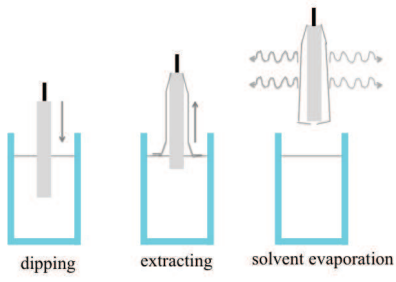

Figure 7.22: *: In the dip coating process, the substrate is dipped into the liquid solution; during the extraction process a solvent-rich film remains on the substrate and, after the low-boiling solvent fraction evaporates, a film is obtained with a thickness that depends on the draw speed.*

For a homogeneous hydrophilic substrate, vertically withdrawn off a liquid container at controlled speed, the thickness of the resulting film is provided by the Landau-Levich equation:

$$t = 0.946 \frac{(\mu U)^{2/3}}{(\rho g)^{1/2}} \left(\frac{1}{\sigma_{LV}} \right)^{1/6}, \tag{7.2}$$

where μ, ρ and σ_{LV} are the liquid viscosity, density and surface tension, respectively; g is the acceleration due to gravity; U is the speed of substrate withdrawal. From Eq. 7.2 it is clear that,

as the withdrawal speed is increased, the resulting thickness also increases: the physical reason is that a faster withdrawal pulls more fluid up onto the surface of the substrate before it flows back down into the solution. Indeed, the experiments I have carried out (see Sect. 5) showed that the thickness is not constant throughout the sample. An uneven thickness of the coating is obviously a source of additional surface degradation; therefore, I have spent a considerable effort, varying the different parameters at play in the process, to optimise the coating uniformity.

7.4.3 Coating by liquid spilling

The coating of the substrate can also be deposited spilling the liquid from the bottom of the container instead of extracting the glass from the top. Of course, as the column of liquid flows, the upper liquid surface moves downwards slower and slower; hence the resulting coating thickness will not be constant unless the container is much higher than the glass length, which was not the case. Fig. 7.23 shows the coating basin and the flat glasses used as test, before being dipped into the liquid. The values for the different speeds on the upper (v_1) and the lower (v_2) part of the glass are also reported.

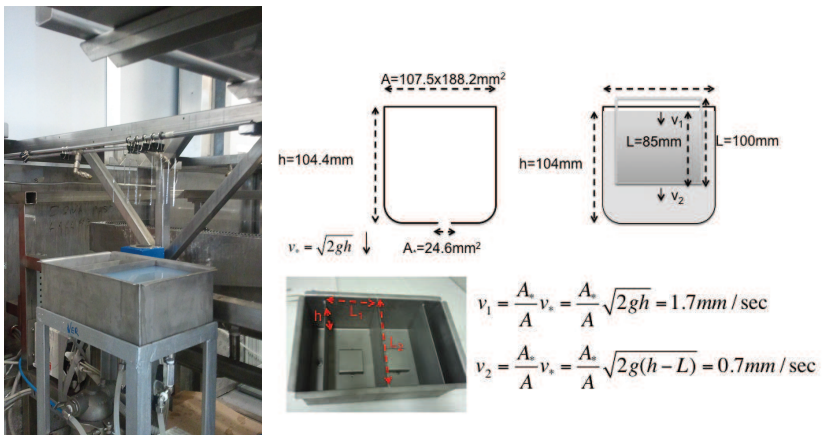

Figure 7.23: *: Left: the container for liquid spilling, inside the clean room environment, Right: the container dimensions and coating speeds, computed as a first estimate assuming the liquid to be non-viscous and non-compressible.*

7.4.4 Selection of the coating: Zeiss versus Lenti

To define the coating material and the process suitable for an effective profile planarization, two different samples were firstly compared: an optical lens from Zeiss and a lens from Lenti srl (Fig. 7.24). The lenses are made of glass and nylon respectively.

The roughness of both samples was measured, before and after the coating, with the AFM in the 100 μm and 10 μm range: the PSD analysis for both samples, before and after coating, is shown in Fig. 7.24. The Lenti lenses, even starting from a rougher substrate, exhibit a lower roughness after coating. Therefore, this coating material was selected for further investigation.

The coating used by the Lenti company is the CrystalCoat^{TM} PF-2500 (produced by SDC Technologies), a polysiloxane based, abrasion-resistant coating. Their nominal deposition process foresees several steps in a clean environment: cleaning in ultrasonic bath, dipping in the bath with CrystalCoat^{TM} PF-2500, extraction at 1 mm/sec speed, drying in clean environment for solvent evaporation, and finally curing at 120°C.

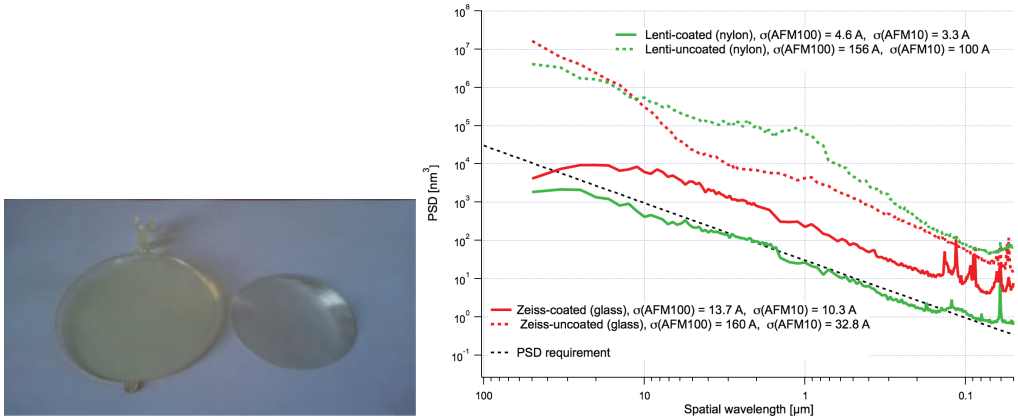

Figure 7.24: *: The lenses used to the preliminary material selection. Left: a Lenti srl lens for sun-glasses (left), a Zeiss optical lens (lens). Right: The PSDs, as computed from the AFM measurements over 100 μm and 10 μm scan lengths, of the Lenti (green) and the Zeiss (red) lenses, before and after coating.*

7.4.5 Preliminary tests

Two slumped glass foils of size 200 × 200 mm^2 and thickness 0.4 mm were intentionally chosen with severe micro-pores defects (much worse than the present state-of-art, as in Fig. 6.15) to test the planarization capability of the CrystalCoat^{TM} PF-2500. A few AFM images of the surface of one of those glass foils are shown in Fig. 7.25. The glass foils were coated at the Lenti laboratories, using their standard coating process. As a first result, we experienced a good adhesion of the CrystalCoat^{TM} PF-2500 on the glass substrate, as we could not strip it out with kapton tape. I have then measured the roughness of the coated film and compared it with the one of the glass before coating. From Fig. 7.25 it appears that the pores were completely filled by the coating. Nevertheless these first tests showed two issues. Firstly, we detected a final micro-roughness higher than the one measured on the Lenti lenses, as visible from comparing the PSD graphs in figures 7.24 and 7.26. This is due to the tolerance of the particular equipment chosen for this first test (note that this is completely within the Lenti tolerances, but it exceeds those for X-ray mirrors). Secondly, from the AFM images with the 100 μm scan range (Fig.7.25), we see an undesired waviness introduced by the coating process itself. This is a real effect and not an artefact of the AFM measurements, as it can be seen in the sodium light images and in the CHR profile measurements (see next section). This waviness was also detected on the Lenti lenses, but it has no relevance for application in the visible range. It was therefore decided to address the roughness issue and the waviness problem separately, performing tests with flat Borofloat33 glass foils with size 100 × 100 mm^2 and thickness 1.75 mm. Since they were not slumped, the surface of those glasses was pore-free. In fact, with those tests I have checked only the roughness and waviness issues, assuming that the coating process is completely effective at filling the pores.

7.4.6 Coating parameter definitions on flat glass foils

To find the optimal coating parameters for the glass foils, I have performed a campaign with flat un-slumped Borofloat33 glass foils, with size 100 × 100 mm^2 and thickness 1.75 mm. The reason of this change is the easier handling of thicker glasses. All the results presented in this section are obtained with these flat glasses. In all cases, two glass foils were coated to check the process repeatability. To define the cause of the increased micro-roughness of our glass foils with respect to the Lenti lenses with nylon substrate, I have considered:

1. the possibility of a different interaction of the CrystalCoat^{TM} PF-2500 with the two substrates, in the reticulation process inside the oven;

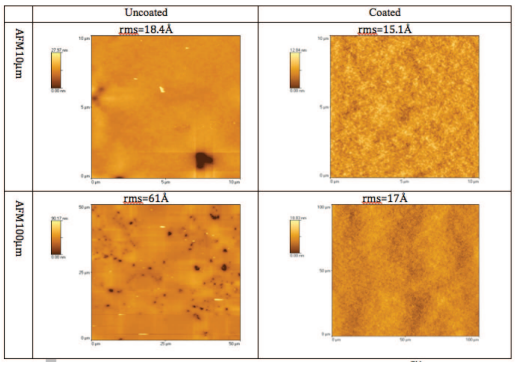

Figure 7.25: *: AFM images of a cylindrical slumped glass before and after coating with CrystalCoat™ PF-2500. The pores are completely filled, but the final micro-roughness of this first test is not as good as the one observed on the Lenti lenses. Moreover, the AFM image with 100 µm scan range shows an undesired waviness coming from the coating process.*

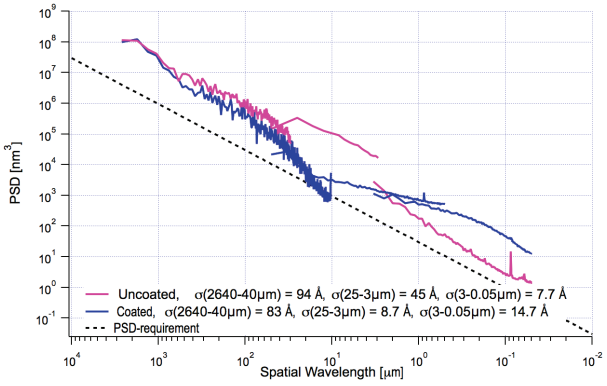

Figure 7.26: *: PSD of the AFM data shown in Fig. 7.25, averaged over three sample positions. Pink dashed curve: the PSD for the slumped uncoated glass. The PSD excess with respect to the requirement and the corresponding rms values are related to the presence of the pores. Blue curve: the PSD for the slumped coated glass. The improvement in the spatial range 25-2 µm is owed to the good filling of the pores, while the worsening in the range 2-0.05 µm is related to the particular equipment chosen for this first test. The values are within the tolerance for applications in the visible range, but not for X-rays.*

2. the performances of the different equipments installed at the Lenti laboratories.

Since the process foresees a final annealing step for the reticulation of the coating, I have produced samples without the last annealing and samples including the final annealing. I have firstly selected the best equipment out of the ones installed at the Lenti laboratories, then I have compared the coating roughness achieved with/without annealing in oven. For the samples coated without the annealing, the surface topography was affected by particulate entrapped in the coating film during the post coating phase without the reticulation process. Indeed, the regions without particulate exhibit a roughness similar to the annealed samples and as good as the one of the Lenti lenses with nylon substrate shown in Fig. 7.24. Therefore, the annealing process does not cause roughness degradation of the coating on the glass. Fig. 7.27 displays the AFM images of the Borofloat glasses coated with the best equipment and with the annealing step, as an evidence of the good reached micro-roughness, and the correspondent PSD analysis.

To address the waviness issue, tests with different pre-treatments of the surface, extraction speeds and coating techniques were carried out.

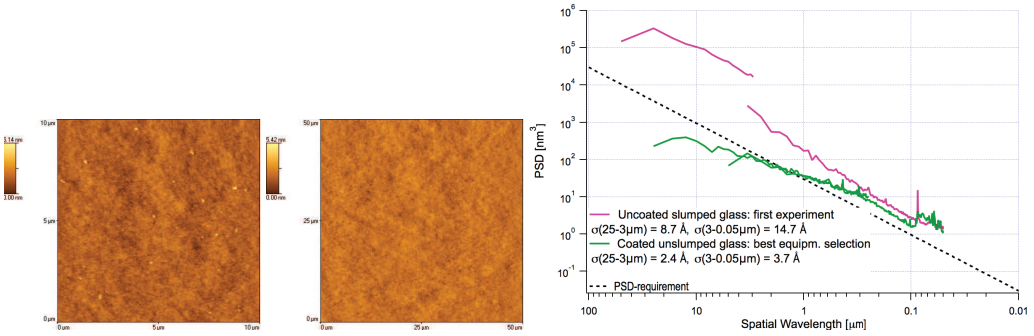

Figure 7.27: *: AFM data of the Borofloat33 surface coated with CrystalCoat™ PF-2500 after the best equipment selection and with the annealing in oven. Left: 10 μm AFM scan scan, rms = 3.9 Å. Center: 50 μm AFM scan scan, rms = 3.9 Å. Right: PSD from the AFM data of a slumped uncoated glass foil (pink dashed curve), and a borofloat glass coated with optimal equipment (green line)*

.

7.4.7 The effect of pre-treatment of the glass surface

The glass surfaces were pre-treated in different ways and two samples were prepared for each case:

1. glass surface functionalization with APTS (monomolecular layer of 3aminopropyltrimethoxysilane) after hydrogen peroxide cleaning [Maddox & Jenkins 1987, Trevisiol et al. 2003]: this reportedly produces better uniformity in the thickness of the coating;

2. preparation with ionic discharge before standard cleaning of Lenti process;

3. cleaning as per the standard Lenti process.

The samples were coated with an extraction speed of 1 mm/sec. The main result was that none of our extra surface preparations could reduce the waviness with respect to the standard Lenti cleaning process. In Fig. 7.28 the images taken with sodium light are shown: the coating is visible over the entire 100×100 mm^2 glass surface, excepting the upper part where the clip for glass holding was positioned during dipping. From these images, I can conclude that the ionic discharge treatment produced a less homogeneous coating. For this sample, the measurements with both Filmetrics and CHRocodile were not accurate because of the poor coating uniformity.

For the samples a and c, we performed thickness measurements with the Filmetrics, returning a thickness value of 2.3 μm for sample a and 2 μm for sample c. Also the profiles of the coated

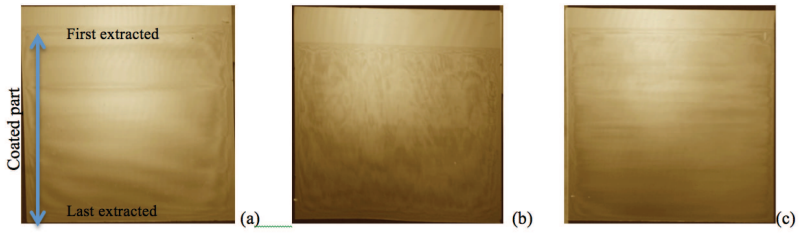

Figure 7.28: *: Interference fringes seen in Sodium light on the 100 × 100 mm^2 glass foils coated with different surface preparations. (a) functionalization with APTS, (b) preparation with ionic discharge, (c) standard cleaning Lenti process (extraction speed for all glasses: 1 mm/sec).*

surfaces were measured. The best performing sample, i.e. the sample c, coated with the standard Lenti process at 1 mm/sec extraction speed, still exhibits waviness contribution at spatial frequencies too high for our imaging quality requirements. In fact, the Half Energy Width (HEW) expected from this coating profile, after subtraction of a parabolic fit, is 139 arcsec. Anyway, this test was not performed using the best performing Lenti equipment (as it was not defined yet at the time of this test); therefore the process still needs to be improved.

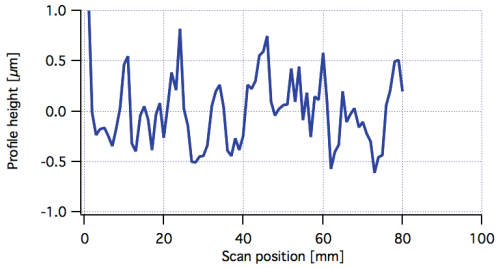

Figure 7.29: *: Residual after a parabolic de-trend of the surface profile of the (c) sample in Fig. 7.28 (coated with the standard Lenti process at extraction speed of 1 mm/sec) as measured with the CHR3300 sensor head mounted on the LTP stage.*

7.4.8 The effect of extraction speed

In order to check for coating uniformity variation with the extraction speed, two samples were coated at a 20 mm/sec extraction speed. The thickness of these samples turned out to be nearly 8 μm. The Sodium lamp interference pattern (Fig. 7.30) exhibits more pronounced waviness than the sample extracted at 1 mm/sec (Fig. 7.28).

The conclusion of this test was that a higher speed degrades the coating uniformity. This was also confirmed by the test with liquid spilling (Fig. 7.32).

7.4.9 Different coating technique: liquid spilling from the bottom of the container

This test was performed to check if the bare gravity contribution of the liquid to empty the container could prevent the waviness detected when the glass was extracted from above the liquid surface. A container was partially filled with the solution of CrystalCoat^{TM} PF-2500; this was kept stirred until the tap was opened and the liquid could flow down. The glass foils were immersed in the liquid, holding them with clips, and the coating was deposited up to the clip position. A hole, present at the bottom of the container, ensured the liquid to flow out. To have an estimate of the upper liquid surface speed, the liquid was supposed to be not-viscous and not-compressible.

Figure 7.30: *: Interference fringes by Sodium lamp illumination on the 100 × 100 mm^2 glass foils coated with an extraction speed of 20 mm/sec.*

In this condition the outflow speed at the hole position is $v^*_{1,2} = \sqrt{2gh_{1,2}}$, where g is the gravity acceleration and $h_{1,2}$ the height of the column of liquid at position 1 and 2 as shown in Fig. 7.23. In this case, the liquid surface speed at position 1 and 2 is $v_{1,2} = \frac{A_*}{A} v^*_{1,2}$ with A^* the area of the hole (diameter=5.6mm) and A the area of the liquid surface. In Fig. 7.31 the image taken in sodium illumination is shown, together with the computed liquid surface speed.

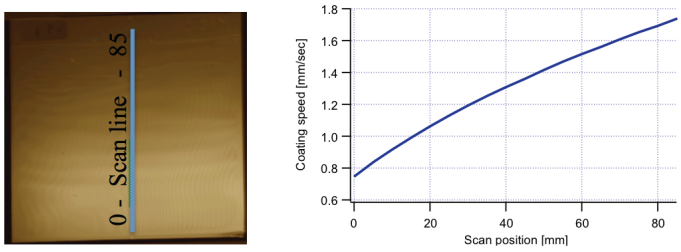

(a) (b)

Figure 7.31: *: (a) Interference fringes by sodium illumination for the glass coated by spilling the liquid from the hole at the bottom of the container. (b) Computed liquid surface speed, decreasing as the column of liquid decreases.*

As in the previous cases, the profile of the coated surface was measured. The residual, after a parabolic de-trend, is shown in Fig. 7.32: it clearly appears that at the bottom part of the glass the residual waviness effect is damped. This data confirms the result found in Sect. 7.4.8, and it paves the way to further experiments, in which the coating behaviour with extraction speed even lower than 1 mm/sec should be tested. Moreover it is suggested to coat glass foils of 100 × 200 mm^2 to check for transient coating effects. In fact, should the coating be smoother after a transient glass coated part, one could consider to coat slumped glasses of larger size (as-slumped) than the nominal one, and then trim the outer edge to the desired 200 × 200 mm^2 size.

7.4.10 Conclusions

In this section, I have shown that the CrystalCoat^{TM} PF-2500 coating and the process of the Italian company Lenti srl is a preferred solution, for our astronomical application, with respect to the Zeiss coating process. The preliminary tests on our thin slumped cylindrical glasses showed that the pores are completely filled, but some roughness/waviness issues were to be addressed. The roughness was optimized by selecting the best equipment out of the ones installed at the Lenti laboratories. To reduce the waviness effect, different parameters were explored. No special surface preparation (as surface functionalization or ion discharge preparation) was effective to improve

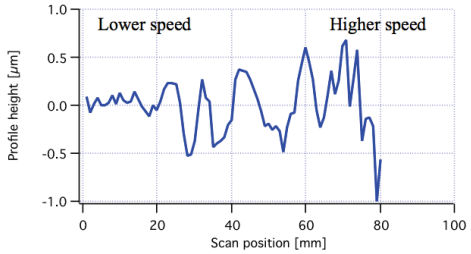

Figure 7.32: *: Residual after a parabolic de-trend of the profile of the sample coated by spilling the liquid from the bottom of the container, as measured with the CHR3300 sensor head mounted on the LTP stage. The profile shows that the coating waviness decreases as the upper surface speed is reduced.*

the situation. In contrast, the reduction of the coating speed revealed to be the most important parameter to minimise the waviness effect. This was found both in the glass extraction tests and in the liquid spilling tests.
Due to overload in production at the Lenti srl company, this research work was discontinued. When possible, it should be continued to define the optimum extraction speed necessary to fill the pores and reduce the waviness effect. A possible transient effect can also be tested by coating longer samples to determine the distance from the beginning of the coating to the coating uniformity edge.

7.5 Indirect slumping

7.5.1 Scientific motivation

In the direct hot slumping technique assisted by pressure, the glass foil is positioned over a convex mould inside a muffle. The optical surface is in contact with the mould and therefore its roughness can be degraded by the contact. In the indirect hot slumping instead, the optical surface is not in contact with the mould, thus preserving the original glass roughness (Fig. 7.33).

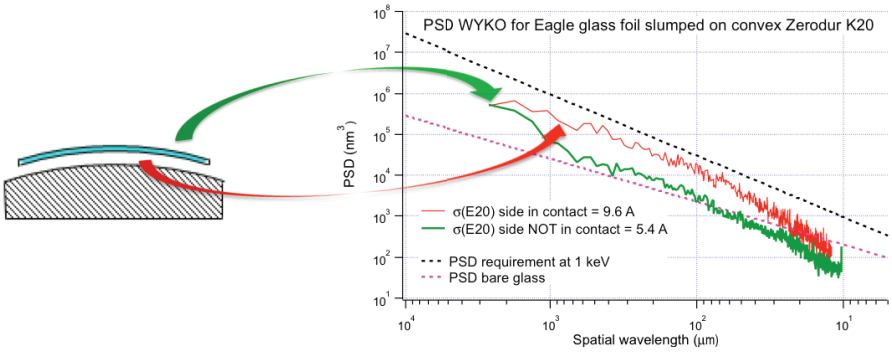

Figure 7.33: *: PSD, from WYKO data, of an Eagle XG glass foil, slumped on the standard convex K20 mould. The red line represent the side in contact with the mould (direct) while the green one represents the side not in contact with the mould (indirect).*

However, a critical point in the indirect setup is the constancy of the glass thickness: any deviation from the nominal thickness would result in shape errors on the optical side. In our case, we are using Eagle XG as glass foils, whose thickness appears much more constant with respect to other glass types, as the Schott AF32, due to the different production process of the two glass types (Fig. 6.1).

Measurements with the CUP (using the CHRocodile sensor in thickness configuration) give quantitative evidence of this difference: two Eagle XG glass foils of 100 $\times$ 100 mm^2 size were measured, giving thickness variation of $\sim$ 1 μm, whereas AF32 glass foils are affected by thickness variation of $\sim$ 5 μm.

7.5.2 Preliminary test on concave K20

As a preliminary test, experiments were performed aimed at clarifying if our setup for pressure application could also work for the indirect case. In Fig. 7.34 the direct and indirect setups are compared.

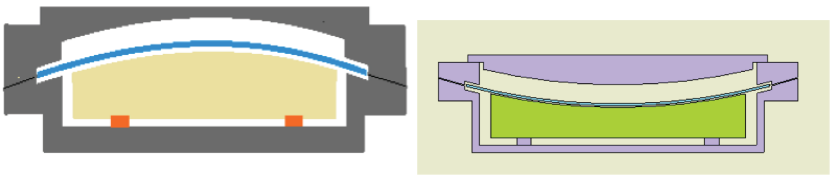

Figure 7.34: *: Our setup uses the glass foil to divide the muffle chamber in two parts and enable the pressure application by removing the air from the bottom chamber. This can be applied to the direct slumping setup (left) and the indirect slumping setup (right).*

A concave cylindrical mould in Zerodur K20 with 2 m radius of curvature, already available in our laboratories, was selected. Despite the low quality of the mould surface, this can be considered

a good test to check the indirect setup with pressure application. The flat muffle (Fig. 7.35), instead of the concave, was used, as the latter was not available. Finally, D263 as glass type was used, being the only one available at INAF-OAB with the proper size for the setup (350 × 350 mm^2).

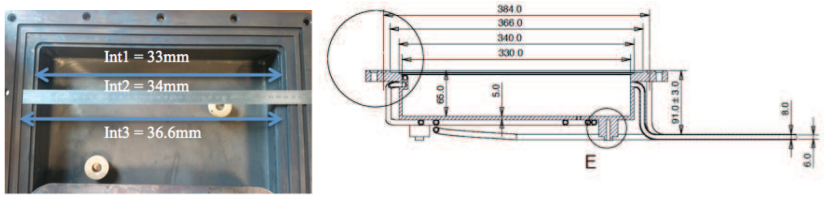

Figure 7.35: *: A picture (left) and a sketch (right) of the flat muffle used for the indirect slumping experiment.*

Fig. 7.36 shows the patterns, present on the mould surface, reproduced on the optical side of the slumped D263 glass, proving that the setup was correctly driving the glass in contact with the mould. The process parameters were the same as for the direct approach. The resulting longitudinal PV of about 40 μm, compared with the 8 μm longitudinal error of the slumping mould, is explained by the mismatch in CTE between the glass and the mould.

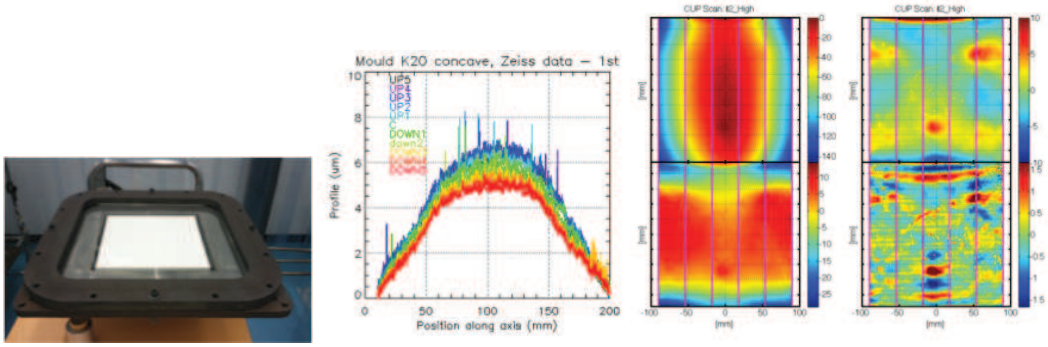

Figure 7.36: *: From left: the setup for the indirect slumping; the longitudinal mould profiles as measured with the Zeiss contact profilometer; the CUP metrological characterization of the optical side of the slumped glass. The CUP data show in the first column the residual with respect to a theoretical cylinder with radius of curvature of 2 m (up) and a patch of the longitudinal scans (down), in the second column the same map after the subtraction of the 4th (up) and 8th (down) order Legendre polynomial. This last map shows features that were present also on the mould side, proving that the glass was driven in contact with the mould.*

.

7.5.3 Roughness data on the indirect glass side

In order to study the roughness of the slumped glass foils on the side not in contact with the mould, I have measured the WYKO roughness of glass foils slumped with various combinations of mould material and mould shape. The profile WYKO data and the resulting PSD are shown in Fig. 7.37, 7.38. It can be seen that:

1. Eagle XG on convex K20: with the mould used for the direct slumping, the indirect side have roughness similar to the brand new glass up to 1 mm.

2. D263 on concave K20: the roughness is very high also at the indirect side because of the low quality of the slumping mould.

3. Eagle XG on flat Si_3N_4 : the roughness is very high also at the indirect side because of the low quality of the slumping mould.

4. Eagle XG on flat K20: even if the K20 roughness was comparable to the one of the convex K20, the indirect side have roughness similar to the brand new glass only up to 100 μm.

5. D263 on concave Fused Silica: on these glass foils, slumped at MPE on 2009 with indirect configuration, the roughness is similar to the ones currently slumped at OAB with the direct configuration.

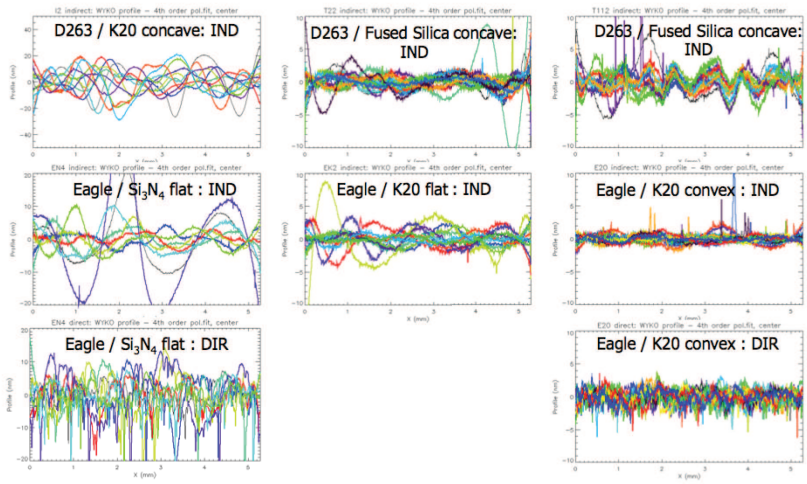

Figure 7.37: *: WYKO profiles of the glass foils slumped with various combinations of mould material and mould shape.*

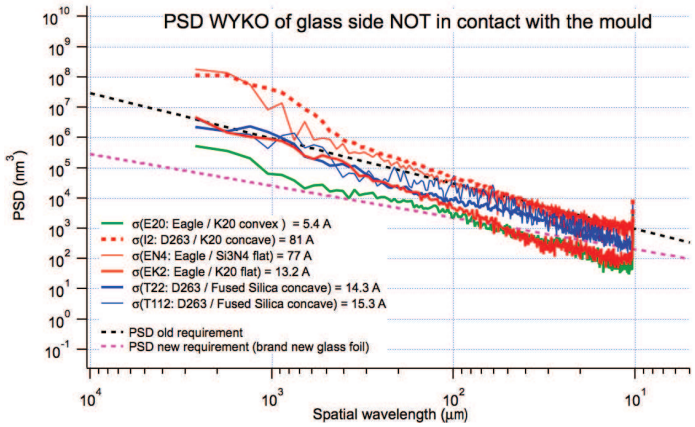

Figure 7.38: *: PSD computed from WYKO data on glass foils shown in Fig. 7.37*

From these data I conclude that the indirect slumping shows a criticality in the millimiter spatial region. This may have two possible explanations:

1. the imperfect setup, as a concave mould with proper roughness and CTE matching with the glass foil was not available,

2. the variation of glass thickness, which is critical also for the Eagle XG case.

The procurement of a K20 concave mould with proper roughness is required to clarify this crucial aspect of the indirect slumping with Eagle XG.

7.5.4 Conclusions

Preliminary slumping tests were performed proving the our setup with pressure application can be used also for the indirect slumping. The WYKO roughness of glass foils slumped with various combinations of mould material and mould shape was measured, showing a criticality in the millimiter spatial region of the indirect glass side. The procurement of a K20 concave mould with proper roughness is required to clarify this crucial aspect of the indirect slumping with Eagle XG.

CHAPTER 8

Integrated Slumped Glass Optics prototypes at OAB: X-ray and UV characterization

In order to ascertain the final performance of X-ray optics, X-ray measurements have to be performed in the X-ray energy band of interest. However, performing a direct characterisation of large optics requires large facilities to obtain broad and low-divergent beams in high vacuum. Operating these facilities is very expensive, therefore they should be used only for optics with expectedly good optical properties. To this end, several methods are available to predict the expected performance in X-rays:

1. Shape and roughness measurements of the slumped glass foils enable the prediction of the HEW in X-rays with physical optics (Section 4.4.6), which simultaneously accounts for both errors. The expected HEW values can be computed in single and double reflection. To this end, LTP data were proved to be more accurate than the CUP data (Section 4.2.7). The limit of this method, both for the LTP and the CUP case, is that the computed HEW does not take into account errors arising from the integration process (not perfect integration moulds, glue shrinkage, dust entrapped). Nevertheless, it is a very powerful method to give a feedback to the slumping process, and it was the one mostly used in this Ph.D. research.

2. In order to have a feedback on the integration process, the lastly-integrated layer of the integrated glass foils can be measured with the CUP (no LTP measurements are possible since the back side is not accessible for the First Contact - Section 4.2.3). Physical optics can be used to predict the HEW in X-rays from the measured CUP data after the integration, but frequency errors smaller than 5 mm are not accounted for, because a high-pass filter at 5 mm is always applied to the CUP data in order to remove the noise of the instrument.

3. The integrated prototypes can be measured in UV light to return a feedback also on the inner layers; the aperture diffraction term is usually subtracted in quadrature from the measured HEW values. The limit in this case is that mid- to high-frequency errors are underestimated, because profile wavelengths smaller than a few centimetres are usually not seen by UV in grazing incidence [Spiga IR02-2013].

Beside these indirect methods, X-ray measurements give the final result. They can be acquired both in-focus and intra-focus. While the first one returns the final HEW value of the prototype, the second one is also very useful, in case the focus cannot be accessed. In fact, if the detector is located at an optimal distance form the mirror, the intensity variations of the intra-focal, full-illumination image in single reflection can be used to reconstruct the profile of the mirror surfaces for all layers in the stack, providing the necessary informations to predict the HEW in focus [Spiga et al. 2013].

During my work at INAF-OAB, three integrated prototypes (Proof Of Concept, POC) have been realized: POC#2, POC#3, and POC#4. Table 8.1 reports a description of the prototypes. They have been tested in X-ray at the PANTER facility (MPE-Germany). I was personally involved in the test of the POC#2, assembled before my Ph.D activity. POC#3 and POC#4 were integrated with glass foils produced during my Ph.D. research. In the near future, a next prototype, POC#5, will be assembled with the best glass foils produced during my research, to prove in X-rays the improvement already assessed by metrology and simulation.

This chapter present the performance predicted from metrology and the results obtained in X-ray and UV, when available.

Table 8.1: *: Description of the prototypes modules realised at INAF-OAB, since 2013: in all the cases Zerodur K20 was used as slumping mould material, BK7 as integration mould (the profile accuracy of BK7 moulds is 8 arcsec HEW in double reflection).*

	POC#2	**POC#3**	**POC#4**	**POC#5**
N of plate pairs	3 + 1	1	3 + 1	4
Configuration	Co-focal	N.A.	Co-focal	Co-focal
Slumped glass material	AF32	Eagle	Eagle	Eagle
Slumping mould material	MK20-10	MK20-20	MK20-10	MK20-20B
Backplane and rib material	BK7	Borofloat	Borofloat	Borofloat
Measured angular resolution of the prototype (HEW)	22 arcsec	30 arcsec	29 arcsec	
Single PP best HEW	20.1 arcsec	5.5 arcsec	10 arcsec	

8.1 The PANTER facility at MPE

PANTER is a large X-ray facility from MPE (Garching, Germany), considered a reference calibration for X-ray optics in Europe. It has an X-ray source distant 124 m from the object under test, in order to minimize the beam divergence. Various X-ray lines can be selected from the sources, ranging from 0.18 keV to 22 keV [Burwitz et al. 2013]. Typically, 0.27 (C-K), 0.93 (Cu-L) and 1.49 (Al-K) keV are selected as X-ray energies for the calibration of our prototypes. Three detectors are available: the Position Sensitive Proportional Counter (PSPC), a spare model of the PSPC on ROSAT, with an area of 80 mm^2 and pixel size of 280 μm, usually used for alignment procedures; the Third Roentgen Photon Imaging Counter (TRoPIC), an eROSITA prototype CCD, with an area of 19.2 mm^2 and pixel size of 75 μm, mounted on the same manipulator of the PSPC; the Princeton Instruments X-ray Imager (PIXI), with an area of about 26 mm^2 and a pixel size of 20 μm, used for the focal extension facility. In fact, the facility has been upgraded in 2013 for testing optics with 20 m focal lengths [Burwitz et al. 2013] (Fig. 8.2), just like the ones produced at the moment at INAF-OAB and also for the present SPO for ATHENA. Depending on the availability of the PANTER facility, either in-focus or intra-focus measurements can be made.

8.2 The UV Vertical Optical Bench at INAF-OAB

An UV vertical bench is installed at INAF-OAB: it was initially designed to test grazing-incidence X-ray mirror shells or modules with focal lengths up to 10 m, and to optimize the integration of

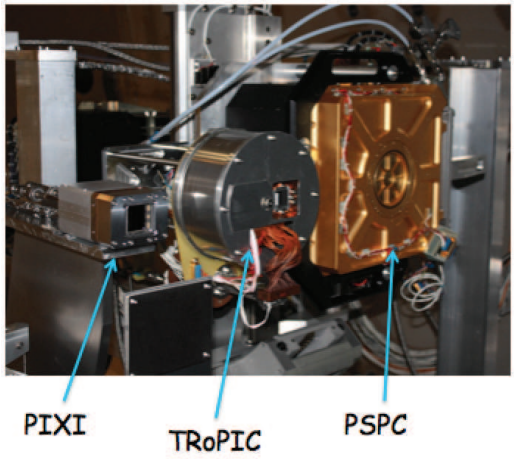

Figure 8.1: *: The three detectors at the PANTER facility. Credits: Burwitz 2013.*

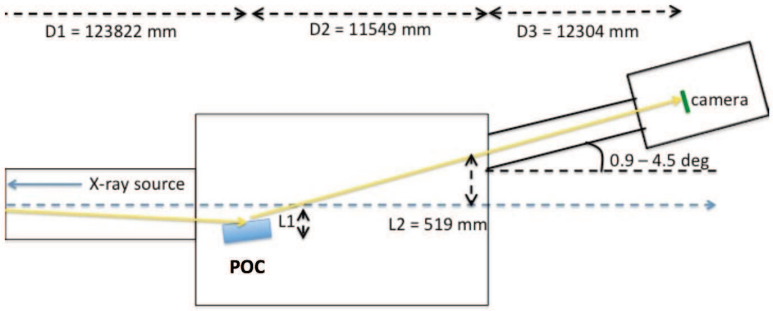

Figure 8.2: *: The extension of the PANTER facility to 20 m focal length. The source is approximatley 123 m distant from the prototype, placed on the manipulator, inside the main test chamber (with the PSPC and TRoPIC detectors). The X-ray beam, reflected by the prototype, reaches the new test chamber housing the PIXI detector at the correct focal length.*

mirror shells onto the supporting structure. In 2013 it has been modified to test optics with 20 m focal length [Spiga IR02-2013] (Fig. 8.3). The source is a Xe-Hg lamp, from which the 365 nm line is selected by a narrow-band filter. The detector is a Apogee Alta® CCD camera, with an area of 26 mm^2, and pixel size of 13 μm, usually operated in under-sampling mode, with an effective pixel size of 26 μm.

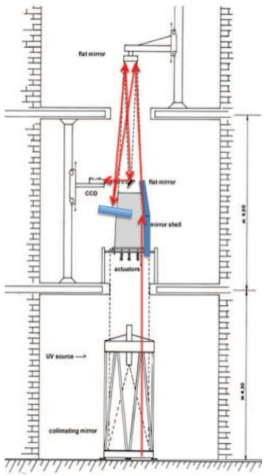

Figure 8.3: *: The UV vertical optical bench at INAF-OAB: the bench, designed for 10 m focal length, was extended to 20 m focal length by the addition of a flat mirror at 5 m distance [Spiga IR02-2013].*

The final HEW measured in UV differs from that measured in X-rays, because wavelengths smaller than a few centimetres are not seen in UV. The aperture diffraction affects all the images: for a perfect Wolter I mirror pair (length = 200 mm, radius = 1 m, f = 20 m) it contributes with 16.3 arcsec at 365 nm. Its contribution can be usually subtracted in quadrature. Despite its limits, the UV measurement is a valid method to roughly assess the quality of all the layers of a grazing-incidence X-ray module.

8.3 POC#2

The POC#2 was integrated in early 2013, with glass foils slumped before my Ph.D. activity. The configuration of this module is described in Table 8.1. AF32 slumped glass foils were preferred to D263, because at that time they were giving the best result, owing to the better CTE matching of the AF32 with the Zerodur K20, compared to the D263 (CTE_{K20} = 2.0 10^{-6}/K, CTE_{AF32} = 3.2 10^{-6}/K, CTE_{D263} = 7.2 10^{-6}/K). The codes of the integrated glass foils are provided in Table 8.2. Three optical layers were integrated, plus one dummy layer.

The ribs and the backplanes were selected in BK7 material. This is a major issue, because there is a CTE mismatch between the ribs and the glass foils (CTE_{BK7} = 7.2 10^{-6}/K). This mismatch would produce a degradation of 2.0 arcsec for each pair plates [IXO-OAB-TN-09 2012], if a temperature mismatch of 1°C between integration and operation/measurement occurs (for comparison, the image degradation using the D263 glass would be only 0.5 arcsec). Two kinds of ribs were selected in order to have a co-focal configuration, i.e. varying the parabola-hyperbola angle in proportion with the distance from the optical axis: parallel ribs are used for the parabolic side and trapezoidal ribs are used for the hyperbolic side. The ribs thickness is variable with an average value of about 2.8 μm and a tolerance of $\pm$ 15 μm. The ribs width is 2 .35 mm with a tolerance of $\pm$ 100 μm. The glue layer used for the integration is Masterbond EP30-2, a glue with extremely low shrinkage. The thickness used is 75 μm, sufficient to absorb the rib thickness

variation. Hence, the ribs do not have to be accurately polished, reducing the cost. The integration moulds in BK7 were figured at Zeeko Ltd to a final HEW of about 3-4 arcsec in single reflection and 8 arcsec in double reflection [Civitani et al. 2014].

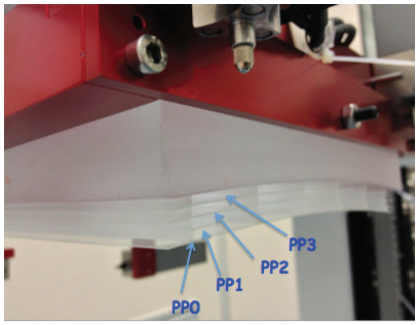

Figure 8.4: *: The prototype POC#2 integrated, viewed sideways to show the four layers of glass foils. For the outermost layer, PP0, the glass foils with better performance, as expected from metrological data after slumping (see Section 8.3.1), were selected. The innermost layer, PP3, is a dummy layer.*

Fig. 8.4 shows the stack of the four plate pairs (PP): the PP0 is the last integrated. The POC#2 optical design has been made in order to use the same integration mould for all layers. In theory in fact, each layer should be integrated on a Wolter I mould with different radius. In this case, a glass foil slumped with no figure error and forced from cylinder to a Wolter I configuration, would result in a HEW less than 1 arcsec (for radius of curvature of 1 m, size of 200 $\times$ 200 mm^2, focal length of 20 m, incidence angle of 0.7 deg, and 6 ribs). All layers would focus at a distance given by $f = r/\tan(4\theta)$ (Eq. 2.8), where r is the radius of curvature of the integration mould, equal in this case with the axial distance of the shell.

In our case instead, the same integration mould is used for different layers. If the shells are integrated in a parallel configuration, their foci are displaced in the focal plane. To bring the foci to superimpose at the axis of the telescope, θ is changed, which means that f changes for each shell. In this way, only one PP in the stack have the correct radius of curvature and cone angle: this was chosen to be the PP1. The best focus of other PPs is translated by few tenth of mm with respect to PP1. In this approximation, assuming perfect mirrors, there is an aberration that increases with the difference of the theoretical radius and the radius of the used integration mould. For PP3 the effect is an HEW contribution of 6 arcsec, for PP2 of 2.9 arcsec, PP1 would have HEW = 0 arcsec for a perfect Wolter I mirror, and for PP0 a 2.8 arcsec degradation would be present.

8.3.1 Metrology before integration

Shape (LTP and CUP) and roughness (WYKO) data were used to predict the HEW value expected in single reflection from the slumped glass foils, after the simulation of a perfect integration (Section 4.4). Table 8.2 reports the result of these computation, for the glass foils integrated into the POC#2. Since the roughness contribution is always less than 1 arcsec at 1 keV X-ray exposure energy, the rms result is reported, rather than the HEW contribution from roughness, to clearly differentiate the roughness of the glass foils. As for the HEW expected from profiles data, it can be seen that HEW values computed from CHR data are consistently larger than those from CUP. Several reasons contribute to this aspect: CHR data are sampled with a higher spatial frequency (step$_{CHR}$ = 1mm, step$_{CUP}$ = 5-10 mm), they include the edges of the glass foils, and finally they are affected by spurious mid-frequency errors, as clarified in Section 4.2.3. For the next prototypes, assembled during my Ph.D. work, CHR measurements were not considered anymore, while LTP was considered as the most reliable to compute HEW values. This is described in

Section 4.4, where I show that the new method developed with LTP and First Contact is also in line with the ZYGO interferometer result (Section 4.2.7), and substantially smaller than the CUP result, especially at the glass edge.

Table 8.2: *: POC#2 integrated glass foils. The HEW values are computed with physical optics from CHR and CUP data, in single reflection assuming a perfect integration. CHR values are computed from 5 scans, 198 mm long, with 1 mm step. CUP values are computed from a sampled area of 180 mm × 180 mm, with 10 mm step in X and 5 mm step in Y. HEW values data from CUP are consistently higher than those from CUP because they are sampled with a higher spatial frequency, include the edge of the glass foils, and are affected by spurious mid-frequency errors, as clarified in Section 4.2.3.*

	PP0		**PP1**		**PP2**		**PP3**	
	Par F19	Hyp F20	Par F6	Hyp F12	Par F3	Hyp F5	Par F7	Hyp F14
HEW expected at 1 keV from CHR [arcsec]	14.9	14.5	15.4	18.5	20	17.5	17	29
HEW expected at 1 keV from CUP [arcsec]	9	8	7	8	8	8	10	15
rms WYKO [Å]	16.3	16.1	15.1	12.9	18	15	12.3	8.1

8.3.2 Metrology after integration

The metrology of the integrated prototype was performed with the CUP available at INAF/OAB. As a consequence of the stacking procedure, the external layer is the only one accessible with our metrological device. In fact, to allow the measurement, the stack needs to be dismounted from the IMA. Therefore, to avoid misalignment in the integration, the measurement is done only for the last layer integrated into the stack. The CUP measurements were done with a sampling of 10 mm in X and 5 mm in Y. After the completion of the POC#2, it has been decided to work with high resolution sampled maps, scanning the glasses with 1 mm sampling. The maps of the external glass foils (F19 parabola, F20 hyperbola) are shown in Fig.s 8.5 and 8.6. Fig. 8.5 shows the results of the maps after the simulation of a perfect integration, while the Fig. 8.6 shows the measured foils after the integration. The corresponding HEW values are also reported, as function of the azimuthal coordinate. The expected HEW in double reflection for PP0 is 17 arcsec [Civitani et al. 2013b].

8.3.3 UV data

Fig. 8.7 reports the images of the three optical layers (PP0, PP1 and PP2), at the position of the best focus for PP1 (as described before, the best focus of the different PPs would not be at the same axial position). The individual PPs have been selected with a dedicated mask (Fig. 8.8-right).

Table 8.7 reports the HEW measured for each PP at its best focus position. The PPO result is in line with the expectation from metrological data after integration ($HEW_{double-refl-CUP}$ = 17 arcsec).

Table 8.3: *: Expected HEW values from UV data of the integrated POC#2, at the best focus position for each PP. The aperture diffraction contribution at 365 nm accounts for 16.3 arcsec. Credits: Civitani et al. 2013b.*

	HEW measured in UV [arcsec]	**HEW in UV after aperture diffraction subtraction [arcsec]**
PP0	22.8	16
PP1	28.2	23
PP2	21.2	15

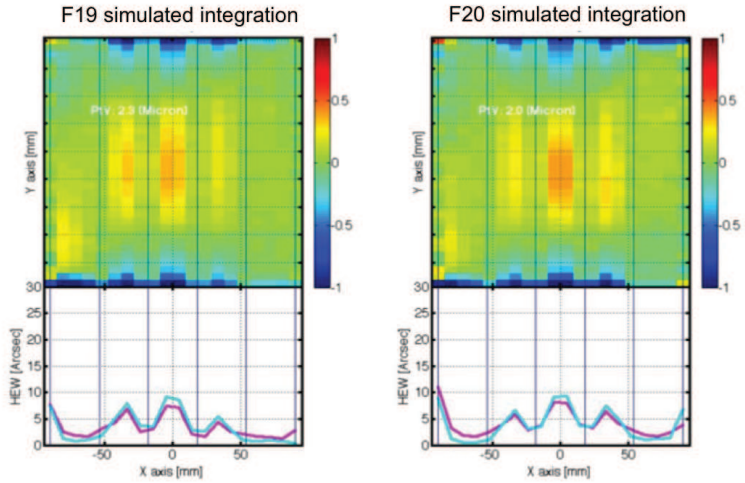

Figure 8.5: *: Shape and expected HEW of F19-F20 integrated into POC#2, as PPO, the external layer. CUP shape after simulated integration, and corresponding HEW. The pink and blue HEW lines are the expected values from ray tracing and Fresnel computation, respectively [Civitani et al. 2014].*

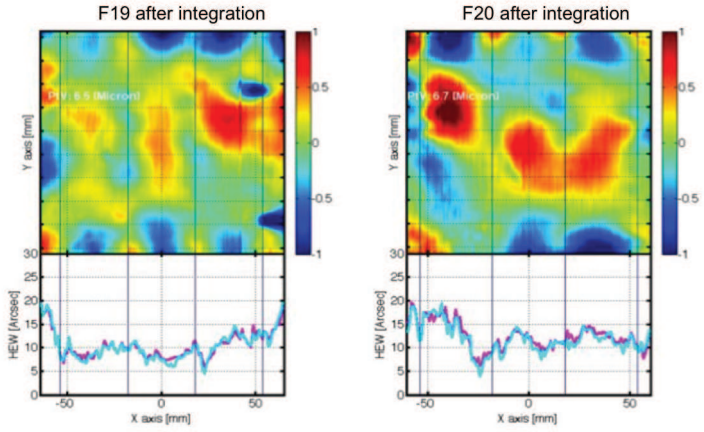

Figure 8.6: *: Shape and expected HEW of F19-F20 integrated into POC#2, as PPO, the external layer. Measured CUP shape after integration, and corresponding HEW. The pink and blue HEW lines are the expected values from ray tracing and Fresnel computation, respectively [Civitani et al. 2014].*

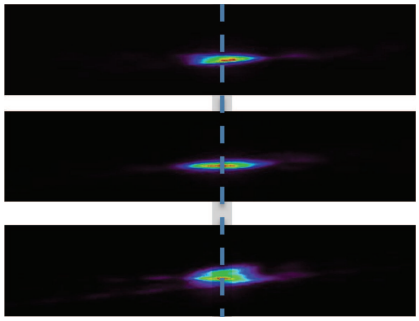

Figure 8.7: *: UV images for PP0, PP1 and PP2, recorded without changing the position of the CCD camera along the optical axis. Credits: Civitani 2013b.*

8.3.4 PANTER data intra-focus

The first X-ray calibration of the POC#2 prototype has been done in spring 2013, when the PANTER extension to 20 m focal length was not available for scheduling reasons. Therefore, the campaign of measurements has been done at 8 m focal length, with the TRoPIC detector, while PSPC was used for the alignment. Fig. 8.8 shows the setup and the mask used to measure each PP. The entire layer or its central part can be selected.

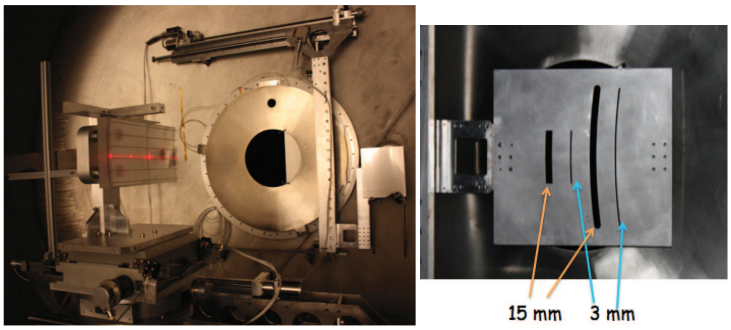

Figure 8.8: *: Left: The POC#2 at the PANTER facility. Right: the masks used for the selection of each PP.*

Since TRoPIC has an area of 19.2 mm^2, while the intra-focal image of a PP would be 133 mm long (and 1.7 mm thick), 14 images were taken per PP, scanning along the trace length [Spiga et al. 2013]. The Carbon target was selected as X-ray source; in addition to the C-K_α line at 0.27 keV, also the 1.8 keV W-M_α line from the Tungsten filament was present. Fig. 8.9 reports the intra-focal images of the PP0, in double reflection at 0.27 and 1.8 keV, and in single reflection both on the parabola and the hyperbola side at 0.27 keV. Single reflection at 1.8 keV is not possible, because the incident angle should be doubled to avoid double reflection, going beyond the glass energy cut-off for reflectivity. From single reflection measurements, a brightness distribution can be observed, closely related to the local curvature in the longitudinal direction. A quantitative reconstruction of the mirror profile can then be obtained under particular assumptions [Spiga et al. 2013]. With this analysis, the ray-tracing computation of the single and double reflection from the PP0 was shown to be in line with the measured X-ray images, therefore validating the method. The in-focus PSF could then be computed from the reconstructed maps. This is shown in Fig. 8.10, returning expected HEW at 0.27 keV of 15.5 arcsec, in line with the 17 arcsec from CUP metrology and with the 16 arcsec from the UV measurements, after subtracting in quadrature the aperture diffraction term.

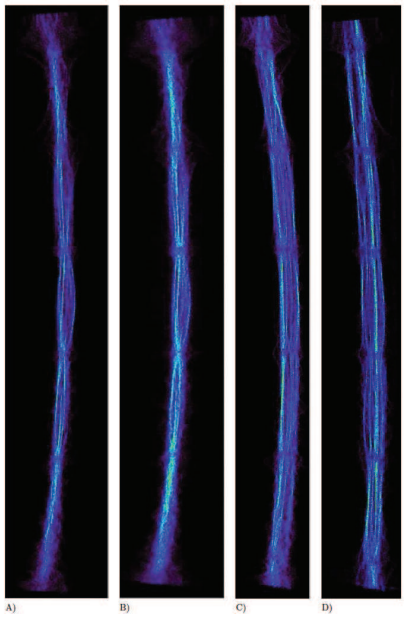

Figure 8.9: *: Collected TRoPIC exposures on intra-focal traces of the PP0. A) double reflection at 0.27 keV. B) double reflection at 1.8 keV. C) single reflection on the parabola at 0.27 keV. D) single reflection on the hyperbola at 0.27 keV. Credits: Spiga et al. 2013.*

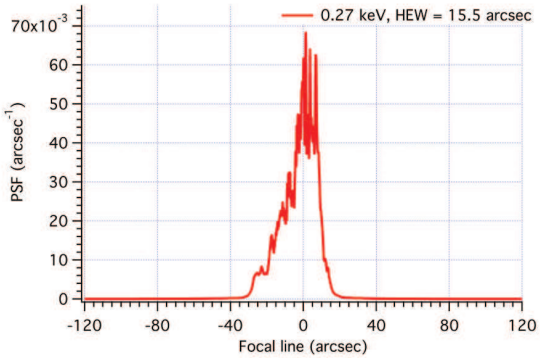

Figure 8.10: *: The predicted PSF at 0.27 keV, as computed [Raimondi & Spiga 2015] from the measured microroughness and the longitudinal profiles reconstructed from the intra-focus images.*

8.3.5 PANTER data in focus

In focus direct X-ray tests could be performed, with the extended PANTER facility, in early 2014. By selecting each layer with the 3 mm thin mask (Fig. 8.8), the best focus for each PP and the corresponding HEW could be determined. The best HEW corresponds to PP0, being 20.3 arcsec at 0.27 keV [Civitani et al. 2014]. Its value increases to 24.9 arcsec at 1.49 keV, because of scattering. By selecting only the central part of the PP0, its HEW decreases to 18 arcsec at 0.27 keV. The complete module HEW is 22.1 arcsec at 0.27 keV, incresing to 25.6 arcsec at 1.49 keV. The increase is due to the roughness of the foils, since the tolerance PSD is tailored to keep the XRS below 1 arcsec, but only for E $<$ 1 keV. Beyond this value, the scattering increases rapidly.

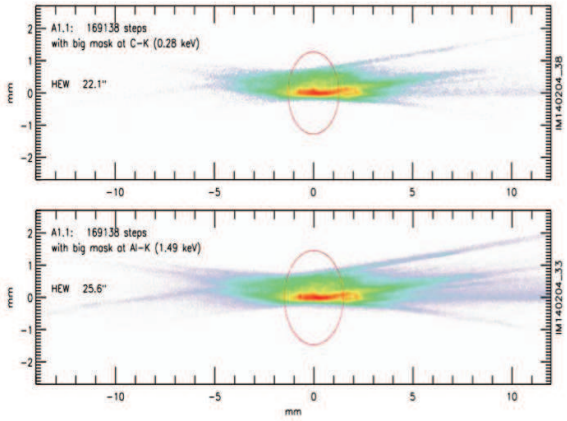

Figure 8.11: *: The focal spot of the POC#2 (all plate pairs, complete azimuthal section) at 0.27 keV and 1.49 keV. Credits: Civitani et al. 2014.*

The measured in-focus HEW of the PP0 is larger (20.3 arcsec) than the expected one from the previously described analysis technique (from 15.5 to 17 arcsec). The reason is that only the central part of the profile, the smoothest one, was reconstructed.

In order to understand these measurements, the roughness of the PP0 after the integration was measured with the WYKO, at different scan positions, namely above the ribs and at the maximal distance from the ribs, in order to quantify the effect of the glue on the glass surface.

8.3.6 Roughness characterisation of POC#2 post-PANTER

After the PANTER campaign, the POC#2 was measured with the WYKO interferometer at the PP0 layer, the only one accessible with the measurement. Three scans were taken (Fig. 8.12), both at the parabola and hyperbola side: on the rib (red line), very close to the rib (orange line) and at the largest distance from the rib (dark green line). Due to limitation in the WYKO positioning in front of the POC#2, only the central rib neighbourhood could be measured. The PSD's from these measurements are over plotted in Fig. 8.13, together with the PSD taken at the central longitudinal scan before the integration (light green line).

These measurements show that the glass portion above the ribs is the most affected by the integration process, most probably a glue effect: either bubbles in the glue or the glue shrinkage was considered as the root cause. The problem is still not fully understood. The expected HEW degradation from roughness at 1.5 keV, considering a PSD like the one measured over the central rib (red line), would be $\sim$ 3 arcsec, consistent with the larger increase measured near the ribs in X-ray going from 0.27 to 1.49 keV.

Figure 8.12: *: Scan positions for WYKO measurements of the POC#2 post-PANTER. The red scan is on the central rib, the orange scan is very close to the central rib; the green scans are at the anti-rib position.*

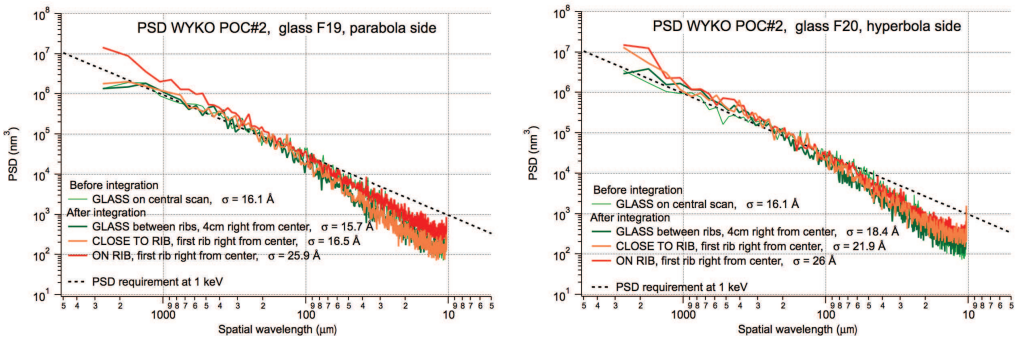

Figure 8.13: *: PSD from WYKO data of the external layer of the POC#2, as measured post-PANTER. Three scan positions, at different distances form the ribs (see Fig. 8.12), were measured, to determine the effect of the glue shrinkage on the roughness values.*

8.4 POC#3

The POC#3 was integrated in 2014. The configuration of this module is described in Table 8.1. In this case, Eagle glass has been used, and the glass foils have been slumped on a new slumping mould of Zerodur K20 (Section 6.5). The introduction of the new slumping mould improved the micro-roughness of the slumped glass foils by about 40 % with respect to the glass foils of POC#2 (passing from 16 nm rms to about 10 nm rms, in the WYKO range). The material of the backplane and the ribs has been modified from BK7 to Borofloat in order to have a better matching with the glass CTE ($CTE_{Borofloat33}$ = 3.25 10^{-6}/K, CTE_{Eagle} = 3.17 10^{-6}/K, CTE_{BK7} = 7.2 10^{-6}/K). A new backplane and new tapered ribs have been procured. The prototype was composed of a single plate pair.

8.4.1 Metrology before integration

The codes of the glass foils, integrated into the POC#3, are given in Table 8.4, together with the expected HEW values computed from LTP and CUP data, considering a single reflection and a perfect integration. The overall HEW values from CUP data are larger than those from LTP. The main reason can be understood by comparison reported in Fig. 8.14. The CUP measurement was done on a 190 × 190 mm^2 area, with a sampling of 1 mm, both in X and Y directions. The LTP scans were performed on five scans: at the central longitudinal position, 45 mm and 86 mm from the centre, in both directions. Clearly, LTP underestimates the glass area. Nevertheless, the HEW_{LTP} values are slightly larger than the HEW_{CUP} for the central scan, similar at the 45 mm scans, and substantially smaller for the 86 mm scans. The difference, in this 86 mm position, is

in line with what observed on the MK20-20B, when measured with both LTP and CUP, and then compared for reference with the ZYGO measurements, in agreement with the LTP result (Section 4.2.7). The main difference is most likely due to the CUP carriages, which are less accurate at the lateral azimuthal positions.

Table 8.4: *: POC#3 integrated glass foils. The HEWs are computed with physical optics from LTP and CUP data, in single reflection considering a perfect integration. LTP values are computed from 5 scans, 198 mm long, with 1 mm step: the data are then subtracted with the FEA profiles, accounting for the gravity and bearing points deformation (Section 4.2.3). CUP values are computed from a sampled area of 190 mm × 190 mm, with 1 mm step. The overall HEW values from CUP data are larger than those from LTP. By comparing the HEW values computed for the single scans in Fig. 8.14, the main difference appears in the lateral portion of the glass foil, where the CUP carriages are less accurate (Section 4.2.7).*

	Par E16	**Hyp** E18
HEW expected at 1 keV, from LTP [arcsec]	3.9	3.3
HEW expected at 1 keV, from CUP [arcsec]	8.5	8.2
rms WYKO [Å]	10.9	9.9

8.4.2 Metrology after integration

The maps of the integrated E16 (parabola) and E18 (hyperbola) are shown in Fig. 8.15 [Civitani et al. 2014]. By comparing the same maps before the integration, when the sole simulation of a perfect integration was performed (Fig. 8.14), the real effect of the integration becomes more evident. The difference between the simulated and the real integration is 0-5 arcsec HEW, along the different longitudinal scans. The integration errors also take into account the intrinsic error of the integration moulds, estimated about 3-4 arcsec HEW.

8.4.3 PANTER data in focus: complete azimuthal section

The POC#3 was measured in X-ray, in focus, in 2014. The performance of the overall prototype is given in Table 8.5 at different energies. The images of the POC#3 in focus at different X-ray

Table 8.5: *: HEW values of the integrated POC#3, measured in X-rays at different energies, at the best focus position of PP0. Credits: Civitani et al. 2014.*

	HEW at 0.27 keV [arcsec]	**HEW at 0.93 keV [arcsec]**	**HEW at 1.49 keV [arcsec]**
PP0	32.6	29.4	29.2

energies are presented in Fig. 8.16.

8.4.4 PANTER data in focus: pencil beam

Despite the result obtained on the complete PP was not improved with respect to the POC#2, this new model was particularly useful to test the pencil beam characterization procedure during the X-ray test at PANTER (Fig. 8.17).

Fig. 8.17 shows the HEW values, determined in focus for PP0, scanning the mirror with a 20 mm × 3 mm slit, along its azimuthal length. The scans have been repeated at different energies. The vertical lines indicate the ribs positions on the glass foils. The figure shows that the scattering effect is not homogeneous on the mirror. For example, an inversion of the expected optical performances vs. energy, is evident in the area between 30 and 60 mm. At lower energy, the HEW is about 55 arcsec, while it decreases to 25 arcsec at 1.49 keV. This effect could be due to dust contamination [O'Dell et al. 1993] and it could be responsible for the higher HEW measured in full illumination mode at 0.27 keV [Civitani et al. 2014].

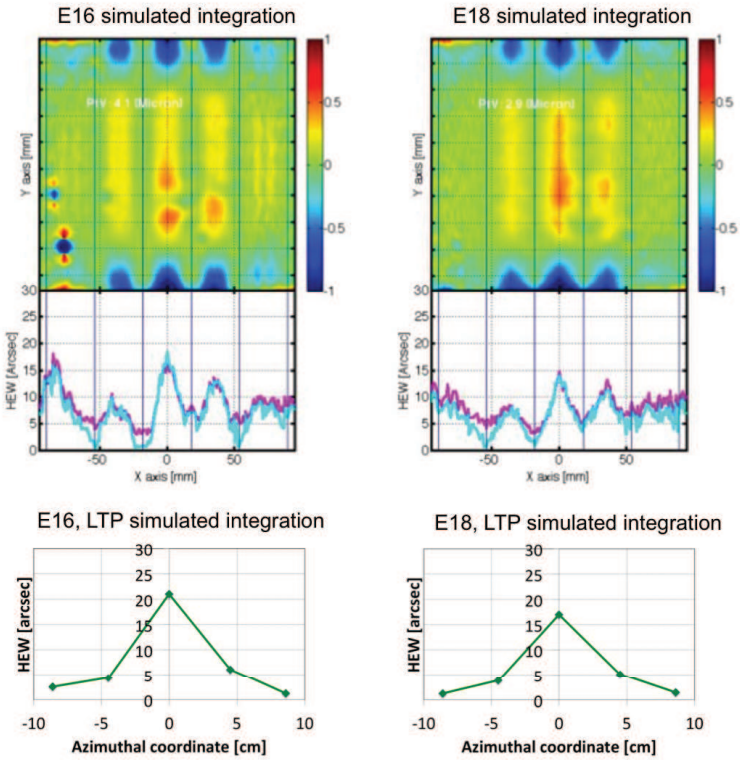

Figure 8.14: *: Shape and expected HEW of E16-E18 integrated into POC#3. Top: CUP shape after simulated integration, and corresponding HEW. The pink and blue HEW lines are the expected values from ray tracing and Fresnel computation, respectively [Civitani et al. 2014]. Bottom: HEW computed for the five LTP scans, after the simulation of the integration. The main difference in the HEW from CUP and LTP data is in the lateral portion of the glass foil, where the CUP carriages are less accurate.*

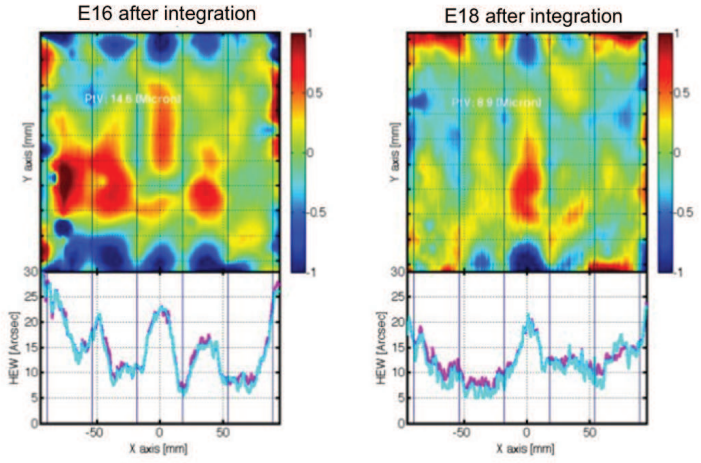

Figure 8.15: *: Shape and expected HEW of E16-E18 integrated into POC#3. Measured CUP shape after integration, and corresponding HEW [Civitani et al. 2015].*

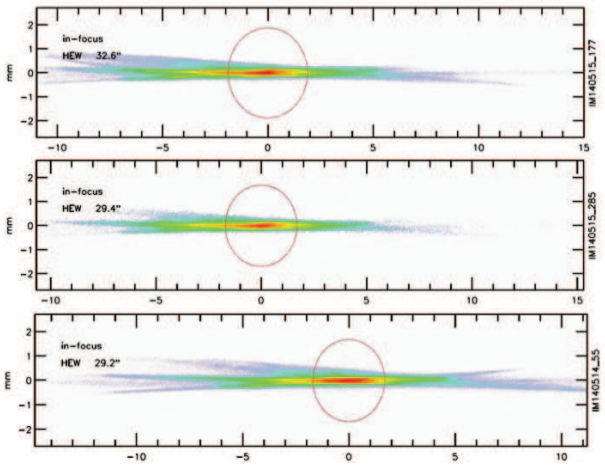

Figure 8.16: *: The focal spot of the POC#3 (complete azimuthal section) at 0.27, 0.93 and 1.49 keV. Credits: Civitani et al. 2014.*

The right portion of the glass foils shows the best result in terms of HEW. In fact, in this area the HEW is lower than 10 arcsec, with a minimum of 5.5 arcsec at 0.27 keV and 7.5 arcsec at 1.49 keV. This is a very positive result, than could be inferred only by the pencil beam scans. This confirms the potentiality of the process.

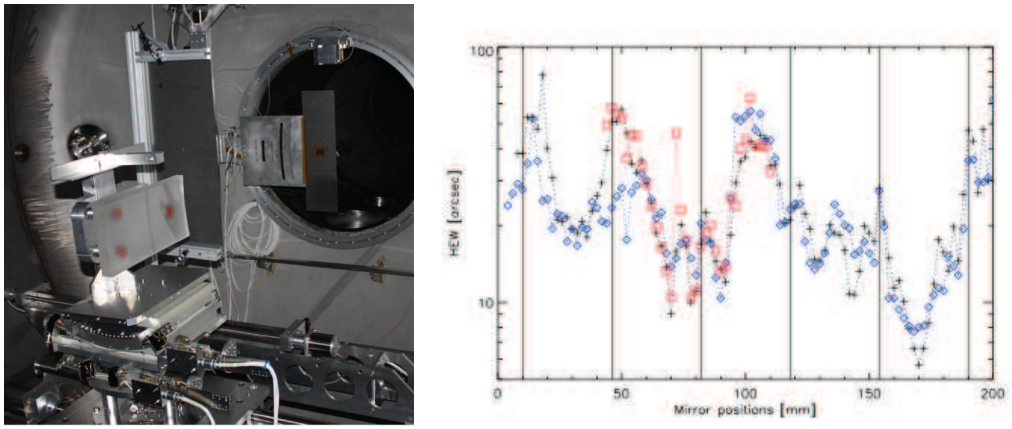

Figure 8.17: *: The POC#3 calibration at PANTER, obtained via pencil beam characterization. Left: a picture showing the prototype and the masks, inside the PANTER chamber. Right: HEW measured @ 0.27 keV (black), @ 0.93 keV (red), and @ 1.49 keV (blue). The black, solid lines indicate the rib positions. Credits: Civitani et al. 2014.*

8.5 POC#4

The POC#4 was integrated in 2015. The configuration of this module is described in Table 8.1. Eagle glass foils have been slumped on the old slumping mould of Zerodur K20, while the new one was been reworked (Section 6.6). The roughness values of the integrated glass foils was therefore like the ones previously integrated into the POC#2 (about 16 Å rms in the WYKO range). The prototype was composed of four layers of glass foils: the optical layers, PP0, PP1 and PP2, made of bare slumped glass, while the dummy layer, PP3, had glass foils coated with gold to experience the integration procedure with coated glass [Civitani et al. 2015].

Fig. 8.18 shows the stack of four plate pairs (PP): PP0 is the lastly integrated, as usual.

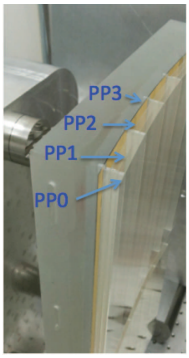

Figure 8.18: *: The prototype POC#4 integrated, showing the four layers of glass foils. PP3, the inner layer, is coated with gold to test the integration process with coated glass foils.*

8.5.1 Metrology before integration

The code of the integrated glass foils are reported in Table 8.6, together with the expected HEW values computed from LTP and CUP data, considering a single reflection and a perfect integration; roughness rms from WYKO data are also listed. As for the POC#3, the HEW values expected from LTP are lower than the one expected from CUP data, mostly due to the less accurate CUP measurement at the edges of the glass foils. Nevertheless, in both cases, the expected values are smaller than for the POC#2 and POC#3 (Fig. 8.19), owing the smaller PV of the slumped glass foils (Section 6.6).

Table 8.6: *: POC#4 integrated glass foils: expected HEW from profile data after the simulation of a perfect integration, and rms values from roughness data.*

	PP0		PP1		PP2		PP3	
	Par E33	Hyp E35	Par E32	Hyp E34	Par E27	Hyp E30	Par E5	Hyp E9
Expected HEW from LTP [arcsec]	5.3	5.3	4.6	5.1	4.7	5.9	5.3	7.2
Expected HEW from CUP [arcsec]	6.8	7.2	6.0	6.4	6.7	7.9	6.7	7.2
Expected HEW from CUP after coating [arcsec]							7.8	9.2
rms WYKO [Å]	15.7	13.4	16.1	13.5	14.5	15.1	18.3	19.3

8.5.2 Metrology after integration

Only the external layer, the PP0, is accessible for CUP measurements. The maps of the integrated E33 (parabola) and E35 (hyperbola) are shown in Fig. 8.20 [Civitani et al. 2015]. The maps show that one side of the parabolic mirror was detached from the ribs during the dismounting procedure from the integration machine. By comparing the same maps, before the integration, when the sole simulation of a perfect integration was performed (Fig. 8.19), the difference in HEW is in the range of 0-5 arcsec, along the different scans. The error takes into account the intrinsic error of the integration moulds (3-4 arcsec for each mould), the presence of dust entrapped during the integration and the glue shrinkage. Anyway, in the region were no local defects are present, the HEW is expected below 10 arcsec.

8.5.3 UV data

In order to have informations on layers others than the external PP0, the POC#4 was measured under the UV bench. The subtraction in quadrature of the diffraction term gives HEW of about 12 arcsec for PP0, in line with the 10 arcsec expected from the CUP metrology after integration [Civitani et al. 2015]. In particular, the central part (i.e. excluding the detached area) returns an expected HEW value of 9.7 arcsec, after the aperture diffraction subtraction.

Table 8.7: *: Expected HEW values from UV data of the integrated POC#4, with and without the subtraction in quadrature of the aperture diffraction term. Credits: Civitani 2015.*

	HEW measured in UV [arcsec]	HEW in UV after aperture diffraction subtraction [arcsec]
PP0	21	12.5
PP1	23.5	16.3
PP2	21	12.5
PP3	39	35

8.5.4 PANTER data in focus: complete azimuthal section

The X-ray measurements were performed in early 2015, in focus, with the PIXI detector. The design of the POC#4 was the same as for the POC#2: the common focus corresponds to the one of the PP1 layer. The HEW of the different layers are reported in Table 8.8. The X-ray measurements confirm that the PP3 is much worse than the others PPs: the integration of a coated layer suggested that an upgrade of the integration procedure was needed, when considering coated glass foils. A deflectometry system is now already installed in the integration machine, in order to detect dust grain entrapped under a coated glass. Anyway, all the HEW values in X-rays are higher than expected from optical and UV metrology (12 to 15 arcsec).

Table 8.8: *: HEW values of the integrated POC#4, measured in X-rays at different energies, at the best focus position for each PP. Credits: Civitani 2015.*

	HEW at 0.27 keV [arcsec]	HEW at 1.49 keV [arcsec]
PP0	20.7	22.9
PP1	27.9	29.5
PP2	32.7	35.1
PP3	54.0	57.4
PP0+PP1+PP2	29.3	31.8

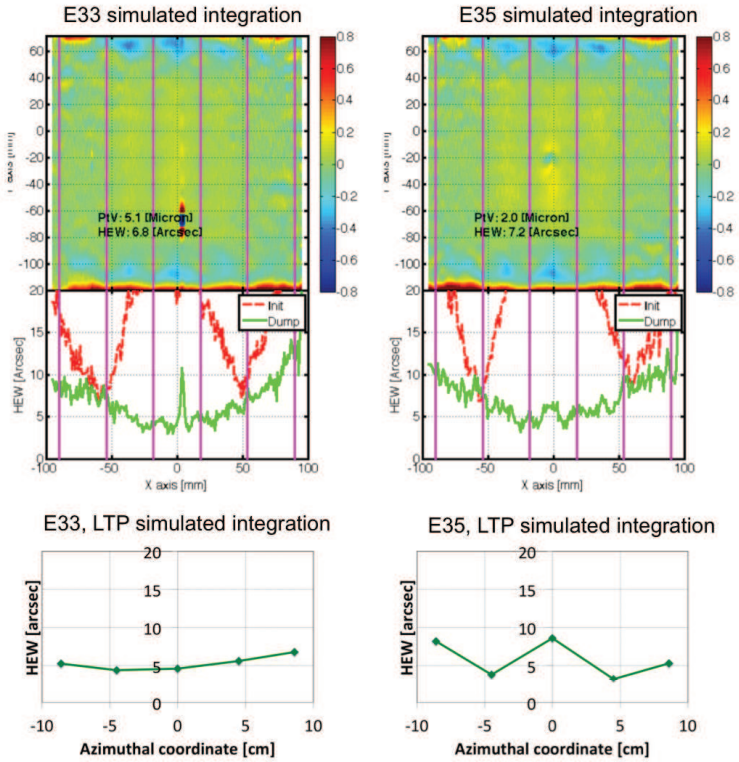

Figure 8.19: *: Shape and expected HEW of E33-E35 integrated into POC#4, as PPO, the external layer. Top: CUP shape after simulated integration, and corresponding HEW [Civitani et al. 2015]. Bottom: HEW computed for the five LTP scans, after the simulation of the integration.*

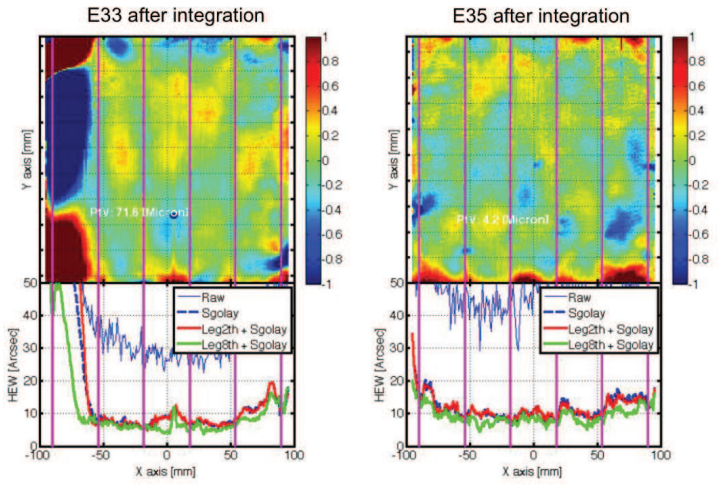

Figure 8.20: *: Shape and expected HEW of E33-E35 integrated into POC#4, as PPO, the external layer. Measured CUP shape after integration, and corresponding HEW [Civitani et al. 2015]. In the left portion of the parabola side (E33), a glass detachment occurred while dismounting from the integration machine.*

8.5.5 PANTER data in focus: pencil beam

In order to understand the difference from X-ray results and UV-optical tests, the pencil beam measurements were carried out on all the layers. The images in Fig. 8.21, especially the first image for PP0, show an inversion of the expected HEW minima and maxima. In theory, the ribs position should be characterised by the maximum error correction, hence the smallest HEW; on the contrary the ribs position corresponds to the largest HEW. Post-PANTER alignment checks were performed on the POC#4: some issues regarding the alignment of the mirrors were reported. Anyway, the problem was not completely clarified. The integration of the next prototype is expected to give better results and to give some insight into the POC#4 results.

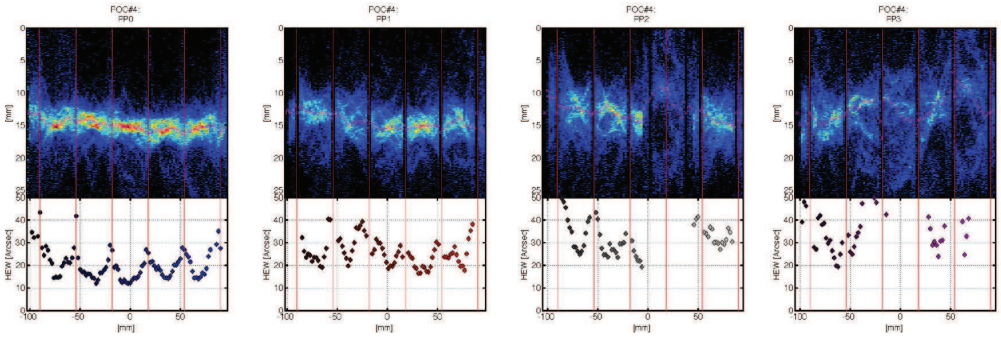

Figure 8.21: *: The POC#4 calibration at PANTER/MPE, obtained via pencil beam characterization measurements @ 0.27 keV. At the top, the reconstructed images. At the bottom, the measured HEW. The red, solid lines indicate the rib positions. From left to right: PP0, PP1, PP2, PP3, where PP0 is the outermost layer. Credits: Civitani et al. 2015.*

8.6 Conclusions

In order to demonstrate that the SGO technology is suitable to make the mirrors for the ATHENA telescope, direct X-ray test has to be performed. The X-ray facility we use, the PANTER/MPE at Garching (Germany) has the required characteristics: long source distance, low divergence, and the possibility to work both in full illumination, to retrieve the final resolution of the optic, and in pencil beam mode, to locally probe the optic. Anyway, due to other research projects to be tested at PANTER, in particular the e-ROSITA module, the facility is not always available. Therefore, we perform measurements able to return a prediction of the optic performance, prior to tests in X-rays. These include optical metrology of single glass foils (shape with LTP and CUP, roughness mainly with WYKO), extensively used in this thesis to give the quickest feedback to the slumping process, optical metrology of the integrated foils (with CUP, only on the external layer) and UV metrology for all the layers. These methods have limitations, and an X-ray test is needed to assess the real performances. In case the facility cannot be used in focus, the tests can also be performed intra-focal, giving essential informations on the integration process for each layer.

The prototypes already integrated with glass foils produced during my Ph.D. activity, POC#3 and POC#4, were tested with the different techniques. POC#3, with glass foils slumped on a newly polished Zerodur K20 mould (MK20-20), showed a best sector of the module with HEW $\sim$ 5 arcsec, in X-rays, measured in focus. Its overall HEW, in X-rays, was anyway larger than the previous prototype (HEW-POC#2 = 22 arcsec, HEW-POC#3 = 30 arcsec), mainly because of a high sag error experienced on the slumped glass foils when using a smooth slumping mould. The POC#4 was produced with glass foils slumped on the same old K20 mould as for the POC#2 (MK20-10), after developing a process that could work both on rough and smooth slumping

mould surfaces. The sag error was reduced from about 10 to 2-4 μm. Owing this improvement and the reduction of the mid-frequency contribution, several sectors of the module (the intra-ribs portions) returned HEW = 10-15 arcsec in X-rays, consistent with the POC#3. The HEW, inferred from optical and UV metrology, was 15 arcsec. Nevertheless, the final total HEW of the module was again higher than the POC#2 (HEW-POC#4 = 29 arcsec). Post-PANTER analyses have correlated this result with a misalignment of the parabolic and hyperbolic segment.

The near future integration of a new module, the POC#5, with glass foils slumped on the newly procured K20 mould (MK20-20B), with reduced low-, mid- and high-frequency errors, will finally clarify the potentiality of the SGO technology. The glass foils therein integrated will be the final result of the optimization work carried out in my Ph.D. research. In Section 6.7 I have extensively shown the improved quality of these slumped glass foils, whose expected resolution in single reflection is about 2 arcsec, to be compared with the 7 arcsec of the ones integrated into the POC#2.

CHAPTER 9

Slumped glass foils as substrates for active optics

9.1 Scientific motivation

In order to push the resolution performances of an X-ray telescope, made by replication technique with slumped glass optics, to the quality achieved by the Chandra telescope (HEW = 0.5 arcsec), whose mirrors were directly polished (Section 2.6), further improvements must be taken into consideration. Several groups are working on the possibilities offered by the use of active corrections. The active optics concept is similar to the one used for adaptive optics, well established for optical telescopes, with the only difference that the correction of the optics figure is performed only once, or with low frequency, and it is intended to correct for residual figure errors (on ground) or contributions from, e.g., the thermal environment and the lower gravity field once in orbit. The synchrotron community has been using active optics, for more than 15 years, to optimise the focusing properties of the beam and possibly to shape the intensity distribution of the focal spot with the desired profile. Many facilities employ mechanically bent optics, however an alternative approach uses piezoelectric bi-morph mirrors (PBM), which alter the focusing capability of the optics via piezoelectric control [Signorato et al. 1998]. However, the know-how of the active optics at the synchrotron facilities cannot be transferred plug-and-play to the X-ray telescopes, as few constrains are imposed in the astronomy field, such as:

1. limited weight to sustain launch;
2. shell nesting to increase the collecting area, as astronomical objects are faint whereas synchrotron sources are powerful.

Due to the tight nesting typical of an X-ray telescope, X-ray active optics cannot use normal actuators on the back of the mirrors, as typically done in optical astronomy. On the contrary, the use of piezoelectric elements acting tangentially, i.e., exerting a strain in a direction parallel to the surface on the rear of the glass foil, enable the changes of the local curvature of the mirror to correct profile errors. There are two competing ways of realising active optics for astronomical applications. The first method is to have individual piezoelectric actuators tiled and bonded onto the back of the mirror. The second method is to create a complete, single layer, coating of thin

piezoelectric material on the reverse of the glass and print the electrode pattern required onto the material to actuate the individual areas. In the following sections, two projects following these different approaches are presented, the AXYOM (Italy) and the X-ray Surveyor (USA). Some of the slumped glass foils, produced during my Ph.D. research, were used for both projects. The first project, is developed in Italy, financed by a PRIN-TECNO INAF grant, with a collaboration led by INAF-OAB: the adoption of the slumped glass foils produced at INAF-OAB is therefore straightforward. The second project is developed at SAO/CfA (Smithsonian Astrophysical Observatory / Center for Astrophysics) and the use of Corning Eagle glass, the one adopted during my Ph.D. work, is a key factor that will be explained in Section 9.3: the collaboration between INAF-OAB and SAO/CfA is intended to provide slumped Eagle glass foils of quality suitable for the project.

9.2 AXYOM

9.2.1 Introduction

Adjustable X-raY optics for astrOnoMy (AXYOM) is a PRIN-TECNO-INAF 2012 project led by INAF-OAB, and performed in collaboration with INAF-OAPA (Osservatorio Astronomico di Palermo) and Università di Palermo [Spiga et al. 2014, Dell'Agostino et al. 2014, Spiga et al. 2015, Spiga et al. 2015b]. It is aimed at developing the actuation, with piezoelectric components commercially available, of thin slumped glass X-ray mirrors, integrated with glass ribs with the process developed at INAF-OAB and described in Section 3.8.5. The innovation therefore consists of the possibility to correct low-frequency errors with the ribs in the integration process, and mid-frequency errors with the piezoelectric elements glued in the space within the ribs. Another innovation of the project is that the optimisation of the shape, through the optimisation of the voltage signal to be provided to the piezoelectric array, will be performed directly in X-ray illumination, in intra-focal setup [Spiga et al. 2015b]. In fact, the standard method is to perform the optimisation with usual metrology, but it is known, and already shown in Chapter 8, that both visible and UV, are affected by the aperture diffraction, and are usually insensitive to undulations in the centimeter range. Instead, in the intra-focal configuration, it is possible to reconstruct the mirror surface with the formalism described in [Spiga et al. 2013], without the need to scan the surface with an X-ray beam, or analyse the reflected beam with a wavefront sensor.

9.2.2 Process description

The mirror substrates adopted for this project are Eagle glass foils slumped during this Ph.D. activity. Due to residual forming errors, the longitudinal profiles exhibit deformations on the order of a few microns on the full length scale, down to less than a tenth of micron over a few centimetres scale. Since the integration corrects for low-frequency errors to an extent that improves as the nearest rib is approached, the maximum error is expected to be in between two adjacent ribs. At these position, piezoelectric elements are glued to perform the correction of the errors in the centimetre scale (Fig. 9.3-left).

Since the piezoelectric elements have to be contacted to interface with the appropriate electronics, conductive tracks have to be printed on the back side of the glass foil.

Two approaches can be followed:

1. to deposit the conductive tracks on a flat glass, then slump the glass foil (Fig. 9.1): by this approach, the metallic pattern is exposed to very high temperature, with the risk of damaging its conductivity. Anyway, this approach was tested, and only a resistance increase of some tens of ohms was observed (this has to be compared with a piezo resistance of 10^{10} Ω). The disadvantage of this method is that the pressure cannot be applied, at least in the standard way, because the glass its already to its final dimension and cannot be used as a membrane to seal the lower part of the muffle.

Figure 9.1: *: The glass foil laying on the cylindrical slumping mould in K20, just after the slumping process. In this case the electrodes have been deposited on the flat glass, prior the slumping.*

2. to deposit the conductive tracks on a slumped glass foil: in this way the slumping process can be performed in its optimal condition, but more difficulties may arise in the photolithographic process of a curved surface.

The second method was adopted for the production of the mirrors integrated in this project. The adopted photolithographic process can be summarised as follows:

1. a layer of 30 nm of Titanium, plus 10 nm of Gold is evaporated onto the back side of the slumped glass foil;
2. a positive photoresist layer is sprayed on the metallic layer;
3. a mask with the printing in positive of the electrodes is positioned in contact with the photoresist;
4. the photoresist is exposed to UV light, while the mask shades the parts where the metal has to be left;
5. the photoresist is developed, leaving a pattern where the mask was present;
6. the metallic layers, uncovered by the photoresist, are removed by chemical etch;
7. the residual of photoresist is removed by a NaOH solution.

After creating the electrode pattern on the back-side of the slumped glass foil, its optical side is coated with a 30 nm layer of Titanium in order to enable the shape measurement with the CUP: in fact without this reflective layer on the optical side, the reflection from the metallic electrodes in the back side of the glass foil would disturb the optical sensor of the profilometer.

Piezoelectric elements are glued in the space between two adjacent ribs. A preliminary analysis was performed [Dell'Agostino et al. 2014] to select the appropriate elements to be used: tangentially-acting piezoceramic transducers were shown to have the sufficient bending strengths to correct deformation of a 0.4 mm thick glass when voltages of a few tens volts are applied. Two models were selected from *Physik Instrumente*: the P-876.SP1 model with a 16 mm $\times$ 16 mm size and 200 μm thickness, and the P-876K015 model with a 50 mm $\times$ 11 mm size and 200 μm thickness (Fig. 9.2) to correct deformations over longer spatial scales and also to activate a longer fraction of the profile with a smaller number of voltage signals.

The piezoelectric elements are glued, by using the low-shrinkage (0.03 %) epoxy resin Masterbond EP30-2, with a thickness of approximately 75 μm, routinely used at INAF-OAB for the integration process with glass ribs. A conductive epoxy glue is then used to create the electrical contacts on the piezo soldering pads. Finally, electric wires are connected to the electrodes (Fig. 9.3), using conductive epoxy.

The active mirror is then integrated with the IMA operated at INAF-OAB: the glass ribs are glued on the back side of the mirror, while forcing the glass foil to replicate the shape of the Wolter-I integration moulds (Fig. 9.3-left), and they are subsequently glued to the backplane (Fig. 9.3-right).

After removing the foil from the integration mould, the foil tends to retrieve its original cylindrical shape for the spring-back effect; therefore shape errors are corrected only partially in between the ribs. The piezoelectric actuators are meant to perform this last shape correction.

Figure 9.2: *: Left: two models of the selected piezoceramic transducers. Right: a detail of the glued piezoelectric patch seen through an uncoated glass foil. The electrical contacts are ensured via two droplets of conductive epoxy.*

9.2.3 State of the art

A first prototype was integrated in July 2015 (Fig. 9.3). It comprises only one glass mirror and two P-876.SP1 actuators, glued in the central glass portion. The BK7 moulds, already available at INAF-OAB, were used for the integration. Only 4 ribs were glued to the mirror, and an aluminum backplane was used.

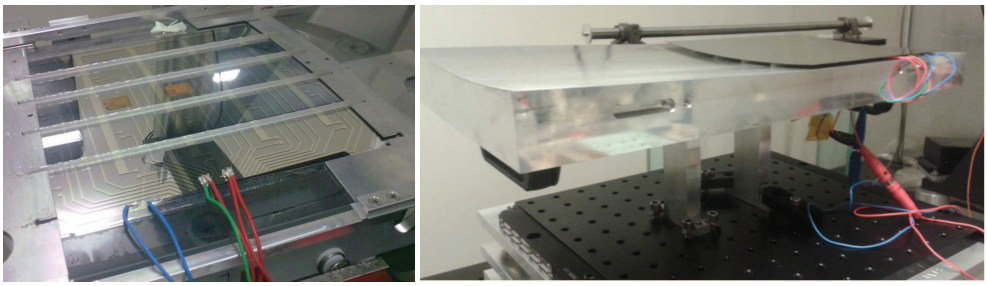

Figure 9.3: *: Left: The first prototype during the integration on the IMA at INAF-OAB. Two piezoelectric elements are glued in the space between the two central ribs. The ribs are perpendicular to the conductive tracks. Right: the integrated mirror onto the backplane, during the measurements with the LTP.*

For this first test, the piezoelectric patches were not integrated forcing the glass in contact with the mould by vacuum suction (as the standard integration procedure would have required). Therefore, the local deformations induced by the glue were much larger than achievable with the correct procedure.

The central glass profile was measured with the LTP, under the activation of the piezoelectric elements: an applied voltage of 25 V resulted in a profile correction of ~ 1 μm (larger than the typical error amplitude over the piezo length), with the influence of the piezo extending outside its surface, owing the elasticity of the foil.

The prototype was then tested in X-rays in July 2015, in intra-focal setup, at XACT, a 35 m long facility available at INAF-OAPA. Since the mirror had only two small piezoelectric actuators, the tests performed at the XACT were not addressed at an effective correction of the mirror profile, but rather to a test of the equipment and of the experimental setup.

The production of a more advanced prototype in already on going, implementing all the lessons learnt from the first prototype. The main goal will be to show the possibility to drive the shape of thin glass X-ray mirrors using the technique of intra-focal X-ray imaging.

9.3 X-ray Surveyor

9.3.1 Introduction

The X-ray Surveyor is a mission concept presented by NASA [Gaskin et al. 2015], in January 2015, in response to the "Planning for the 2020 Decadal Survey: An Astrophysics Division white paper" (Web reference: 2020 Decadal Survey). The goal is to look beyond Chandra, therefore combining comparable angular resolution with greatly increased photon throughput. A preliminary optical design for the X-ray Surveyor mirror system incorporates a segmented optic similar to Constellation-X [Petre et al. 2006], but with a 3 m diameter, a 10 m focal length and a 0.5 arcsec HEW at 1 keV. Large effective area (few-square meters) is accomplished by nesting 292 segmented shells into 42 individual mirror modules, later assembled into the final structure.

To maintain sub-arcsec resolution over a large effective area, a number of efforts are on going. These include both active (piezoelectric actuator deposition [Reid et al. 2014] and magnetorestrictive optics [Ulmer et al. 2012]) and passive (differential deposition [Kilaru et al. 2011], ion implantation [Chalifoux et al. 2015] and low stress single crystal silicon mirrors [Riveros et al. 2014] methods to achieve the desired imaging. We hereafter focus on the piezoelectric actuator deposition.

9.3.2 Process description

Motivated initially by the Generation-X mission concept [Reid et al. 2004], the Smithsonian Astrophysical Observatory (SAO) is nowadays leading a comprehensive research program to develop active x-ray telescopes. Originally, the Gen-X approach, US based, was to deposit a piezoelectric film (PZT, lead zirconate titanate), while the SMART-X consortium, UK based, was gluing shaped piezoelectric PZT pads to the back of the mirror [O'Dell et al. 2011]. More recently, SAO continued the work on the deposition process for the SMART-X mission concept [Vikhlinin et al. 2012]. Nowadays [Gaskin et al. 2015], this approach is adopted for the X-ray Surveyor mission concept.

Pennsylvania State University (PSU) is developing thin-film piezoelectric (PZT) ceramic actuator arrays for thin x-ray mirrors, [Wilke et al. 2013]. A thin-film process sputters, onto the back of a segmented mirror, a uniform ground-electrode layer of Pt with thickness of 100 nm [Cotroneo et al. 2012], a uniform PZT layer of thickness 1.5 μm, and finally a patterned electrode layer of Pt, obtained with a photolithographic process.

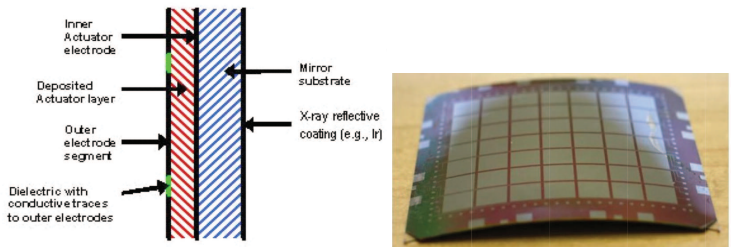

Figure 9.4: *: Left: a cross section of the thin-film piezoelectric array (not to scale). Right: An early prototype of a cylindrical, piezoelectrically adjustable glass mirror, of size 100 × 100 mm^2. Credits: PSU/Johnson-Wilke.*

The advantages of this method include the fact that no print-through is created as the material is deposited directly onto the mirror without the need of bonding. The main disadvantage is that the piezoelectric material requires annealing, and therefore also the mirror has to undergo a thermal cycle which could result in irreversible degradation of the mirror shape. PZT is commonly used in micro-electromechanical (MEMS) systems for sensors and actuator applications using a typical temperature of crystallization of $\sim$ 700 °C. This temperature is too high for glasses as their annealing point is close or even lower. Therefore, PSU research was at first addressed at

developing a PZT deposition process with lower crystallization temperature, which could be set to 550 °C.

On the other side, SAO has been investigating various glasses with somewhat different annealing temperatures: Schott D263 (557 °C), Schott AF45 (663 °C), and Corning Eagle (722 °C). Fig. 9.5 shows the different result on the D263 and Eagle flat glasses upon the deposition and annealing at 550 °C of the piezoelectric film [Cotroneo et al. 2011]. This result defined the Eagle glass as compatible to the newly developed PZT deposition process. Finally, since the deposition chamber can house only 100 × 100 mm^2 mirrors, this is the size used at the moment for all tests.

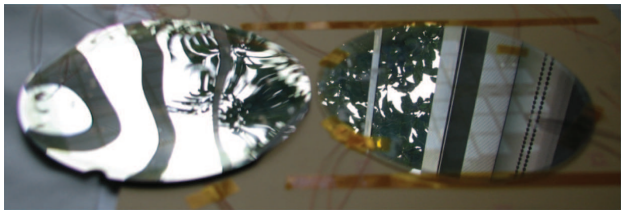

Figure 9.5: *: Different result on the D263 (left) and Eagle (right) glasses, after the deposition and annealing at 550 °C of the piezoelectric film. The D263 is strongly deformed, because D263 annealing temperature (557 °C) is too close to the PZT crystallisation temperature (550 °C). Credits: Cotroneo et al. 2011.*

9.3.3 State of the art

In 2011, the first active mirror prototypes were realised: the PZT film was deposited on a D263 glass wafer, with thickness of 0.4 mm and diameter of 4 inches [Cotroneo et al. 2011]. Fig. 9.6 shows the mask pattern and the printed array, realised at PSU on a D263 substrate.

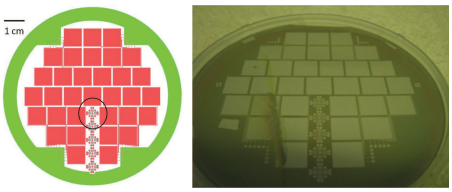

Figure 9.6: *: Left: the mask pattern realised at PSU for the 100 mm diameter test glass, including the strain gauges (encircled in black). Right: A picture of a D263 glass sample after the piezo deposition.*

For the reason discussed in the previous section, the realised array had a 1 mm amplitude warp. Therefore, to measure the influence function[1] of the individual piezoelectric cell, an instrument with large dynamic range, and poor precision, was used (Coordinate Measuring Machine - CMM - MISTRAL Brown Sharpe). Nevertheless, a good matching between the FEA and the measured response was obtained (Fig. 9.7-left).

In 2012, other prototypes ware realised with Corning Eagle, to reduce the warping [Cotroneo et al. 2012]. Anyway, commercial glasses show a deviation from flatness of the order of several tens of microns, still too high to allow the use of high-precision instruments with small dynamic range (e.g. phase-shift interferometers). Different sputtering methods and cleaning procedures were used in order to improve the yield of the cells (ratio of working electrodes over the total number). All the samples were found to have a yield higher than 95%, to be compared to the yield of the previous set with an average of 64%. The influence function for a couple of activated piezo elements was first measured with the CMM on some samples. To improve the sensitivity, a newly acquired non-contact profilometer was used to test all the actuator cells on a new sample.

[1] The influence function of an actuator is defined as the change in surface shape when the actuator is powered with a 1 V voltage.

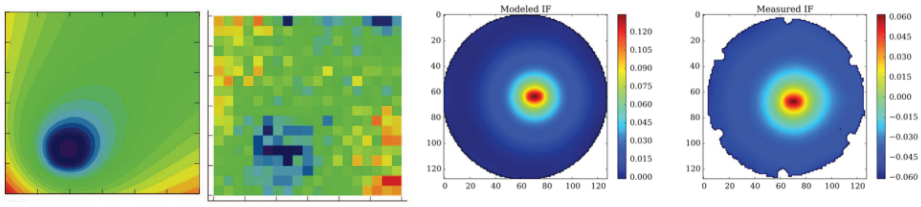

Figure 9.7: *: Left: a deformation map, based upon a finite-element analysis, of the response to a surface-tangential stress in a single cell, and the actual deformation, measured with the CMM. Credits: O'Dell 2011. Right: a deformation map, based upon a finite-element analysis, of the response of a single cell, and the actual deformation, measured with the optical profilometer and the WFS. Credits: Allured et al. 2015.*

All the actuators responses were found in the range needed for the actual mirror correction, with a relatively homogeneous behavior ($\sim$ 500 ppm strain is necessary to correct figure errors of a glass segment, going from $\sim$ 7 to 0.5 arcsec HEW [Reid et al. 2012]).

In 2014, the non-contact profilometer was improved with a Wave Front Sensor (WFS) [Allured et al. 2014], and the measured influence function for a central pixel of a flat mirror, was found to be in agreement with the influence function computed with FEA, with a rms difference of 8.7 nm, within the metrology noise (Fig. 9.7-right).

The electronics system was improved, in order to control more than 100 actuator cells; also the yield of the piezo cells was considerably improved [Johnson-Wilke et al. 2014]. All these upgrades made possible to induce a pre-determined figure change onto a flat mirror, activating a large number of cells with the computed influence function [Allured et al. 2015]. An Eagle flat wafer, with thickness 0.4 mm and diameter 100 mm, and a measured figure of the order of 100 μm PV, was coated with the PZT with a map of 88 active cells of size 5×10 mm^2 (Fig. 9.8-left). Due to the large figure error or the sample, a sub-arcsecond correction was not possible. Therefore the test was used to show that a pre-determined figure could be reached with high accuracy. An axial sinusoidal ripple of 0.3 μm amplitude and 50 mm spatial wavelength was introduced onto the mirror. The result of this test was that the desired ripple on the mirror was achievied within 0.9 arcsec rms axial slope (Fig. 9.8-right).

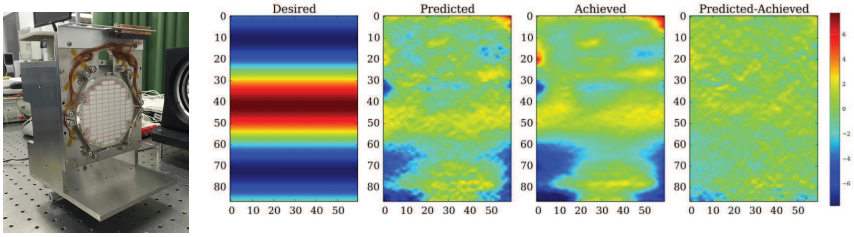

Figure 9.8: *: Left: the flat Eagle mirror for deterministic figure control. Right: Axial slope residuals of the experimental ripple introduction. On the far right, the residuals between the predicted post-correction figure and the measured post-correction figure (0.9 arcsecond rms slope). Credits: Allured et al. 2015.*

The metrological system was then adapted to measure cylindrical optics, preparing the way to induce a pre-determined figure change to a cylindrical mirror [Allured et al. 2015]. To this end, cylindrical mirrors, slumped in my Ph.D. activity, were provided to SAO. The next section presents the characterisation of the slumped samples, trimmed to the size of 100×100 mm^2, required for SAO activity.

9.4 Production of slumped glass foils for the X-ray Surveyor study

9.4.1 Cross check characterisation on slumped glass foils at INAF-OAB and SAO/CfA

The first step of this collaboration was meant to determine if the quality of our slumped glass foils was compliant with the SAO requirement for mid-frequency errors, rms(1 ÷10 mm) = 1 nm. To this end, a slumped glass foil (code E21, Section 6.5) was selected for cross check. The CUP map and the LTP characterisation are shown in Fig. 9.9. The best area of size 100 × 100 mm^2 was selected out of the CUP map (black box in the CUP map of Fig. 9.9). In order to compute the rms value, in the spatial wavelength range 2 ÷10 mm[1], the PSD was computed from the five LTP scans, of length 200 mm, and the three LTP scans in the selected region of length 100 mm, as per the SAO size request. In this area, the rms (2 ÷10 mm) turned out as 16.5 nm, much higher than the SAO requirement. Anyway, the rms from WYKO measurements on E21, in the spatial wavelength 2.5 mm ÷10 μm was 1.3 nm (Section 6.5), suggesting that the LTP rms in the millimetre range was affected by the sag error of the glass foil. In fact, the Fourier contribution of a polynomial is spread over all spatial wavelengths. Therefore, a low frequency error in the slumped glass foil would not contribute to the PSD in the millimetre spatial range only in case of a sinusoidal error, whereas it would contribute in case of polynomial errors.

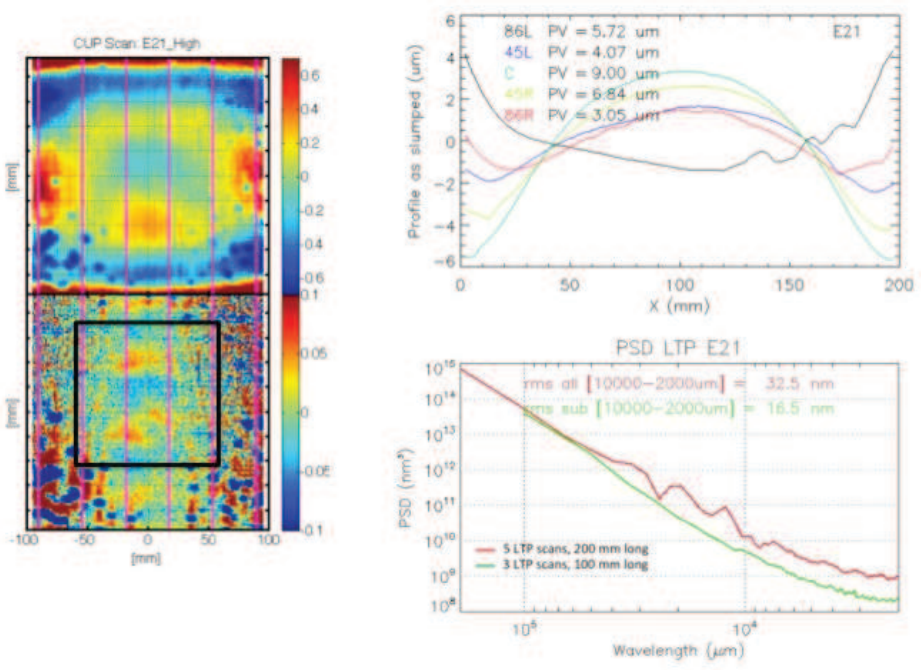

Figure 9.9: *: E21 measurements at INAF-OAB. Left: the residual of the CUP map after the subtraction of the cylinder of radius 1 m, and after removing the Legendre polynomials up to the 2nd order (top) or 8th order (bottom). Right: the five LTP scans (top) and the PSD (bottom) computed both from the five LTP scans (red curve), of length 200 mm, and the three LTP central scans (green curve) in the selected region of length 100 mm, giving rms(2 ÷10 mm) = 16.5 nm.*

[1] Due to the 1 mm step of the LTP scan, the minimum measured spatial wavelength is 2 mm (see Chapter 4)

E21 was sent to SAO for cross check measurements on the WFS mounted on their optical profilometer (Fig. 9.10). Since, at the time of the measurement, only the setup for flat glass foils was available, a limited portion of glass could be sampled in each measurement. The result was rms(1-10 mm) $\sim$ 2-3 nm in the selected 100 $\times$ 100 mm^2 glass sub region, within the instrumental noise. Therefore, the glass foil was suitable for SAO tests.

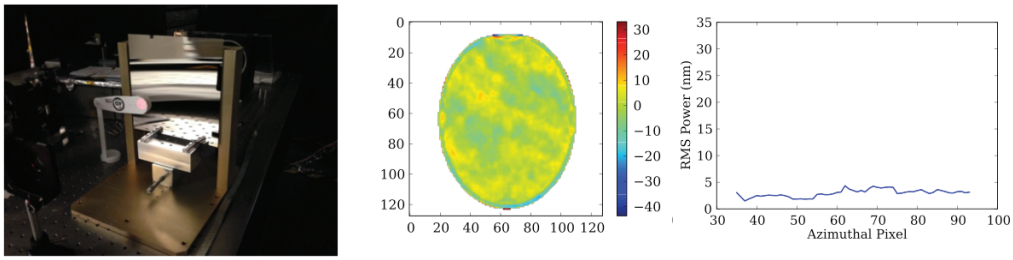

Figure 9.10: *: E21 measurements at SAO. Left: the coated glass on the supporting structure. Center: a map obtained with the WFS mounted on the optical profilometer. Right: the rms(1 ÷10 mm) from the PSD at different azimuthal positions is $\sim$ 2-3 nm.*

In order to better understand the quality of our slumped glass foils in the 1 ÷10 mm range, another glass foil (code E32, Section 6.6) was measured with the LTP at INAF-OAB. Fig. 9.11 shows a disagreement between the LTP (red line) and WYKO (blue line) PSDs, on the five measured scans with 200 mm length, while WYKO is in perfect agreement with the central LTP measurement over 100 mm length, after removing a best fit 4th order polynomial. This is due to the fact that the polynomials, present in the LTP profile measurements, have Fourier components in all frequency ranges, while, for the WYKO, the short scans are not affected by a polynomial curvature. Just like the E21, the PSD was also computed for the three LTP central scans, with 100 mm length (green line). Also in this case, the LTP and WYKO PSDs do not have an overlapping region.

To exclude the contribution from polynomials in the LTP data, only the central scan was measured in the region from 50 to 150 mm. The measurement was performed both with the standard step size of 1 mm (purple thick line) and the more refined 0.1 mm (purple dotted line). A 4th order polynomial de-trend was then applied to the 0.1 mm step data. Finally in this case, the LTP and WYKO PSDs are in perfect accord, and rms (2 ÷10 mm) = 3.2 nm. This result was consistent with the SAO measurement, and confirmed these slumped glass foils to be compliant with the request for a pre-determined figure control of a cylindrical mirror.

9.4.2 Shape modification after cutting the slumped glass foils

Slumped glass foils are produced at INAF-OAB with an initial size of 340 $\times$ 340 mm^2. They are then trimmed to the size of 200 $\times$ 200 mm^2. Due to process constrains in the deposition of the piezo-electric elements, the size required by SAO is 100 $\times$ 100 mm^2. Preliminary measurements performed on our slumped glass foils, after cutting them to 100 $\times$ 100 mm^2 with the Penett MDI tool, as described in Section 5.4, returned the indication of shape modification after cutting. It is not clear, at the moment, whether the shape modification is induced by the cutting process or by the release of internal stresses in the slumped glass foil.

In order to characterize the shape change with the cutting, two slumped glass foils were measured after a progressive cut from 200 $\times$ 200 mm^2 to 100 $\times$ 100 mm^2. The CHR optical sensor, installed on the LTP, was used to measure the modification in the glass profiles, as this method is more accurate than the LTP-FEA in the low frequency range. The results were also compared with the LTP data of the starting shape. The glass foils E46 and E56 had been selected for the cutting procedure. The shape profiles of these glass foils after slumping were different (Fig. 9.12),

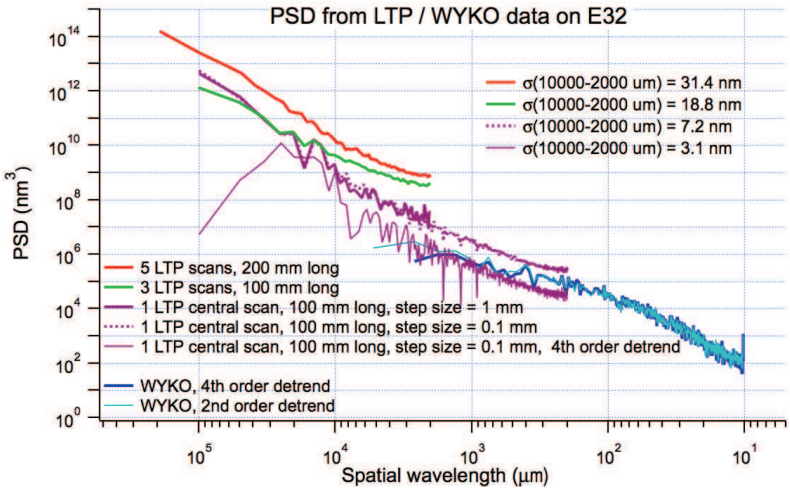

Figure 9.11: *: PSD from LTP and WYKO data, for the glass foil E32. The PSD from LTP data are computed in several cases: the five LTP scans with length of 200 mm (red curve, rms = 31.4 nm), the three central LTP scans with length of 100 mm (green curve, rms = 18.8 nm), the central LTP scan with length of 100 mm and step size of 1 mm (thick purple curve), the central LTP scan with length of 100 mm and step size of 0.1 mm (purple dotted curve, rms = 7.2 nm), the central LTP scan with length of 100 mm and step size of 0.1 mm, after a 4th order de-trend (thin purple curve, rms = 3.1 nm, in agreement with SAO result).*

due to the different pressure conditions during the slumping process (see Section 6.7).

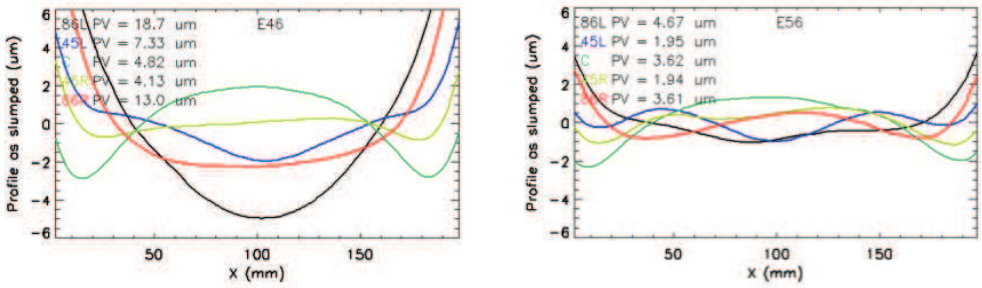

Figure 9.12: *: LTP profiles of the E46 and E56 glass foils in size of 200 × 200 mm^2.*

The comparison of the E46 and E56 glass shape profiles measured by LTP and CHR at different sizes are shown in Figs. 9.13, 9.14, 9.15. The measurements were carried out along three positions: at the central scan and at 45 mm off the central scan, both in left and right directions. The observed change in glass shape is in the same direction in each measured line; in particular, the central scan reverses its concavity, going concave upwards.

Fig. 9.16 shows the CUP maps of E46 and E56 at different sizes. The information retrieved from these measurements is on the overall glass foil, instead than only on three scans; the CHR, LTP and CUP results are fully consistent. Moreover, the CUP maps at 100 × 100 mm^2 size, show a very similar mid-frequency pattern (bottom line of Fig. 9.16), consistent with the replication of the K20 pattern (Fig. 6.68).

The two glass foils, cut to 100 × 100 mm^2, were therefore sent to SAO for the deterministic figure correction test. The process is now on going to coat, measure and activate the slumped foils.

Further analysis are planned at INAF-OAB to cast some light on the reason of the shape changing with the cutting.

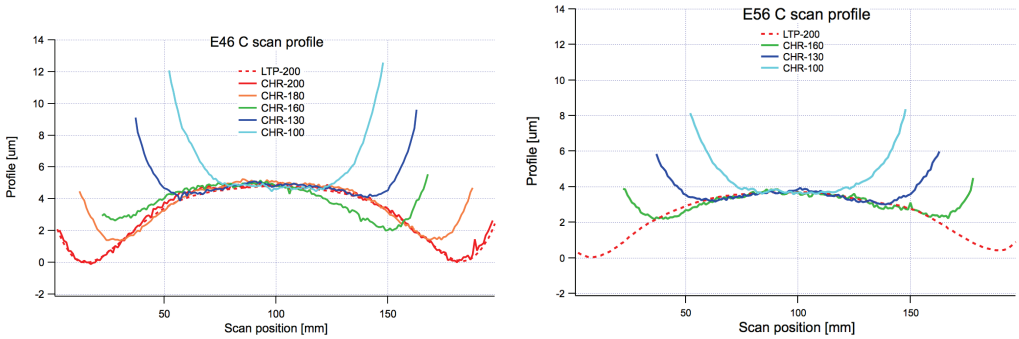

Figure 9.13: *: Profile changes after cutting at the central scan, for E46 (left) and E56 (right).*

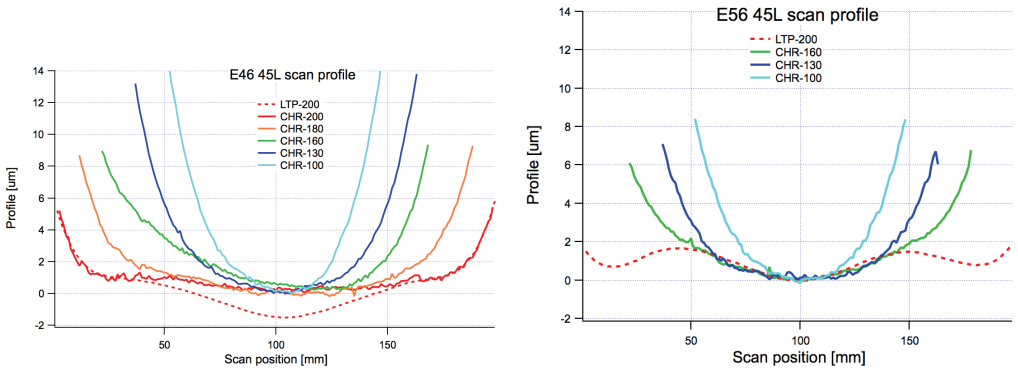

Figure 9.14: *: Profile changes after cutting at the scan 45 mm left from the central one, for E46 (left) and E56 (right).*

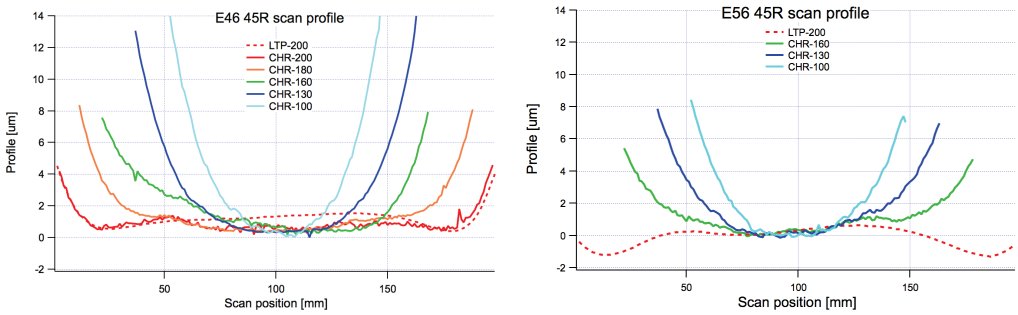

Figure 9.15: *: Profile changes after cutting at the scan 45 mm right from the central one, for E46 (left) and E56 (right).*

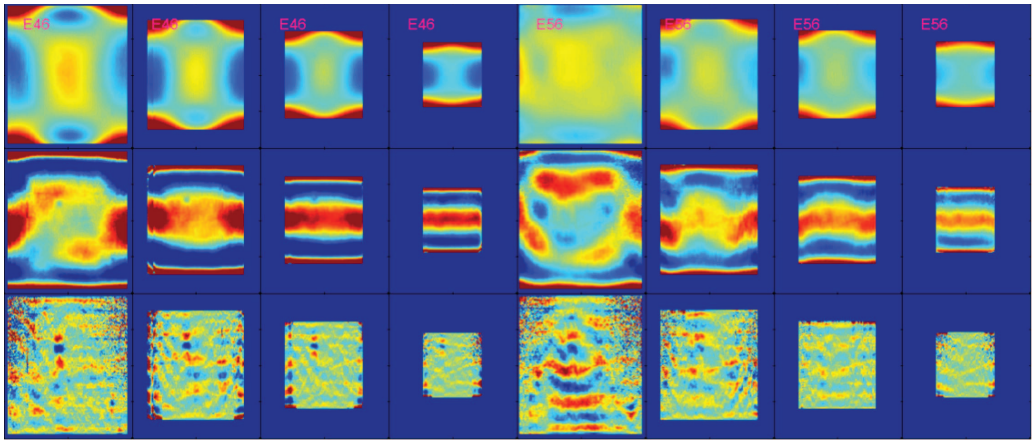

Figure 9.16: *: E46 and E56 comparison with CUP at different cut size. Top: linear residuals from profiles along the optical axis (color scale PV: 8 μm). Center: residuals after removing the Legendre polynomials up to the 2nd order (Color scale PV: 1.2 μm). Bottom: residuals after removing the Legendre polynomials up to the 8th order (Color scale PV: 0.2 μm). The glass foils cut to 100 × 100 mm^2 show a very similar mid-frequency pattern, consistent with the replication of the K20 pattern. Credits: CUP maps by M. Civitani.*

CHAPTER 10

Scattering and reflectivity measurements of multilayer coatings for X-ray mirrors

10.1 Predicting the X-ray scattering from a graded multilayer

10.1.1 Scientific motivation

Thin glass mirrors can also be adopted for high-energy X-ray telescopes. To this end, the surface roughness of the slumped glass foil have to be kept very small, as the reflectivity decreases with the roughness increase (Eq. 2.20). It was already shown (Fig. 2.1) that the reflectivity of the glass mirror is near 100 % for very small incident angles up to a cut off energy, where the reflectivity suddenly drops. The use of a high Z coating (Au, Ir, Pt) extends the reflectivity beyond the cut-off energy. Anyway, in order to go to the high X-ray energy range, multilayer coatings are required (Section 2.5). In this case, not only the glass roughness substrate need to be small, but also the multilayer growth process need to be accurately controlled.

Interface imperfections in the growth process are known to degrade the mirror optical performance by causing non-specular scattering, which can be computed with Eq. 2.25. In order to estimate the roughness impact on the Point Spread Function (PSF), a roughness measurement of all the multilayer interfaces would be needed, to compute the interfacial Power Spectral Densities (P_{j}) and the Crossed Spectral Densities ($C_{\mathrm{j}m}$) for all the couples of interfaces, and eventually compute the multilayer diagram scattering described by Eq. 2.25. However, only the outer surface of the multilayer is accessible to direct topography measurements using, e.g., an Atomic Force Microscope (AFM). X-ray reflectivity (XRR) measurements as a function of the incidence angle, combined with a detailed fit routine to interpret the reflectivity scans [Spiga et al. 2007, Spiga 2008], allows a non-destructive, in-depth analysis of the multilayer stack structure (layer thickness in the stack, uniformity, smoothness), but does not enable the reconstruction of the PSD evolving throughout the stack. An XRS computation based upon the sole thickness description and the outer surface PSD, assuming the rough topography to be exactly replicated in the stack, would in general return a diagram mismatching the experimental data (Fig. 10.1-left).

An IDL code was already developed [Canestrari et al. 2006] to model the layer roughening

during the growth of periodic multilayers (Fig. 10.1-right). My work consisted in extending the program to graded (Section 2.5) multilayers [Salmaso et al. 2011, Salmaso et al. 2013].

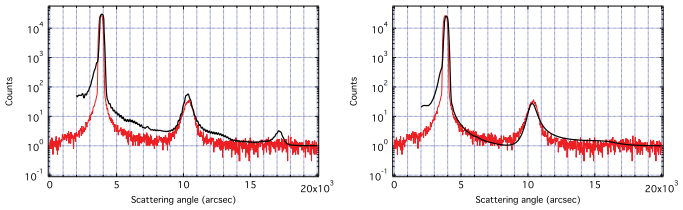

Figure 10.1: *: Experimental (red lines) X-ray scattering for a periodic multilayer vs. modeling (black lines). A Si sample was coated by e-beam evaporation with 40 bilayers of W/Si with thickness d_W= 19.3 Å and d_{Si}= 26.7 Å. The sample was already characterised in [Canestrari et al. 2006]. Assuming a constant PSD in the stack returns a poor modeling (left). Accounting for the roughness evolution through the stack reproduces more correctly the experimental XRS curve (right) [Canestrari et al. 2006, Salmaso et al. 2013].*

10.1.2 The roughness evolution model for a multilayer, implemented in an IDL code

For both periodic and graded multilayers, the reflecting layer deposition process triggers an evolution of the roughness from the substrate to the outermost layer. The roughness growth model [Stearns et al. 1998] describes the evolution of the rough profile $z(x)$ with the thickness τ of the film. For a single layer deposited onto a substrate, this equation reads

$$\frac{\partial z(x)}{\partial \tau} = -\nu \left|\nabla^n z(x)\right| + \frac{\partial \eta}{\partial \tau}. \tag{10.1}$$

The model describes the roughening of the surface as a competition between a surface relaxation process and the increase in roughness due to the random nature of the deposition process. The relaxation process is parametrized with ν and the positive integer n, which varies with the kinetic mechanism that dominates the smoothing process [Stearns et al. 1998]. The increase in roughness results from the deposition process and is described by a random shot noise term η. The solution of Eq. 10.1, in terms of surface PSD [Stearns et al. 1998], is

$$P^{\text{int}}(f) = \Omega \frac{1 - \exp(-2\nu|2\pi f|^n \tau)}{2\nu|2\pi f|^n}, \tag{10.2}$$

where $P^{\text{int}}(f)$ is the "intrinsic" bi-dimensional PSD of the layer surface, i.e., the PSD that the surface layer would have if the substrate were ideally smooth. This PSD is characterized by a plateau up to the maximum frequency corresponding to the cutoff wavelength $l^* = (\nu\tau)^{\frac{1}{n}}$, then decreases as a power-law of spectral index n. Ω represents the volume of the deposited atom, molecule, or nanocrystal.

When a stack of N alternated layers is considered, the situation is complicated by the presence of two elements with different properties, i.e., different values of the parameters Ω, ν, and n. However, the formalism can be extended by considering each single layer (whose upper surface is labelled with j = 0, 1,... N moving from the substrate towards the surface) as growing upon its underlying layer, which acts as its "substrate". In this way, one can write [Stearns et al. 1998] the PSD of the j^{th} interface as a sum of the intrinsic contribution of the layer itself (P_j^{int}) and of a term representing the rough profile partially inherited from the previous layer (P_j^{ext}):

$$P_j(f) = P_j^{\text{int}}(f) + P_j^{\text{ext}}(f) = P_j^{\text{int}}(f) + a_j(f) P_{j-1}(f), \tag{10.3}$$

where a_j is a *replication factor* that describes to which extent the microrelief components of the $(j-1)^{\text{th}}$ interface are replicated in the j^{th} layer, and it is expressed as

$$a_j(f) = \exp(-\nu \left|2\pi f\right|^n \tau_j). \tag{10.4}$$

Like the P^{int} term, the replication factor exhibits a cutoff at the spatial wavelength $l^* = (\nu\tau)^{\frac{1}{n}}$, that represents the transition above which surface features are damped out. At wavelengths larger than l^*, the surface topography is almost entirely replicated: the superimposition of the intrinsic term thereby triggers a progressive roughening of the multilayer interface, as a function of f, to an extent depending on the values of the growth parameters.

The IDL-based program, developed by Canestrari and Spiga, implemented this formalism for periodic multilayer. The values of the parameters Ω, ν and n, described in equations 10.2, that best fit the growth from the substrate to the outer PSD, are computed by recursive application of Eq. 10.3, for both the high- and low-Z density elements. Once the fitting parameters are found, it is possible to compute the P_j's and the C_{jm}'s, which are the physical quantities that affect the intensity and the mutual coherence of the scattered waves, which in turn interfere to build up the XRS diagram (Eq. 2.25). In fact, the P_j are computed by iterating Eq. 10.3 j times from the substrate, while the PSD between the generic j^{th} and the m^{th} interface, with $j < m$ can be simply computed from the replication factors (Eq. 10.4):

$$C_{jm}(f) = a_m(f) \cdot a_{m-1}(f) \cdot \ldots \cdot a_{j+1}(f) P_j(f). \tag{10.5}$$

The extension of this formalism, to include the graded multilayer case, was obtained by modifying the program for two aspects:

1. the layer thickness τ is not constant for graded multilayers, therefore thickness values as per the widespread *supermirror* design [Joensen et al. 1995], defined in Eq. 2.24, were included;
2. the T_j coefficients of Eq. 2.25, which represent the field amplitude transmittance of the j^{th} layer, were computed from the recursive theory of multilayer reflectivity [Spiga Ph.D. thesis 2005], in order to be applicable both to periodic and graded multilayers, whereas the previous method [Canestrari et al. 2006] was using an exponential decrease of the intensity throughout the stack, applicable only to periodic multilayer in Bragg incidence. This method was validated by comparing its results with the findings of the IMD program [Windt 1998], obtaining a very good agreement both for the periodic and the graded multilayer case.

10.1.3 X-ray scattering simulation versus experiments for a periodic multilayer

In order to validate the modified program, I have first considered a periodic multilayer and I have compared the modelled X-ray scattering with the experiments. The sample was already characterized in [Canestrari et al. 2006]: 40 bilayers of W/Si with d_{W} = 19.3 Å and d_{Si} = 26.7 Å were deposited by e-beam evaporation onto a Silicon wafer. In order to show the impact of the PSD evolution in the XRS diagram, I have preliminarily assumed no evolution of the PSD throughout the stack with a complete correlation ($C_{jm} = P_j = P_{\text{outer}}$) at all frequencies. The modeling clearly overestimates the measurement (Fig. 10.1-left): as expected, this denotes a gradual evolution of the roughness from the substrate from the outer surface. Moreover, the hypothesis of a complete correlation at all frequencies ($a_j = 1$ for all j, Eq. 10.4) endows the simulation with a second XRS peak near 17000 arcsec, which is not observed in the experimental XRS curve. In contrast, setting the Spectral Density functions resulting from the correct modeling of the roughness growth yields a modeling in much better accord with the experimental scan (Fig. 10.1-right). The model-data matching also proves the correct trend of the electric field coefficients throughout the stack, computed using the more general method.

10.1.4 X-ray scattering simulation versus experiments for a graded multilayer

The modified program was then applied to graded multilayers: I have considered a graded multilayer with 100 bilayers of Pt/C deposited by magnetron sputtering onto a Silicon wafer, with layer thickness values given by the power law $d(j) = a(b + j)^{-c}$, where d is the d-spacing and

j is the bilayer index from the top of the stack. The nominal power-law parameter values of the sample are

Pt : a = 31.0 Å, b = -0.94, c = 0.23,
C: a = 53.0 Å, b = -0.88, c = 0.21,

where Platinum is the first layer deposited onto the substrate. The roughness of the outermost Carbon layer in the 10 μm – 5 nm spatial wavelength range was measured with the AFM, while the substrate roughness was supposed to be the same of a standard Silicon wafer [Vernani et al. 2006], e.g., 2 Å rms in that spectral window. The multilayer surface, as measured with the AFM, exhibits crowded point-like defects in ejection (Fig. 10.2-left) that increase the rms of the external surface to 3.7 Å in the same spectral range. Besides, other defects of bigger size (highlighted by the red arrow in Fig. 10.2-left) increase the rms from 3.7 Å to 7.3 Å in the 10 μm scan. These bigger defects are homogeneously distributed over the sample, but it is difficult to ascertain if they are surface contaminations or they stem from the roughness growth itself. In the latter case, such defects would be effective for X-ray scattering, whilst in the former one, 8.045 keV X-rays would be almost unaffected by their presence. Fig. 10.2-right shows the PSD of the outer C layer, both including (green curve) and excluding (red curve) the bigger defects.

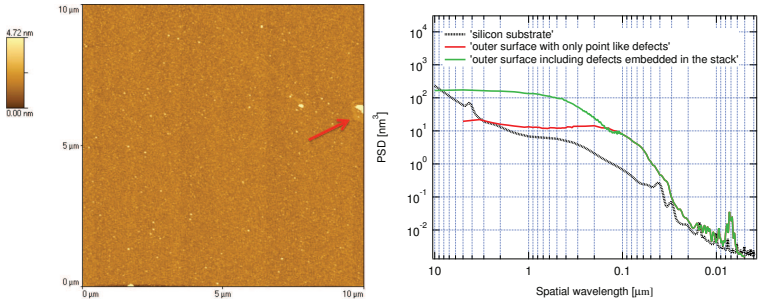

Figure 10.2: *: Roughness analysis from AFM scans of the outer C surface of the multilayer sample (100 bilayers of Pt/C). The AFM image (left) shows that the surface is crowded with point-like defects in ejection, and also exhibits some defects of bigger size. The PSD computation (right) was performed both including (green curve) or excluding (red curve) the bigger defects. rms(Si substrate, black curve) = 2 Å, rms(outer C layer, only small defects) = 3.7 Å, rms(outer C layer, also bigger defects) = 7.3 Å.*

The XRR of the sample at 8.045 keV was measured with the BEDE-D1 diffractometer. The PPM program [Pythonic Program for Multilayers, developed by A. Mirone, ESRF, [Spiga et al. 2007]] was applied to perform a detailed fit of the reflectivity curve and return the best-fit power-law parameters for the stack (Tab. 10.1, fit 'A'). The layer thickness values, found in this first analysis, were used to model the roughness growth.

Table 10.1: *: Power law parameters of the supermirror structure (Eq. 2.24), determined to fit the experimental XRR curve with the PPM program.*

Case	Pt: a [Å], b, c	C: a [Å], b, c
Fit A	31.08, -0.90, 0.30	53.16, -0.96, 0.19
Fit B	31.00, -0.94, 0.23	53.00, -0.88, 0.21

The XRS of the sample was measured with the BEDE-D1 diffractometer (red curve of Fig. 10.4), for X-rays impinging at the second peak after the critical angle ($\theta_i \simeq 3000$ arcsec, Fig. 10.3), and the scattering diagram was simulated (Eq. 2.25). The XRS diagram simulated with the parameters given by 'fitA' did not perfectly match the measured XRS (Fig. 10.4-left). This denotes some departure of the actual thickness trend from the modeled one.

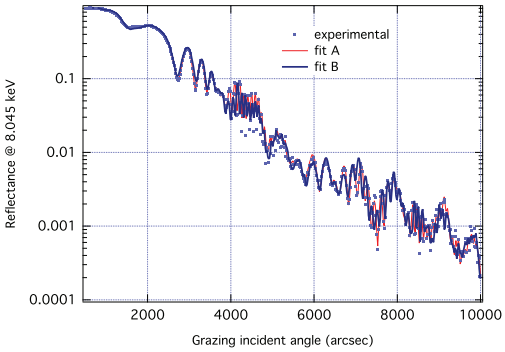

Figure 10.3: *: XRR angular scan at 8.045 keV (dotted blue curve) of the multilayer sample (100 bilayers of Pt/C), compared to the reflectivity computed with the PPM program (red and blue solid curves), for the two slightly different stack models reported in Table 10.1. They both match the XRR measurement, but only the fit 'B' is also in agreement with the peak positions seen in the XRS scans (Fig. 10.4).*

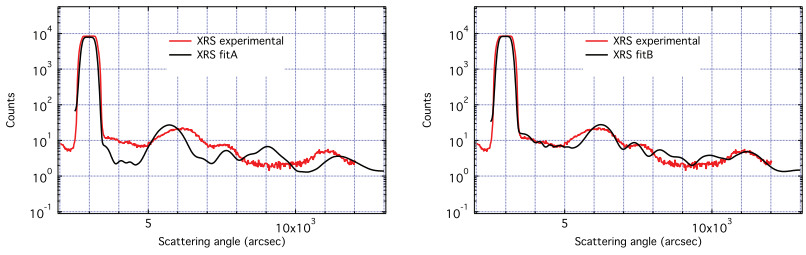

Figure 10.4: *: Experimental XRS of the graded multilayer sample (red lines) at θ_i = 3000 arcsec, compared with the simulated ones from the PSD evolution, including the major defects (Fig. 10.2-right, green line), using 'fit A' (left) and 'fit B' (right) of Tab. 10.1. Using fit B' reproduces much better the observed XRS peak positions.*

A slightly different power law (Tab. 10.1, fit B) was found to match much better the scattering peak positions (Fig. 10.4-right). This new power-law actually returns layer thickness values that do not differ by more than 3 Å from the first one, but in the outermost C layer, which is 15 Å thicker. Quite surprisingly, the XRR measurements actually matches both A and B power laws (Fig. 10.3). A possible interpretation could be that the specular reflectivity at 8.045 keV is a little sensitive to the thickness of the outer C layer, because most of the XRR curve features that drive the fit program are determined more by the multilayer internal structure, rather than by the thickness of the capping layer. In contrast, an XRS measurement can be more sensitive to the increased roughness generated by a thicker C layer.

Finally, the XRS computation was performed using the stack parameters given by 'fit B', and the two sets of roughness evolutions parameters, Ω, ν, and n, obtained to fit the two PSDs shown in Fig. 10.2-right.

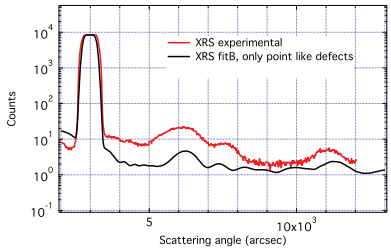

Figure 10.5: *: The simulated X-ray scattering diagram (black line), obtained by using the stack parameters given by 'fit B' and the roughness evolutions parameters that fit the PSD given by the sole point-like defects (red PSD in Fig. 10.2-right), is underestimating the measured X-ray scattering, proving that the bigger defects are related to the deposition process, and not just dust contaminations.*

If the sole point-like defects are included and the growth parameters are tuned accordingly, the peak heights are underestimated in the simulated XRS diagram (Fig. 10.5). Conversely, if all the visual defects in the AFM maps are used to compute the final PSD of the multilayer, the scattering diagram matches much better the experimental XRS curve (Fig. 10.4-right). It follows that the bigger defects observed on the multilayer surface (Fig. 10.2) are related to the deposition process, and not just dust contaminations.

10.1.5 Conclusions

The XRS sensitivity of a multilayer to the roughness evolution and to the actual thickness trend in the stack makes it a powerful diagnostic instrument, provided that it is coupled to an opportune modeling of the PSD evolution and that the XRS pattern can be reliably modeled. So far [Canestrari et al. 2006, Schroder et al. 2007] the modelization of XRS for multilayers was limited to the periodic case. I have shown that the formalism can be extended to graded multilayers. The upgraded code is validated for both periodic and graded multilayers, with a good accord between experimental data and model findings.

The comparison between XRR and XRS fitting shows that for graded multilayers the XRS is more sensitive than XRR to the actual thickness trend in the stack, since even a few angströms variation significantly changes the XRS peak positions.

Finally, different kind of defects observed in AFM scans are included in the PSD analysis. The subsequent data-model comparison give a power instrument to recognize defects as surface contamination or interfacial defects that contribute to the X-ray scattering of the multilayer.

10.2 Reflectivity measurements in synchrotron light of multilayer-coated polarizing mirrors for the LAMP telescope

10.2.1 Scientific motivation

Polarimetry is a powerful observational technique in X-ray astronomy, useful to enhance our understanding of the emission mechanism, geometry and magnetic field arrangement of many compact objects. Despite major progress in X-ray imaging, spectroscopy and timing, a much less attention has been paid to X-ray polarimetry. In the past, polarimeters were flown aboard rockets [Angel 1969], the Orbiting Solar Observatory (OSO-8) [Novick 1975, Weisskopf et al. 1976] and ARIEL-V satellites [Gowen 1977]. The sensitivity was so low that even $\sim 10\%$ of polarisation (about the maximum expected from typical sources) would not have been detected from some of the brightest X-ray sources in the sky. Statistically significant X-ray polarisation was detected in only one X-ray source, the Crab Nebula (19-σ detection by the OSO-8, [Weisskopf et al. 1978]). In the OSO-8 satellite, the polarimeter consisted of small graphite crystals mounted on two segments of a paraboloidal surface, which reflect 2.6 keV (or 5.2 keV on the 2nd order) X-rays at near 45 deg onto the gas proportional counters.

The introduction of X-ray optics produced a dramatic improvement in sensitivity. Nowadays, X-ray polarimetry is possible with two approaches:

1. endowing a focusing X-ray telescope with a pixelated detector having polarimetric capabilities (Fabiani et al. 2014). Sensors based on the photoelectric effect have the required polarimetric capabilities, since photoelectrons derived from polarized photons have emission azimuthal directions distributed as $\cos^2(\phi)$, where ϕ is the angle with respect to the polarization vector. This is the concept adopted for X-ray Imaging Polarimetry Explorer (XIPE), proposed to ESA for the M4 call with launch in 2025, and currently selected for study phase;
2. using imaging mirrors reflecting at the polarization angle (for X-rays, it is about 45 deg): this is the approach adopted by the Lightweight Asymmetry and Magnetism Probe (LAMP) project, developed at Tsinghua University in China.

This section focus on the LAMP project. The primary targets of LAMP include the thermal emission from the surface of pulsars and the synchrotron emission produced by relativistic jets in blazars [She et al. 2015]. Their emission is peaked in the soft X-ray band near 250 eV, and would be impossible to be detected by gas photoelectric polarimetry, which is typically sensitive only above 2 keV.

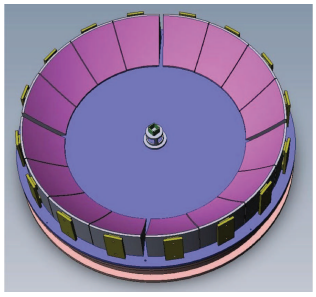

Figure 10.6: *: A schematic drawing of the LAMP polarimetric instrument. Credits: She 2015.*

To reach these objectives, LAMP is designed to reflect 250 eV X-rays with 16 segments of paraboloidal mirrors (Fig. 10.6), at incidence angles near 45 degrees: in these conditions, only the component perpendicular to the incidence plane (s-polarization) is reflected, while the parallel component (p-polarization) is absorbed. The mirrors, with radius from 201 to 286 mm, focus the

X-rays onto four detectors, each facing four segments of mirrors, at a 120 mm distance. The collecting area of the telescope is about 1300 cm^2 [She et al. 2015].

Unlike grazing-incidence soft X-ray optics, for which a simple high-Z layer (e.g., gold) is sufficient, multilayer coatings are needed to have high reflectivity at 45 degrees incidence. The multilayers have to be periodic to enhance the reflectivity near 250 eV, according to the first-order Bragg law (Eq. 2.23). Replacing the values for θ and λ in Eq. 2.23, we obtain d = 3.5 nm, which makes the deposition of high-reflectivity multilayer coatings with this low thickness definitely challenging.

To demonstrate the multilayer reflectivity performances, representative Co/C and Cr/C samples have been deposited onto different kinds of substrates (silicon, glass, electroformed nickel), varying the composition of the sputtering gas (pure argon, or argon with a few percent of nitrogen), and therefore the nitruration degree of chromium, cobalt, and carbon. Co/C multilayers on electroformed nickel substrate are considered the baseline [Wen et al. 2015], but other combinations were also studied.

Reflectivity measurements of these samples [Spiga et al. 2015c] have been carried out at BEAR (Bending magnet for Emission, Absorption and Reflectivity) beamline at the Elettra light source (Sincrotrone Trieste, Italy): this facility, in fact, provides an X-ray beam almost completely polarized, with selectable energy in the appropriate range, filtered to a passing band narrower than 0.5 eV. The system also includes a precise goniometric system, able to rotate the sample in the incidence plane, and also about the incidence direction. The samples were therefore measured in polarized X-rays from 240 to 290 eV, in the 40-50 deg angular range.

10.2.2 BEAR at Elettra - Sincrotrone Trieste

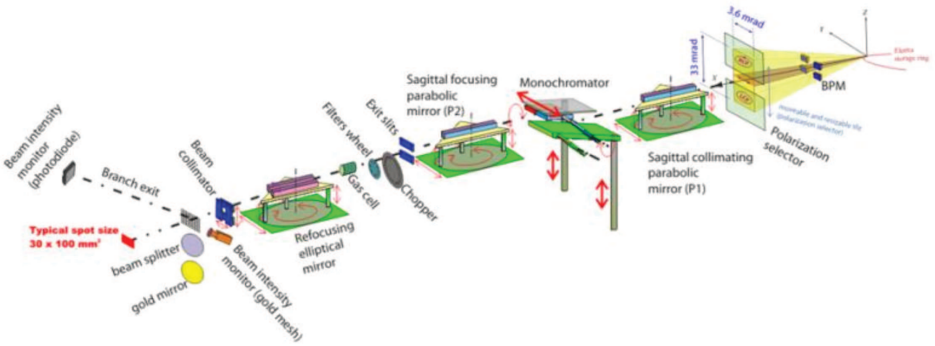

Figure 10.7: *: Layout of the BEAR beamline at Elettra - Sincrotrone Trieste. At the entrance of the beamline, the polarization selector allows selecting linearly polarized light (http://www.elettra.trieste.it/lightsources/elettra/elettra-beamlines/bear/beamline-description.html).*

BEAR is a beamline at Elettra (Sincrotrone Trieste) dedicated, among other things, to reflectivity measurements (Fig. 10.7). The source of BEAR is the ELETTRA bending magnet. The beam line operates in the 3-1600 eV spectral region. The beam line is equipped with a device for selecting the polarisation light. Ideally, the synchrotron radiation light in the orbit plane is linearly polarized, while would be circularly polarized at 90 deg off the orbit plane (respectively right circular and left circular over and below the orbit plane). A double vertical slit stage can be used to deliver alternatively linear, right or left circular polarization light. For our experiment, we needed a linearly polarized beam, hence, a 2 mm aperture was selected: this corresponds to 99% of polarized rays in the horizontal plane [Spiga et al. 2015c].

The layout with two parabolic mirrors and one elliptical mirror is designed to be theoretically aberration free. A monochromator enables the selection of the desired line, by varying the in-

cidence angle on the grating. We have selected a highly monochromatic setup: a 70 μm wide aperture corresponding to an energy resolution E/ΔE = 1500, i.e. ΔE = 0.16 eV at E = 250 eV. After being refocused to the exit slits by the parabolic mirror P2 (Fig. 10.7), the beam traverses a filter that removes higher order harmonics: in our case it was a 0.6 μm Ag filter.

The sample chamber is equipped with motors enabling movements of the sample holder in all directions, accurate alignment, and reflectivity scans in a very wide angular range. A sample insertion chamber is available to change a sample without venting the measuring chamber.

Finally, the detector used is a photodiode located 160 mm from the sample, with an entrance window of 8 mm $\times$ 8 mm, yielding an acceptance angle of $\Delta\theta$ = 2.8 deg.

10.2.3 Preliminary roughness measurements of the samples

Multilayer coatings with Co/C and Cr/C have been deposited onto different kinds of substrates: electroformed nickel, glass and silicon. Substrate samples in electroformed nickel have been provided by MLT by replication of a highly polished, 2-inch diameter fused silica master by General Optics, with standardized roughness of $\sim$ 1 Å at spatial wavelengths below 1 μm. The masters were coated with a 50 nm thick gold layer deposited by e-beam evaporation, electroformed with nickel, and separated from the master. The thickness of the gold layer is kept to an optimal value to minimize the roughness growth. The resulting disks have been characterized in roughness with the AFM both by 10 μm and 2 μm scans. They were then diced by electroerosion into squared samples (13 mm $\times$ 13 mm, 1 mm thick). Eventually, the samples were coated at IPOE with Cr/C and Co/C multilayers, with variable percent of nitrogen in the sputtering gas (pure argon, argon + 2%, 4%, and 6% of N_2, with a working pressure of 0.133 Pa, Wen et al. 2015) aiming at a reflectivity enhancement. The nominal multilayer recipe is a stack of 100 couples of layers, where Co (or Cr) layers are 1.4 nm thick and C layers are 2.1 nm thick. During the same coating run, squared samples of D263 glass, with 0.3 mm thickness, and silicon wafers were coated to disentangle the roughness introduced by the multilayer growth from the one of the substrate.

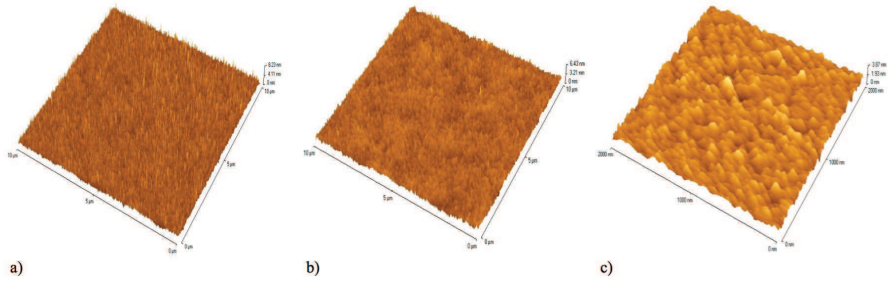

Figure 10.8: *: AFM measurements of nickel samples: a) before coating: 10 μm scan, σ = 6.2 Å; b) after coating, 10 μm scan, σ = 5.4 Å; c) before coating, 2 μm scan, σ = 3.4 Å.*

Roughness measurements were repeated, after the multilayer coating on the electroformed nickel substrate, over the 10 μm range (usually the most concerned one by the issue of roughness growth, Salmaso et al. 2011). No relevant changes in the roughness were observed: this rules roughness amplification out in the stack. The measured roughness was 5-6 Å in the 10 μm AFM scan, and 3.4 Å in the 2 μm AFM scan [Tayabaly IR05-2014]. As for the D263 glass, the rms roughness was found to be 2.3 Å in the 2 μm AFM scan [Wen et al. 2015], which indicates that multilayer deposited on D263 glass substrates should have a better performance than those in nickel. For silicon, we assumed the roughness to be 0.7 Å rms, typical of the pristine surface of commercial silicon wafers.

The roughness impact on the reflectivity at 250 eV energy, and 45 degrees incident angle, is not as low as in grazing-incidence. In fact, the reflectivity of a surface decreases exponentially

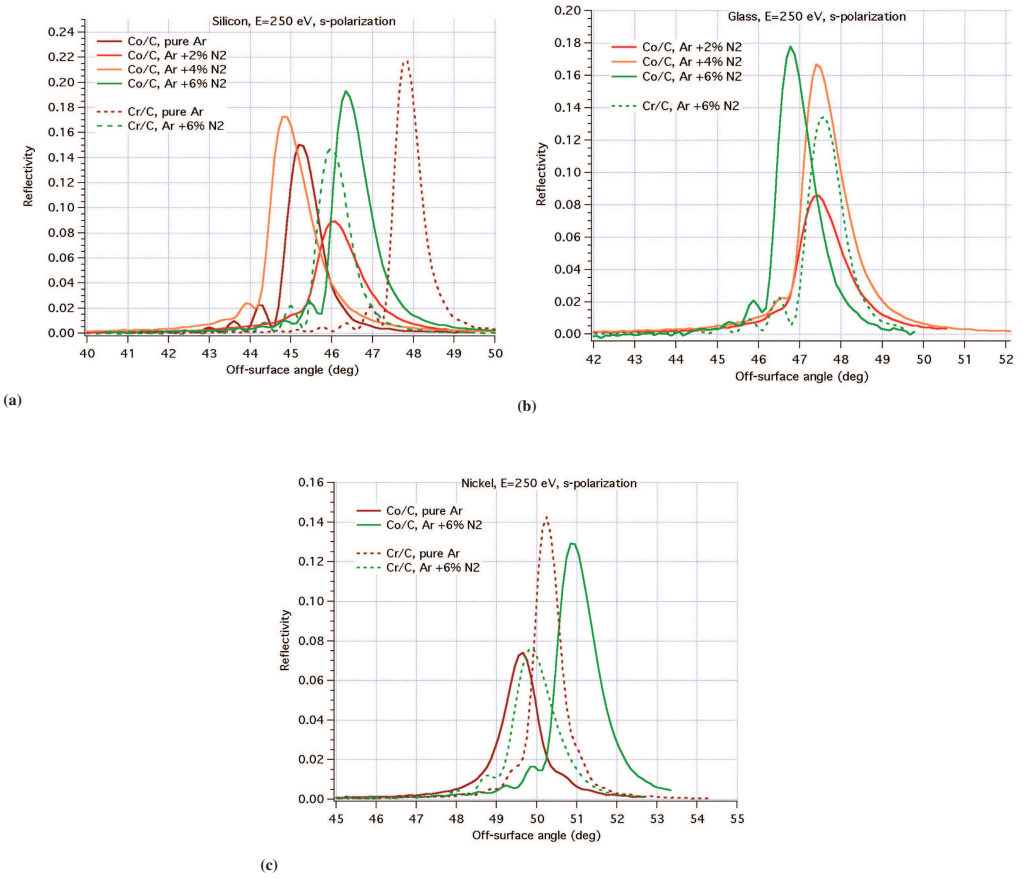

Figure 10.9: *: Angular reflectivity scans, at the fixed X-ray energy of 250 eV, of a few samples deposited on Silicon (a), D263 (b) and electroformed Nickel (c).*

with the square of $\sigma \sin\theta/\lambda$ (Debye-Waller formula, Eq. 2.20): therefore the roughness impact becomes more relevant as θ increases. The roughness has to be kept much smaller than the d-spacing [Spiga et al. 2015c]: since $d = 3.5$ nm, the roughness has to be less than a few angstrom, exactly as required in hard X-ray optics. In the BEAR setup, the detector acceptance angle was set to $\Delta\theta = 2.8$ deg. The large value of $\Delta\theta$ allows us including a very large fraction of the scattered beam; hence, the reflectivity measurement should fit surface roughness measurements over a 1 μm range (i.e., the rms measured by an AFM over a region of 1 μm size).

10.2.4 Reflectivity results

Both angular scans and energy scans (refer to the description of the BEDE-D1 diffractometer in Section 4.3.4) were performed at BEAR for each sample. Angular scans are performed at a fixed setting of the monochromator, while scanning the θ angle. Energy scans are obtained keeping the sample in a fixed position, while scanning the X-ray energy E.

Fig. 10.9 shows the angular scans of few samples, on the different substrates. The higher reflectivity is measured for the samples with silicon substrate, as expected from the different substrate roughness. All the Bragg peaks show an asymmetry: in fact they exhibit secondary peaks at smaller incidence angles, suggesting some a-periodicity of the stack. For all the substrates, the reflectivity of Co/C samples increases with the nitrogen inlet, while reactive sputtering with

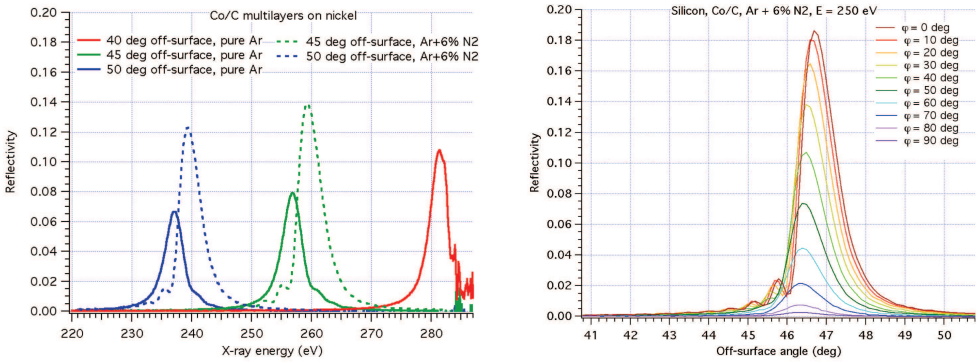

Figure 10.10: *: Left: Energy reflectivity scans, at the fixed incidence angles, of a few Co/C samples deposited on electroformed Nickel. Right: Angular reflectivity scans, at the fixed X-ray energy of 250 eV, of a Co/C sample deposited on Silicon, for different values of the ϕ angle between the polarization plane and the incidence plane, from almost pure s-polarization (ϕ = 0 deg) to almost pure p-polarization (ϕ = 90 deg).*

nitrogen degrades the performances of Cr/C multilayers. For nickel samples, the Bragg peak is found at larger angles than those of the other samples: this means that the d-spacing is smaller, probably because of the different position in the sputtering chamber. For all substrates, the Co/C multilayer have bandwidth significantly wider than the Cr/C multilayer. Since the maximization of the integral reflectivity is requested in order to get a high throughput of photons for LAMP, Co/C multilayer fabricated using reactive sputtering with nitrogen is judged to give the best results [Wen et al. 2015].

Fig. 10.10-left shows the energy scans of the Co/C samples deposited on electroformed Nickel: also in this case the presence of nitrogen is beneficial for Co/C multilayers. Finally 10.10-right shows the angular scans of the Co/C samples deposited on Silicon, obtained rotating the experimental chamber from $\phi = 0$ deg (s-polarisation) to $\phi = 90$ deg (p-polarisation), always keeping the incidence near the polarization angle. As a small issue, the angular scales of the different scans are not exactly aligned because the θ alignment is not exactly maintained during the rotation in ϕ. Most important, at ϕ = 90 deg, the reflectivity is much less then 1% and mostly related to the residual elliptical polarization in the incident beam.

10.2.5 Conclusions

The reflectivity measurements campaign, performed in synchrotron light at 250 eV, at the BEAR beam line of Elettra (Sincrotrone Trieste), on polarizing mirror samples with periodic Co/C and Cr/C multilayer coatings , show that the LAMP approach to astronomical X-ray polarimetry is feasible, even if the unusually large incidence angle (45 degrees) poses a challenge to roughness and d-spacing control. Nevertheless, also the samples deposited on the rougher electroformed nickel substrate, a standard material to fabricate the optics of X-ray telescopes, show good polarizing and reflectivity properties. Reactive sputtering with 6% nitrogen can effectively improve the quality of Co/C multilayers. The R_s/R_p ratio for the Co:N/C:N multilayer is more than 70, which is compliant for the application of LAMP.

CHAPTER 11

Conclusions and final remarks

The main motivation behind this Ph.D. research was the improvement of the Slumped Glass Optics (SGO) technology for X-ray telescopes, whose development started at INAF-OAB in 2009. Until 2013, OAB worked under ESA contract aimed to develop in Europe a process alternative to the one based on Silicon Pore Optics; SPO is the baseline technology adopted to reach the angular resolution of 5 arcsec HEW, required by the ATHENA mission.

The state of the art of SGO at INAF-OAB, before this research, was summarised by the last prototype realized under ESA contract, the Proof Of Concept (POC) #2, realised in early 2013 using Schott AF32 glass foils slumped on Schott Zerodur K20 mould, selected for its glass anti-sticking properties. The achieved result was $\sim$ 22 arcsec HEW, measured in-focus, with full illumination at 0.27 keV at the X-ray PANTER/MPE facility in Munich.

To improve this result, I have modified the process and the setup with respect to the previous one. The metrological analysis of the slumped glass foils was used as feedback to improve the slumping process. All the slumped glass foils were measured in shape and roughness, in order to asses their optical quality: for each glass foil, the HEW expected in single reflection, after the simulation of an ideal integration, was computed.

As a very preliminary result, I have developed a new method to precisely characterise the mid frequency errors of the glass foils (Section 4.2.3). For comparison, the performance of a glass foil adopted as reference, slumped with the same parameters of the glass foils integrated onto the POC#2, was valued 13 arcsec with the old method (CHR-RD mounted on the LTP, and both side glass measurement to correct for the gravity and bearing points deformation) and 6.8 arcsc with the method developed (pure LTP with First Contact to remove the reflection from the back side of the glass, and FEA to correct for the gravity and bearing points deformation) (Section 6.3.2).

An existing model, developed by Jimenez-Garate in 2003 to model the relaxation of ripples in the slumped glass foil when in contact with the slumping mould, was modified to include the application of pressure (Section 6.4): the model was compared to the experimental results, paving the way to a better understanding of the process of ripple formation. The application of pressure was found to be essential, also from the theory viewpoint, to reduce the mid-frequency errors of the slumped glass foils, very critical for the final performances of the optics.

As for the slumping process (Chapter 6), while keeping keatite as slumping mould material, I have changed the glass type from Schott AF32 to Corning Eagle XG. I have developed cleaning protocols, used different thermal cycles and different pressures conditions, and reconditioned the pressure control system. I have optimised the mould height with experiments based on Finite Element Analysis, and reduced the thermal gradients inside the mould and the glass foils. In each step, few parameters were modified to improve the quality of the slumped glass foils. While some resulted in a real improvement, others did not improve the result, but increased the understanding of the process (pressure value, pressure application time, annealing time, etc.). The final result, compared to the glass foil used as reference for the POC#2 glass quality (HEW = 6.8 arcsec), is a **HEW of 2.2 arcsec**, expected in single reflection at 1 keV X-ray energy and 0.7 deg incidence angle, after the simulation of an ideal integration. Ten glass foils were slumped with the same process condition, proving that the result is stable to within 0.3 arcsec. This value is almost in line with the 2 arcsec accounted for the slumped glass foils in the error budget for ATHENA. About 1 arcsec is due to replication of the mid-frequency errors in the slumping mould which, owing to the improved result in the slumping, are now a limiting factor in the quality of the slumped glass foils. From the point of view of roughness, the contribution to the HEW, of the slumped glass foils, is guaranteed to be less then 1 arcsec at 1 keV. The roughness of the slumped glass foils was improved from the initial 21 Å to 11 Å of the last foils. Very recent results prove that the roughness of the slumped glass foils can be further reduced to $\sim$ 7 Å, making the technology attractive also for higher X-ray energies and higher incidence angles.

The glass foils slumped during this Ph.D. have been used for the production of two SGO prototypes for the ATHENA mission (Chapter 8): the POC#3, (with 2 glass foils assembled) is characterised by HEW value of 5.5 arcsec at 0.27 keV in the best portion of the module, as tested at the PANTER facility; the POC#4 (with 8 glass foils) has overall expected HEW of about 15 arcsec from metrological data after integration, but the result in X-ray was much higher because of accidental problems during the integration. The next prototype, the POC#5 with the best eight glass foils produced during my Ph.D. activity, will be integrated on improved BK7 integration mandrels and tested in X-rays to assess the improvement already proven by metrology and simulations.

Some of the produced slumped glass foils have also been used for studies of active profile corrections with piezoelectric elements, both for the AXYOM project (Italy) and X-ray Surveyor (USA) (Chapter 9). Concerning the X-ray Surveyor, D263 glass foils produced by NASA/GSFC cannot be used for incompatibility with the piezo deposition process. On the contrary, Eagle glass foils slumped at INAF-OAB represent an ideal source for their activities.

Alternative materials and techniques have been used in this research to further improve the result (Chapter 7). To reduce the surface micro roughness of the slumped glass foils, I have proven that the slumping technique with pressure application can be applied also to the indirect slumping, in which the optical surface of the glass is not in contact with the mould, thus preserving its initial micro-roughness. Moreover, the dip coating technique was studied to fill the micro-pores present on the surface of the glass foils slumped with the direct technique. Alternative materials for the slumping mould were tested, defining Si_3N_4 as a very promising candidate, owing to its higher rigidity with respect to Zerodur K20 and therefore preferable to avoid the mould deformations experienced with K20. The Gorilla glass (normally used for smartphones and tablets), was proven to preserve the surface quality of the glass foils, once slumped and chemically tempered to increase the telescope resistance to launch.

Finally, I have also studied the properties of multilayer coatings for X-ray optics (Chapter 10). I have upgraded an IDL code to simulate the roughness growth in the multilayer deposition process, extending the computations from periodic to the more general case of graded multilayers. I have also contributed to the X-ray measurements at the BEAR beamline of the Elettra synchrotron in Trieste, on multilayers deposited on glass, silicon and electroformed nickel, for the polarimetric LAMP project.

The following research contributions result from this Ph.D. work:

1. development of a precise characterisation method for mid frequency errors of the glass foils;
2. development of cleaning and annealing protocols for the K20;
3. development of a close and open loop control for pressure application;
4. development of an analytical model to implement the pressure in the Jimenez model for ripple formation;
5. angular resolution improvement from 6.8 to 2.2 arcsec HEW for figure errors;
6. roughness improvement of the slumped glass foils from 21 to 7 Å rms in the WYKO frequency range;
7. production of slumped Eagle glass foils for the X-ray Surveyor tests on active deterministic figure correction with piezoelectric cells;
8. definition of the tempering process on slumped Gorilla glass as suitable for X-ray telescopes;
9. preliminary approaches aimed at further decrease the roughness contribution: use of the dip coating technique to fill the pores of the slumped glass foils and use of the indirect slumping approach to preserve the roughness of the native glass;
10. preliminary test on Si_3N_4 as slumping mould material;
11. extension from periodic to the more general graded multilayers of an existing IDL code to simulate the roughness evolution in the multilayers and the X-ray scattering;
12. contribution to the technology advancement of X-ray polarimetry for the LAMP mission.

Possible developments of this activity include:

1. improvement of the slumping mould replication in the low-frequency range. These errors, in fact, are efficiently damped in our integration scheme, but still an issue in the slumping process.
2. definition of a polishing process for the K20 surface aimed at roughness reduction. The replication of the mould roughness (σ_{Mould} = 130 Å) onto the slumped glass foil (σ_{Glass} = 7 Å) suggests that a reduction to σ_{Mould} = 70 Å could be sufficient to preserve the original glass roughness ($\sigma_{\mathrm{Bare-glass}}$ = 3.6 Å). This seems to be possible as reported by Zeiss (Section 3.6.2).
3. definition of a polishing/annealing process aimed at avoiding the K20 deformation with the first thermal cycle.

A list of publications derived from my Ph.D. work is reported hereafter.

Author's list of publications

Paper published

- **Salmaso, B.**, Civitani, M., Brizzolari, B., Basso, S. Ghigo, M., Pareschi, G., Spiga, D., Proserpio, L., Suppiger, Y., *Development of mirrors made of chemically tempered glass foils for future X-ray telescopes*, Experimental Astronomy, Vol. 39, Issue 3, p. 527-545 (2015)
- **Salmaso, B.**, *Gorilla glass for x-ray telescopes*, SPIE Newsroom. DOI: 10.1117/2.1201509.006122 (2015)
- Spiga, D., Barbera, M., Collura, A., Basso, S., Candia, R., Civitani, M., Di Bella, M., Di Cicca, G., Lo Cicero, U., Lullo, G., Pelliciari, C., Riva, M., **Salmaso, B.**, Sciortino, L., Varisco, S., *Manufacturing an active X-ray mirror prototype in thin glass*, Journal of Synchrotron Radiation Vol. 22, Issue 1, to be published in Jan 2016
- Proserpio, L., Basso, S., Borsa, F., Citterio, O., Civitani, M., Ghigo, M., Pareschi, G., **Salmaso, B.**, Sironi, G., Spiga, D., Tagliaferri, G., D'Este, A., Dall'Igna, R., Silvestri, M.m Parosi, G., Martelli, F., Bavdaz, M., Wille, E., *Evaluation of the surface strength of glass plates shaped by hot slumping process*, Optical Engineering, 53, Issue 8, 085101 (2014)
- **Salmaso, B.**, Spiga, D., Canestrari, R., Raimondi, L., *X-ray scattering of periodic and graded multilayer: comparison of experiments to simulation from surface microroughness characterization*, Nuclear Instruments and Methods in Physics Research A, Vol. 710, p. 106-113 (2013)
- Civitani, M., Basso, S., Citterio, O., Conconi, P., Ghigo, G., Pareschi, G., Proserpio, L., **Salmaso, B.**, Sironi, G., Spiga, D., Tagliaferri, G., Zambra, A., Martelli, F., Parodi, G., Fumi, P., Gallieni, D., Tintori, M., Bavdaz, M., Wille, E., *Accurate integration of segmented X-ray optics using interfacing ribs*, Optical engineering, Vol. 52, Issue 9, 091809 (2013)

Conference proceedings

- **Salmaso**, B., Basso, S., Brizzolari, C., Civitani, M., Ghigo, M., Pareschi, G., Spiga, D., Tagliaferri, G., Vecchi, G., *Direct hot slumping of thin glass foils for future generation X-ray telescopes: current state of the art and future outlooks*, Proceedings of the 2014 International Conference on Space Optics (2015)
- **Salmaso**, B., Basso, S., Brizzolari, C., Civitani, M., Ghigo, M., Pareschi, G., Spiga, D., Tagliaferri, G., Vecchi, G., *Slumped Glass Optics for X-ray telescopes: advances in the hot slumping assisted by pressure*, Proc SPIE 9603, 96030O (2015)
- Civitani, M., Basso, S., Brizzolari, C., Ghigo, M., Pareschi, G., **Salmaso, B.**, Spiga, D., Tagliaferri, G., Vecchi, G., Breuning, E., Burwitz, V., *Slumped glass optics with interfacing ribs for high angular resolution X-ray astronomy: a progress report*, Proc SPIE 9603, 96030P (2015)
- Spiga, D., **Salmaso, B.**, She, R., Tayabaly, K., Wen, M., Banham, R., Costa, E., Feng, H., Giglia, A., Huang, Q., Muleri, F., Pareschi, G., Soffitta, P., Tagliaferri, G., Valsecchi, G., Wang, Z., *Testing multilayer-coated polarizing mirrors for the LAMP soft X-ray telescope*, Proc SPIE 9603, 96031B (2015)

- She, R., Feng, H., Soffitta, P., Muleri, F., Xu, R., Li, H., Bellazzini, R., Wang, Z., Spiga, D., Minuti, M., Brez, A., Spandre, G., Pinchera, M., Sgro, C., Baldini, L., Wen, M., Shen, Z., Pareschi, G., Tagliaferri, G., Tayabaly, K., **Salmaso, B.**, Zhan, Y, *LAMP: a micro-satellite based soft X-ray polarimeter for astrophysics*, Proc. SPIE 9601, 96010I (2015)

- **Salmaso, B.**, Basso, S., Brizzolari, C., Civitani, M.M., Ghigo, M., Pareschi, G., Spiga, D., Tagliaferri, G., Vecchi, G., *Production of thin glass mirrors by hot slumping for X-ray telescopes: present process and ongoing development*, Proc SPIE 9151, 91512W (2014)

- Civitani, M., Basso, S., Ghigo, G., Pareschi, G., **Salmaso, B.**, Spiga, D., Tagliaferri, G., Vecchi, G., Burwitz, V., Hartner, G., Menz, B., *X-ray optical units made of glass: achievements and perspectives*, Proc. SPIE 9144, 914416 (2014)

- Basso, S., Buratti, E., Civitani, M.M., Pareschi, G., **Salmaso, B.**, Spiga, D., Tagliaferri, G., Eder, J., *A high resolution large x-ray mission based on thin glass: optomechanical design*, Proc. SPIE 9144, 91444C (2014)

- Spiga, D., Barbera, M., Basso, S., Civitani, M., Collura, A., Dell'Agostino, S., Lo Cicero, U., Lullo, G., Pelliciari, C., Riva, M., **Salmaso, B.**, Sciortino, L., *Active shape correction of a thin glass/plastic X-ray mirror*, Proc. SPIE 9208, 92080A (2014)

- **Salmaso, B.**, Bianco, A., Citterio, O., Pareschi, G., Pariani, G., Proserpio, L., Spiga, D., Mandelli, D., Negri, M., *Micro-roughness improvement of slumped glass foils for X-ray telescopes via dip coating*, Proc. SPIE 8861-60 (2013)

- Proserpio, L., Crimi, G., Ghigo, M., Pareschi, G., **Salmaso, B.**, D'Este, A., Dall'Igna, R., Silvestri, M., Parodi, G., Martelli, F., *Evaluation of the surface strength of glass plates shaped by hot slumping process*, Proc. SPIE 8861, 88610S (2013)

- Civitani, M., Ghigo, M., Basso, S., Proserpio, L., Spiga, D., **Salmaso, B.**, Pareschi, G., Tagliaferri G., Burwitz, V., Hartner, G.D., Menz, B., Bavdaz, M., Wille, E., *Direct hot slumping and accurate integration process to manufacture prototypal x-ray optical units made of glass*, Proc. SPIE 8861, 886110 (2013)

- Spiga, D., Basso, S., Bavdaz, M., Burwitz, V., Civitani, M., Citterio, O., Ghigo, M., Hartner, G., Menz, B., Pareschi, G., Proserpio, L., **Salmaso, B.**, Tagliaferri, G., Wille, E., *Profile reconstruction of grazing-incidence X-ray mirrors from near-fiels X-ray full imaging*, Proc. SPIE 8861, 88611F (2013)

- Ghigo, M., Proserpio, L., Basso, S., Citterio, O., Civitani, M., Pareschi, G., **Salmaso, B.**, Sironi, G., Spiga, D., Tagliaferri, G., et al., *Slumping technique for the manufacturing of a representative x-ray grazing incidence mirror module for future space missions*, Proc. SPIE 8884, 88841Q (2013)

- Bavdaz, M., Wille, E., Wallace, K., Shortt, B., Fransen, S., Rando, N., Collon, M., Ackermann, M., Vacanti, G., Guenther, R.,Haneveld, J., Riekerink, M.O., Koelewijn, A., van Baren, C., Kampf, D., Zuknik, K.H., Reutlinger, A., Christensen, F., Della Monica Ferreira, D.,Jakobsen, A.C., Krumrey, M., Mller, P., Burwitz, V., Pareschi, G., Ghigo,M., Civitani, M., Proserpio, L., Spiga, D., Basso, S., **Salmaso, B.**, Gallieni, D., Tintori, M., Fumi, P., Martelli, F., Parodi, G., Ferrario, I., Povey, I., *X-ray optics developments at ESA*, Proc. SPIE 8861, 88610L (2013)

- Proserpio, L. Basso, S., Civitani, M., Citterio, O., Conconi, P., Ghigo, M., Pareschi, G., **Salmaso, B.**, Spiga, D., Tagliaferri, G., *Segmented glass optics for next generation X-ray telescopes*, Memorie della Societa Astronomica Italiana, Vol. 84, p. 819 (2013)

- Spiga, D. Pareschi, G., Pelliciari, C., **Salmaso, B.**, Tagliaferri, G., *Functional tests of modular elements of segmented optics for X rays telescopes via an expanded beam facility*, Proc. SPIE 8443, 84435F (2012)

- Ghigo, M., Basso, S., Borsa, F., Bavdaz, M., Citterio, O., Civitani, M., Conconi, P., Pagano, G., Gallieni, D., Martelli, F., Parodi, G., Pareschi, G., Proserpio, L., **Salmaso, B.**, Sironi, G., Spiga, D., Tagliaferri, G., Tintori, M., Wille, E., Zambra, A., *Development of high angular resolution x-ray telescopes based on slumped glass foils*, Proc. SPIE 8443, 84430R (2012)

- **Salmaso, B.**, Spiga, D., Canestrari, R., Raimondi, L., *Accurate modeling of periodic and graded multilayer X-ray scattering from surface microroughness characterization*, Proc. SPIE 8147, 814710 (2011)

- Spiga, D., Raimondi, L., Furuzawa, A., Basso, S., Binda, R., Borghi, G., Cotroneo, V., Grisoni, G., Kunieda, H., Marioni, F., Matsumoto, H., Mori, H., Miyazawa, T., Negri, B., Orlandi, A., Pareschi, G., **Salmaso, B.**, Tagliaferri, G., Uesugi, K., Valsecchi, G., Vernani, D., *Angular resolution measurements at SPring-8 of a hard X-ray optic for the New Hard X-ray Mission*, Proc. SPIE 8147, 81470A (2011)

- Proserpio, L., Ghigo, M., Basso, S., Conconi, P., Citterio, O., Civitani, M., Negri, R., Pagano, G., Pareschi, G., **Salmaso, B.**, Spiga, D., Tagliaferri, G., Tintori, M., Terzi, L., Zambra, A., *Production of the IXO glass segmented mirrors by hot slumping with pressure assistance: tests and results*, Proc. SPIE 8147, 81470M (2011)

- Basso, S., Pareschi, G., Citterio, O., Spiga, D., Tagliaferri, G., Raimondi, L., Sironi, G., Cotroneo, V., **Salmaso, B.**, Negri, B., Attinà, P., Borghi, G., Orlandi, A., Vernani, D., Valsecchi, G., Binda, R., Marioni, F., Moretti, S., Castelnuovo, M., Burkert, W., Freyberg, M.J., Burwitz, V., *The optics system of the New Hard X-ray Mission: status report*, Proc. SPIE 8147, 814709 (2011)

- Orlandi, A., Basso, S., Borghi, G., Binda, R., Citterio, O., Grisoni, G., Kools, J., Marioni, F., Missaglia, N., Negri, B., Negri, R., Pareschi, G., Raimondi, L., Ritucci, A., **Salmaso, B.**, Sironi, G., Spiga, D., Subranni, R., Tagliaferri, G., Valsecchi, G., Vernani, D., *Technologies for manufacturing of high angular resolution multilayer coated optics for the New hard X-ray Mission*, Proc. SPIE 8076, 807606 (2011)

- Pareschi, G., Basso, S., Bavdaz, M., Conconi, C., Citterio, O., Civitani, M., Friedrich, P., Gallieni, D., Ghigo, M., Guldimann, B., Martelli, F., Pagano, G., Parodi, G., Proserpio, L., **Salmaso, B.**, Schael, A., Spiga, D., Tagliaferri, G., Tintori, M., Vongehr, M., Zambra, A., *Hot slumping glass technology in Europe for the IXO segmented mirrors*, IXO science meeting 2010, Paris (2010)

- Ghigo, M.,Basso, S.,Bavdaz, M., Conconi, P., Citterio, O., Civitani, M., Friedrich, P., Gallieni, D., Guldimann, B., Martelli, F., Negri, R., Pagano, G., Pareschi, G., Parodi, G., Proserpio, L., **Salmaso, B.**, Scaglione, F., Spiga, D., Tagliaferri, G., Terzi., L., Tintori, M., Vongehr, M., Wille, E., Winter, A., Zambra, A., *Hot slumping glass technology for the grazing incidence optics of future missions with particular reference to IXO*, Proc. SPIE 7732, 77320C (2010)

- Civitani, M., Basso, S., Bavdaz, M., Citterio, O., Conconi, P., Gallieni, D., Ghigo, M., Guldimann, B., Martelli, F., Pagano, G., Pareschi, G., Parodi, G., Proserpio, L., **Salmaso, B.**, Spiga, D., Tagliaferri, G., Tintori, M., Wille, E., Zambra, A., *IXO x-ray mirrors based on slumped glass segments with reinforcing ribs: optical and mechanical design, image error budget, and optics unit integration process*, Proc. SPIE 7732, 773242 (2010)

- Civitani, M., Basso, S., Bianco, A., Conconi, P., Citterio, O., Ghigo, M., Pagano, G, Pareschi, G., Proserpio, L., **Salmaso, B.**, Spiga, D., Tagliaferri, G., Zambra, A., Friedrich, P., Vongehr, M., Schael, A., Parodi, G., Martelli, F., Gallieni, D., Tintori, M., Bavdaz, M., Guldimann, B., *Hot slumped glass segments with reinforcing ribs technology for the manufacturing of the IXO telescope modules*, Proceedings of the 2010 International Conference on Space Optics (2010)

Internal Report

- Holyszko, J., **Salmaso, B.**, Civitani, M., *Characterization of the profiles of glass foils after cutting and annealing*, INAF/OAB internal report 13/2015
- **Salmaso, B.**, Brizzolari, C., Pariani, G., Spiga, D., *LTP and ZYGO comparison of the profile measurements of the MK20-20B slumping mould*, INAF/OAB internal report 04/2015
- **Salmaso, B.**, Brizzolari, C., Arcangeli, L., Rossi, M., Spiga, D., *Characterization of the Zerodur K20-20B cylindrical slumping mould polished by Hellma*, INAF/OAB internal report 03/2015
- **Salmaso, B.**, Spiga, D., *Acceptance test and calibration of the Explorer Atomic Force Microscope new head*, INAF/OAB internal report 02/2015
- **Salmaso, B.**, Brizzolari, C., Basso, S., Civitani, M., Spiga, D., *Optimization of the slumping process of Eagle XG on Zerodur K20: fine tuning for the production of POC4 glass foils*, INAF/OAB internal report 01/2015
- **Salmaso, B.**, Brizzolari, C., Civitani, M., Sanvito, G., Spiga, D., *Slumping Eagle XG on new Zerodur K20 MK20-20 mould*, INAF/OAB internal report 15/2014
- **Salmaso, B.**, Brizzolari, C., Civitani, M., *Characterization of the Silicon cylindrical slumping mould polished by HELLMA*, INAF/OAB internal report 11/2014
- **Salmaso, B.**, Brizzolari, C., *Sticking of Eagle glass on Zerodur K20-20: failure analysis*, INAF/OAB internal report 06/2014
- Tayabaly, K., Spiga, D., **Salmaso, B.**, Valsecchi, G., Banham, R., Missaglia, N., Pareschi, G., Tagliaferri, G. *Electroformed nickel samples for the polarimetric LAMP X-ray telescope: sample roughness characterization*, INAF/OAB internal report 05/2014
- **Salmaso, B.**, Crimi, G., *Cleaning of Ruths primary mirror*, INAF/OAB internal report 04/2014

  Spiga, D., Civitani, M., Burwitz, V., Burkert, W., Menz, B., Hartner, G., Salmaso, B., Basso, S., Pareschi, G., Tagliaferri, G., et al., *Proof of Concept No. 2 optic with slumped glasses: tests in focus at PANTER*, INAF/OAB internal report 03/2014
- **Salmaso, B.**, Brizzolari, C., *From AF32 to Eagle XG: characterization of glasses slumped on Zerodur K20-10 mould*, INAF/OAB internal report 02/2014
- **Salmaso, B.**, Brizzolari, C., Spiga, D., *Characterization of the Zerodur K20-20 cylindrical slumping mould polished by HELLMA*, INAF/OAB internal report 01/2014
- **Salmaso, B.**, *Fine-tuning of slumped AF32 glasses on a Zerodur K20 mould.*, INAF/OAB internal report 14/2013

- **Salmaso, B.**, Basso, S., *LTP profiles of AF32 glasses with FEA correction: a method to remove spurious mid-frequency errors*, INAF/OAB internal report 12/2013
- Spiga, D., Civitani, M., Proserpio, L., **Salmaso, B.**, Basso, S., Burwitz, V., Menz, B., Hartner, G., Budau, B., *IXO backup optics with slumped glasses: PANTER test of the Proof of Concept 2 optic*, INAF/OAB internal report 10/2013
- **Salmaso, B.**, Bianco, A., Proserpio, L. Ghigo, M., Spiga, D., *IXO glasses cleaning procedure after slumping: removing residuals affecting the high frequency region.* , INAF/OAB internal report 01/2013
- Spiga, D., Civitani, M., Proserpio, L., Ghigo, M., Basso, S., **Salmaso, B.**, Pareschi, G., Zambra, A., Pagano, G., Burwitz, V., Menz, B., Hartner, G., Budau, B., Friedrich, P., Winter, A., *IXO back-up optics with slumped glasses: XOU-BB tests at PANTER and INAF/OAB*, INAF/OAB internal report 05/2012
- Spiga, D., **Salmaso, B.**, Proserpio, L., Ghigo, M., Basso, S., Civitani, M., Pareschi, G., Sironi, G., Pagano, G., Zambra, A., Burwitz, V., Burkert, W., Hartner, G., Budau, B., *IXO back-up optics with slumped glasses: Proof of Concept (PoC) tests at PANTER and INAF/OAB*, INAF/OAB internal report 04/2012
- **Salmaso, B.**, Spiga, D., *AFM analysis of test wafers coated with Cr-Ni-Au layers: roughness characterization*, INAF/OAB internal report 01/2012
- Raimondi, L., **Salmaso, B.**, Spiga, D., Valsecchi, G., Orlandi, A., Borghi, G., Rossi, M., Marioni, F., Basso, S., Burwitz, V., et al., *X-ray tests at PANTER on the TDM3 optic prototype for the New Hard X-ray Mission*, INAF/OAB internal report 06/2011
- Spiga, D., Proserpio, L., Pagano, G., **Salmaso, B.**, *Characterization of slumped glasses for the IXO backup optics project, phase 2*, INAF/OAB internal report 05/2011
- Spiga, D., Raimondi, L., **Salmaso, B.**, *High-resolution X-ray scattering measurement of slumped glasses*, INAF/OAB internal report 04/2011
- Raimondi, L., Spiga, D., **Salmaso, B.**, *IXO slumped glasses D5 and D7: analysis of spatial wavelength impact on the Point Spread Function by means of the Fresnel diffraction*, INAF/OAB internal report 03/2011
- **Salmaso, B.**, Raimondi, L., Negri, R., Spiga, D., Binda, R.,Orlandi, A., Valsecchi, G., *Hard X-ray mirrors for NHXM: reflectivity and roughness characterization of mirror shell samples*, INAF/OAB internal report 02/2011
- Spiga, D., Raimondi, L., **Salmaso, B.**, Valsecchi, G., Orlandi, A., Borghi, G., Binda, R., Basso, S., Borrelli, D., Marioni, F., Ferretti, L., Freyberg, M., Burkert, W., Hartner, G., Budau, B., Tagliaferri, G., Pareschi, G., *X-ray tests at PANTER on the TDM2 optic prototype for the New Hard X-ray Mission*, INAF/OAB internal report 06/2010
- Spiga, D., Raimondi, L., **Salmaso, B.**, Negri, R., *Reflectivity and stress characterization of W/Si and Pt/C multilayer samples for the New Hard X-ray Mission phase B development*, INAF/OAB internal report 03/2010

APPENDIX $\mathcal{A}$

The SPO technology

Silicon Pore Optics (SPO) is the baseline technology to be used for the production of the ATHENA telescope. This technology was first introduced by Beijersbergen et al. (2004) and subsequently applied to the ESA XEUS mission, (Kraft et al., 2005), and later for IXO, (Collon et al., 2010). The SPO technology has now been under development by ESA and Cosine Measurement Systems (http://cosine.nl) for over a decade. SPO utilises commercially available 300 mm Si wafers as starting material, thank to their surface figure and roughness quality ideally suited to X-ray optics applications.

The wafers, with a thickness of 0.775 mm, are double sided polished with the two surface very parallel, hence with very small thickness variations (Total Thickness Variation < 0.3 μm). The manufacture of Si pores using wafers is illustrated in Fig. A.1-left. The wafers are diced into rectangles, typically 66 mm wide.

The wedging process, consisting in growing an oxide layer with linearly increasing thickness, is performed to taper plates along the optical axis so as to create, when they are elastically bent and stacked, a conical approximation to a Wolter I optics. The wedging process slightly degrades the roughness surface from the original rms $\approx$ 1 Å to $\approx$ 3-4 Å, still very good for X-ray applications.

The ribbing process is performed with a slightly modified standard semiconductor dicing saw: it dices grooves into the silicon substrate, thereby creating the pores forming the channels for the X-rays to pass through, and simultaneously the ribs necessary for the stack bonding. For the development, the ribs dimensions were: pitch = 1 mm, width = 0.15 mm. height = 0.605 mm , therefore the membrane left from the silicon wafer is very thin and flexible, with thickness = 170 μm. Before the stacking, a "damage etch" is performed to remove any residual micro-crack, a well known side effect of dicing [Bavdaz et al. 2010]. A potassium hydroxide (KOH) solution is used to anisotropically and selectively etch damaged silicon material inside the diced grooves, while a protective coating is preventing the top surface of the ribs from being etched. This has also the advantage to suppress unwanted X-ray reflection by the surface within the groves.

A reflective coating (Ir + B_4C) is applied for optimization of the reflectivity of the mirror plates. Patterning of the coated surface is necessary to ensure bondability of the silicon mirror plates during the stacking process. Owing to the excellent smoothness of the silicon surface, the

plates can be optically bonded: either hydrophilic or hydrophobic bonding can be used, depending if the silicon surface is oxidised or not.

The wafers stacking (Fig. A.1-right) is performed against a Silicon mandrel made by Carl-Zeiss. Initially, a conical approximation of the parabola/hyerbola integration mandrels were used; in this case a pore of the mirror module focuses only in the azimuthal direction and therefore resulting in a X-ray spot as high as a pore. This was not a limitation for the original XEUS configuration. Now for ATHENA, the shorter focal length requires the mirrors to be curved also in the longitudinal direction in order not to limit the angular resolution [Willingale et al. 2014]. In fact, for pore height of 0.605 mm and 12 m focus, the resulting HEW, considering a perfect optics, would be 5.2 arcsec. Therefore, integration silicon mandrels were produced with a secondary curvature in the longitudinal direction [Collon et al. 2014].

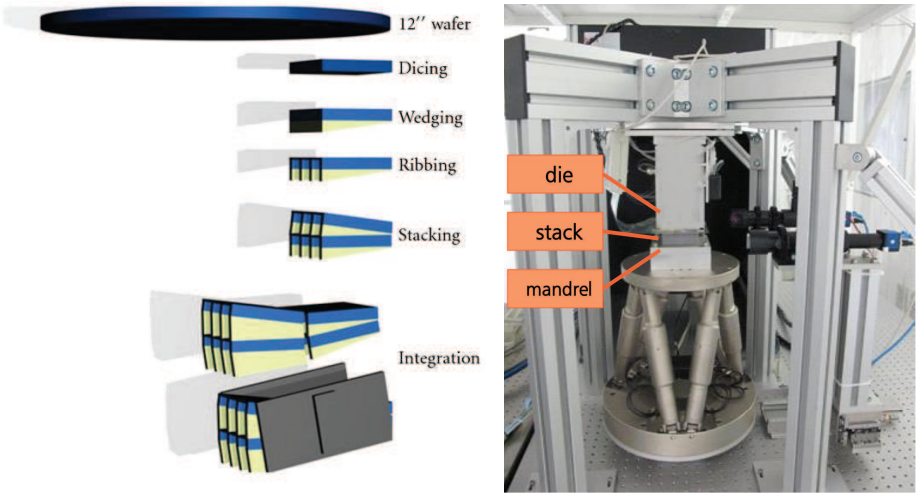

Figure A.1: *: Left: The production of the SPO modules starts with commercial silicon wafers and utilises processes available in the semiconductor industry. Right: The Silicon mandrel used for integration. Credits: ESA.*

Two wafer stacks are assembled to compose a SPO module (Fig. A.2-left). The grazing angles of the two reflections are set to be equal so the kink angle between the axis of pores in the 1st stack and the axis of pores in the 2nd stack must be set precisely at twice the grazing angle. Finally, the SPO modules are integrated to create the complete optics. Fig. A.2-right illustrates the concept with a layout example using 972 MMs distributed over 19 rings [Wille et al. 2015].

In order to maximise the on-axis collecting area of the SPO, the axial length of each reflecting surface, L (the height of the diced wafers) must be set such that

$$\frac{d}{L} = \tan(\theta), \tag{A.1}$$

where θ is the incident angle and d is the radial width of the pore, strictly determined by the thickness of the Silicon wafers and the thickness of the membrane which support the reflecting structure. Recalling (Section 2.2.2) that, in the double cone approximation of the Wolter optics, $r = f\tan(4\theta)$, where f is the focal length and r is the radius the mirror, it follows that the axial length of each pore is proportional to the inverse of the radial position (Eq. A.2, Fig. A.3-top). Using the focal length f = 12 m, the inner ring of modules at r = 285 mm has an axial length of L = 101.9 mm for each stack, the outer ring at r = 1437 mm has L = 20.3 mm.

$$L \approx \frac{4fd}{r}. \tag{A.2}$$

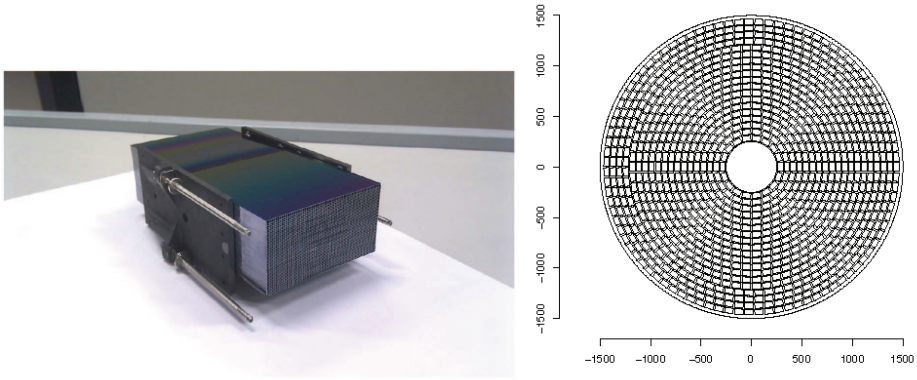

Figure A.2: *: Left:A complete SPO module comprising two stacks. Right: SPO module layout to create a complete mirror. Credits: Willingale 2013.*

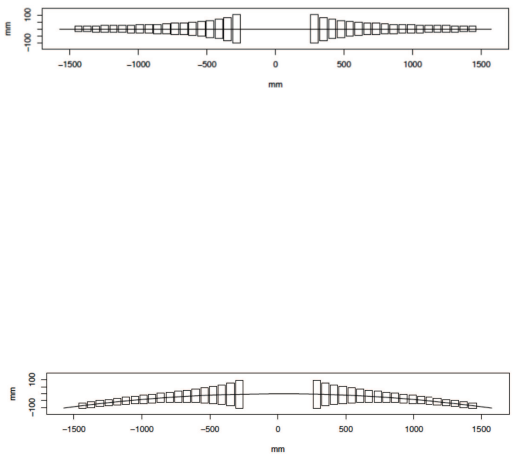

Figure A.3: *: Top: Axial length distribution of SPO modules across the aperture. Bottom: SPO module integrated across a spherical principal plane in the Wolter-Schwartzschild configuration. Credits: Willingale 2013.*

As for the off-axis response, the angular resolution of a Wolter I optic degrades rapidly with off-axis angle. The situation can be improved using the Wolter-Schwartzschild (Section 2.3.2) design using surfaces of revolution which approximately fulfill the Abbe sine condition (Section 2.3). In this layout, the modules are arranged on a spherical surface with a radius equal to the focal length (Fig. A.3-bottom).

Fig. A.4 shows the PSF obtained from complete mirror modules with a resolution of 7.5 arcsec HEW on 4 plate pairs and 16.6 arcsec on an entire module of 45 plates. The modules were designed for 50 m focal length optics (XEUS). This result was obtained with a first generation automated stacking robot operating at a radius of 2 m [Collon et al. 2014].

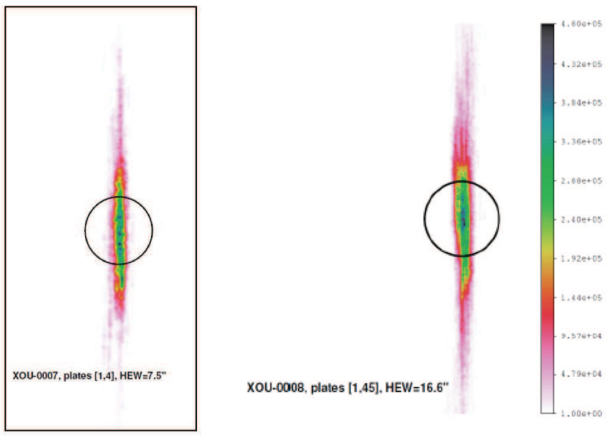

Figure A.4: *: Left: The PSF of a 4 plates measured in X rays. Right: The PSF of a 45 plates measured in X rays. Credits: ESA.*

A second generation stacking robot was then developed to produce f = 20 m optics with a radius of curvature of 0.74 m [Collon et al. 2014]. HEW of 13 arcsec was obtained on 1 plate pair with conical mandrels, this value increasing with the number of plate pairs. Silicon mandrels with a longitudinal curvature were developed, improving the figure error of the integration mandrels from 3.6 (with the sole axial curvature) to 1.9 arcsec (with a longitudinal curvature for the second mandrel) in double reflection, as measured at the X-ray pencil beam facility (XPBF) at BESSY with an energy of 2.8 keV in focus. The wedge uniformity and the plate cleanliness were also improved, resulting in an improved HEW of 4.5 arcsec obtained from 1 plate pair [Collon et al. 2014].

Bibliography

[Adamson & Gast 1997] Adamson, A.W. and A.P. Gast, Physical Chemistry of Surfaces, New York: Wiley-Interscience, (1997)

[Akilian 2008] Akilian, M., "Methods of Improving the Surface Flatness of Thin Glass Sheets and Silicon Wafers", PhD Thesis, Massachusetts Institute of Technology (2008)

[Allured et al. 2014] Allured, R., Cotroneo, V., Johnson-Wilke, R., et al., "Measuring the performance of adjustable X-ray optics with wafefront sensing", Proc. SPIE, 9144, 91441D (2014)

[Allured et al. 2015] Allured, R., Ben-Ami, S., Cotroneo, V., Marquez, V., McMuldroch, S., Reid, P. B., Schwartz, D. A., Trolier-McKinstry, S., Vikhlinin, A. A., Wallace, M.L., " Improved control and characterization of adjustable x-ray optics", Proc. SPIE 9603, 9603iM (2015)

[Angel 1969] Angel, J. R. P., "Polarization of Thermal X-Ray Sources", Astrophysical Journal 158, 219 (1969)

[Aschenbach 2009] Aschenbach, B., "Realization of X-ray telescopes: from design to performance", Experimental Astronomy 26, 95 (2009)

[ATHENA assessment study report 2011] Lumb, D.H., Nandra, K., et al., "ATHENA. The extremes of the Universe: from black holes to large-scale structure", Assessment Study Report, ESA (2011)

[Bavdaz et al. 2010] Bavdaz, M., Collon, M.m Beijersbergen, M., Wallace, K., Wille, E., "X-Ray Pore Optics Technologies and Their Application in Space Telescopes", X-ray Optics and Instrumentation 2010, 295095 (2010)

[Bavdaz 2013] Bavdaz, M., "X-ray optics developments at ESA", Proc. SPIE 8861, 88610L (2013)

[Basso et al. 2014] Basso, S., et al., "A high resolution large x-ray mission based on thin glass: optomechanical design", Proc. SPIE 9144, 91444C (2014)

[IXO-BCV-RE-002 2011] ESA contract 22545 document: IXO PROJECT-Design of a X-ray Optical Unit using glass mirrors, IXO-OAB-TN-03, Issue 1, (2011)

[IXO-OAB-TN-09 2012] ESA contract 22545 document: IXO PROJECT-POC2 design and manufacturing, IXO-OAB-TN-09, Issue 1, (2012)

[Beijersbergen et al. 2004] Beijersbergen, M., Kraft, S., Bavdaz, M., et al., "Development of X-ray pore optics: novel high-resolution silicon millipore optics for XEUS and ultra-low mass glass micropore optics for imaging and timing", Proc. SPIE 5539 , pp. 104-115 (2004)

[Bellazzini et al. 2013] Bellazzini, R., Brez, A., Costa, E., Minuti, M., Muleri, F., Pinchera, M., Rubini, A., Soffitta, P., and Spandre, G., "Photoelectric x-ray polarimetry with gas pixel detectors", Nuclear Instruments and Methods in Physics Research Section A: Accelerators, Spectrometers, Detectors and Associated Equipment 720, 173-177 (2013)

[Biskach et al. 2014] Biskach, M.P., et al., "Alignment and integration of thin, lightweight x-ray optics into modules", Proc SPIE 9144, 914446 (2014)

[Brizzolari 2015] Brizzolari, C., Development of hot-slumped glass mirrors with pressure assistance for the Athena X-ray telescope", MS thesis Università Milano - Bicocca (2015)

[Bobzin et al. 2014] Bobzin, K., Bagcivan, N., Brögelmann, T., Münstermann, T., "Correlation between Chemical Glass Components and the Glass Sticking on Sputtered PtIr Physical Vapour Deposition Coatings for Precision Blank Moulding", Material Sciences and Applications, 5, 316-329 (2014)

[Burwitz et al. 2013] Burwitz, V., Bavdaz, M., Pareschi, G., Collon, M., Burkert, W., Spiga, D., Hartner, D., Ackermann, M., Menz, Benedikt, Civitani, M. "In focus measurements of IXO type optics using the new PANTER X-ray test facility extension", Proc. SPIE 8861, 88611J (2013)

[Canestrari et al. 2006] Canestrari, R., Spiga, D., Pareschi, G., "Analysis of microroughness evolution in x-ray astronomical multilayer mirrors by surface topography with the MPES program and by x-ray scattering", Proc SPIE 6266, 626613 (2006)

Bibliography

[Canestrari et al. 2008] Canestrari, R., Ghigo, M., Basso, S., Spiga, D., Preserpio, L., "Lightweight optical segment prototype for adaptive optics manufactured by hot slumping", Proc SPIE 7015, 70153S (2008)

[Chalifoux et al. 2015] Chalifoux, B., Wright, G., Heilmann, R. K., Schattenburg, M. L., "Ion implantation for figure correction of thin x-ray telescope mirror substrates", 9603, 96031K (2015)

[Chambure et al. 1996] Chambure, D., Lain, R., Van Katwijk, K., Van Casteren, J., Glaude, P., "The Status of the X-ray flight mirror production for the ESA XMM spacecraft", Proc. SPIE 3144 (1996)

[Chan et al. 2015] Chan, K.W., et al., "Alignment, bonding and testing mirrors for lightweight x-ray telescopes", Proc SPIE 9603, 96030Z (2015)

[Charles &Seward] Philip A. Charles, Frederick D. Seward, "Exploring the X-ray universe", (1995)

[Chen & Yi 2008] Chen, Y., Yi, A.Y., "Numerical Simulation and Experimental Study of Residual Stresses in Compression Molding of Precision Glass Optical Components", Journal of manufacturing Science and Engineering, vol. 130, 051012-1 (2008)

[Chen 2010] Chen, Y., "Thermal forming process for precision freeform optical mirrors and micro glass optics", PhD thesis (2010)

[Church 1979] Church, E.L., "Role of surface topography in X-ray scattering", Proc SPIE 184, 196 (1979)

[Church 1988] Church, E.L., "Fractal surface finish", Vol. 27 (1988)

[Church & Takacs 1986] E.L. Church, P.Z. Takacs, "The interpretation of glancing incidence scattering measurements", Proc. SPIE 640, 126-133 (1986)

[Civitani et al. 2010] Civitani, M., Basso, S., Bavdaz, M., Citterio, O., Conconi, P., Gallieni, D., Ghigo, M., Guldimann, B., Martelli, F., Pagano, G., Pareschi, G., Parodi, G., Proserpio, L., Salmaso, B., Spiga, D., Tagliaferri, G., Tintori, M., Wille, E., Zambra, A., "IXO x-ray mirrors based on slumped glass segments with reinforcing ribs: optical and mechanical design, image error budget, and optics unit integration process", Proc. SPIE 7732, 773242 (2010)

[Civitani et al. 2010b] Civitani, M.M., Ghigo, M., Citterio, O. Conconi, P. Spiga, D. Pareschi, G. Proserpio, L., "3D characterization of thin glass x-ray mirrors via optical profilometry", Proc. SPIE 7803, 78030L (2010)

[Civitani et al. 2011] Civitani, M., Basso, S., Bavdaz, M., Citterio, O., Conconi, P., Gallieni, D., Ghigo, B., Martelli, F., Pareschi, G., Parodi, G., Proserpio, L., Sironi, G., Spiga, D., Tagliaferri, G., Tintori, M., Wille, E., Zambra, A., "An Integration Machine for the assembly of the X-ray Optic Units based on thin slumped glass foils for the IXO mission", Proc. SPIE 8147, 81470R (2011)

[Civitani et al. 2013] Civitani, M., Basso, S., Citterio, O., Conconi, P., Ghigo, G., Pareschi, G., Proserpio, L., Salmaso, B., Sironi, G., Spiga, D., Tagliaferri, G., Zambra, A., Martelli, F., Parodi, G., Fumi, P., Gallieni, D., Tintori, M., Bavdaz, M., Wille, E.: "Accurate integration of segmented X-ray optics using interfacing ribs", Optical engineering 52, (9), 091809 (2013)

[Civitani et al. 2013b] Civitani, M., Ghigo, M., Basso, S., Proserpio, L., Spiga, D., Salmaso, B., Pareschi, G., Tagliaferri, G., Burwitz, V., Hartner, G. D., Menz, B., Bavdaz, M., Wille, E., "Direct hot slumping and accurate integration process to manufacture prototypal X-ray Optical Units made of glass", Proc. SPIE Vol. 8861 886110-1 (2013)

[Civitani et al. 2014] Civitani, M., Basso, S., Ghigo, G., Pareschi, G., Salmaso, B., Spiga, D., et al., "X-ray Optical Units made of glass: achievements and perspectives", Proc. SPIE 9144, 914416 (2014)

[Civitani et al. 2015] Civitani, M.M., Basso, S., Ghigo, M., Salmaso, B., Spiga, D., Tagliaferri, G., Vecchi, G., Hartner, G.D., Menz, B., Burwitz, V., Pareschi, G., "Slumped glass optics based on thin hot formed glass segments and interfacing ribs for high angular resolution x-ray astronomy: performances and development status", Proc. SPIE 9603, (2015)

[Coherent Inc. Application report 2008] Coherent Inc. Application report, Laser glass cutting in flat panel display production (2008): https://www.coherent.com/downloads/LaserGlassCuttingInFlatPanelDisplayProduction.pdf

[Collon et al. 2014] Collon, M., et al., "Making the ATHENA optics using Silicon Pore Optics", Proc. SPIE 9144, 91442G (2014)

[Collon et al. 2009] Collon, M. J., et al., "Stacking of silicon pore optics for IXO", Proc. SPIE, 7437 (2009)

[Conconi & Campana 2001] Conconi, P., Campana, S., "Optimization of grazing incidence mirrors and its application to surveying X-ray telescopes", Astronomy Astrophysics 372, 1088 (2001)

[Conconi et al. 2010] Conconi, P., Campana, S., Tagliaferri, G., Pareschi, G., Citterio, O., Cotroneo, V., Proserpio, L., Civitani, M., "A wide field X-ray telescope for astronomical survey purposes: from theory to practice", Monthly Notices of the Royal Astronomical Society 405, 877 (2010)

[Cotroneo et al. 2009] Cotroneo, V., Pareschi, G., Spiga, D., Tagliaferri, G., "Optimization of the reflecting coating for the New Hard X-ray Mission", Proc. SPIE 7437, 743717 (200)

[Cotroneo et al. 2011] Cotroneo, V., Davis, W.N., Reid, P.B., Schwartz, D., Trolier-McKinstry, S., Wilke, R.H.T, "Adjustable grazing incidence x-ray optics: measurement of actuator influence functions and comparison with modeling", Proc. SPIE 8147, 81471R-1 (2011)

[Cotroneo et al. 2012] Cotroneo, V., Davis, W. N., Marquez, V., Reid, P. B., Schwartz, D. A., Johnson-Wilke, R. L., Trolier-McKinstry, S. E., Wilke, R. H. T., "Adjustable grazing incidence x-ray optics based on thin PZT films", Proc. SPIE 8503, 850309 (2012)

[Craig et al. 2000] Craig, W.W., Hailey, C.J., Jimenez-Garate, M., Windt, D.L., "Development of Thermally Formed Glass Optics for Astronomical Hard X-ray Telescopes", Optics Express 178, Vol. 7, No. 4 (2000)

[Craig et al. 2011] Craig, W. W., et al., "Fabrication of the NuSTAR Flight Optics", Proc. SPIE 8147, 81470H (2011)

[Croston et al. 2013] Croston, J.H., Sanders, J.S., et al., "AGN feedback in Galaxy Clusters and Groups", An Athena+ supporting paper, (2013)

[Daoudi et al. 1994] Daoudi, J., Irving, E., Pons, N., "A multivariable predictive control with internal model of a laminated windshield bending furnace". IEEE Conference on Control Applications, Proceedings v.3, 1897-1902 (1994)

[Dell'Agostino et al. 2014] Dell'Agostino, S., Riva, M., Spiga, D., Basso, S., Civitani, M., "Integrated modeling for parametric evaluation of smart x-ray optics", Proc. SPIE 9150, 915021 (2014)

[Dohering et al. 2004] Döhring, T., et al., "Forming mandrels for X-ray telescopes made of modified Zerodur", Proc. SPIE 5168, (2004)

[Doyle 1994] Doyle, P.J. , "Glass Making Today", R.A.N. Publishers, Ohio (1994)

[Egle et al. 2004] Egle, W., et al., "Figuring, polishing, metrology and performance-analyses of Wolter type 1 forming mandrels for the Constellation-X mirror development", Proc. SPIE 5488, (2004)

[Fabiani et al. 2014] Fabiani, S., Costa, E., Del Monte, E., Muleri, F., Soffitta, P., Rubini, A., Bellazzini, R., Brez, A., de Ruvo, L., Minuti, M., Pinchera, M., Sgr, C., Spandre, G., Spiga, D., Tagliaferri, G., Pareschi, G., Basso, S., Citterio, O., Burwitz, V., Burkert, W., Menz, B., Hartner, G., "The Imaging Properties of the Gas Pixel Detector as a Focal Plane Polarimeter", ApJ Suppl. 212, 25 (2014)

[Falanga et al. 2014] Falanga, M., Belloni, T., Casella, P., Gilfanov, M., Jonker, P., King, A., "The physics of accretion onto black holes", Space Science Reviews Vol. 183, Issues 1-4 (2014)

[Fischbach 2010] Fischbach, K.D., "Modeling Sticking Force in Compression Glass Molding Systems", MS thesis of the Ohio State University, (2010)

[Friedrich et al. 2005] Friedrich, P., et al.: "Recent results on manufacturing of segmented x-ray mirrors with slumped glass". Proc. SPIE 5900, 59000W (2005)

[Friedrich et al. 2006] Friedrich, P., Aschenbach, B., Braig, C., Bruninger, H., Budau, B., et al.: "Manufacturing of Wolter-I mirror segments with slumped glass". Proc. SPIE 6266, 62661G (2006)

[Fulcher 1925] Fulcher, G. S. , "Analysis of recent measurements of the viscosity of glasses", J. Am. Ceram. Soc., 8(6), 339-355 and 8(12), 789-794, 1925

[Gaskin et al. 2015] Gaskin, J.A., et al., " The X-ray Surveyor mission: a concept study", Proc. SPIE 9601, 96010J (2015)

[Gordon & Catching 1994] Gordon, T.E., Catching, B.F., "Status of the Advanced X-Ray Astrophysics Facility (AXAF) optics production program", Proc. SPIE 2263, 233 (1994)

[Ghigo et al. 2006] Ghigo, M., Basso, S., Citterio, Mazzoleni, F., Vernani, D. , "Manufacturing of lightweight glass segments for adaptive optics", Proc. SPIE 6272, 62720X (2006)

[Ghigo et al. 2008] Ghigo, M., Canestrari, R., Proserpio, L., Dell'Orto, E., Basso, S., Citterio, O., Pareschi, G.,Parodi, G., "Slumped glass option for making the XEUS mirrors: preliminary design and ongoing developments", Proc. SPIE 7011 (2008)

[Ghigo et al. 2010] Ghigo, M., et al. "Hot slumping glass technology for the grazing incidence optics of future missions, with particular reference to IXO", Proc. SPIE 7732, 77320C (2010)

[Ghigo et al. 2012] Ghigo, M. , Basso, S. , Borsa, F., Bavdaz, M., Citterio, O. , Civitani, M. , et al., "Development of high angular resolution x-ray telescopes based on slumped glass foils", Proc. SPIE 8443, 84430R (2012)

[Gowen 1977] Gowen, R.A., "Stellar X-ray polarimetry from the Ariel-V satellite", Ph.D. thesis, University of Leicester (1977)

[Griffith 1924] Griffith, A.A.: The theory of rupture. The First International Congress for Applied Mechanics, Delft, Netherlands, (1924).

[Harrison et al. 2006] Harrison, F.A., Christensen, F. E., Charles Hailey, W. C., Baumgartner, W., Chen, C. M. H., Chonko, J., Cook, W. R., Koglin, J., Madsen, K.K., Pivavoroff, M., Boggs, S., Smith, D., "Development of the HEFT and NuSTAR focusing telescopes", Experimental Astronomy 20, 131-137 (2006)

[Hock et al. 2003] Hock, M., Schäffer, E., Döll, W., Kleer, G., "Composite coating materials for the moulding of diffractive and refractive optical components of inorganic glasses", Surface and coating technology, 163-164, 689-694 (2003)

[Hailey 2010] Hailey, C.J., "The Nuclear Spectroscopic Telescope Array (NuSTAR): Optics overview and current status", Proc. SPIE 7732, 77320T (2010)

[Inglis 1913] Inglis, C.E.: "Stresses in a plate due to the presence of cracks and sharp corners. Institute of Naval Architecture", (1913)

[Jain Ph.D. thesis 2006] Jain, A., "Experimental study and numerical analysis of compression moulding process for manufacturing precisen aspherical glass lenses", Ph.D. thesis (2006)

[Jimenez et al. 2003] Jimenez-Garate, M. A., Hailey, C. J., Craig, W. W., Christensen, F. E., "Thermal forming of glass microsheets for x-ray telescope mirror segments", Applied Optics 42, 4 (2003)

[Joensen et al. 1995] Joensen K.D., Voutov, P., Szentgyorgyi, A. et al., Appl. Opt. 34, ,7935-7944 (1995)

[Johnson-Wilke et al. 2014] Johnson-Wilke, R.L., Wilke, R.H.T., M. Wallace, M., Ramirez, J.I., Prieskorn, Z., et al., " ZnO thin film transistors and electronic connections for adjustable x-ray mirrors: SMART-X telescope", Proc. SPIE 9208, 920809 (2014)

[Kilaru et al. 2011] Kilaru, K., Ramsey, B. D., Gubarev, m., Gregory, D., "Differential deposition technique for figure corrections in grazing-incidence x-ray optics", Opt. Eng., 50 (10), 106501 (2011)

[Kirkpatrick & Baez1948] Kirkpatrick, P., Baez, A.V., "Formation of Optical Images by X-Rays", J. Opt. Soc. Am. 38, 766 (1948)

[Koglin et al. 2004] Koglin, J.E., Hubert Chen, C.M., Chonko, J., Christensen, F.E., Craig, W.W. et al.: Production and calibration of the first HEFT hard X-ray optics module. Proc. SPIE 5168, 100 (2004)

[Kraft et al. 2005] Kraft, S. et al., "Development of modular high-performance pore optics for the XEUS x-ray telescope", Proc. SPIE 5900, 297-308 (2005)

[Kulp Master thesis 2012] Kulp, A.: "Analysis of Strength Variation in Glass Due to Ion Exchange". Master thesis, Virginia Polytechnic Institute and State University, (2012)

[Liddle & Loveday 2009] Liddle, A., Loveday, J., "The Oxford companion to cosmology", Oxford University Press, USA (2009)

Bibliography

[Maddox & Jenkins 1987] Maddox, P. H., Jenkins, D., "3-Aminopropyltriethoxysilane (APES): a new advance in section adhesion", Journal of Clinical Pathology, 40 (1987)

[Michette 1986] Michette, A.G., "Optical systems for soft X-rays", Springer-Verlag, (1986)

[Milillo 2012] Milillo, "Overflow down-draw with improved glass melt velocity and thickness distribution", http://www.freshpatents.com/-dt20120503ptan20120103019.php

[Nandra et al. 2014] Nandra, K., Barcons, X., Barret, D., Fabian, A., den Herder, J.W., Piro, L., Watson, M.: Athena: "The Advanced Telescope for High Energy Astrophysics. Mission proposal", http://www.the-athena-x-ray-observatory.eu

[Novick 1975] Novick, R., "Stellar and Solar X-Ray Polarimetry", Space Science Review 18, 389-408 (1975)

[O'Dell et al. 1993] O'Dell, S. L., Elsner, R. F., Kodziejczak, J. J., et al., "X-ray evidence for particulate contamination on the AXAF VETA-1 mirrors", SPIE Proc. 1742, 171-182 (1993)

[O'Dell et al. 2011] O'Dell, S. L., Atkins, C., Button, T. W., Cotroneo, V., Davis, W. N., Doel, P., Feldman, C. H., Freeman, M. D., Gubarev, M. V., Kolodziejczak, J. J., Michette, A. G., Ramsey, B. D., Reid, P. B., Rodriguez Sanmartin, D., Saha, T. T., Schwartz, D. A., Trolier-McKinstry, S., Wilke, R. H. T., Willingale, R., Zhang, W. W., "Toward active x- ray telescopes", SPIE 8147, 1Q 14pp (2011)

[Pareschi et al. 2011] Pareschi, G., Basso, S., Bavdaz, M., Citterio, O., Civitani, M. M., Conconi, P., Gallieni, D., Martelli, F., Parodi, G., Proserpio, L., Sironi, G. Spiga, D:, Tagliaferri, G., Tintori, M., Wille, E., Zambra, A., "IXO glass mirrors development in Europe", Proc. SPIE 8147, 81470L (2011)

[Parodi et al. 2011] Parodi, G., Martelli, F., Basso, S., Citterio, O. Civitani, M., Conconi, P., Ghigo, M., Pareschi, G., Zambra, A., "Design of the IXO optics based on thin glass plates connected by reinforcing ribs", Proc. SPIE 8147, 81470Q (2011)

[Petre et al. 2006] Petre, R., at al., "The Constellation-s spectroscopy x-ray telescope: recent technology development", Proc. SPIE 6266, 62661Q (2006)

[Proserpio Ph.D. thesis 2011] Proserpio, L., "Development of the glass slumping technology for the production of the x-ray mirrors aboard the International X-ray Observatory optical module", Ph.D. thesis (2011)

[Proserpio et al. 2010] Proserpio, L., Civitani, M., Ghigo, M., Pareschi, G., "Thermal shaping of thin glass substrates for segmentes grazing incidence active optics", Proc. SPIE 7803, 78030K-2 (2010)

[Proserpio et al. 2011] Proserpio, L., Ghigo, M., Basso, S., Conconi, P., Citterio, O., Civitani, M., Negri, R., Pagano, G., Pareschi, G., Salmaso, B., Spiga, D., Tagliaferri, G., Tintori, M., Terzi, L., Zambra, A. "Production of the IXO glass segmented mirrors by hot slumping with pressure assistance: tests and results", Proc. SPIE 8147, 81470M (2011)

[Proserpio et al. 2013] Proserpio, L., Crimi, G., Salmaso, B., Ghigo, M., D'Este, A., Dall'Igna, R., Silvestri, M., Parodi, G., Martelli, F.: "Evaluation of the surface strength of glass plates shaped by hot slumping process", Proc. SPIE 8861, 88610S (2013)

[Proserpio et al. 2014] Proserpio, L., Basso, S., Borsa, F., Citterio, O., Civitani, M., Ghigo, M., Pareschi, G., Salmaso, B., Sironi, G., Spiga, D., Tagliaferri, G., D'Este, A., Dall'Igna, R., Silvestri, M., Parodi, G., Martelli, F. Bavdaz, M., Wille, E., "Evaluation of the surface strength of glass plates shaped by hot slumping process", Opt. Eng. 53(8), 085101(2014)

[Proserpio et al. 2015] Proserpio, L., at al.: "Addredding the problem of glass thickness variation in the indirect slumping technology", Proc. SPIE 9603, 96030T (2015)

[Raimondi & Spiga 2010] Raimondi, L., Spiga, D., "Self-consistent computation of x-ray mirror point spread functions from surface profile and roughness", Proc. SPIE 7732, 77322Q (2010)

[Raimondi & Spiga 2011] Raimondi, L., Spiga, D., "Point Spread Function of real Wolter-I X-ray mirrors: computation by means of the Huygens-Fresnel principle", Proc. SPIE 8147, 81470Z (2011)

[Raimondi & Spiga 2015] Raimondi, L., Spiga, D., "Mirror for X-ray telescopes: Fresnel diffraction-based computation of point spread functions from metrology", AA 573, A22 (2015)

[Rekhson et al. 1991] Rekhson, S., Lu, Z.H., Day, C., "Computer Modeling of Glass Processing", Coll. Papers from the 52nd Conf. on Glass Problems Nov 12 13, 65-77 (1991)

[Reid et al. 2004] Reid, P. B., Cameron, R. A., Cohen, L., Elvis, M., Gorenstein, P., Jerius, D., Petre, R., Podgorski, W. A., Schwartz, D. A., Zhang, W. W., "Constellation-X to Generation-X: evolution of large collecting area moderate resolution grazing incidence x-ray telescopes to larger area high-resolution adjustable optic", SPIE 5488, 325-334 (2004)

[Reid et al. 2012] Reid, P.B., Aldcroft, T.L., Cotroneo, V., Davis, W., Johnson-Wilke, R.L., et al., "Technology development of adjustable grazing incidence X-ray optics for sub-arcsecond imaging". Proc. SPIE 8443, 8443 (2012)

[Reid et al. 2014] Reid, P.B., Aldcroft, T.L., Allured, R., Cotroneo, V., Johnson-Wilke, R.L., Marquez, V., et al., "Development status of adjustable grazing incidence optics for 0.5 arcsecond x-ray imaging", Proc. SPIE 9208, 920807 (2014)

[Riveros et al. 2014] Riveros, R. E., Bly, V. T., Kolos, L. D., McKeon, K. P., Mazzarella, J. R., Miller, T. M., Zhang, W. W., "Fabrication of single crystal silicon mirror substrates for x-ray astronomical missions", Proc. SPIE 9144, 914445 (2014)

[Salmaso et al. 2011] B. Salmaso, D. Spiga, R. Canestrari, L. Raimondi, "Accurate modeling of periodic and graded multilayer x-ray scattering from surface microroughness characterization", Proc. SPIE 8147, 814710 (2011)

[Salmaso et al. 2013] Salmaso, B., Spiga, D., Canestrari, R., Raimondi, L., "X-ray scattering of periodic and graded multilayer: comparison of experiments to simulation from surface microroughness characterization", Nuclear Instruments and Methods in Physics Research A, 7, 1006-113, (2013)

[Salmaso IR01-2013] Salmaso, B. and Bianco, A. and Proserpio, L. and Ghigo, M. and Spiga, D., "IXO glasses cleaning procedure after slumping: removing residuals affecting the high frequency region", IR-OAB-2013-01 (2013)

[Salmaso IR12-2013] Salmaso, B., Basso, S., "LTP profiles of AF32 glasses with FEA correction: a method to remove spurious mid-frequency errors", IR-OAB-2013-12 (2013)

[Salmaso IR14-2013] Salmaso, B., Spiga, D., "Fine-tuning of slumped AF32 glasses on a Zerodur K20 mould", IR-OAB-2013-14 (2013)

[Salmaso et al. 2014] Salmaso, B., Basso, S., Brizzolari, C., Civitani, M.M., Ghigo, M., Pareschi, G., et al., "Production of thin glass mirrors by hot slumping for X-ray telescopes: present process and ongoing development", Proc SPIE 9151, 91512W (2014)

[Salmaso et al. ICSO2014] Salmaso, B., Basso, S., Brizzolari, C., Civitani, M., Ghigo, M., Pareschi, G., Spiga, D., Tagliaferri, G., Vecchi, G., "Direct hot slumping of thin glass foils for future generation X-ray telescopes: current state of the art and future outlooks", Proc. ICSO, (2014)

[Salmaso IR01-2014] Salmaso, B., Brizzolari, C., Spiga, D., Rossi, M., "Characterization of the Zerodur K20-20 cylindrical slumping mould polished by HELLMA", INAF/OAB internal report 01/2014

[Salmaso IR02-2014] Salmaso, B., Brizzolari, C., Spiga, D., From AF32 to Eagle XG: characterization of glasses slumped on Zerodur K20-10 mould", INAF/OAB internal report 02/2014

[Salmaso IR11-2014] Salmaso, B., Brizzolari, C., Civitani, M., Spiga, D., "Characterization of the Silicon cylindrical slumping mould polished by HELLMA", INAF/OAB internal report 11/2014

[Salmaso IR15-2014] Salmaso, B., Brizzolari, C., Civitani, M., Spiga, D., Sanvito, G., "Slumping Eagle XG on new Zerodur K20 MK20-20 mould", INAF/OAB internal report 15/2014

[Salmaso IR03-2015] Salmaso, B., Brizzolari, C., Spiga, D., Arcangeli, L., Rossi, M., "Characterization of the Zerodur K20-20B cylindrical slumping mould polished by HELLMA", INAF/OAB internal report 03/2015

[Salmaso IR04-2015] Salmaso, B., Brizzolari, G., Spiga, D., "LTP and ZYGO comparison of the profile measurements of MK20-20B slumping mould", INAF/OAB internal report 04/2015

[Salmaso et al. 2015] Salmaso, B., Brizzolari, C., Basso, S., Civitani, M.M., Ghigo, M., Pareschi, G., Spiga, D., Tagliaferri, G., Vecchi, G., "Slumped Glass Optics for X-ray telescopes: advances in the hot slumping assisted by pressure", Proc SPIE 9603, 96030O (2015)

[Schattenburg et al. 2015] Schattenburg, M.L., et al., "Progress report on air bearing slumping of thin glass mirrors for x-ray telescopes", Proc. SPIE 9603, (2015)

[Scherer 1986] Scherer, George W., "Relaxation in glass and composites" (1986)

[Schroder et al. 2007] Schröder, S., Feigl, T., Duparré, A., Tünnerrmann, A., "EUV reflectance and scattering of Mo/Si multilayers on differently polished substrates", Optics Express, Vol. 51 No. 21, (2007)

[She et al. 2015] She, R., Feng, H., Soffitta, P., Muleri, F., Xu, R., Li, H., Bellazzini, R., Wang, Z., Spiga, D. , Minuti, M., Brez, A., Spandre, G., Pinchera, M., Sgro, C., Baldini, L., Wen, M., Shen, Z., Pareschi, G. , Tagliaferri, G. , Tayabaly, K. , Salmaso, B. , Zhan, Y., "LAMP: a micro-satellite based soft x-ray polarimeter for astrophysics edit this publication", Proc. SPIE 9601, 96010I (2015)

[Shelby 2005] Shelby, J.E., "Introduction to glass science and technology", The royal society of chemistry (2005)

[Signorato et al. 1998] Signorato, R., Hignette, O. Goulon, J., "Multi-segmented piezoelectric mirrors as active/adaptive optics components", Journal of Synchrotron Radiation, 5, 797 (1998)

[Spiga Ph.D. thesis 2005] Spiga, D., "Development of multilayer-coated mirrors for future X-ray telescopes", Ph.D. Università deli Studi Milano Bicocca (2005)

[Spiga 2007] Spiga, D., "Analytical evaluation of the X-ray scattering contribution to imaging degradation in grazing-incidence X-ray telescopes", Astronomy Astrophysics 468, issue 2 pp. 775-784 (2007)

[Spiga et al. 2007] Spiga, D., Pareschi, G., Cotroneo, V., Canestrari, R., Mirone, A., Ferrero, C., Ferrari, C., Lazzarini, L., Vernani, D., "Multilayer coatings for x-ray mirrors: extraction of stack parameters from x-ray reflectivity scans and comparison with transmission electron microscopy results", Opt. Eng. 46, 086501 (2007)

[Spiga 2008] D. Spiga, "Extraction of multilayer coating parameters from X-ray reflectivity data", Modern developments in X-ray and neutron optics, p. 233-251, Springer Series in Optical Sciences (2008)

[Spiga 2011] Spiga, D., "Optics for X-ray telescopes: analytical treatment of the off-axis effective area of mirror in optical modules", AA 529, A18 (2011)

[Spiga et al. 2013] Spiga, D., Basso, S., Bavdaz, M., Burwitz, V., Civitani, M., Citterio, O., Ghigo, M., Hartner, G., Menz, B., Pareschi, G., Proserpio, L., Salmaso, B., Tagliaferri, G., Wille, E., "Profile reconstruction of grazing-incidence x-ray mirrors from intra-focal x-ray full imaging", Proc. SPIE 8861, 88611F (2013)

[Spiga IR02-2013] Spiga, D., Basso, S., Civitani, M., "Extending the INAF/OAB ultraviolet vertical optical bench to a 20 m focal length", INAF/OAB internal report 02/2013

[Spiga et al. 2014] Spiga, D., Barbera, M., Basso. S., Civitani, M., Collura, A., Dell'Agostino, S., Lo Cicero, U., Lullo, G., Pellicciari, C., Riva, M., Salmaso, B., Sciortino, L., "Active shape correction of a thin glass/plastic X-ray mirror", Proc. SPIE 9208, 92080A-3, (2014)

[Spiga & Raimondi 2014] Spiga, D., Raimondi, L., "Predicting the angular resolution of X-ray mirrors", SPIE Newsroom 005233 (2014)

[Spiga IR05-2011] Spiga, D., Proserpio, L., Pagano, G., Salmaso, B., "Profile characterisation of slumped glasses for the IXO backup optics project, phase 2", IR-OAB-2011-05 (2011)

[Spiga et al. 2015] Spiga, D., Barbera, M., Collura, A., Basso, S., Candia, R., Civitani, M., Di Bella, M., Di Cicca, G., Lo Cicero, U., Lullo, G., Pellicciari, C., Riva, M., Salmaso, B., Sciortino, L., Varisco, S., "Manufacturing and testing a thin glass mirror shell with piezoelectric active control", Proc. SPIE 9603, 96031N (2015)

Bibliography

[Spiga et al. 2015b] Spiga, D., Barbera, M., Collura, A., Basso, S., Candia, R., Civitani, M., Di Bella, M., Di Cicca, G., Lo Cicero, U., Lullo, G:, Pellicciari, C., Riva, M., Salmaso, B., Sciortino, L., Varisco, S., "Manufacturing an active X-ray mirror prototype in thin glass", Journal of Synchrotron Radiation, Vol 23, Issue 1 (2015), (2016)

[Spiga et al. 2015c] Spiga, D. , Salmaso, B. , She, R., Tayabaly, K. , Wen, M., Banham, R., Costa, E., Feng, H., Giglia, A., Huang, Q., Muleri, F., Pareschi, G. , Soffitta, P., Tagliaferri, G. , Valsecchi, G., Wang, Z., "Testing multilayer-coated polarizing mirrors for the LAMP soft X-ray telescope", Proc. SPIE 9603, 96031B (2015)

[Stearns et al. 1998] Stearns, D.G., Gaines, D.P., Sweeney, D.W., Gullikson, E.M., "Nonspecular x-ray scattering in a multilayer-coated imaging system", J. Appl. Phys. 84, 1003 (1998)

[Stokes Ph.D. thesis 1998] Stokes, Y.M., "Very viscous flows driven by gravity, with particular application of slumping of molten glass", Ph.D. thesis, University of Adelaide (1998)

[Sung 2013] Sung, E., "Non-touch thermal air-bearing shaping of x-ray telescope optics", Proc. SPIE 8861, 88610R (2013)

[Tayabaly IR05-2014] Tayabaly, K. , Spiga, D. , Salmaso, B. , Valsecchi, G., Banham, R., Missaglia, N., Pareschi, G. , Tagliaferri, G., "Electroformed nickel samples for the polarimetric LAMP X-ray telescope: sample roughness characterization", IR-OAB-2014-05 (2014)

[Takacs et al. 1987] Takacs, P.Z., Qian, S., Colbert, J., "Design of a long trace surface profiler", Proc. SPIE 749 (1987)

[Tao et al. 2013] Tao, B., Shen, L., Yi, A., Li, M., Zhou, J., "Reducing refractive index variations in compression molded lenses by annealing", Optics and photonics journal 3, 118-121 (2013)

[Trevisiol et al. 2003] Trevisiol, E., Le Berre-Anton, V., Leclaire, J., Pratviel, G., Caminade, A.M., Majoral, J.P., Franaois, J. M. , Meunier, B., "Dendrislides, dendrichips: a simple chemical functionalization of glass slides with phosphorus dendrimers as an effective means for the preparation of biochips", New J. Chem., 27, 1713 (2003)

[Underwood 2009] Underwood, J.H., "X-ray data booklet, Section 4.1: Multilayers and Crystals", LBNL University of California Berkeley (2009)

[Uhlmann et al. 1980] Uhlmann, D.R., ed. Elasticity and Strength in Glasses. Glass: Science and Technology. Vol. 5, Academic Press: New York. 218-251 (1980).

[Ulmer et al. 2012] Ulmer, M. P., Wang, X., Cao, J., Savoie, J., Bellavia, B., Graham, M. E., Vaynman, S., "Progress report on using magneto-strictive sputtered thin films to modify the shape of a x-ray telescope mirror", SPIE 8503, 85030C (2012)

[Van Speybroeck & Chase 1972] van Speybroeck, L.P., Chase, R.C., "Design parameters of paraboloid-hyperboloid telescopes for X-ray astronomy", Vol. 11 (1972)

[Vernani et al. 2006] Vernani, D., Pareschi, G., Mazzoleni, F., Spiga, D., Valtolina, R., "Surface characterization of superpolished substrates for X- ray and neutron multilayer optics", Mater. Struct. 13, 71-75 (2006)

[Vikhlinin et al. 2012] Vikhlinin, A., Reid, P., Tananbaum, H., Schwartz, D. A., Forman, W. R., Jones, C., Bookbinder, J., Cotroneo, V., Trolier-McKinstry, S., Burrows, D., Bautz, M. W., Heilmann, R., Davis, J., Bandler, S. R., Weisskopf, M. C., Murray, S. S., "SMART-X: Square Meter Arcsecond Resolution x-ray Telescope", Proc. SPIE 8443, 16 12pp (2012)

[Von Bieren 1983] von Bieren, K., "Interferometry of wavefronts reflected off conical surfaces" Appl. Opt. 22, 2109 (1983)

[Wen et al. 2015] Wen, M., Huang, Q., She, R., Jiang, L., Zhang, Z., Wang, Z., Feng, H., Spiga, D. , Giglia, A., "High efficiency carbon-based multilayers for LAMP at 250 eV edit this publication", Proc. SPIE 9603, 96031A (2015)

[Weisskopf et al. 1976] Weisskopf, M. C., Cohen, G. G., Kestenbaum, H. L., Novick, R., Wolff, R. S., and Landecker, P. B., "The X-ray polarization experiment on the OSO-8", NASA Special Publication 389, 81-96 (1976)

[Weisskopf et al. 1978] Weisskopf, M. C., Silver, E. H., Kestenbaum, H. L., Long, K. S., Novick, R., "A precision measurement of the X-ray polarization of the Crab Nebula without pulsar contamination", ApJL220, L117-L121(1978)

[Weisskpft 2012] Weisskopt, M.C. "Chandra X-ray optics", Optical Engineering 51(1), 011013 (2012)

[Wilke et al. 2013] Wilke, R. H. T., Johnson-Wilke, R. L., Cotroneo, V., Davis, W. N., Reid, P. B., Schwartz, D. A., Trolier- McKinstry, S., "Sputter deposition of PZT piezoelectric films on thin glass substrates for adjustable x-ray optics", Apl. Opt. 52, 3412-3419 (2013).

[Windt 1998] Windt, D.L., "IMD-software for modeling the optical properties of multilayer films", Comput. Phys. 12, 360370 (1998)

[Windt 2015] Windt, D.L. "Advancement in hard X-ray multilayers for X-ray astronomy", Proc. SPIE 9603, 96031C (2015)

[Wille et al. 2015] Wille, E., Bavdaz, M., Oosterbroek, T., Collon, M., Ackermann, M., Guenther, R., Vacanti, G., Vervest, M., Yanson, A., vanBaren, C., Haneveld, J., Koelewijn, A., Leenstra, A., Pareschi, G. , Civitani, M. , Conconi, P., Spiga, D. , Valsecchi, G., Marioni, F., Zuknik, K., Schweitzer, M., "Silicon Pore Optics Mirror Modules for Inner and Outer Radii", Proc. SPIE 9603, 96030L (2015)

[Willingale et al. 2014] Willingale, R., Pareschi, G., Christensen, F., den Herder, J-W., Ferreira, D., Jakobsen, A., Ackermann, M., Collon, M., Bavdaz, M., "Science requirements and optimization of the silicon pore optics design for the Athena mirror", Proc. SPIE 9144, 91442E (2014)

[Winter et al. 2010] Winter, A., Vongehr, M., Friedrich, P.: Light weight optics made by glass thermal forming for future x-ray telescopes. Proc. SPIE 7732, 77320B (2010)

[Winter et al. 2012] Winter, A., et al., "Leight-weight glass optics for segmented X-ray mirrors", Proc. SPIE 8450, 84502E (2012)

[Winter et al. 2013] Winter, A., et al., "Leight-weight glass mirror systems for future x-ray telescopes", Proc. SPIE 8861, 88610Q (2013)

[Winter et al. 2014] Winter, A., et al., "Progress on indirect glass slumping for future x-ray telescope optics", Proc. SPIE 9144, 91441C (2014)

[Winter et al. 2015] Winter, A., et al., "Indirect glass slumping for future x-ray missions: overview, status and progress", Proc. SPIE 9603, 96030S (2015)

[Whitted 1980] Whitted, T., "An Improved Illumination Model for Shaded Display", Commun. ACM 23, 343-349 (1980)

[Wolter 1952] Wolter, H., Glancing Incidence Mirror Systems as Imaging Optics for X-rays in Ann. Physik, vol. 10, 1952, p. 94

[Zhang et al. 2003] Zhang, W.W., Chan, Kai-Wing, Content, D., Owens, S., Petre, R., Serlemitsos, P., Saha, T., Song, Y., "Development of mirror segments for the Constellation-X observatory" Proc. SPIE 4851, (2003)

[Zhang et al. 2007] Zhang, W.W., Bolognese, J., Chan, K.W., Content, D.A., Hadjimichael, T.J., Charles He, et al.: "Constellation-X mirror technology development", Proc. SPIE 6688, 668802, (2007)

[Zhang et al. 2010] Zhang, W.W., Atanassova, M., Biskach, M., et al.: "Mirror Technology Development for the International X-ray Observatory Mission (IXO)". Proc. SPIE 7360, 73600J (2010)

[Zhang et al. 2014] Zhang, W.W., et al.: "Affordable and lightweight high-resolution x-ray optics for astronomical missions", Proc. SPIE 9144, 914415-1 (2014)

[Zhao et al. 2004] Zhao, Ping and Jerius, Diab H. and Edgar, Richard J. and Gaetz, Terrance J. and Van Speybroeck, Leon P. and Biller, Beth and Beckerman, Eli and Marshall, Herman L., "Chandra X-ray Observatory mirror effective area", Proc. SPIE 5165, 482 (2004)

[Web reference: LMXB] http://www-xray.ast.cam.ac.uk/xray_introduction/Blackholebinary.html

[Web reference: SNR] http://sci.esa.int/integral/50934-integral-finds-titanium-in-supernova-remnant-1987a/

[Web reference: Chandra] http://cxc.cfa.harvard.edu/cdo/about_chandra/

[Web reference: XMM] http://xmm.esac.esa.int/external/xmm_user_support/documentation/uhb_2.1/node37.html

[Web reference: Schott-1] http://www.nec-schott.co.jp/english/download/schott-brochure-technical-glasses_english.pdf?highlighted_text=fused+silica+data+sheet

[Web reference: Schott-2] http://www.us.schott.com/advanced_optics/english/about-ao/competencies/process-capabilities.html

[Web reference: Britglas] http://www.britglass.org.uk/types-of-glass

[Web reference: Zerodur-1] http://fp.optics.arizona.edu/optomech/student\%20reports/tutorials/Tutorial_Russell,\%20Robert.pdf

[Web reference: Zerodur-2] http://www.schott.com/advanced_optics/german/download/schott_zerodur_katalog_july_2011_en.pdf

[Web reference: FirstContact] http://www.photoniccleaning.com

[Web reference: 2020 NASA Decadal Survey]

[Web reference: D263] http://www.schott.com/advanced_optics/english/download/schott-d-263-t-eco-thin-glass-may-2013-eng.pdf

[Web reference: AF32] http://www.schott.com/advanced_optics/german/download/schott-af-32-eco-thin-glass-may-2013-eng.pdf

[Web reference: Eagle] https://abrisatechnologies.com/specs/Corning\%20Eagle\%20XG\%20Spec\%20Sheet.pdf

[Web reference: Gorilla] http://www.corninggorillaglass.com/uploads/kcfinder/files/GG2\%20PI\%20Sheet\%20Rev\%20b_050912.pdf

[Web reference: K20] http://www.schott.com/advanced_optics/german/download/schott_zerodur_katalog_july_2011_en.pdf

[Web reference: SiO2] http://www.corning.com/media/worldwide/csm/documents/5bf092438c5546dfa9b08e423348317b.pdf

[Web reference: Si] http://www.el-cat.com/silicon-properties.htm

[Web reference: Si3N4] http://www.bettinitextile.it/ENG/2_Materials_04.htm

[Web reference: Al2O3] http://www.bettinitextile.it/ENG/2_Materials_04.htm

Acknowledgments

We have to go back to 2009 when the story started.
Graduated in 1993, working in a semiconductor company for eight years, being at home to grow my three wonderful kids for six years, I started looking back again for science in 2009. My e-mail to the Observatory in Merate, explaining who I was and what my wishes were, found two great open persons: Giovanni Pareschi, at that time the Director of the Observatory, and Daniele Spiga, which became my supervisor. I keep on trying to figure out how this all went. The only thing I am sure of is that in 2009 I started working at the Observatory. Therefore, first and foremost I would like to thank Giovanni and Daniele: their trust, guidance, enthusiasm and insight during my research were exactly what I needed at the beginning and along my Ph.D. work. The optimism, the strong happy spirit and the generosity of Giovanni are very necessary to always go further and overcome the difficulties. The deep knowledge and the rigorous method of Daniele were very much needed by my neurons to start working again. I never cease to admire and value his ability to quickly get to the heart of a matter, and give, what has always proved to be, sound advice and direction.

I also appreciate the suggestions, assistance and comments of all the Observatory members whom I had a chance to work with during the course of this research, especially my tutor Roberto della Ceca, and Paolo D'Avanzo for being the first to answer to my infinite questions.

I owe many thanks to the members of my research group, for being more than just colleagues. Thank you for all your support: Laura Proserpio who introduced me to the world of slumping; Mauro Ghigo with his skills in realizing new ideas, and his precious support in developing my ideas; Marta Civitani for her measurements with the CUP; Stefano Basso for his help with the Finite Element Analysis; Gabriele Vecchi for useful discussion; Rodolfo Canestrari for his first support on the IDL programming on multilayers and for his prompt help when necessary; Claudia Brizzolari for sharing the work during her master thesis at INAF-OAB; Joanna Holyszko for her help since last september when I was mostly focused on writing my thesis. A special thought goes to Kashmira Tayabaly, for the nice time spent together, for the long talks, for the perseverance in organising our group meeting, so useful, so profitable.

Thanks are also due to Andrea Bianco for his direction and suggestions regarding chemistry matters and for the happy teas together, Giorgio Pariani for his help with the ZYGO interferometer, Marco Riva and Matteo Aliverti for the great help in pressure and temperature data acquisition.

I would also like to thank the staff of the Work Shop, particularly Sergio Cantù, for solving my mechanical problems with the instruments and realising the pieces I needed.

I want to mention also Rachele Millul, Raffaella Ferrara, and Roberto Moncalvi whose always thorough given help with administrative matters has been much appreciated.

Many persons external to the Observatory helped me in this research. I would like to thank

Marcos Bavdaz and Eric Wille from ESA for their guidance on the IXO-backup project, William Zhang from NASA/GSFC for open discussion on the hot slumping process, Vadim Burwitz for his friendly support at PANTER. I am indebted with Joseph Canale and Scott Van Etten, both of Corning Inc. NY, for provision of data on properties of specific Corning glasses. My thanks goes to Yves Suppiger from EuropTec for the kindness and the support in the tempering of Gorilla glass. Thanks also goes to Thorsten Doehring for useful information on the Zerodur K20. I thank Roberto Dall'Igna from Stazione Sperimentale del Vetro for helping me in the world of glass properties. Giancarlo Parodi, Enrico Buratti and Primo Attinà are also acknowledged for very useful discussions during my work on Gorilla glass. Special gratitude goes to external companies who gave me a strong support providing their facilities: Danilo Mandelli, Marco Negri and Gianfranco Giuliani from Lenti Srl for the dip coating, and Giuliano Sanvito from Gambetti Kenologia Srl for the plasma etch of slumped glass foils. Finally all the group from CfA is acknowledged for their collaboration and profitable meetings and discussions.

On a personal note, I have been blessed to have three wonderful kids: they have been my source of inspiration and strength. A special thank to all my family for help and support. Finally, to my cat for sitting always with me in the part of the thesis written at home, and to my frog for always shining for me.

Io intendo per scultura quella che si fa per forza di levare.

Michelangelo Buonarroti